

RAREFACTION WAVE GUN PROPULSION

by

Eric Lee Kathe

A Thesis Submitted to the Graduate

Faculty of Rensselaer Polytechnic Institute

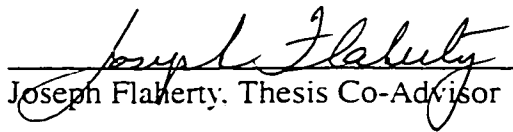
in Partial Fulfillment of the

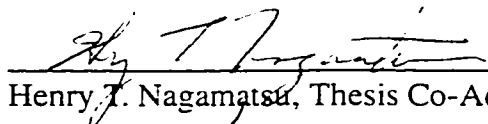
Requirements for the Degree of

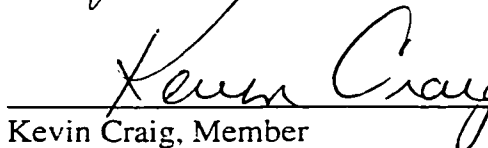
DOCTOR OF PHILOSOPHY

Major Subject: Mechanical Engineering

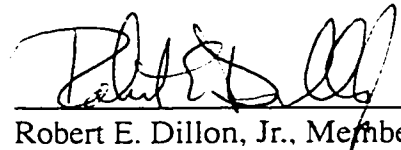
Approved by the  
Examining Committee:

  
Joseph Flaherty, Thesis Co-Advisor

  
Henry T. Nagamatsu, Thesis Co-Advisor

  
Kevin Craig, Member

  
Stephen Derby, Member

  
Robert E. Dillon, Jr., Member

  
Henrik Hagerup, Member

  
Henry Snick, Jr., Member

Rensselaer Polytechnic Institute  
Troy, New York

May 2002

Report Documentation Page				Form Approved OMB No. 0704-0188	
Public reporting burden for the collection of information is estimated to average 1 hour per response, including the time for reviewing instructions, searching existing data sources, gathering and maintaining the data needed, and completing and reviewing the collection of information. Send comments regarding this burden estimate or any other aspect of this collection of information, including suggestions for reducing this burden, to Washington Headquarters Services, Directorate for Information Operations and Reports, 1215 Jefferson Davis Highway, Suite 1204, Arlington VA 22202-4302. Respondents should be aware that notwithstanding any other provision of law, no person shall be subject to a penalty for failing to comply with a collection of information if it does not display a currently valid OMB control number.					
1. REPORT DATE <b>18 MAY 2002</b>		2. REPORT TYPE <b>N/A</b>		3. DATES COVERED <b>-</b>	
4. TITLE AND SUBTITLE <b>Rarefaction Wave Gun Propulsion (RAVEN)</b>				5a. CONTRACT NUMBER	
				5b. GRANT NUMBER	
				5c. PROGRAM ELEMENT NUMBER	
6. AUTHOR(S)				5d. PROJECT NUMBER	
				5e. TASK NUMBER	
				5f. WORK UNIT NUMBER	
7. PERFORMING ORGANIZATION NAME(S) AND ADDRESS(ES) <b>Rensselaer Polytechnic Institute, Troy, NY</b>				8. PERFORMING ORGANIZATION REPORT NUMBER	
9. SPONSORING/MONITORING AGENCY NAME(S) AND ADDRESS(ES)				10. SPONSOR/MONITOR'S ACRONYM(S)	
				11. SPONSOR/MONITOR'S REPORT NUMBER(S)	
12. DISTRIBUTION/AVAILABILITY STATEMENT <b>Approved for public release, distribution unlimited</b>					
13. SUPPLEMENTARY NOTES					
14. ABSTRACT					
15. SUBJECT TERMS					
16. SECURITY CLASSIFICATION OF:			17. LIMITATION OF ABSTRACT <b>SAR</b>	18. NUMBER OF PAGES <b>316</b>	19a. NAME OF RESPONSIBLE PERSON
a. REPORT <b>unclassified</b>	b. ABSTRACT <b>unclassified</b>	c. THIS PAGE <b>unclassified</b>			

LIST OF TABLES .....	viii
LIST OF FIGURES .....	x
ACKNOWLEDGEMENTS .....	xvi
ABSTRACT .....	xviii
Part 1: INTRODUCTION.....	1
Part 2: HISTORICAL BACKGROUND .....	5
2.1    The Davis Gun .....	5
2.2    Muzzle Brakes .....	6
2.3    Rocket Launcher.....	6
2.4    Recoilless Rifles .....	8
2.5    Front Orifice Recoilless Gun .....	12
2.6    Regenerative Liquid Propellant Recoilless Rifles .....	14
Part 3: DESCRIPTION OF GUN PROPULSION .....	15
3.1    Energy Content of Propellants .....	15
3.2    Closed-Breech Interior Ballistics .....	18
3.2.1    A Brief Description of the Interior Ballistics of a Typical Gun..	18
3.2.2    Empirical Performance Relationship for Closed-Breech Guns ..	23
3.3    Recoilless Gun Ballistics .....	26
3.3.1    The Perforated Cartridge Case .....	27
3.3.2    Interior Ballistics of a Recoilless Rifle. ....	29
3.3.3    Observations on Propulsive Stability of a Recoilless Rifle .....	31
3.3.4    Empirical Performance Relationship for Recoilless Rifles .....	32
3.4    Davis Gun Ballistics .....	34
3.4.1    Empirical Performance Relationship for Davis Guns. ....	35
3.5    Front Orifice Recoilless Gun .....	38
3.5.1    The Interior Ballistics of a Front Orifice Recoilless Rifle.....	38
3.5.2    Performance Relationship for a Front Orifice Recoilless Rifle ..	39
3.6    Graphical Representation of Empirical Relationships .....	40

Part 4: RAVEN PROPULSION .....	42
4.1    A Brief Description.....	42
4.1.1    Approximate Delay Time for Synchronized Venting .....	43
4.1.2    Zero Gas Velocity Zone .....	44
4.1.3    Reduced Barrel Heating .....	44
4.1.4    Percentage of Gases Ejected Rearward .....	45
4.2    Upper Bound on Recoil Abatement .....	45
4.2.1    Operating Temperatures Within a Gun.....	46
4.2.1.1    Reservoir Temperature at Shot-Exit.....	47
4.2.1.2    Sensible Temperature at Shot-Exit.....	49
4.2.2    Flow Through a Nozzle .....	50
4.2.3    Tabulated Results .....	58
4.2.4    A Parametric Study.....	59
4.2.4.1    Estimation of Gas Momentum .....	60
4.2.4.2    The Effect of a Muzzle Brake.....	61
4.2.4.3    Recoil Reduction Potential of RAVEN .....	64
Part 5: DESIGN AND DEVELOPMENT OF RAVEN 35MM TEST FIXTURE.....	67
5.1    Basic Parameters of the Fielded 35mm System .....	67
5.1.1    The 35mm Oerlikon KD Series Gun .....	67
5.1.2    The Oerlikon 35mm TP Practice Shell.....	67
5.1.3    Geometry of the 35mm TP Round .....	68
5.1.3.1    Cartridge Case Volume.....	69
5.1.3.2    Length From Back of Case to Base of Projectile .....	70
5.1.4    Rifling.....	70
5.1.5    Bullet Resistance Curve .....	71
5.1.6    Propellant Chemical Properties .....	72
5.1.7    Propellant Grain Geometry.....	74
5.1.8    Interior Ballistics.....	75
5.2    Mechanics of Venting .....	76
5.2.1    Five Principal Requirements of a RAVEN Vent.....	76
5.2.1.1    Reliable Vent Timing .....	77
5.2.1.2    Flow Area Comparable to Bore .....	77



5.2.1.3	Swift Operation . . . . .	77
5.2.1.4	Erosion Tolerance . . . . .	78
5.2.1.5	Minimize Degradation of Muzzle Velocity . . . . .	78
5.2.2	Vent Commencement Time. . . . .	78
5.2.3	Blow-Back Recoil and the Inertial Breech RAVEN Vent. . . . .	79
5.2.4	Cartridge Case Notch . . . . .	82
5.2.5	Vent Flow Area . . . . .	83
5.2.6	Speed of Opening . . . . .	85
5.2.7	Mass of the Inertial Breech. . . . .	85
5.2.8	Shear Plug. . . . .	87
5.2.9	Vent Geometry . . . . .	90
5.2.9.1	Computing the Distance to the Vent Port . . . . .	90
5.2.9.2	Shape of the Vent Port . . . . .	93
5.2.9.3	Configurations Tested. . . . .	94
5.3	Recoil Buffering . . . . .	96
5.3.1	General Approach . . . . .	96
5.3.2	Primary Recoil Brakes . . . . .	97
5.3.3	Secondary Recoil and Gun Mount . . . . .	102
5.4	Non-Venting Benchmark . . . . .	103
5.5	Sensors Employed. . . . .	105
5.5.1	Ballistic Pressure Probes. . . . .	105
5.5.2	Thermocouples. . . . .	105
5.5.3	Recoil Motion . . . . .	106
5.5.4	Muzzle Velocity . . . . .	107
Part 6: EXPERIMENTAL INVESTIGATION OF RAVEN . . . . .		109
6.1	Conduct of the Experiment. . . . .	109
6.1.1	First Function Tests. . . . .	109
6.1.2	Video of the First RAVEN firing . . . . .	110
6.1.3	Pressure Data . . . . .	113
6.1.4	Primary Recoil Arrestors . . . . .	115
6.1.5	Test Matrix Evaluated. . . . .	118
6.1.6	Corrupted or Missing Data: NaN. . . . .	118

6.2	Measured Effect on Projectile Propulsion .....	119
6.3	Measured Ballistic Pressure Data .....	121
6.3.1	Effect on Peak Pressure .....	124
6.3.2	Juxtaposition of Venting to Non-Venting Cases .....	125
6.3.3	Determination of Projectile Traverse .....	127
6.3.4	Determination of Rarefaction Wave Front Traverse .....	127
6.3.5	Spatial Pressure Gradient .....	133
6.3.6	Combined Pressure Travel Time Curves .....	135
6.3.7	Measured Vent Time and Relative Projectile Travel .....	137
6.3.8	Integrated Chamber Pressure Impulse .....	139
6.4	Measured Recoil Results .....	142
6.4.1	Challenges to Achieve Free Recoil .....	142
6.4.1.1	Premature Engagement of the Secondary Recoil Brakes .....	142
6.4.1.2	Incomplete Primary Braking .....	142
6.4.1.3	Friction .....	143
6.4.2	Phase-Plane Representation of Recoil Motion .....	144
6.4.3	Determination of Measured Recoil Momentum .....	150
6.5	Effect on Barrel Heating .....	152
Part 7: THEORY .....		155
7.1	Lumped Parameter Interior Ballistics Model .....	155
7.1.1	Equation of Motion for the Projectile .....	155
7.1.2	Equation of Motion for the Recoiling Mass .....	157
7.1.2.1	Forces Applied to the Gun Barrel .....	160
7.1.2.2	Forces Acting on the Breech .....	161
7.1.2.3	Closed-Breech Recoil .....	161
7.1.2.4	Blow-Back Recoil .....	162
7.1.2.5	Transitional Recoil .....	162
7.1.3	Propellant Burning Rate .....	164
7.1.3.1	Propellant Ignition .....	166
7.1.4	Propellant Progressivity .....	167
7.1.4.1	Form Function for Propellant .....	167
7.1.4.2	Inhibited Propellants .....	170
7.1.5	Gas Property Gradient Model .....	173

7.1.5.1	Pressure Gradient . . . . .	175
7.1.5.2	Propellant Gas Density . . . . .	175
7.1.5.3	Temperature Gradient . . . . .	176
7.1.5.4	Sonic Speed Gradient . . . . .	177
7.1.5.5	Velocity Gradient . . . . .	177
7.1.5.6	Mapping Axial Position to Volume . . . . .	178
7.1.6	Heat Transfer to Gun and Bullet . . . . .	179
7.1.7	Energy Sinks . . . . .	181
7.1.7.1	Energy Lost to Projectile Translation . . . . .	182
7.1.7.2	Energy Lost to Projectile Rotation . . . . .	182
7.1.7.3	Energy Lost To Kinetic Energy of Propellant . . . . .	182
7.1.7.4	The Energy Lost to Projectile Friction . . . . .	183
7.1.7.5	The Energy Lost to Breech Friction . . . . .	183
7.1.7.6	The Energy Lost to Recoil Kinetic Energy . . . . .	183
7.1.7.7	Energy Lost to Air Resistance . . . . .	184
7.1.7.8	Energy Lost to Heat Transfer . . . . .	184
7.1.7.9	Sum of Energy Sinks . . . . .	184
7.1.8	Equation of State . . . . .	185
7.1.9	Determination of Mean Temperature . . . . .	186
7.1.10	Integration . . . . .	187
7.1.11	Determination of Right Running Characteristics . . . . .	188
7.2	Modeling the 35mm Test Fixture . . . . .	189
7.2.1	Ballistic Matching . . . . .	189
7.2.1.1	Matching Vent Time . . . . .	192
7.2.2	Pressure Time and Pressure Travel Curves . . . . .	193
7.2.3	Energy Considerations . . . . .	195
7.2.4	Determination of Right Running Characteristics . . . . .	197
7.2.5	Inertial Breech Behavior . . . . .	200
Part 8:	DISCUSSION OF RESULTS . . . . .	204
8.1	Muzzle Velocity . . . . .	204
8.2	Peak Pressure . . . . .	205
8.3	Rarefaction Wave Traverse Tracking . . . . .	206
8.3.1	Vent Time . . . . .	210

8.3.2	Right Running Characteristics	211
8.4	Chamber Pressure Impulse	212
8.5	Measured Recoil Velocity	213
8.6	Measured Recoil Momentum	215
8.7	Scrutiny of Light-Early Shot 2-6-3	217
8.8	Reduction in Barrel Heating	218
Part 9: CONCLUSIONS		220
9.1	Recommendation for Future Investigation	220
9.1.1	Performance	221
9.1.1.1	Recoilless Synchronized RAVEN	221
9.1.1.2	High Efficiency Recoilless RAVEN	221
9.1.1.3	Near Synchronized RAVEN	221
9.1.1.4	Lowest Heat Launcher	222
9.1.2	Blast	222
9.1.2.1	Blast Characterization	222
9.1.2.2	Blast Mitigation	222
9.1.3	Venting Mechanics	223
9.1.3.1	Alternatives to the Inertial Breech	223
9.1.3.2	Transients Immediately Following Venting	223
9.1.3.3	Heat Transfer and Erosion at the Vent	223
Part 10: Literature Cited		224
Appendix A: Data collected		230
Appendix B: Matlab® files		261
	ff1dperf.m	262
	runR2dxvf.m	264
	R2dxf.m	267
	R2dlf.m	281

## LIST OF TABLES

Table 3.1-1:	Thermodynamic Properties Representative of a Typical Propellant . . . .	18
Table 3.2-1:	Orthodox Charge Configuration, Muzzle Velocity, and Ballistic Efficiency . . . . .	26
Table 3.3-1:	Ballistic Efficiency of Prior Recoilless Rifles . . . . .	32
Table 3.3-2:	Recoilless Charge Configuration, Muzzle Velocity, and Ballistic Efficiency . . . . .	33
Table 3.4-1:	Davis Gun Configuration, Muzzle Velocity, and Ballistic Efficiency . . .	37
Table 4.2-1:	Estimated Ratio of Thermal Losses to Projectile Kinetic Energy . . . . .	48
Table 4.2-2:	Operating Temperatures of a Typical Gun . . . . .	58
Table 5.1-1:	Characteristics of Oerlikon KD Series 35mm Gun [47]. . . . .	67
Table 5.1-2:	Characteristics of 35mm Practice Shell TP. . . . .	68
Table 5.1-3:	Rifling Parameters . . . . .	71
Table 5.1-4:	Bore Resistance Profile. . . . .	72
Table 5.1-5:	Thermodynamic Properties of M1 Propellant and Black Powder. . . . .	73
Table 5.1-6:	Measured Geometry of 35mm TP Propellant Grains . . . . .	74
Table 5.1-7:	Design Interior Ballistic Data From Fig. 5.1-4. . . . .	76
Table 5.2-1:	Synchronized Vent Timing for Guns [6,3] . . . . .	79
Table 5.2-2:	Inertial Breech Configurations Tested . . . . .	87
Table 5.2-3:	Vent Stroke Estimates Assuming 300kg Barrel. . . . .	93
Table 5.2-4:	Recoil Distances to Vent For Different Configurations. . . . .	94
Table 5.5-1:	Location of Barrel Pressure Probes. . . . .	105
Table 5.5-2:	Location of Barrel Thermocouples. . . . .	106

Table 5.5-3:	Recoiling Masses.....	107
Table 6.1-1:	Configuration Identification Number of Shots Fired.....	118
Table 6.2-1:	Muzzle Velocities [m/s].....	120
Table 6.3-1:	Peak Pressure [MPa]. ....	125
Table 6.3-2:	Duration of Concurrent Venting and Propulsion and Percent Projectile Travel at Venting [ms/%]. ....	138
Table 6.3-3:	Integrated Chamber Pressure Impulse [Ns].....	141
Table 6.4-1:	Measured Momentum [Ns]. ....	151
Table 6.5-1:	Max Bore Temperature Change (Mean/Std.) [K]. ....	152
Table 7.1-1:	Shot-Start and Breech-Start Configurations and Equations of Motion. .	164
Table 7.2-1:	Results of Closed-Breech Interior Ballistic Model. ....	191
Table 7.2-2:	Relative Magnitudes of Model Energy Sinks.....	196
Table 7.2-3:	Modeled Muzzle Velocity and Pressure For Inertial Breech Configurations.	203

# LIST OF FIGURES

Figure 2.1-1	Davis Gun Mounted to a World War I Martin Bomber [8]. . . . .	5
Figure 2.2-1	Firing of M198 155mm Towed Howitzer Demonstrating Diversion of Propellant Gases by Means of a Muzzle Brake. . . . .	6
Figure 2.3-1	Goddard Recoilless Launcher (a) and Rocket-Projectiles (b) [10]. . . . .	8
Figure 2.4-1	Russian 76.2mm Recoilless Rifle, Model 1936 [10]. . . . .	10
Figure 2.4-2	Recoilless Rifle Drawing from Cook's 1921 Patent. . . . .	11
Figure 2.4-3	M18 57mm Recoilless Rifle. . . . .	12
Figure 2.5-1	Diagram Showing the Principles Involved in the "Front Orifice" Type Recoilless Rifle [14, 8, 3]. . . . .	13
Figure 2.6-1	Regenerative Liquid Propellant Recoilless Gun [16]. . . . .	14
Figure 3.2-1	A Typical Cartridge Case [24] . . . . .	19
Figure 3.2-2	Line Drawing of Pressure Action Within a Gun Chamber After the Bullet Has Traveled About One Caliber [56]. . . . .	20
Figure 3.3-1	Schematic of Recoilless Rifle Nozzle, Chamber, and Pressure Acting on the Base of the Projectile [8]. . . . .	27
Figure 3.3-2	Photo of 57mm Recoilless Rifle Cartridge Components Including Primer Powder (a), Primer (b), Perforated Cartridge Case (c), Impregnated Paper Liner (d), Propellant Bed (e), Closure Plug (f), Spacer (g), Projectile with Pre-Engraved Rotating Band, (h), and Assembled Cartridge (i) [27, 28]. . . . .	28
Figure 3.3-3	Drawing of a Recoilless Rifle Depicting Propellant Gases Escaping to the Rear While the Projectile Is Propelled Forward [29]. . . . .	29
Figure 3.6-1	Graphical Presentation of Empirical Muzzle Velocity Relations and Actual Performance Points for Fielded Weapon Systems. . . . .	41
Figure 4.2-1	Nozzle Expansion Ratio Required to Achieve a Given Mach Number for a Representative Propellant Gas of 1.25. . . . .	53

Figure 4.2-2	Muzzle Brake Efficiency as a Function of Muzzle Velocity for M109 and M198 Muzzle Brakes [44]. . . . .	63
Figure 4.2-3	Recoil Reduction Potential for Muzzle Brakes and RAVEN. . . . .	66
Figure 5.1-1	35mm TP Round: Assembled Cartridge (a), Projectile (b), and Cartridge Case Drawing (c). . . . .	69
Figure 5.1-2	Cross-section of Rifling Profile [49]. . . . .	70
Figure 5.1-3	Images of Propellant Grains Showing Generally Cylindrical Shape (a) and Indicating the Diameter of the Center Perforation (b). . . . .	74
Figure 5.1-4	Pressure, Travel, and Velocity Time Curve for Gun Design [55]. . . . .	75
Figure 5.2-1	Inertial-Breech Bolt-Action RAVEN Vent In Operation. . . . .	82
Figure 5.2-2	Detail Modification of Drawing 31223 Showing Cartridge Case Notch and Extraction Rim Removed (English Units) [49]. . . . .	83
Figure 5.2-3	Flow Area, In Circular Bore (a), Around Circumferential Port (b). . . . .	84
Figure 5.2-4	Shear Plugs for the Nose of the Inertial Breech in the Sheared (a) and Un-Sheared (b) State. . . . .	89
Figure 5.2-5	View of Several Test Components: Shear Plug (Sheared) (a), Breech Obturator (b), Ruptured Cartridge Case Head (c), Chamber Plug (Nozzle) (d), Sheared Ring from Shear Plug (e), Ruptured Cartridge Case Body (f), and Projectile (g). . . . .	95
Figure 5.2-6	Internal Working of RAVEN 35mm Test Fixture [49]. . . . .	95
Figure 5.3-1	Example of Copper Crush Tube Showing 5 Accordion Folds to the Right. . . . .	98
Figure 5.3-2	Estimated Shock Arresting Loads of Off the Shelf Copper Tubing. . . . .	99
Figure 5.3-3	Raven 35 Assembly Drawing (a) and Photograph (b) [49]. . . . .	101
Figure 5.3-4	Free Recoil Mount and Ring-Spring Recoil Arrestors [49]. . . . .	102
Figure 5.3-5	Longitudinal Section of a Ring Spring Pack [63]. . . . .	103



Figure 5.4-1	RAVEN 35 Non-Venting Inertial Breech Assembly [49]. . . . .	104
Figure 5.5-1	Spring Loaded Bayonet Style Thermocouple Mount Hole. . . . .	106
Figure 5.5-2	Picture of Ballistic Screens Immediately Down Range of the Muzzle. .	107
Figure 6.1-1	ARES Test Range. . . . .	109
Figure 6.1-2	Image of Cartridge Case (Split Lengthwise) That Healed Above a Properly Ruptured Case. (Note the Neck Deformation.) . . . . .	110
Figure 6.1-3	Firing Video Sequence Before Firing (a) First Frame After Firing (b), Case Head Ejection (c), Case Body Ejection (d). . . . .	111
Figure 6.1-4	Pressure Time Trace from Closed-Breech Function Test Firing 1-2-3. .	113
Figure 6.1-5	Pressure Time Trace from Heavy-Late Vented Function Test Firing 1-2-6. . . . .	114
Figure 6.1-6	Post Crushing Images of a Good Crush Tube (a) and a Ripped Crush Tube (b). . . . .	116
Figure 6.1-7	Copper Tubing Setup For Final RAVEN Tests. . . . .	117
Figure 6.2-1	Plot of Muzzle Velocity as a Function of the Percent Travel of the Projectile at Venting. . . . .	120
Figure 6.3-1	Pressure Time Trace from Closed-Breech Test Matrix Firing 2-1-3. . .	121
Figure 6.3-2	Pressure Time Trace from Non-Venting Test Matrix Firing 2-9-4. . . .	122
Figure 6.3-3	Pressure Time Trace from Heavy-Early Vent Test Matrix Firing 2-3-5.	123
Figure 6.3-4	Pressure Time Trace from Light-Nominal Test Matrix Firing 2-5-1. . .	123
Figure 6.3-5	Distribution of Muzzle Velocity as a Function of the Maximum Measured Chamber Pressure. . . . .	124
Figure 6.3-6	Juxtaposed Plot of Chamber Pressure for Heavy-Early and Non-Venting. . . . .	126
Figure 6.3-7	Juxtaposed Plot of Chamber Pressure for Light-Nominal and Non-Venting. . . . .	126

Figure 6.3-8	Identification of Rarefaction Wave Head By Means of Local Minimum of Second Derivative of the Logarithm. ....	129
Figure 6.3-9	Identification of Rarefaction Wave Head By the Intersection of Exponential Curve Fits to the Data Adjacent to the Predicted Point....	130
Figure 6.3-10	Identification of Rarefaction Wave Head at the P4 Probe.....	132
Figure 6.3-11	Spatial Gradient of Pressure Within Gun at Shot-Exit for Non-Venting Versus a Heavy-Early Vent.....	134
Figure 6.3-12	Spatial Gradient of Pressure Within Gun at Shot-Exit for Non-Venting Versus a Light Nominal Vent. ....	135
Figure 6.3-13	Integrated Pressure Travel Time Curve for the Non-Vented configuration Shot 2-9-4. ....	136
Figure 6.3-14	Integrated Pressure Travel Time Curve for the Heavy-Early configuration Shot 2-3-5. ....	136
Figure 6.3-15	Integrated Pressure Travel Time Curve for the Light-Nominal configuration Shot 2-5-1. ....	137
Figure 6.3-16	Duration of Concurrent Venting and Projectile Propulsion Versus Percent Projectile Travel at Venting. ....	139
Figure 6.3-17	Integrated Chamber Pressure Impulse as a Function of the Projectile Travel at the Commencement of Venting. ....	140
Figure 6.4-1	Recoil Phase Plane Response of the Third Closed-Breech Shot.....	145
Figure 6.4-2	Recoil Phase Plane Response of Fourth Non-Venting Shot. ....	147
Figure 6.4-3	Recoil Phase Plane Response of Heavy-Early Shot 2-3-5.....	149
Figure 6.4-4	Recoil Phase Plane Response of Light-Nominal Shot 2-5-1.....	150
Figure 6.4-5	Plot of Measured Launch Momentum (Impulse) as a Function of the Percent Travel of the Projectile at Venting. ....	151
Figure 6.5-1	Plot of Thermocouple K1 Max Temperature Rise as a Function of the Percent Travel of the Projectile at Venting. ....	153

Figure 6.5-2	Plot of Thermocouple K2 Max Temperature Rise as a Function of the Percent Travel of the Projectile at Venting. ....	153
Figure 6.5-3	Plot of Thermocouple K3 Max Temperature Rise as a Function of the Percent Travel of the Projectile at Venting. ....	154
Figure 6.5-4	Plot of Thermocouple K4 Max Temperature Rise as a Function of the Percent Travel of the Projectile at Venting. ....	154
Figure 7.1-1	Simplified Chamber Geometry and Inertial Reference Position Definitions .....	159
Figure 7.1-2	Typical Shapes of Propellant Grains [21]. ....	168
Figure 7.1-3	Splinters Resulting From a Seven Perf Grain [19]. ....	170
Figure 7.2-1	Pressure and Travel Versus Time for 35mm Closed-Breech Gun.....	194
Figure 7.2-2	Pressure and Travel Plot for the 35mm Closed-Breech Gun.....	195
Figure 7.2-3	Synchronized Rarefaction Wave Front Propagation (a) and Velocity Contributions (b). ....	199
Figure 7.2-4	Pressure and Travel Plot for the 35mm Light Venting Breech RAVEN.	200
Figure 7.2-5	Recoil Motion of Light Inertial Breech and Gun Barrel (a) and Close-up of the Shearing Action (b). ....	202
Figure 7.2-6	Recoil Velocity of Light Inertial Breech and Barrel. ....	203
Figure 8.3-1	Juxtaposition of Model and Experimentally Inferred Projectile and Rarefaction Wave Progression for the Heavy/Early Configuration. ...	207
Figure 8.3-2	Juxtaposition of Model and Experimentally Inferred Projectile and Rarefaction Wave Progression for the Heavy/Nominal Configuration..	207
Figure 8.3-3	Juxtaposition of Model and Experimentally Inferred Projectile and Rarefaction Wave Progression for the Heavy/Intermediate Configuration.....	208
Figure 8.3-4	Juxtaposition of Model and Experimentally Inferred Projectile and Rarefaction Wave Progression for the Light/Early Configuration. ....	208

Figure 8.3-5	Juxtaposition of Model and Experimentally Inferred Projectile and Rarefaction Wave Progression for the Light/Nominal Configuration.. .	209
Figure 8.3-6	Juxtaposition of Model and Experimentally Inferred Projectile and Rarefaction Wave Progression for the Light/Intermediate Configuration.....	209
Figure 8.3-7	Juxtaposition of Model and Experimentally Inferred Projectile and Rarefaction Wave Progression for the Light/Late Configuration. . . . .	210
Figure 8.6-1	Predicted Recoil Performance for 35mm RAVEN and Muzzle Brakes.	215

## ACKNOWLEDGEMENTS

The author wishes to express his gratitude to Drs. Henry T. Nagamatsu and Joseph Flaherty for their patient guidance through this effort and the mentorship of Dr. Patrick M. Vottis at Benét Laboratories over the last ten years through gun propulsion programs as diverse as electromagnetic coil-guns, gun barrel vibration absorbers, and fire out of battery recoil.

This effort would not have been possible without the encouragement received, in the face of the initial community skepticism of the concept, from Dr. Robert E. Dillon, Jr. then at Rose Hulman Institute of Technology and currently the Associate Director of Benét Labs for Technology, Dr. Bruce Burns of the Army Research Laboratory (ARL), Aberdeen, Maryland, and Mark Ford of Picatinny Arsenal, New Jersey.

Dr. Sam Sopok and Mark Witherell of Benét and Douglas Coats and Stuart Dunn of Software Engineering Associates, Inc., Carson City, Nevada are gratefully acknowledged for their collaboration with the author to produce the first computational validation of the propulsion concept. Terence P. Coffee of ARL is commended for his independent computational validation. The interior ballistic model included within this thesis benefited greatly from the teachings of Fred Robbins (retired ARL) of Fre-Lin Associates, Havre de Grace, MD.

Special thanks are extended to Drs. Henry Sneck, Henry Scarton, and Andrew Lemnios who have the dubious honor of having been prior doctoral thesis advisors for the author as the focus of research efforts relevant to Army armament programs shifted through electromagnetic coil-gun recoil, structural dynamics of guns and gun barrel vibration absorbers to the present topic of a novel form of gun propulsion.

The experimental apparatus and results presented in this thesis reflect well upon the contributions of many who warrant acknowledgement. The author is deeply indebted to Richard Tortorici, and Michael J. Glennon of Benét who worked with the initial rough sketches of the apparatus to create an intricate solid model and conduct structural stress analysis of the fixture respectively.

The fine crew of engineers and technicians at ARES, Inc. of Port Clinton, Ohio are to be acknowledged for their contributions. The author is grateful for the efforts and insightful understanding of Andrew Kertis, Jr. as the lead engineer for the manufacture and assembly of the apparatus; Norm Stamm as the firing range officer; and Phil Connor, Liny Earhart, Keith Ohm, Ken Roder, Brian Stamm, and Steve Zimmerman who all contributed to manufacture and testing of the hardware.

The timely establishment of the contracts to conduct collaborative research with ARES could not have been achieved without the diligence of Anthony D. Gabriele, and Laurence R. Marten of Benét, Herbert J. Roder and Ann Yamrik of Ares, and Ruthann Schultz of Picatinny Arsenal.

A special thanks is due to my wife, Kim, for her constant faith, support, loving encouragement, and for the ability to always look forward.

## **ABSTRACT**

A new species of gun propulsion that dramatically reduces recoil momentum imparted to the gun is presented. First conceived by the author on 18 March 1999, the propulsion concept is explained, a methodology for the design of a reasonable apparatus for experimental validation using NATO standard 35mm TP anti-aircraft ammunition is developed, and the experimental results are presented. The firing results are juxtaposed by a simple interior ballistic model to place the experimental findings into a context within which they may better be understood.

Rarefaction wave gun (RAVEN) propulsion is an original contribution to the field of armament engineering. No precedent is known, and no experimental results of such a gun have been published until now. Recoil reduction in excess of 50% was experimentally achieved without measured loss in projectile velocity.

RAVEN achieves recoil reduction by means of a delayed venting of the breech of the gun chamber that directs the high enthalpy propellant gases through an expansion nozzle to generate forward thrust that abates the rearward momentum applied to the gun prior to venting. The novel feature of RAVEN, relative to prior recoilless rifles, is that sufficiently delayed venting results in a rarefaction wave that follows the projectile though the bore without catching it. Thus, the projectile exits the muzzle without any compromise to its propulsion performance relative to guns that maintain a sealed chamber.

# **Part 1**

## **INTRODUCTION**

The firing of a gun results in a momentum exchange between the motion of the projectile and propellant gases and the recoil of the gun system. It is the principal intent of the rarefaction wave gun (RAVEN) to reduce or eliminate gun recoil by venting a substantial portion of the propellant gases rearward through the breech while the bullet is concurrently being propelled forward through the bore of the gun. What is unprecedented is that RAVEN may achieve this recoil advantage without slowing the projectile relative to a gun that maintains a sealed breech.

The recoil reduction is achieved by delaying the venting of the breech to a time after the projectile has begun its motion down the barrel, but prior to shot-exit. This releases high pressure gases that may be accelerated rearwards through an expansion nozzle. The momentum imparted to the gases develops an applied forward thrust to reduce recoil. Within the gun, venting the chamber produces a forward moving rarefaction wave (sometimes called an expansion wave) that propagates through the propellant gas column towards the moving projectile. Rarefaction waves traverse gas columns at the same velocity as sound waves, following the  $C_-$  or  $C_+$  characteristic line through the gas [2]. Ahead of the rarefaction wave front, the propellant gas column is unaffected by the venting. Behind the wave front, the propellant gas is subject to the effects of the venting manifest as decreased pressure, density, temperature, and forward flow velocity relative to the gas properties that would exist if the venting had not occurred. Reduction in propulsion of the projectile may only develop after the rarefaction wave front reaches the



base of the projectile. By design of a suitable delay for the venting, such degraded propulsion may be altogether avoided if desired by the designer by allowing the projectile to reach the muzzle of the gun prior to the rarefaction wave front.

A second problem that arises when firing a projectile from a gun is that heat is transferred from the hot propellant gases to the gun barrel. As the temperature of the barrel wall rises, several negative consequences ensue including: increased susceptibility to erosion, decreased modulus of elasticity, and thermal relaxation of desirable prestress within the cannon barrel. RAVEN may reduce this heat transfer by commencing the venting of the hot propellant gases through the breech before the projectile has exited the muzzle. This will reduce the duration of exposure of the bore to the hot gases. For much of the heat transfer event, the venting will also favorably effect the heat transfer by reducing the gas temperature, density, and flow speed along the wall. As with recoil reduction, this thermal management advantage may be achieved without reducing performance relative to a gun that maintains a sealed breech by a requisite delay of the venting of the breech.

Considering the novelty of the basic premise of RAVEN and the potential relevance of such a propulsion technology to reduce recoil and heat transfer imposed upon guns a need exists to systematically study the behavior of RAVEN. This study may be divided into three steps: (i) develop a suitable interior ballistics model that can predict the propagation rate of the rarefaction wave while the projectile is being propelled through the gun; (ii) develop a method to estimate the recoil momentum and heat imparted to the gun; (iii) experimentally validate that recoil and heat transfer are being reduced.

The first and third needs are addressed in this dissertation. Preliminary success in achieving the second need has been achieved by three separate investigations. First, Kathe and Dillon [3] employed a one-dimensional (1D) Van Leer's flux splitting method [4] to solve the Euler equations of compressible flow. Second, Coffee [5] employed a 1D finite volume model. Third, Kathe et al. [6], leveraged ongoing collaborative efforts between Sopok and Dunn to develop a Navier-Stokes-based gun tube boundary layer (GTBL) code for thermo-chemical erosion modeling. The first and third of these methods employed Gough's [7] NOVA interior ballistic modeling code to define the solution ahead of the rarefaction wave.

To achieve experimental validation, a standard medium caliber gun design was altered to provide for a delayed venting of the breech. The venting was accomplished by elongating the chamber of the gun by means of a chamber extension to receive a heavy breech block. Rather than fixing the breech block to the gun barrel, the block was free to be propelled rearwards by the same propellant gases that propel the projectile forward, while maintaining a gas seal between itself and the extended chamber. When the breech block is propelled rearward to the end of the chamber, the gas seal is broken and the propellant gases commence venting. This may be considered an inertial containment method and the breech block may be termed an "inertial breech." The vent timing of this system was controlled by employing different chamber extension geometries, altering the inertial breech traverse required to vent the gun. A second vent timing control parameter was to employ a heavy or light inertial breech. The lighter breech provided an earlier vent timing for a given chamber extension geometry than its heavier counterpart.

The experimental results included a measure of net recoil momentum imparted to the gun, the increase in barrel wall temperature following firing at four locations along the barrel, pressure measurements at fourteen locations along the barrel, and projectile velocity. A total of seven venting configurations were fired along with two baseline configurations that did not vent through the breech. The non-venting configurations included a traditional fixed-breech gun and an inertial breech gun that employed a chamber extension of sufficient length to prevent venting.

The results indicated that recoil and net barrel wall heating for the earliest venting gun was reduced by over 50% and 40% respectively without appreciable reduction in measured muzzle velocity. The pressure sensor measurements also enabled the projectile and rarefaction wave front propagation down the bore to be tracked.

Computer modeling of the interior ballistics of the gun to predict the propagation rate of the rarefaction wave while the projectile is being propelled through the gun was achieved by modifying an accepted lumped parameter model. The modifications were required to accommodate the unusual inertial breech operation and provide a means to model the propagation rate of the rarefaction wave through the gun bore. After parametric tuning of the model to match the interior ballistic performance of the fixed-breech non-venting baseline, the model effectively predicted the release times and propagation rates of the rarefaction wave fronts.

## **Part 2**

# **HISTORICAL BACKGROUND**

### **2.1 The Davis Gun**

The idea of eliminating recoil from weapon systems is not new. Leonardo da Vinci (1452-1519) is believed to have left a sketch of a recoilless gun concept depicting two projectiles fired simultaneously in opposite directions from a common straight cannon [8]. This gun was later made practical by the construction of the Davis gun in 1914 (see Fig. 2.1-1) [8], which was employed for anti-submarine use.

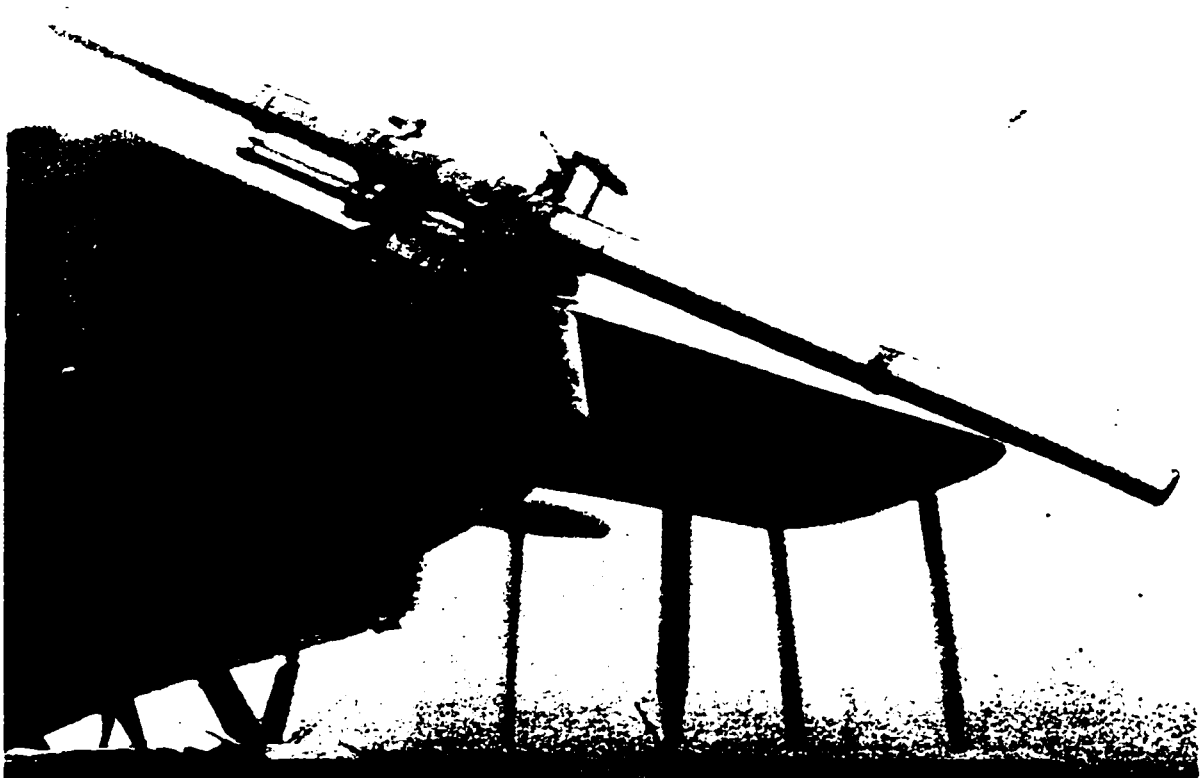


**Figure 2.1-1 Davis Gun Mounted to a World War I Martin Bomber [8].**

## 2.2 Muzzle Brakes

Reduction of the momentum of gun launch by redirection of the muzzle gas efflux from a gun has been the topic of earnest research since the first known application of a muzzle brake to a cannon by French Colonel, Chevalier Truielle de Beaulieu in 1842 [9]. An image of a current baffled muzzle brake during firing is depicted in Fig. 2.2-1.

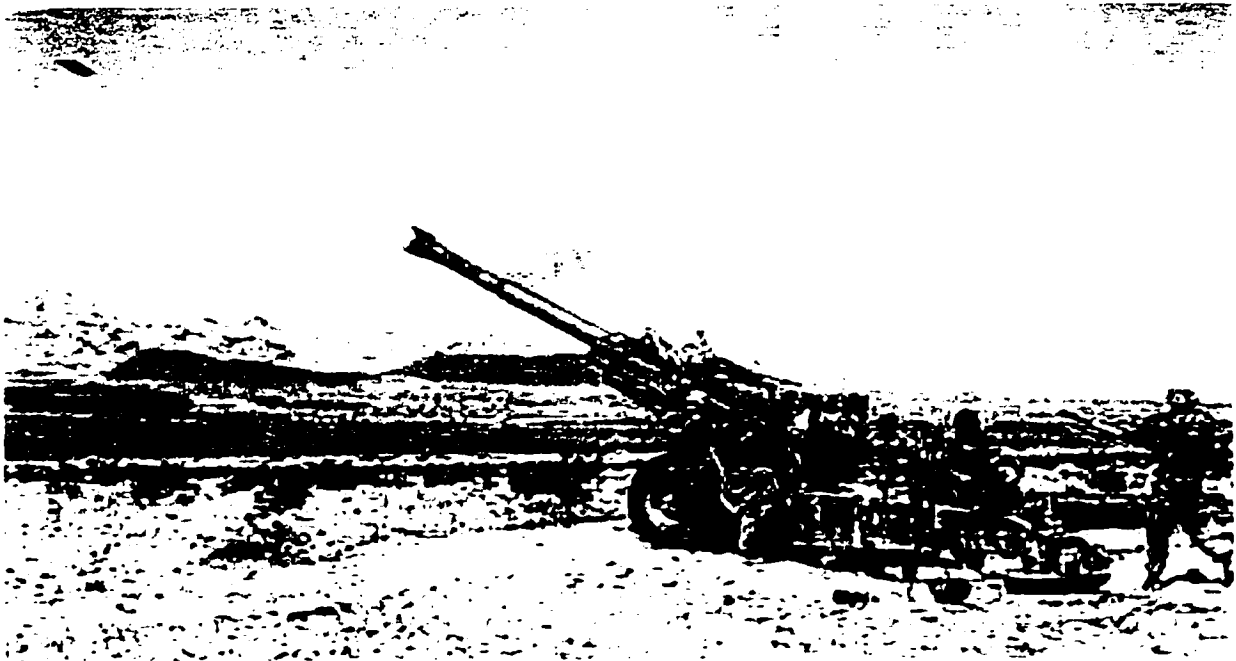


**Figure 2.2-1 Firing of M198 155mm Towed Howitzer Demonstrating Diversion of Propellant Gases by Means of a Muzzle Brake.**

## 2.3 Rocket Launcher

The first known reduction to practice of a gun system that incorporated diversion of propellant gases vented through the breech of a gun was achieved by R. H. Goddard of the Smithsonian Institution. A forerunner of the World War II rocket launcher, M1A1 "Bazooka," the Goddard recoilless gun projectile included an integral propelling

charge and de Laval nozzle. The launcher tube merely provided a containment structure to direct the course of the rocket-projectile, and act as a blast tube to duct the rearward supersonic jet to the breech of the weapon. The principal disadvantage of the Goddard gun was the lack of developed muzzle velocity. One must bear in mind that the entire rocket burn must be confined to the minimum duration that the rocket will remain in the launch tube. Once outside the launch tube, the back-blast of a late burning rocket would constitute a substantial hazard to the gunner as is made very clear by the gunner position depicted in Fig. 2.3-1. During testing of several such guns in November 1918, the highest attained muzzle velocity was 160m/s [10].



**Figure 2.3-1** Goddard Recoilless Launcher (a) and Rocket-Projectiles (b) [10].

## **2.4 Recoilless Rifles**

A recoilless rifle is similar to the Goddard Gun in that the propelling gases are discharged out the rear of the launcher to compensate for the forward momentum imparted to the projectile. However, for a recoilless gun, the propellant and de Laval nozzle are not

coupled to the projectile as it traverses the bore of the launcher. Rather, in a recoilless rifle the de Laval nozzle is integral with the launcher and the propellant charge is free to distribute itself and burn along the entire length of the propellant gas column between the breech of the gun and the base of the projectile. This affords a substantial advantage in that projectile design is no longer constrained to incorporate the nozzle structure. Further, the propellant is not subjected to the acceleration loads of launch, greatly reducing the tendency of the propellant grains structure to break-up exposing too much surface area for a controlled burn.



The first known recoilless rifle was achieved by the Russians in 1936 using a design based upon a patent filed by the Russian mathematician, Riabouchinski in 1917 [8]. A picture of this gun is included in Fig. 2.4-1.

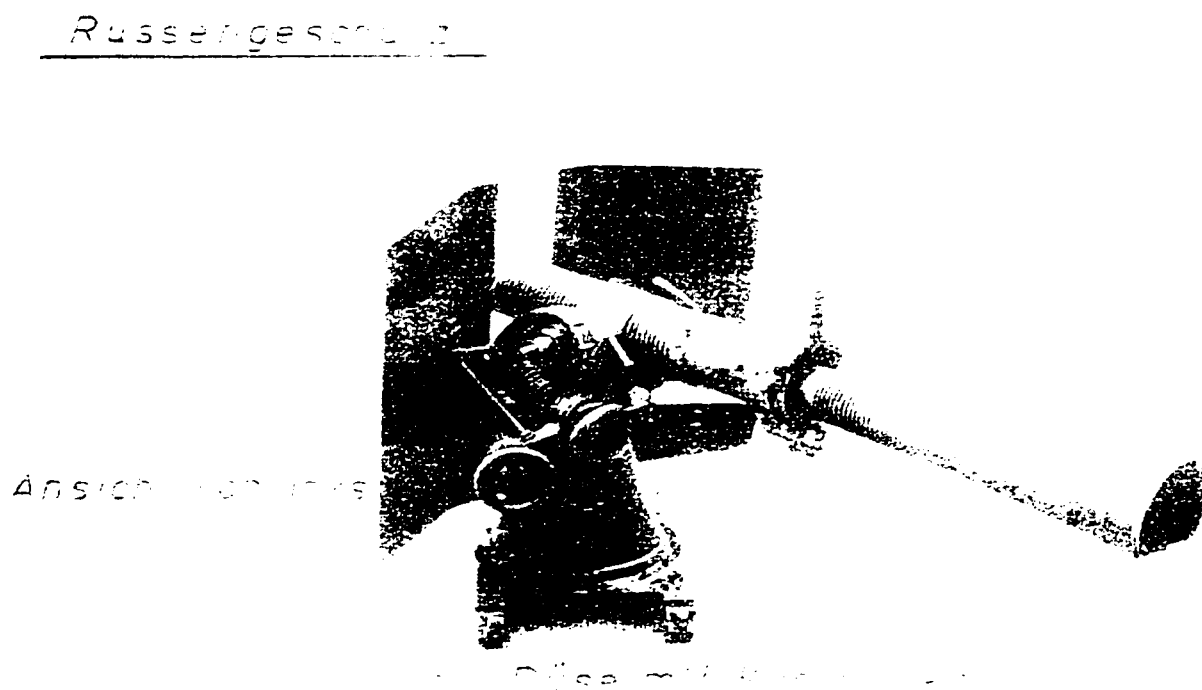


**Figure 2.4-1 Russian 76.2mm Recoilless Rifle, Model 1936 [10].**

In the West, R. Studler is credited by J. S. Hatcher with the successful U.S. efforts to design a man-portable recoilless rifle that could fire a 1.36kg shell at 366m/s to a range of 3650m with accuracy comparable to that of an M1 rifle [11]. Studler's efforts were influenced by the patent of C. J. Cook [12] for a recoilless rifle prior to the manufacture of the Russian rifle shown in Fig. 2.4-1 [13] as cited by [10]. One of the drawings from Cook's patent is included as Fig. 2.4-2. The result of the World War II effort was the 57mm M18, a picture of which is included in Fig. 2.4-3.

C. J. COOKE.  
NON-RECOIL GUN.  
APPLICATION FILED MAR. 24, 1920.

1,380,358.

Patented June 7, 1921.

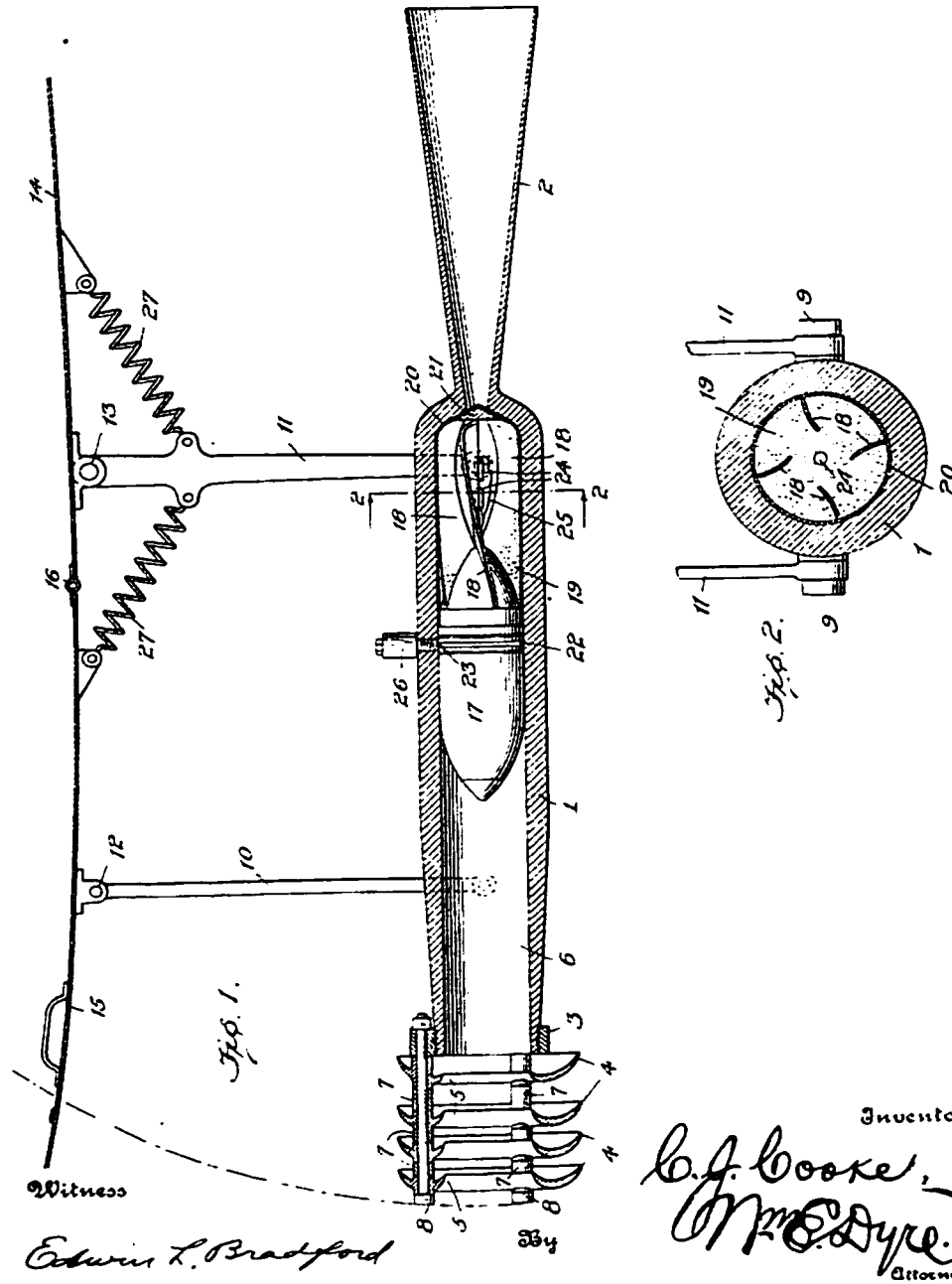


Figure 2.4-2 Recoilless Rifle Drawing from Cook's 1921 Patent.



**Figure 2.4-3 M18 57mm Recoilless Rifle.**

## **2.5 Front Orifice Recoilless Gun**

A distinct subset of the recoilless rifle is the front orifice gun. In such a system, the motion of the projectile uncovers the nozzle ports early in the ballistic cycle, but at some delay time after the shot-start pressure is reached [14, 8, 3]. This gun operates in three phases as depicted in Fig. 2.5-1. First, before the base of the bullet begins to uncover the nozzle ports at position 2, the gun is operating as an orthodox (closed-breech) gun with no rearward gas efflux compensating for the momentum imparted to the projectile. When

the base of the projectile is in the process of uncovering the nozzle ports from position 2 to 3, the rearward propellant gas efflux commences, with an increasing throat area where the gases escape through the throttle formed between the base of the projectile and the nozzle ports. Finally, in the third phase from position 3 and beyond the nozzle ports are completely opened. As a consequence of the first phase of operation with no propellant gas recoil compensation, the thrust developed in the third phase must overcompensate to achieve a net balance of near zero recoil momentum.

The propulsion efficiency advantages of the front orifice recoilless rifle are substantial, due to two primary benefits. First, prior to venting, the orthodox (closed-breech) operation results in better ignition of the propellant bed than traditional recoilless

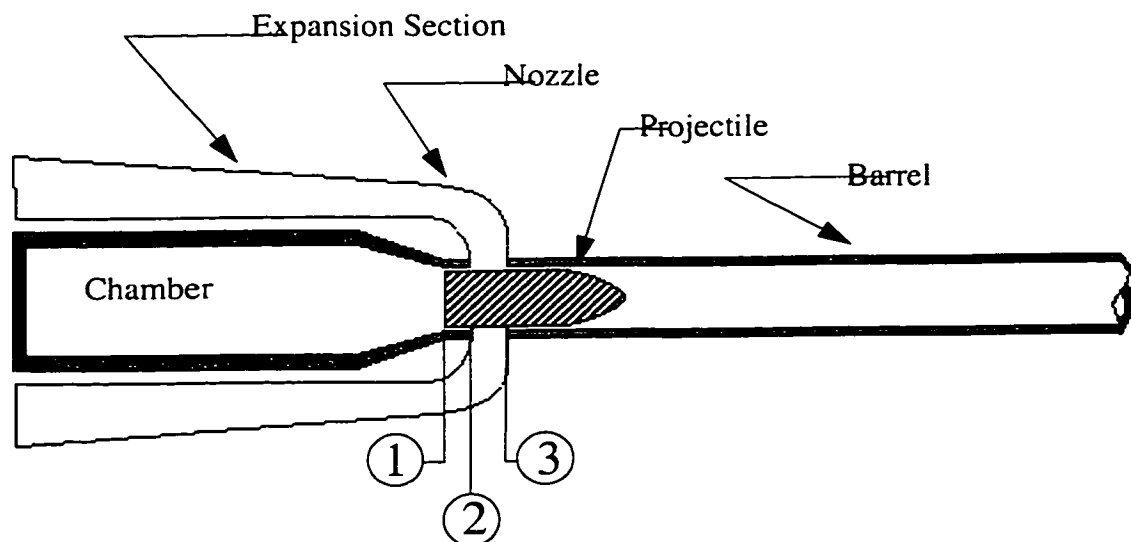


**Figure 2.5-1** Diagram Showing the Principles Involved in the “Front Orifice” Type Recoilless Rifle [14, 8, 3].

rifles. Second, the delayed venting reduces the ejection of unburned propellant through the nozzles.

## 2.6 Regenerative Liquid Propellant Recoilless Rifles

The use of a liquid propellants within recoilless rifles was fostered by, e.g., Ashley [15], Bulman [16, 17], Graham [16], and Cyzsz [18] for airborne applications. By combining the motion of the regenerative liquid propellant piston with that of pintle control for the nozzle throat of the recoilless gun, Bulman and Graham [16] were able to provide a small back blast “precursor” flow prior to the main back blast event. This enabled a plume to be developed within a plume to shift the back blast as far away from the gun as possible [17]. A drawing from Bulman and Graham’s patent is shown in Fig. 2.6-1.

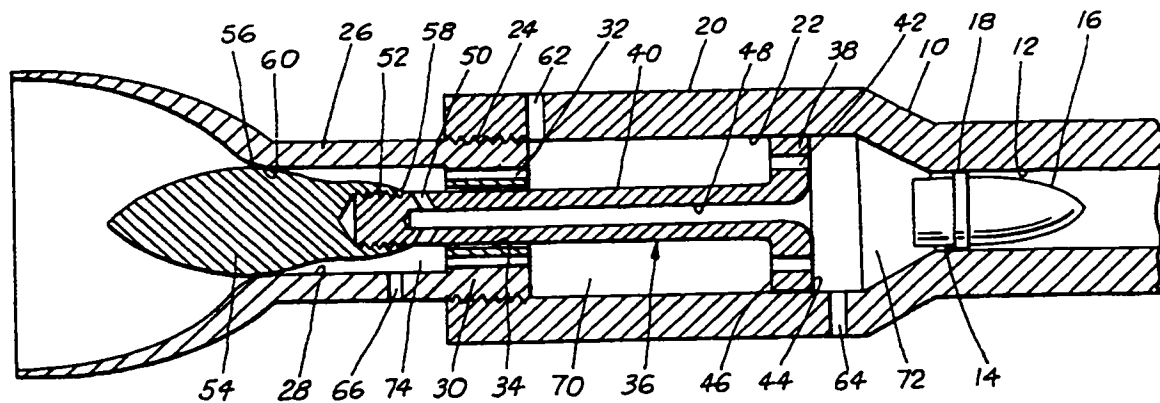


**Figure 2.6-1 Regenerative Liquid Propellant Recoilless Gun [16].**

## Part 3

### DESCRIPTION OF GUN PROPULSION

A gun system is a heat engine that obtains energy from a chemical reaction source, imparts desired propulsion energy to the projectile, and distributes the remaining energy to a number of sinks including barrel heating and muzzle blast [19].

#### 3.1 Energy Content of Propellants

In order to understand the gun propulsion of a projectile, it is essential to understand the source of energy. The propellant in a round of ammunition is often referred to as the “charge.” The most common metric of propellant energy, is variously called the “impetus,” “specific energy,” or misleadingly, “force” [20]. It is a measure of the mass specific energy liberated and has units of energy per mass [21].

$$F = RT_o, \quad (3.1-1)$$

where  $F$  is the force,  $R$  is the mass specific gas constant for the propellant gas, and  $T_o$  is the adiabatic flame temperature for the propellant. The force of common propellants is typically near 1 MJ/kg. The mass specific gas constant for the propellant gas  $R$  is:

$$R = \frac{R_u}{m_m}, \quad (3.1-2)$$

where the universal gas constant  $R_u = 8,314 \text{ J/kmol/K}$  and  $m_m$  is the propellant’s molecular mass.

The molecular mass of common propellants is near 25kg/kmol resulting in a specific gas constant of approximately 330 J/kg/K. Using (3.1-1) reveals the adiabatic flame temperature of a typical propellant as approximately 3000K.

The mass specific internal energy of propellant gases released during combustion in a constant volume bomb may be related to the adiabatic flame temperature as

$$U_o = C_v T_o. \quad (3.1-3)$$

For a perfect gas, the constant volume specific heat may be computed as

$$C_v = \frac{R}{\gamma - 1}, \quad (3.1-4)$$

where  $\gamma$  is the ratio of specific heats:

$$\gamma = C_p / C_v, \quad (3.1-5)$$

where  $C_p$  is the constant pressure specific heat.

Propellant gases are not perfect gases, so particular care must be taken in the quantification of their specific heats. Corner [22] has argued that  $C_p$  does not occur in equations that govern the interior ballistics of guns. Therefore, the ratio of specific heats may be defined by (3.1-4) using a representative mean value of the constant volume

specific heat of the propellant gases within a gun. This mean constant volume specific heat may be experimentally determined from the internal energy averaged over a representative interval of temperatures that will occur within a gun from the adiabatic flame temperature to 70% of the adiabatic flame temperature [22]. Typical values of  $\gamma$  so defined range from 1.22 to 1.28 with 1.25 being a representative value. Thus,  $C_p$  as computed by (3.1-5) will be subject to real gas deviations from perfect gas relationships. This method of using the perfect gas relationship for a real gas maintains the fidelity of (3.1-3) and allows the mass specific heat of explosion to be accurately related to the force (3.1-1) using the relationship of (3.1-4) as

$$U_o = \frac{F}{\gamma - 1}. \quad (3.1-6)$$

For a typical propellant gas with a force of 1MJ/kg and a ratio of specific heats of 1.25, the chemical energy released by burning is 4MJ/kg.

Tables of the thermodynamic properties of common propellant gases are included within [21] and [23]. Thermodynamic properties of a typical propellant, that will provide a point of reference for later Sections, appear in Table 3.1-1. The covolume (to be defined later in Section 7.1.8.) constitutes the first virial coefficient for an improved



equation of state and may be considered the smallest volume to which the propellant gas may be compressed.

**Table 3.1-1: Thermodynamic Properties Representative of a Typical Propellant**

Properties of a Typical Propellant	
Adiabatic Flame Temperature	3007K
Force	1 MJ/kg
Heat of Explosion	4 MJ/kg
Molecular Mass	25kg/kmol
Gas Constant	332.5 J/kg/K
Ratio of Specific Heats	1.25
Covolume	1000 cm <sup>3</sup> /kg

## **3.2 Closed-Breech Interior Ballistics**

The most typical configuration for gun launch of a projectile is closed-breech firing. In such a gun, the propellant gases are prevented from escaping from the chamber and barrel until the bullet exits the muzzle, at which time the gases are free to escape through the muzzle. When discussion includes guns of the closed-breech and recoilless type, the closed-breech is commonly termed an “orthodox” gun [22].

### **3.2.1 A Brief Description of the Interior Ballistics of a Typical Gun.**

The gun is composed of a rifled barrel, generally closed at the back by a movable breech block which may be termed a bolt for automatic weapons, and loaded with a round of ammunition that includes a cartridge case, primer/igniter, bed of

propellant grains, and a projectile which is generally crimped by the mouth of the cartridge case at the cannelure. Figure 3.2-1 is drawing of a typical round of ammunition.

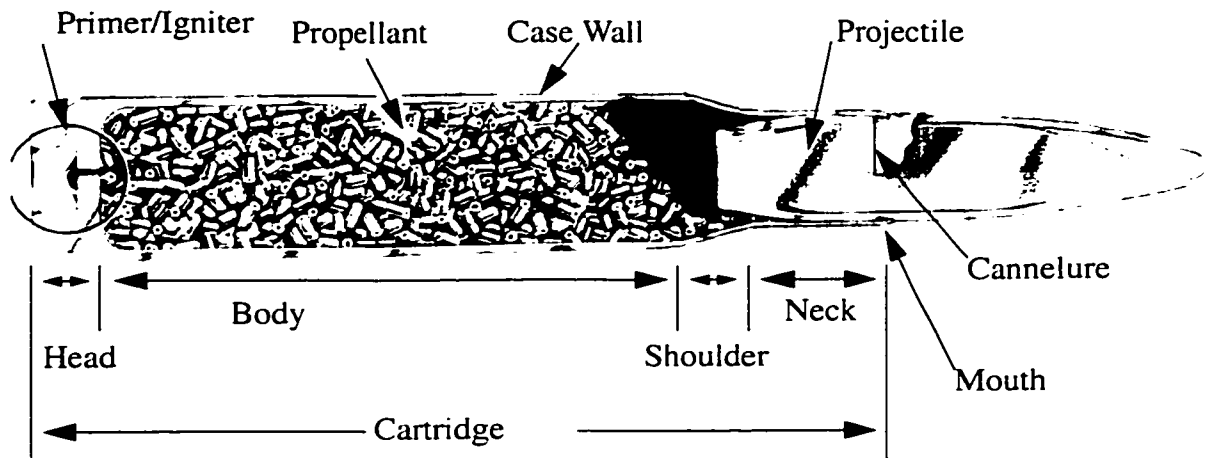


**Figure 3.2-1 A Typical Cartridge Case [24]**

Upon firing the igniter, a relatively small amount of chemical material such as black powder is burned releasing hot gases and burning particles into the bed of propellant within the cartridge case. The propellant, heated sufficiently by the action of the igniter, begins to burn itself. As the propellant burns, the pressure within the cartridge case swiftly rises, causing a substantial increase in the rate of burning. When it reaches sufficient pressure, nominally 5MPa, the projectile is released when the crimps of the cartridge case are no longer able to contain the projectile. Upon release of the crimps, the rotating band of the projectile is extruded into the rifling grooves of the barrel as the projectile first

begins to move down the bore. A depiction of the action within a gun after the bullet has traversed about one caliber<sup>i</sup> is included in Fig. 3.2-2.

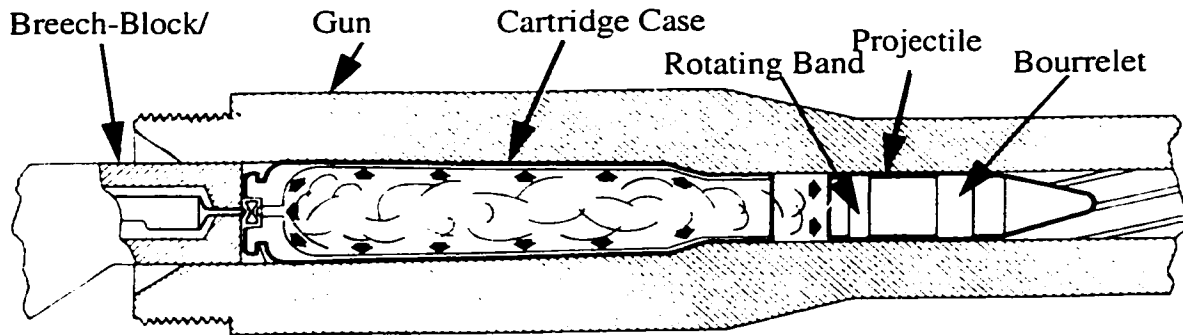


**Figure 3.2-2 Line Drawing of Pressure Action Within a Gun Chamber After the Bullet Has Traveled About One Caliber [56].**

The projectile of Fig. 3.2-1 does not include a separate rotating band. For small caliber projectiles, the body of the bullet (or an integral gilding metal jacket) is extruded into the rifling grooves. The outer diameter of these projectiles is generally 25  $\mu$ m greater than the groove diameter [24]. For larger caliber projectiles, generally 25mm diameter and up, a separate band is incorporated into the projectile immediately forward of the cannellure that is supposed to extrude into the rifling grooves, while maintaining a tight grip upon the projectile. Such a band is depicted in Fig. 3.2-2. Thus, the rotating band may

- 
- i. The term caliber has two meanings for guns. First, it is the diameter of the bore. For rifled guns, the caliber is the diameter from land to land, not groove to groove. Second, caliber is a normalized unit of axial length. Thus, when a bullet has traversed one caliber, it has moved one bore diameter down the barrel. It is quite common for the length of a gun barrel to be expressed as the calibers of bullet travel from its chambered position to the muzzle. Accordingly, this metric of length does not include the length of the gun chamber.

impart spin from the twist of the barrel rifling to the bullet while providing a positive gas seal. Design considerations for such bands are discussed in [25]. Additionally, a front bore riding surface termed a “bourrelet” may be incorporated to provide stability to the projectile during launch.

As the projectile is propelled through the bore, the burning propellant grains and propellant gases begin to move and increase their volume. This transition from a fixed to a moving bullet is widely termed “shot-start.” Most generally for a large caliber gun, the propellant is engineered to continue burning at a sufficient rate that the peak pressure is reached after the bullet has traveled some distance through the bore of the gun.

For example, a 105mm tank gun may reach peak pressure after the bullet has traveled one third of meter down the barrel [26]. The original chamber volume of this gun prior to shot-start is nearly 6 liters [26]. The available volume for the propellant is increased to nearly 9 liters by the time the peak pressure is reached. The engineering implication for this delayed peak pressure behavior is that the maximum pressure requirements for the gun barrel and breech are substantially reduced and the acceleration loading of the projectile structure is also reduced.

As the projectile is propelled through the barrel, energy released by the burning propellant is transferred to the translational and, to a much lesser extent, the rotational kinetic energy of the projectile. The propellant gases and unburned propellant grains that are moving through the gun also increase their kinetic energy. The distribution of the kinetic energy of the propellant results in a pressure gradient with the highest pressures

occurring at the breech where the propellant velocity is near zero. The lowest pressure is at the base of the projectile where the gas is moving the fastest. Thermal energy is also released by friction between the barrel and projectile and heat transfer from the hot propellant gases to the colder walls of the barrel, breech face, and rear face of the projectile. In addition, a modest amount of energy is manifest as the kinetic energy of the gun barrel and breech as they are propelled rearwards in reaction to the forward momentum imparted to the projectile and propellant.

When the base of the projectile exits the muzzle of the gun barrel, widely termed “shot-exit,” the propellant gases are no longer constrained behind the bullet and they expand around the bullet to form muzzle blast. Although some modest continued propulsion of the bullet after shot-exit may occur, the vast majority of the propulsion is complete by the time of shot-exit.

After the projectile has exited the muzzle, the propellant gases and any unburned bits of propellant are ejected from the gun during a process termed “blow-down.” Substantial continued momentum may be imparted to the gun during this process. Similarly, heat transfer to the bore continues during blow-down. For portions of the bore near to the muzzle, the vast majority of the heat transfer occurs during blow-down because the duration of blow-down is long relative to the very brief time that this section of the bore is exposed to the propellant gases prior to shot-exit.

### 3.2.2 Empirical Performance Relationship for Closed-Breech Guns

Simple relations to predict the performance of a gun based upon the characteristics of the ammunition to be fired are desirable. A reasonably accurate and widely used relationship between the muzzle velocity  $v_m$  of a projectile and the ratio of propellant (charge) mass  $m_c$  to projectile mass  $m_p$  has been published by Ogorkiewicz [20]

$$v_m = 1500(m/s) \left( \frac{m_c}{m_p} \right)^{0.45} . \quad (3.2-1)$$

Thus, when a cartridge constructed with equal weights of propellant and projectile, a muzzle velocity of 1,500m/s may be anticipated. A graphical representation of the this empirical relationship will be presented later in Section 3.6 as Fig. 3.6-1. Although (3.2-1) may appear completely empirical, it is not. The formula may be decomposed into a ratio of propellant chemical energy to projectile kinetic energy modified by a velocity dependent ballistic efficiency. To begin, the ballistic efficiency  $\epsilon_B$  may be defined using (3.1-6) as [22,21]

$$\epsilon_B = \frac{\frac{1}{2} m_p v_m^2}{m_c U_o} = \frac{(\gamma - 1) v_m^2}{2F} \left( \frac{m_p}{m_c} \right) . \quad (3.2-2)$$

Ballistic efficiencies may nominally be anticipated to be 30% [22]. In general, to obtain a higher muzzle velocity for a given projectile mass, more propellant is required. As more propellant is introduced, a greater percentage of the chemical energy released by the burning of the propellant is manifest as kinetic energy of the propellant behind the projectile. Thus, we may anticipate a declining efficiency with higher muzzle velocities. Solving (3.2-2) for the muzzle velocity yields

$$v_m = \sqrt{\epsilon_B} \sqrt{\left(\frac{2F}{(\gamma - 1)}\right)} \sqrt{\left(\frac{m_c}{m_p}\right)}. \quad (3.2-3)$$

Using a typical propellant force of 1MJ/kg and  $\gamma = 1.25$  as discussed in Section 3.1, the middle radical of (3.2-3) may be computed to be 2,828m/s. Scaling this by the square root of a 30% ballistic efficiency, the muzzle velocity may be estimated as 1,549m/s multiplied by the square root of propellant to projectile mass ratio. Recasting the velocity relationship of Ogorkiewicz (3.2-1) into a form consistent with (3.2-3)

$$v_m = \left( 1500(m/s) \left(\frac{m_c}{m_p}\right)^{-\left(\frac{1}{20}\right)} \right) \sqrt{\left(\frac{m_c}{m_p}\right)}. \quad (3.2-4)$$

Combining (3.2-3) and (3.2-4), the Ogorkiewicz velocity relationship (3.2-1) may be interpreted as a ballistic efficiency estimate

$$\epsilon_B \approx \left( \frac{(\gamma - 1)}{2F} (1500(m/s))^2 \right) \left( \frac{m_c}{m_p} \right)^{-\left(\frac{1}{10}\right)} . \quad (3.2-5)$$

Using the typical propellant properties listed in Table 3.1-1, the muzzle velocities (3.2-1) and ballistic efficiencies (3.2-5) for several charge configurations are listed in Table 3.2-1. It may be appreciated that the tenth root of the propellant to projectile ratio used to compute the ballistic efficiency of (3.2-5) achieves the anticipated decrement of ballistic efficiency with higher muzzle velocities.

It is important to note the basic flaw in the ballistic efficiency computed via (3.2-5). The muzzle velocity computed by (3.2-1) does not consider the thermodynamic properties of the propellant employed. The ballistic efficiency derived in (3.2-5) does consider the propellant properties. Thus, if a comparison is made between two propellants, one with a greater force than that of the other, the muzzle velocity computed by (3.2-1) will not reflect a higher anticipated muzzle velocity for the higher energy propellant. However, the ballistic efficiency computed by (3.2-5) will compare difference in chemical energy of the two propellants and thus, declare the efficiency of the higher force propellant to be lower than its lower energy counterpart. Therefore, it is important that (3.2-5) not be considered of utility for the computation of ballistic efficiency when comparing configurations with different propellant properties.

Ogorkiewicz includes a comparison of his empirical muzzle velocity relationship versus current guns indicating the relationship is reasonably valid for muzzle



velocities from 300m/s to 1,700m/s [20]. The muzzle velocity computations using (3.1-1) and ballistic efficiency computations using (3.1-5) for several propellant to projectile mass ratio's (charge configurations) based upon the typical propellant properties listed in Table 3.1-1 are included below in Table 3.2-1.

**Table 3.2-1: Orthodox Charge Configuration, Muzzle Velocity, and Ballistic Efficiency**

$m_c/m_p$	$v_m$	$\epsilon_b$
0.25	804m/s	32.3%
0.5	1098m/s	30.1%
0.75	1318m/s	28.9%
1	1500m/s	28.1%
1.25	1658m/s	27.5%

A more advanced model of the interior ballistics of an orthodox gun will be presented later in Section 7.1.

### 3.3 Recoilless Gun Ballistics

A recoilless gun differs from an orthodox gun in that the chamber of the gun does not constrain all of the propellant gases to remain within the gun until shot-exit. Instead, the forward recoil momentum imparted to the projectile and those gases exiting the muzzle is countered by ejecting the majority of the propellant gases rearward through a de Laval nozzle. The rate of the rearward mass efflux of the gases may be controlled by sizing the throat of the de Laval nozzle to maintain recoil balance. A simple schematic of a recoilless rifle is depicted in Fig. 3.3-1.

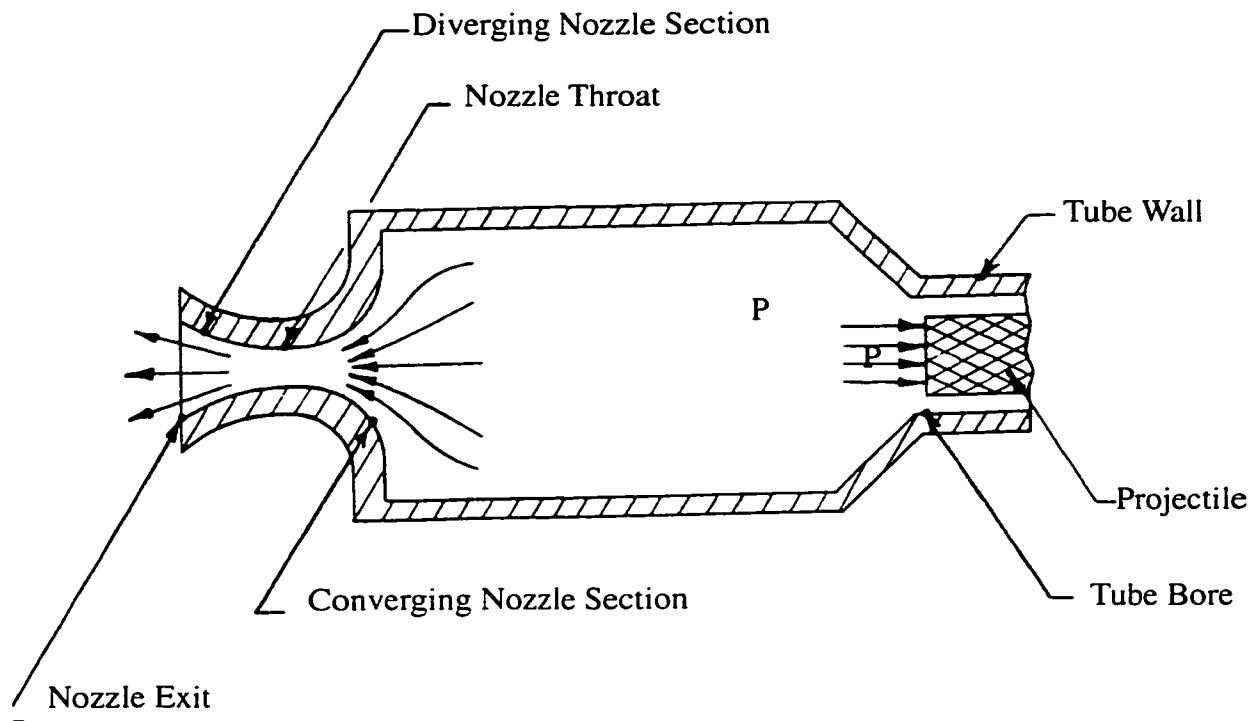


**Figure 3.3-1 Schematic of Recoilless Rifle Nozzle, Chamber, and Pressure Acting on the Base of the Projectile [8].**

### 3.3.1 The Perforated Cartridge Case

In the United States, the chamber configurations of recoilless rifles have largely been limited to those that incorporate a perforated cartridge case. The M18, 57mm recoilless rifle incorporated this design approach. In addition, to reduce the engraving forces for a recoilless rifles, the rotating bands of their projectiles are pre-engraved. Thus, the force required immediately following shot-start for extrusion of the rotating bands into the rifling grooves may be obviated. An image of the ammunition developed for this gun is included in Fig. 3.3-2.

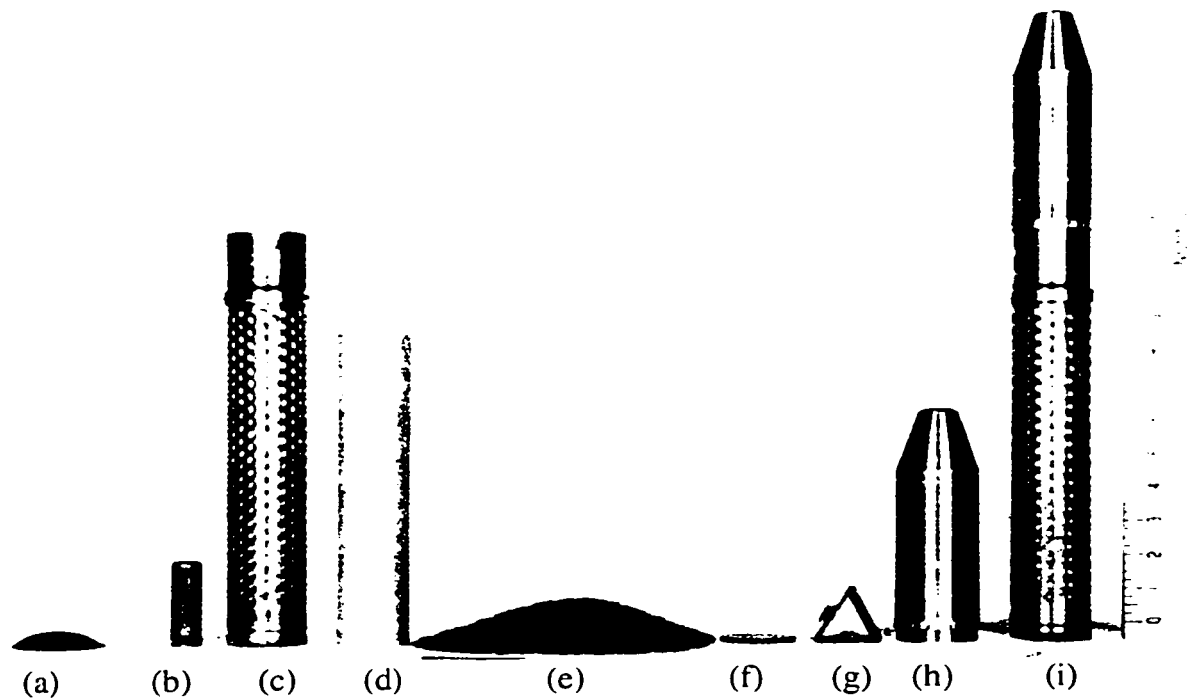


**Figure 3.3-2 Photo of 57mm Recoilless Rifle Cartridge Components Including Primer Powder (a), Primer (b), Perforated Cartridge Case (c), Impregnated Paper Liner (d), Propellant Bed (e), Closure Plug (f), Spacer (g), Projectile with Pre-Engraved Rotating Band, (h), and Assembled Cartridge (i) [27, 28].**

The chamber of a recoilless gun firing perforated cartridge case ammunition is enlarged to provide an annular path for the propellant gases to vent radially out of the cartridge case. The gases are then drawn rearwards to an interrupted annular de Laval nozzle for expulsion from the gun. The cartridge case is constrained at the front end by the chamber geometry leading to the bore of the gun. At the back end, the interrupted annular nozzle provides a solid center for housing the firing mechanism and providing a firm constraint for the back of the cartridge case. Thus, the cartridge case is simply supported at its front and rear while being suspended in the middle. Rifling torque is compensated for

by means of canting the nozzles to provide the required reaction torque. A drawing of the 106-MM Recoilless Rifle M40A2 while firing a projectile is included within Fig. 3.3-3.

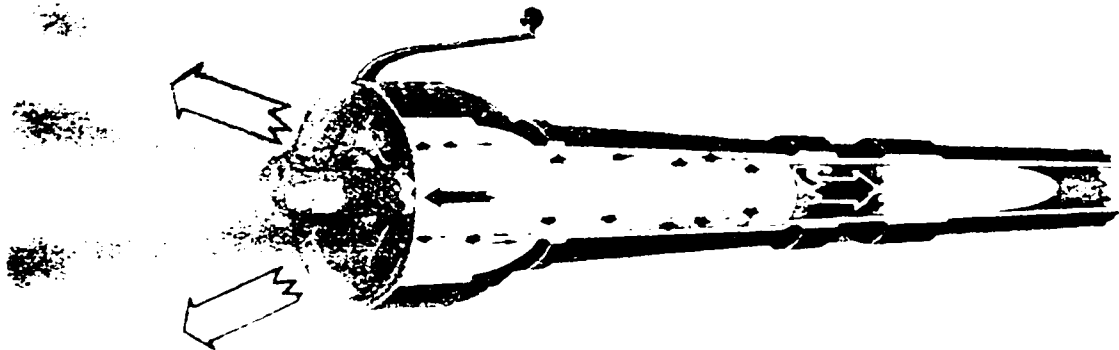


**Figure 3.3-3 Drawing of a Recoilless Rifle Depicting Propellant Gases Escaping to the Rear While the Projectile Is Propelled Forward [29].**

### 3.3.2 Interior Ballistics of a Recoilless Rifle.

The recoilless rifle is composed of a rifled barrel, generally closed at the back by a movable breech block, and loaded with a round of ammunition that includes a perforated cartridge case, cartridge case liner, igniter, bed of propellant grains, and a pre-engraved projectile which is lightly crimped by the mouth of the cartridge case at the cannellure.

Upon firing the igniter, a relatively small amount of chemical material such as black powder is burned releasing hot gases and burning particles into the bed of propellant within the cartridge case. The propellant, heated sufficiently by the action of the igniter, begins to burn itself. As the propellant burns, the pressure within the cartridge case swiftly rises, causing a substantial increase in the rate of burning. When it reaches sufficient pressure, the crimps of the cartridge case are no longer able to contain the projectile. At

this pressure, the cartridge case liner also ruptures at the perforations along the body of the cartridge case. Upon release of the crimps, the projectile is free to travel down the bore. Because of the pre-engraving of the rotating band, the forces associated with extrusion of the rotating band into the rifling of an orthodox gun is greatly reduced.

Once the bullet is free to travel down the bore, and the propellant has ruptured the cartridge case liner, a momentum balancing propulsion results. The pressure in the chamber during this period is determined by the amount of propellant that has been burned, the amount of propellant gas and unburned propellant that has been discharged through the nozzle, the available volume behind the projectile into which the propellant gas expands, and the temperature of the propellant gas [8]. A depiction of the action within a gun after the bullet has traversed about two calibers is shown in Fig. 3.3-3.

As with an orthodox gun, kinetic energy is imparted to both the bullet and the propellant gases that follow the bullet through the bore. Thus, a pressure gradient may be anticipated to result along the bore. In stark contrast with an orthodox gun, much of the propellant energy is expended by the kinetic energy of the gases discharged rearward through the nozzle. In addition, substantial quantities of unburned propellant grains may be discharged during the interior ballistic process.

Thermal energy is also released by friction between the barrel and projectile and heat transfer from the hot propellant gases to the colder walls of the barrel, breech face, nozzle, and rear face of the projectile. However, due to the recoilless operation, virtually no recoil energy is manifest as kinetic energy of the gun barrel and breech.

When the base of the projectile exits the muzzle of the recoilless rifle, the propellant gases are no longer constrained behind the bullet and they expand around it to form muzzle blast. After the projectile has exited the muzzle, the propellant gases and any unburned bits of propellant are ejected from the gun.

### 3.3.3 Observations on Propulsive Stability of a Recoilless Rifle

In general, the chamber pressure of a recoilless rifle is substantially lower than the peak pressure of an orthodox gun. Historically, the muzzle velocity of such guns is also quite low, not much higher than 500m/s; thus, the pressure gradient developed along the bore of the gun is not pronounced. Therefore, the difference between chamber pressure applied over the bore area is not much greater than the force being imparted to the projectile.

Because of the increased rate of propellant discharge from the nozzle with increased chamber pressure, chamber pressure within a recoilless rifle operates in a far more stable environment than its closed-breech counterpart. If the chamber pressure increases, the mass efflux rate will increase tending to lower the pressure. If the chamber pressure decreases, the mass efflux rate will decrease tending to increase the pressure. This stability results in designs that reach a mode of operation that may encroach upon steady state.

For example, if the ejection of unburned propellant could be prevented and the pressure gradient along the bore kept low by a low muzzle velocity, a constant pressure burn rate of the propellant could maintain momentum balance by selection of the throat

area and operating pressure. To the degree that the pressure gradient within the bore is small and, thus, the mass efflux through the bore is small, the design is similar to that of a rocket required to produce a thrust equal to the product of bore area and chamber pressure. The strong analogy to rocket design may be drawn for liquid propellant recoilless gun concepts such those developed in the 1970's [16,18].

#### 3.3.4 Empirical Performance Relationship for Recoilless Rifles

Simple relations to predict the performance of a recoilless rifle, based upon the characteristics of the ammunition to be fired are desirable. Relative to orthodox guns, recoilless rifle design is subject to greater parametric variation and variety. Often, recoilless rifle design is driven heavily by a desire to minimize the weight of the system resulting in parametric configurations that sacrifice thermodynamic efficiency.

A reasonable path forward is to leverage the performance results of prior recoilless rifles and extend their measured efficiencies. The ballistic efficiency, as defined by (3.2-2), for three recoilless rifles is provided in Table 3.3-1.

**Table 3.3-1: Ballistic Efficiency of Prior Recoilless Rifles**

Weapon	Round	Muzzle Velocity	Ballistic Efficiency
57mm M18	M306A1	366m/s [30,8]	5.2% [8]
75mm M20	M309A1	302m/s [30,8]	-na-
105mm M27	M323	341m/s [8]	5.8% [8]
106mm M40	M344	503m/s [30,8]	7.1% [8]

A simple graphical relationship of the muzzle velocity of a recoilless rifle as a function of the propellant to projectile mass ratio is presented in Figure 5-2 of [8]. Olcer

and Levin [8] are credited with this graphical method. The method includes two performance lines that bracket the performance of a recoilless rifle based upon an ad-hoc definition of efficiency for recoilless rifles. A second order polynomial fit of the higher efficiency performance line is given by

$$v_m = 1238(m/s)\left(\frac{m_c}{m_p}\right) - 346(m/s)\left(\frac{m_c}{m_p}\right)^2. \quad (3.3-1)$$

A graphical representation of this empirical relationship will be presented later in Section 3.6 as Fig. 3.6-1. The velocity and ballistic efficiency estimates using (3.3-1) and (3.2-2), respectively, for several charge configurations using the typical propellant properties of Table 3.1-1 are presented in Table 3.3-2.

**Table 3.3-2: Recoilless Charge Configuration, Muzzle Velocity, and Ballistic Efficiency**

$m_c/m_p$	$v_m$	$\epsilon_b$	Validity
0.25	288m/s	4.1%	Valid: Within Prior Design Space.
0.5	533m/s	7.1%	
0.75	734m/s	9.0%	Questionable: Extrapolated Beyond Prior Design Space.
1	892m/s	9.9%	
1.25	1007m/s	10.1%	

Tables 3.2-1 and 3.2-2 both support the increase in ballistic efficiency with increased muzzle velocity. This is in contrast with the decreasing efficiency of an orthodox gun with increased muzzle velocity (3.2-5). Note that in the limit, as very little propellant is used, the kinetic energy imparted to the propellant will become negligible



relative to that of the projectile. Thus, an orthodox gun is efficient at low muzzle velocities.

For a recoilless rifle, like an orthodox gun, only a small amount of propellant energy is required to propel a projectile at a low muzzle velocity. However, a high nozzle velocity is required to achieve recoil compensation by discharging a major portion of the small amount of propellant gases rearwards. Thus, more energy is required, and subsequently more propellant. As the muzzle velocity increases, more propellant is required for bullet propulsion. As more propellant is required, the rearwards nozzle velocity required for momentum balance decreases.

Historically, recoilless guns have not been used to achieve high velocities relative to orthodox guns. There are two basic reasons for this, both of which are related to the pragmatic requirement for high velocity rounds to be fired from high pressure guns. First, recoilless guns are employed principally to reduce the weight of the gun system relative to an orthodox gun. A high pressure recoilless gun barrel would be heavy. Second, high pressure recoilless rifles, with subsequent increases in propellant gas density, would suffer substantial increases in nozzle heat transfer and subsequent erosion. A comprehensive discussion of recoilless rifle nozzle erosion is included within [8].

### **3.4 Davis Gun Ballistics**

The interior ballistics of a Davis gun may be considered as special case of the closed-breech gun. In their pioneering paper on Lagrange's Ballistic Problem, Love and Pidduck [31] observe that if a gun is symmetric about its center and fires two projectiles of

equal weight in opposite directions that there is “never any (gas) velocity at the section midway between (the projectiles).” Thus, the Davis gun is equivalent to back to back closed-breech guns.

There is, however, a flaw in this approach if applied to a true Davis gun. (Love and Pidduck’s analysis [31] was applied to an orthodox gun.) The pressure waves developed within the chamber between the two projectiles may include even wave forms. That is, oscillatory amplitude at the section midway between the two projectiles. This behavior may have substantial effects on the development of pressure waves during the ignition of the propellant bed which are generally exacerbated by increased ratios of chamber length to diameter. Pressure wave ignition instabilities in guns has been an active research topic that is discussed in [32]. By a suitable redesign of a Davis gun chamber to maintain a length to diameter ratio commensurate with that of a closed-breech gun, ignition instabilities may be avoided.

One additional difference between the operation of a Davis gun is that no kinetic energy is imparted to the gun barrel; that is no energy is lost to recoil of the cannon. Other than this difference qualitative behavior is identical to that presented in Section 3.2.1.

#### 3.4.1 Empirical Performance Relationship for Davis Guns

For simplicity consider the mass of the dummy projectile that is fired in a direction opposite to that of the ordnance projectile to be a propellant mass with negligible

internal energy, an empirical relationship based upon Ogorkiewicz's relationship (3.2-1) may be formulated. Define the Davis gun charge mass

$$m_c' = 2m_c + m_p, \quad (3.4-1)$$

where  $m_p$  and  $m_c$  constitute the mass of the projectile and charge for the ordnance and by symmetry, recoil halves of the ammunition. Using the effective Davis gun charge mass (3.4-1) the ratio of  $m_c$  and  $m_p$  results in:

$$\frac{m_c}{m_p} = \frac{\frac{1}{2}(m_c' - m_p)}{m_p} = \frac{1}{2} \left( \frac{m_c'}{m_p} - 1 \right). \quad (3.4-2)$$

It is clear from the form of (3.4-2) that the ratio of effective Davis gun propellant to projectile mass may not be less than one. A ratio of unity corresponds to the limit of two projectiles (one ordnance and one dummy) with negligible propellant mass. Inserting (3.4-2) into (3.2-1) results in

$$v_m = 1500(m/s) \left( \frac{1}{2} \left( \frac{m_c'}{m_p} - 1 \right) \right)^{0.45}. \quad (3.4-3)$$

As the ratio of propellant to projectile mass becomes large, a Davis gun becomes half as efficient as a closed-breech gun. This thought experiment however is not particularly useful as this ratio is rarely larger than 1.2 for an orthodox gun which

corresponds to 3.4 for the Davis gun. A graphical representation of the this empirical relationship will be presented later in Section 3.6 as Fig. 3.6-1. The velocity and ballistic efficiency estimates using (3.4-3) and (3.2-2), respectively, for several charge configurations using the typical propellant properties of Table 3.1-1 are presented in Table 3.4-1.

**Table 3.4-1: Davis Gun Configuration, Muzzle Velocity, and Ballistic Efficiency**

$m_c/m_p$	$v_m$	$\epsilon_b$
1	0m/s	nan <sup>†</sup>
1.5	804m/s	16.2%
2	1098m/s	15.1%
2.5	1318m/s	14.5%
3	1500m/s	14.1%
3.5	1658m/s	13.8%
4	1800m/s	13.5%

†. Nan is the IEEE arithmetic representation for Not-a-Number.

The inefficiency of Table 3.4-1, and the increased gun barrel mass required to shoot a projectile out of both ends, have left the Davis gun with few armament applications. Some notable attempts have been made for special applications [33,34]. It is worth noting that a Davis gun is fully capable of firing high-pressure high-velocity rounds subject to similar limitations (such as maximum pressure) to that of an orthodox gun — subject to the dramatic weight penalties of both the launcher and ammunition.

### **3.5 Front Orifice Recoilless Gun**

The front orifice recoilless rifle is typified by the T135 105mm design series developed by the Frigidare Division of the General Motors Corporation to meet the requirements of a new “Battalion Anti-Tank” (BAT) weapon system. Those requirements were nominally to fire an 8kg projectile at 530m/s with a total system mass as near to 90kg as possible [8]. The lightest gun tested was the T-135-7 with a mass of 140kg; thus, the program was terminated for not meeting the weight objectives. The extreme focus on gun weight reduced emphasis on ballistic efficiency. For example, the operating pressure of the chamber had to be kept very low. As a direct result of this, the orifice location was placed just forward of the mouth of the cartridge case, a position that is desirable to reduce chamber pressures but that may be anticipated to reduce efficiency. The front orifice gun was schematically depicted in Fig. 2.5-1.

As the orifice location is moved towards the muzzle, the distinction between the front orifice recoilless rifle and a muzzle brake becomes blurred. However, as the orifice is moved further down bore, the ability to attain recoillessness becomes more challenging since the efficiency of the closed-breech operation prior to venting may impart more momentum to the projectile than may be compensated for by the rearward flow of the propellant gases.

#### **3.5.1 The Interior Ballistics of a Front Orifice Recoilless Rifle.**

The gun is composed of a rifled barrel, generally closed at the back by a movable breech block, and loaded with a round of ammunition. The cartridge for a front

orifice recoilless rifle shares the basic characteristics of the orthodox cartridge depicted in Fig. 3.2-1. It also shares the same ballistics until the projectile first encounters the front orifice (corresponding to motion of the base of the bullet from (1) to (2) as depicted in Fig. 2.5-1). In particular, during this period of operation, recoil momentum is imparted to the gun.

For the test configuration of the T135 series of front orifice recoilless rifles, the closed-breech travel distance was only about 20% of one caliber. This very limited travel is likely an artifact of the severe weight restrictions placed upon the gun design.

While the projectile uncovers the orifice ports, the throat of the nozzle may be anticipated to be coincident with the ports. Thus, a time varying throat area is achieved. Once the ports are fully open, the throat of the nozzle moves out to a constriction placed where the blast tubes cant rearward.

For the duration of the firing process, the front orifice recoilless rifle acts as a recoilless rifle excepting for the forward location of the orifice as described in Section 3.3.2.

### 3.5.2 Performance Relationship for a Front Orifice Recoilless Rifle

Since no front orifice recoilless rifle was fielded, the available ballistic data is not representative of the performance that would be obtained from such a weapon. Many non-optimal charge configurations were fired whose efficiency would be insufficient in a final configuration. Ammunition to be fielded must be subject to a parametric optimization process that eliminates poor designs.

Undaunted by the recognized lack of sound basis for an empirical determination of the performance of a front orifice recoilless rifle, a linear curve fit for the number five model of the 105mm T135 gun has been published as Fig. 9 of Ref. [14]. The line fit was executed over the limited propellant to projectile mass ratio of 36% to 44% when firing an 8kg projectile. The result is

$$v_m = 1300(m/s) \left( \frac{m_c}{m_p} \right) - 60(m/s). \quad (3.5-1)$$

This performance level is very similar to the recoilless rifle fit attributed to Olcer and Levin [8]. The muzzle velocities predicted by (3.5-1) are 408m/s and 512m/s for propellant to projectile mass ratios of 36% and 44%, respectively. Using (3.3-1), velocities of 401m/s and 478m/s are estimated, respectively.

### **3.6 Graphical Representation of Empirical Relationships**

The results of the empirical relationships between muzzle velocity and the ratio of propellant to projectile mass are shown graphically in Fig. 3.6-1. For perspective, the actual performance of many of the available 57mm to 105mm direct fire rounds of ammunition are included based upon Ref. [35] (used by permission).

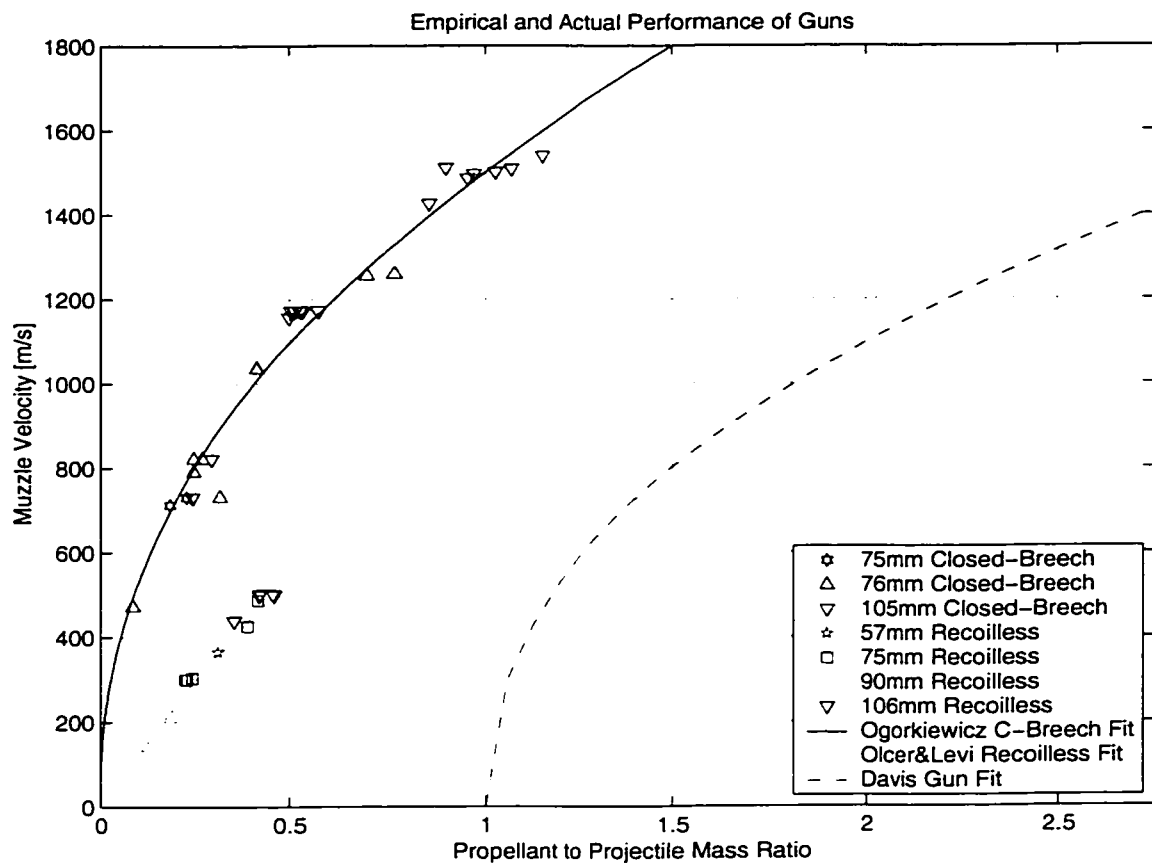


**Figure 3.6-1 Graphical Presentation of Empirical Muzzle Velocity Relations and Actual Performance Points for Fielded Weapon Systems.**



## **Part 4**

# **RAVEN PROPULSION**

### **4.1 A Brief Description**

The central premise of RAVEN propulsion is that a delayed venting at the rear of the gun chamber while a projectile is concurrently being propelled forward through the bore will release a forward traveling rarefaction wave. Ahead of the wave, the propellant gases and any entrained burning grains of propellant will be unaffected by the venting. They literally won't have "heard" the vent prior to the arrival of the wave.

The most intriguing of times to vent the rear of the chamber is one that will cause the rarefaction wave front to reach the base of the projectile as the projectile exits the muzzle. Thus, the projectile's propulsion will not have been compromised, and the maximum duration of concurrent venting and projectile propulsion will have been achieved. Such timing may be referred to as synchronized vent timing.

It is important to recognize that synchronized timing is not the only relevant timing for RAVEN. Venting earlier in the ballistic cycle may enable greater thermal and recoil reduction at the cost of decreased ballistic efficiency (3.2-2). It may be anticipated that the decrease in efficiency will be very small for guns that vent just a little early. Venting later may reduce the back-blast generated. Venting later will also eliminate the potential for muzzle velocity variation caused by variation in the vent timing that may result from imperfections in mechanical implementation.

#### 4.1.1 Approximate Delay Time for Synchronized Venting

A simple approximate means to estimate the duration of concurrent venting and propulsion for a synchronized RAVEN where the rarefaction wave front reaches the base of the projectile as the projectile exits the muzzle is desired.

First, it is known that the rarefaction wave must traverse the length of the gun,  $L_g$ , from the location of the vent to the end of the muzzle. Second, an estimate of the rarefaction wave propagation speed is required. As discussed in Part 1, the wave propagation speed will be equal to the sum of the local sonic velocity of the propellant gases at the wave-front and the translational velocity of the gases at the wave-front both of which will vary as the gun is traversed. The local gas velocity will increase from near zero at the rear of the gun chamber (prior to venting) to the projectile velocity,  $v_p$  at the muzzle. The sonic velocity will be generally decreasing as the gas expands, lowering its temperature. However; since the sonic velocity will later be shown to be proportional to the root of the temperature, in Section 4.2.3, and since the propellant continues to burn as the projectile is propelled, the loss of sonic velocity will be modest and a representative mean value may be employed. Thus, a crude approximation to the delay time for a synchronized venting,  $\Delta t_{sv}$  may be stated as

$$\Delta t_{vs} = \frac{L_g}{c + \frac{v_p}{2}}, \quad (4.1-1)$$

where it is well known that the sonic velocity  $c$  within a gun may be generally estimated as 1,000m/s [36] if a better approximation is not available. The results of a more refined analysis of a rarefaction wave propagation will later be graphically presented in Fig. 7.2-3.

#### 4.1.2 Zero Gas Velocity Zone

An effect of the venting is that the gases vented through the rear of the gun achieve a rearward sonic velocity at the throat of the vent. The gases just behind the base of the projectile travel forward at the projectile velocity. Therefore, somewhere within the gun, behind the rarefaction wave front, the gases will have zero velocity.

#### 4.1.3 Reduced Barrel Heating

Net heat flux at any axial location along the bore of a gun is governed by the time integral of the temperature difference between the propellant gases and the wall surface temperature multiplied by a heat transfer coefficient both evaluated at the axial location of interest and both being a function of time. The heat transfer coefficient may be approximated as proportional to the propellant gas density and its velocity at the axial location of interest [21].

Due to the expansion of the gases behind the rarefaction wave front, the temperature and density of the gas will decrease, reducing their contribution to heat transfer. As noted in Section 4.1.2, the gas velocity should decrease throughout the gun, with the exception of an increased rearward velocity within the gun chamber. Thus, for much of the bore, the gas velocity contribution to heat transfer will be reduced. Since RAVEN expels propellant gases out the back, while the projectile is in bore, it is clearly

removing the hot propellant gases from behind the bullet. After shot-exit, RAVEN expels gases out both the front and back of the gun hastening the blow-down process. For an orthodox gun, none of the hot gases are expelled until the bullet is out and then all of the gases must exit through the muzzle. Thus, the duration of the heat transfer integral will be reduced for a RAVEN relative to an orthodox gun; particularly near the muzzle.

It may therefore be stated with confidence that net heat transfer to the bore of a RAVEN will be lower than that of a comparable orthodox gun.

An analysis conducted by Witherell [6] indicated a one third reduction in overall heat transfer to a RAVEN, with a fifty percent reduction for the forward half of the barrel.

#### 4.1.4 Percentage of Gases Ejected Rearward

A simple approximate formula to determine the percentage of the propellant gases that will be ejected from the back of the gun has remained elusive thus far. Dillon [3] estimated that 66% of the propellant gases will be ejected rearwards for a synchronized vent timing of a 120mm tank gun firing a 1650m/s projectile. An independent assessment by Coats and Dunn [37] estimated a 65% rearward mass efflux for the same configuration. The recoil momentum reduction afforded by RAVEN will be largely determined by the percentage of gas ejected out the back. This is the topic of the next Section.

## **4.2 Upper Bound on Recoil Abatement**

The recoil reduction potential for RAVEN and current technology muzzle brakes will be extrapolated across viable gas gun velocities using simple empirical

relationships. The quantitative findings of this parametric study must be considered to provide perspective as opposed to true predictions because of the extrapolated nature of the study; particularly at higher muzzle velocities.

#### 4.2.1 Operating Temperatures Within a Gun

In the following analysis, perfect gas theory will be used. It is understood that this theory is inaccurate at, e.g., higher pressures. Nevertheless, it should be qualitatively correct. The enthalpy relationships are

$$C_p = \frac{\gamma R}{\gamma - 1}, \quad (4.2-1)$$

$$H(T) = m_c C_p T. \quad (4.2-2)$$

Extending the total internal energy to any temperature, as opposed to just the mass specific internal energy at the adiabatic flame temperature as done in (3.1-3), is achieved by

$$U(T) = m_c C_v T. \quad (4.2-3)$$

A means to estimate the maximum recoil reduction that can be achieved using propellant gas may be determined by examination of the gas enthalpy remaining in the gas after the bullet is propelled through the muzzle. This may then be related to the maximum rearward velocity (and thus, momentum) that may be imparted to the gases that exit out the back through an expansion nozzle.

Assume that all the propellant is burned prior to shot-exit, then the total energy liberated by the propellant burn may be computed from (4.2-3), (3.1-3), and (3.1-4) as

$$U_o = m_c C_v T_o = m_c \frac{RT_o}{(\gamma - 1)}. \quad (4.2-4)$$

#### 4.2.1.1 Reservoir Temperature at Shot-Exit

Regardless of the ultimate motion of the gases as the burning proceeds, energy is expended by the gases during the launch of the projectile. The energy is lost to several energy sinks that are described in Section 7.1.7; however, it suffices to note that the energy sinks are dominated by the translational kinetic energy of the projectile, the heat transfer to the gun barrel walls, breech face, and base of the projectile, and the kinetic energy imparted to the propellant gases propelled through the bore behind the projectile. Since the reservoir properties are of interest, the energy manifest as kinetic energy of the propellant gas is recoverable and need not be decremented from the reservoir internal energy of the gases at shot-exit.

Corner [22] has argued that the heat transfer to the gun may be reasonably assumed proportional to the muzzle energy. Defining  $\Upsilon$  as the ratio of energy lost to heat transfer to the translational kinetic energy of the projectile results in

$$E_h \approx \Upsilon E_{pt} , \quad (4.2-5)$$

where  $E_h$  is the total heat transfer into the gun walls, breech face, and base of the projectile during launch, and the translation energy of the projectile is

$$E_{pt} = \frac{1}{2}m_p v_m^2. \quad (4.2-6)$$

Corner [22] has suggested that heat transfer  $E_h$  is rarely more than 30% of the muzzle energy  $E_{pt}$ . Using this suggested upper bound as an estimate to maintain a conservative study of the upper bound for recoil abatement,  $\Upsilon = 0.3$ . Thermal analysis conducted by Witherell [6] based on Navier Stokes simulations of RAVEN [38] indicate a one third reduction of bore heating relative to an orthodox gun launch, decrementing  $\Upsilon = 0.2$ . These are recorded in Table 4.2-1.

**Table 4.2-1: Estimated Ratio of Thermal Losses to Projectile Kinetic Energy**

Gun	$\Upsilon$
Orthodox	30%
RAVEN	20%

Decrementing the energy liberated by the burning of the propellant (4.2-4) by these two major energy sinks (4.2-6) and (4.2-5),

$$U(T_1) = m_c \frac{RT_o}{(\gamma - 1)} - (1 + \Upsilon) \frac{1}{2}m_p v_m^2 = m_c C_v T_1 = m_c \frac{R}{(\gamma - 1)} T_1. \quad (4.2-7)$$

One may consider the remaining internal energy in (4.2-7) to be the energy of the propellant gases following shot-exit if the muzzle of the gun were corked behind the projectile and all of the gases were to come to rest adiabatically. The temperature of these gases is of interest and may be computed from (4.2-7) using (4.2-3), dividing by  $m_c C_v$  to solve for the temperature and then employing (3.1-4) to simplify as

$$T_1 = T_o - \frac{\left(\frac{(1 + \Upsilon)}{2} m_p v_m^2\right)}{(m_c C_v)} = T_o - \frac{(1 + \Upsilon)(\gamma - 1)}{2R} \left(\frac{m_p}{m_c}\right) v_m^2. \quad (4.2-8)$$

This temperature will be used to approximate the reservoir gas energy and enthalpy available to drive the gases through a de Laval nozzle.

#### 4.2.1.2 Sensible Temperature at Shot-Exit

The sensible temperature at shot-exit is also of interest. It may be used to lower-bound the sonic velocity contribution to the rarefaction wave propagation velocity discussed in Section 4.1.1.

A variation of (4.2-8) may be used to estimate the gas temperature at shot-exit that further decrements the internal energy of the propellant gas by the kinetic energy imparted to the propellant gas as the gases are propelled through the bore behind the projectile. (In (4.2-8) it was assumed that the kinetic energy of the propellant gases was adiabatically recovered.) Using the Lagrange gradient assumption [39,19] the kinetic energy imparted to the propellant gas,  $E_p$  may be approximated as



$$E_p = \frac{m_c}{6} v_p^2. \quad (4.2-9)$$

At shot-exit the projectile velocity is the muzzle velocity. This energy sink may be included with the heat transfer and projectile kinetic energy sinks to estimate the overall temperature of the propellant gas at shot-exit in analogy with (4.2-8) as

$$T_e = T_o - \frac{\left( \frac{(1 + \Upsilon)}{2} m_p + \frac{1}{6} m_c \right) v_m^2}{(m_c C_v)}. \quad (4.2-10)$$

#### 4.2.2 Flow Through a Nozzle

Gas flow through an ideal nozzle is governed by the first law of thermodynamics as expressed via the energy equation (often referred to as the Bernoulli equation). Neglecting gravitational forces as small, the change in kinetic energy of the gases may be directly related to the change in enthalpy [40]. The enthalpy, like the internal energy, is a function only of temperature. Using the relations (4.2-1) and (4.2-2) at the estimated reservoir temperature at shot-exit (4.2-8)

$$\begin{aligned} H(T_1) &= m_c \frac{\gamma R}{\gamma - 1} \left( T_o - \frac{(1 + \Upsilon)(\gamma - 1)}{2R} \left( \frac{m_p}{m_c} \right) v_m^2 \right) \\ &= m_c \left( \frac{\gamma R}{\gamma - 1} \right) T_o - \frac{(1 + \Upsilon)}{2} \gamma m_p v_m^2. \end{aligned} \quad (4.2-11)$$

Using the energy equation [40] the kinetic energy of the propellant gases exhausted from the gun system will decrement the enthalpy

$$H(T_2) + \frac{1}{2}m_c v_c^2 = H(T_1). \quad (4.2-12)$$

The temperature of the gases as they depart the nozzle,  $T_2$  is related to the magnitude of the exhaust velocity and is given by

$$v_c = \sqrt{\frac{2}{m_c} m_c C_p (T_1 - T_2)} = \sqrt{2 \left( \frac{\gamma R}{\gamma - 1} \right) (T_1 - T_2)}. \quad (4.2-13)$$

If the gun were to discharge into a vacuum through an arbitrarily large nozzle, the gases would theoretically cool to absolute zero if realistic effects such as condensation of the gas into a liquid would did occur. Setting  $T_2$  to zero constitutes an upper bound on the exhaust velocity magnitude. Doing this in (4.2-13) results in the accepted value for this thought exercise [8].

The amount that the gas temperature decreases from the reservoir temperature and the speed that the gases attain is a function of the nozzle design. It is well known that guns have ample gas energy and pressure to meet the requirements for de Laval nozzle operation to reach the sonic velocity at the throat through the vast majority of the gas discharge event [8]. (For common propellants the ratio of atmospheric (discharge) pressure to chamber pressure need only be 0.55 [22].) Heat conduction and other loss

factors are also ignored in keeping with the intent of identifying an upper bound upon the performance. What remains is the geometric expansion ratio of the nozzle from the throat to the exit plane. The relationship between expansion ratio and Mach number [40] is

$$\frac{A_e}{A^*} = \frac{1}{M} \left[ \left( \frac{2}{\gamma + 1} \right) \left( 1 + \frac{\gamma - 1}{2} M^2 \right) \right]^{\left( \frac{\gamma + 1}{2(\gamma - 1)} \right)}, \quad (4.2-14)$$

where  $A_e$  is the exit area of the nozzle and  $A^*$  is the area of the throat. The resulting relationship between Mach number at the exit and the expansion ratio from the throat is shown in Fig.4.2-1 for a representative  $\gamma$  of 1.25.

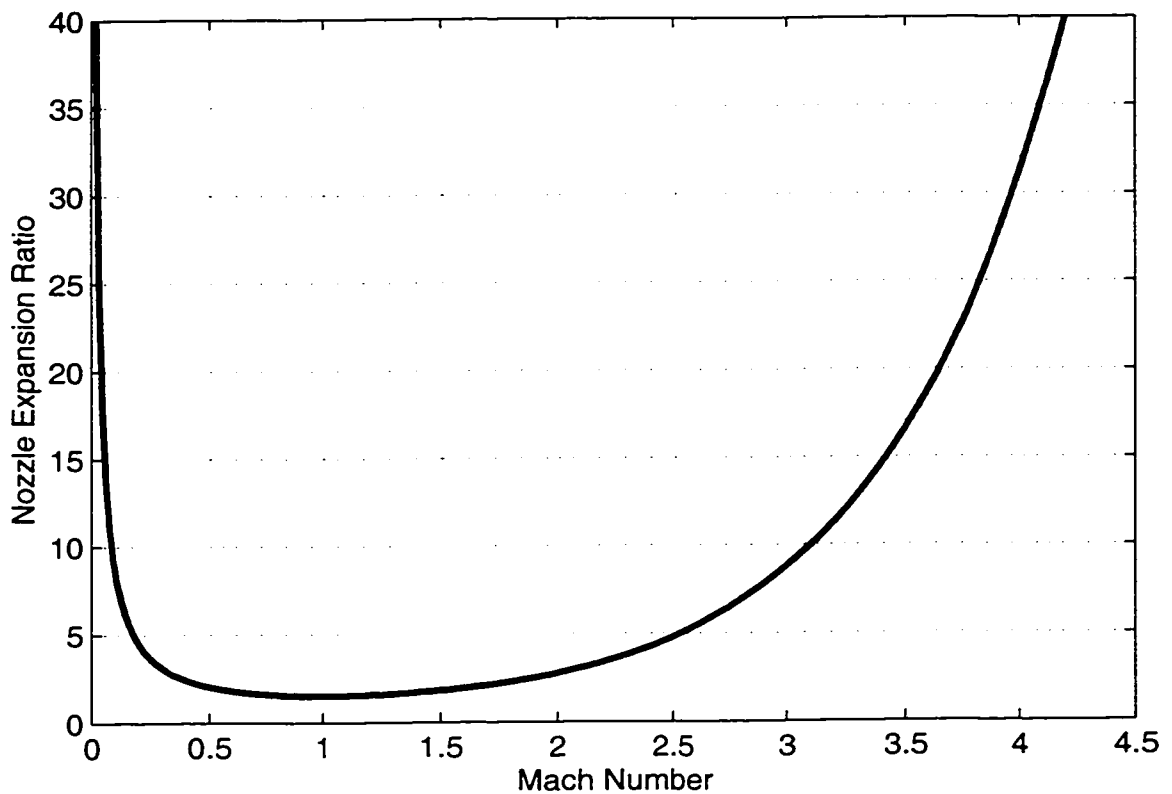


**Figure 4.2-1 Nozzle Expansion Ratio Required to Achieve a Given Mach Number for a Representative Propellant Gas  $\gamma$  of 1.25.**

Some perspective on reasonable area ratios for large caliber guns may be attained by examining at the cross-sectional area of current breech rings as compared to the bore area. This ratio is approximately 16 for current tank guns. (For example, the breech ring of the M68 105mm tank gun is approximately 0.43m in diameter. Dividing by the 0.105m bore diameter and squaring results in a ratio of 16.8) If one were to incorporate a modestly larger nozzle, say 50% larger in diameter than the breech ring, while venting through a throat of bore area, the expansion ratio would be 40 and result in an exit Mach

number in excess of four. The subsequent analysis is not particularly sensitive to this number so four will be used.

The temperature of the reservoir may be related to the Mach number [40] as

$$\frac{T_1}{T_2} = 1 + \frac{(\gamma - 1)}{2} M^2. \quad (4.2-15)$$

Using (4.2-8)

$$T_2 = \frac{T_o - \frac{(1 + \gamma)(\gamma - 1)}{2R} \left( \frac{m_p}{m_c} \right) v_m^2}{1 + \frac{(\gamma - 1)}{2} M^2}. \quad (4.2-16)$$

More directly, (4.2-15) may be used to compute the temperature difference within (4.2-13) as

$$T_1 - T_2 = \left( \frac{(\gamma - 1)}{2} M^2 \right) \left( \frac{T_o - \frac{(1 + \gamma)(\gamma - 1)}{2R} \left( \frac{m_p}{m_c} \right) v_m^2}{1 + \frac{(\gamma - 1)}{2} M^2} \right). \quad (4.2-17)$$

Inserting (4.2-17) into (4.2-13) and simplifying

$$v_c = \sqrt{\frac{\gamma R M^2 \left( T_o - \frac{(1 + \Upsilon)(\gamma - 1)}{2R} \left( \frac{m_p}{m_c} \right) v_m^2 \right)}{1 + \frac{(\gamma - 1)}{2} M^2}}. \quad (4.2-18)$$

Thus, the effect of the energy imparted to the projectile and the heat transfer losses may be interpreted as a decrement on the adiabatic flame temperature.

Squaring (3.2-3) and inserting the definition of force from (3.1-1), the relationship between the muzzle velocity, the ratio of propellant to projectile mass, and the definition of ballistic efficiency (3.2-2), we find

$$v_m^2 = \epsilon_B \left( \frac{2RT_o}{\gamma - 1} \right) \left( \frac{m_c}{m_p} \right). \quad (4.2-19)$$

Inserting this definition into (4.2-18) and simplifying

$$v_c = \sqrt{\left( \frac{\gamma R M^2}{1 + \frac{(\gamma - 1)}{2} M^2} \right) T_o (1 - (1 + \Upsilon) \epsilon_B)}. \quad (4.2-20)$$

Assuming the ballistic efficiency to be approximately 30% (as argued in Section 3.2.2), and a  $\Upsilon$  of 20% for a RAVEN (as presented in Table 4.2-1), the ideal nozzle exit velocity is reduced by 20% from the specific impulse that it would have for a simple rocket. For a typical propellant, as represented by Table 3.1-1, with an adiabatic

flame temperature of 3,007K, the decrement reduces the nozzle exit velocity from 2,582m/s to 2,067m/s.

As discussed in Section 3.2.2, the ballistic efficiency is not strongly related to velocity as may be inferred from (3.2-5). It may be approximated as 30% over a muzzle velocity range of interest. Since thermal losses are assumed proportional to projectile kinetic energy, as developed in (4.2-5) and Table 4.2-1, it may be seen that the decrement of flame temperature for the purposes of computing the specific impulse is expected to be relatively insensitive to muzzle velocity. The decrement should be approximately 40% and 36% for an orthodox gun and RAVEN, respectively.

The nozzle exit velocity may be converted to the weight specific impulse by dividing it by the earth's gravitational constant,  $9.81\text{m/s}^2$ . Using this inconsistent impulse unit, the 2,582m/s and 2,067m/s nozzle velocities may be converted to 263 s and 211 s, respectively.

The result of (4.2-18) constitutes the purpose of this derivation. It represents a realistic upper bound on the mass specific rearward momentum that could be imparted to propellant gases that have been used to propel a projectile from a gun without regard to the mechanism used to achieve it. This upper bound is relevant for any RAVEN launcher as well as any clever muzzle brake devices that would obstruct the bore at the muzzle following shot-exit. It is also a valid upper limit for recoil amplifiers (nozzles at the muzzle used to increase recoil momentum imparted to the gun, occasionally used for

recoil operated automatic weapon). We may now use (4.2-18) to bracket the net recoil imparted to any gun  $I_g$

$$-m_p v_m - m_c v_c \leq I_g \leq -m_p v_m + m_c v_c. \quad (4.2-21)$$

The left side of (4.2-21) corresponds to a recoil amplifier ejecting gases forward and the right side to recoil abatement that ejects gases rearward. The magnitude of the left side corresponds to the greatest rearward recoil momentum that could be imparted to the gun. The right side corresponds to the least rearward momentum. For current high performance kinetic energy rounds, there is sufficient specific impulse in the propellant gases to completely negate the rearward momentum imparted by the projectile and, thus, result in a net forward momentum imparted to the gun. Accessing the specific impulse of the propellant gas to encroach upon recoillessness with little if any compromise in projectile propulsion is the essence of the contribution of RAVEN propulsion to armament engineering.

It is important to note that rearward recoil of the gun implies negative momentum. This is consistent with the forward velocity of the projectile being considered positive. However, since for an orthodox gun there is little potential for confusion, rearward momentum is widely considered positive [41]. Thus, the form of (4.2-21) deviates from the normal conventions of recoil computation but is nevertheless consistent. It is anticipated that this form will reduce confusion when dealing with forward thrust generated by the rearward expansion nozzle of a RAVEN.



### 4.2.3 Tabulated Results

Neglecting the co-volume which is to be discussed in Section 7.1.8, average sound velocity as a function of mean temperature  $\bar{T}$  may be approximated as [40]

$$\bar{c} = \sqrt{\gamma R \bar{T}}. \quad (4.2-22)$$

The results for the systems presented in Table 3.2-1 based upon the typical propellant properties listed in Table 3.1-1 and thermal behavior of an orthodox gun presented in Table 4.2-1 are presented below in Table 4.2-2.

**Table 4.2-2: Operating Temperatures of a Typical Gun<sup>†</sup>**

$m_c/m_p$	$v_m$ (m/s)	$\Upsilon$	$T_1$ (K)	$T_e$ (K)	$T_2$ (K)	$\bar{c}_e$ m/s
0.25	804	1.3	1744	1663	581	831
		1.2	1841	1760	614	855
0.5	1098	1.3	1829	1678	610	835
		1.2	1919	1768	640	857
0.75	1318	1.3	1875	1658	625	830
		1.2	1963	1745	654	852
1	1500	1.3	1908	1626	636	822
		1.2	1922	1710	664	843
1.25	1658	1.3	1932	1587	644	812
		1.2	2015	1670	672	833

†.  $\bar{c}_o$  is 1118m/s for the typical adiabatic flame temperature of 3007K listed in Table 3.1-1. This neglects the co-volume effect to be presented later in Section 7.1.5.4 resulting in an underestimate of the actual sonic velocity.

The curious increase in muzzle exit temperature and sonic velocity relative to the propellant to projectile mass ratio for the slowest configurations may be attributed to the decreasing ballistic efficiency with increased muzzle velocity (3.2-5). For slow projectiles, the efficiency of launch implies that the propellant gas transferred more of its energy to the projectile, decreasing its temperature further than the less efficient launches at higher velocities. However, the added burden of the kinetic energy imparted to the propellant gas itself, as reflected in (4.2-10), quickly reverses this early trend.

#### 4.2.4 A Parametric Study

To lend perspective on recoil momentum, a parametric study will consider the momentum imparted to a gun as a function of muzzle velocity. It will be assumed that virtually no degradation in muzzle velocity will be tolerated. Therefore, prior recoilless rifles (Sections 2.4 and 3.3) or large muzzle brakes employed by guns of very poor ballistic efficiency (such as discussed by Corner [22]) will not be considered.

The momentum imparted to an orthodox gun may be divided into three components corresponding to the projectile momentum  $I_p$ , the momentum imparted to the gases up to shot-exit  $I_c$ , and the momentum imparted to the gases during blow-down of the gun after shot-exit  $I_{bd}$ , i.e.,

$$I_g = I_p + I_c + I_{bd}. \quad (4.2-23)$$

#### 4.2.4.1 Estimation of Gas Momentum

Using the Lagrange gradient assumption, the momentum imparted to the gases prior to shot-exit may be estimated as [39, 19]

$$I_c = m_c \frac{v_m}{2}. \quad (4.2-24)$$

This may be interpreted as the center of mass of the propellant following the base of the projectile through the gun, but lagging behind such that it is always halfway between the front face of the breech and rear face of the projectile. For the purposes of this parametric study, this assumption is adequate.

Formulae have been developed based upon the Hugoniot's gas flow theory that drop second and higher powers of the ratio of propellant to projectile mass [22, 42]. Since this ratio exceeds one for current tank gun ammunition of interest, these formulae are subject to question over an important range of the parametric study. A simple formula to estimate the average outflow velocity of the propellant gases from the muzzle,  $v_{cm}$  is the geometric norm of the sonic velocity at shot-exit and the muzzle velocity [36]

$$v_{cm} = \sqrt{\gamma R T_e + v_m^2}. \quad (4.2-25)$$

The total propellant gas momentum may now be computed using (4.2-25)

$$I_{ct} = m_c v_{cm}. \quad (4.2-26)$$

The blow-down momentum may be computed by subtracting the momentum imparted to the propellant gases prior to shot-exit (4.2-24) from the total gas momentum to yield

$$I_{bd} = I_{ct} - I_c. \quad (4.2-27)$$

#### 4.2.4.2 The Effect of a Muzzle Brake

Muzzle brakes deflect the exhausting propellant gases laterally, thereby reducing the forward momentum imparted to the gases and consequently reducing the rearward momentum imparted to the gun. There are two simple formulae in current use to determine the recoil reduction afforded by a muzzle brake, based upon a recoil metric associated with the brake geometry. The first is to assign a performance metric to a given muzzle brake based upon the ratio of total gas momentum that it may eliminate from the total gun recoil. Dillon [43] has termed this metric  $\Gamma$  and it is given as

$$I_g = I_p + (1 - \Gamma)I_{ct}. \quad (4.2-28)$$

This metric is widely used (for example Schmidt [44]) but has not historically been the metric employed in the United States and Great Britain where the Corner [22] momentum index  $\beta$  is generally used [45]. The Corner index is less intuitive than  $\Gamma$ , but is nearly as simple to implement. Rather than considering the muzzle brake to reduce the momentum imparted to the gun as proportional to the entire gas momentum, the Corner index considers the momentum reduction to be proportional only to the blow-down momentum [22,46]. Thus,

$$I_g = I_p + I_c + (1 - \beta)I_{bd}. \quad (4.2-29)$$

Corner's argument for this index was an apparent belief that it better accommodated the inevitable changes in muzzle brake performance when firing different charge configurations. Upon inspection of (4.2-25) it may be appreciated that lower velocity guns will have a greater percentage of the gas momentum imparted during blow-down as the gases speed up to exceed their sonic velocity.<sup>i</sup> Thus, the Corner  $\beta$  definition anticipates decreased  $\Gamma$  performance with increased muzzle velocities. This trend is consistent with the decreasing  $\Gamma$  as a function of muzzle velocity for the M198 single baffle howitzer brake presented by Schmidt [44] and shown in Fig. 4.2-2. Unfortunately, the opposite trend occurs with the double baffle M109 brake in the same paper and Figure. Since Schmidt's [44] results are available in the literature, and Schmidt has extrapolated the muzzle velocity dependence upon  $\Gamma$  to high muzzle velocities, his muzzle brake relationships will be used. Schmidt's [44] data is reproduced in Fig. 4.2-2 which also includes the results of curve fits presented in (4.2-30) and (4.2-31).

---

i. This may sound non-credible to those most familiar with steady state nozzle flow. Gun blow-down is not steady—it is highly transient. The gases within a constant cross-sectional area bore expand and gain velocity as they are propelled through the bore and out the muzzle.

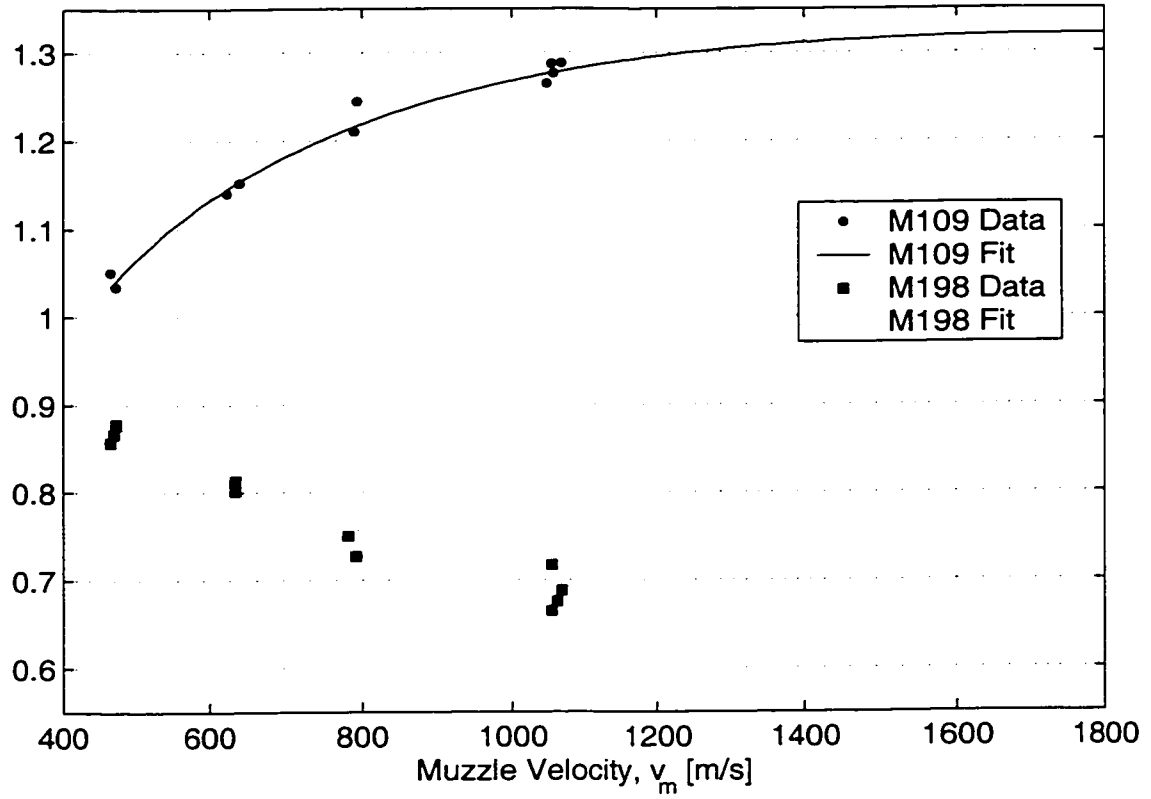


**Figure 4.2-2 Muzzle Brake Efficiency  $\Gamma$  as a Function of Muzzle Velocity for M109 and M198 Muzzle Brakes [44].**

Normalizing the muzzle velocity to its magnitude in m/s, fits for the two brakes are

$$\Gamma_{M109} = -0.159(\ln(v_m))^2 + 2.380(\ln(v_m)) - 7.586, \quad (4.2-30)$$

$$\Gamma_{M198} = 0.019(\ln(v_m))^2 - 0.473(\ln(v_m)) + 3.069, \quad (4.2-31)$$

where “ln” is the natural logarithm.

#### 4.2.4.3 Recoil Reduction Potential of RAVEN

The performance of RAVEN will be assumed to be very closely related to the percentage of the propellant gas  $\alpha$  that is ejected from the breech. The utility of a muzzle brake for RAVEN may be substantial. The specific forward impulse imparted to that portion of the propellant gases ejected out the muzzle will be assumed equivalent to the orthodox case as computed by (4.2-25). This is likely a conservative assumption, with the anticipation that the muzzle ejection velocity will be reduced for a RAVEN. The use of a muzzle brake may be anticipated to reduce the specific impulse of percentage of the gases ejected from the muzzle. Thus, the net momentum imparted to a RAVEN may be estimated as

$$I_g = -m_p v_m - (1 - \Gamma)(1 - \alpha)m_c v_{cm} + \alpha m_c v_c, \quad (4.2-32)$$

where negative magnitudes imply rearward recoil momentum imparted to the gun.

The magnitudes of the recoil momentum computed by (4.2-32) are plotted in Fig.4.2-3. The plot includes an orthodox gun with no gases vented out the back ( $\alpha = 0$ ) with a bare muzzle, an M109 muzzle brake (4.2-30), a  $\Gamma = 1$  muzzle brake, and an M198 double baffle muzzle brake (4.2-31). The range in recoil momentum between the bare muzzle and  $\Gamma = 1$  muzzle brake is lightly shaded, indicating the range of momentum reduction that may be available by modest to moderately aggressive muzzle brakes.

RAVENs that discharge half ( $\alpha = 50\%$ ) and three quarters ( $\alpha = 75\%$ ) of the propellant gas through the breech are shown with a bare muzzle, and with a  $\Gamma = 1$  muzzle brake. As in the orthodox case, shading indicates the range of momentum reduction that may be achieved with modest to moderately aggressive muzzle brakes. It should be noted, that the design requirements and performance for a RAVEN muzzle brake would be dramatically different as less gas would be applied through the brake. Finally, a hypothetical RAVEN that discharges all of the propellant rearwards through a Mach 4 expansion nozzle is shown. This constitutes an upper limit that could not be achieved in practice.



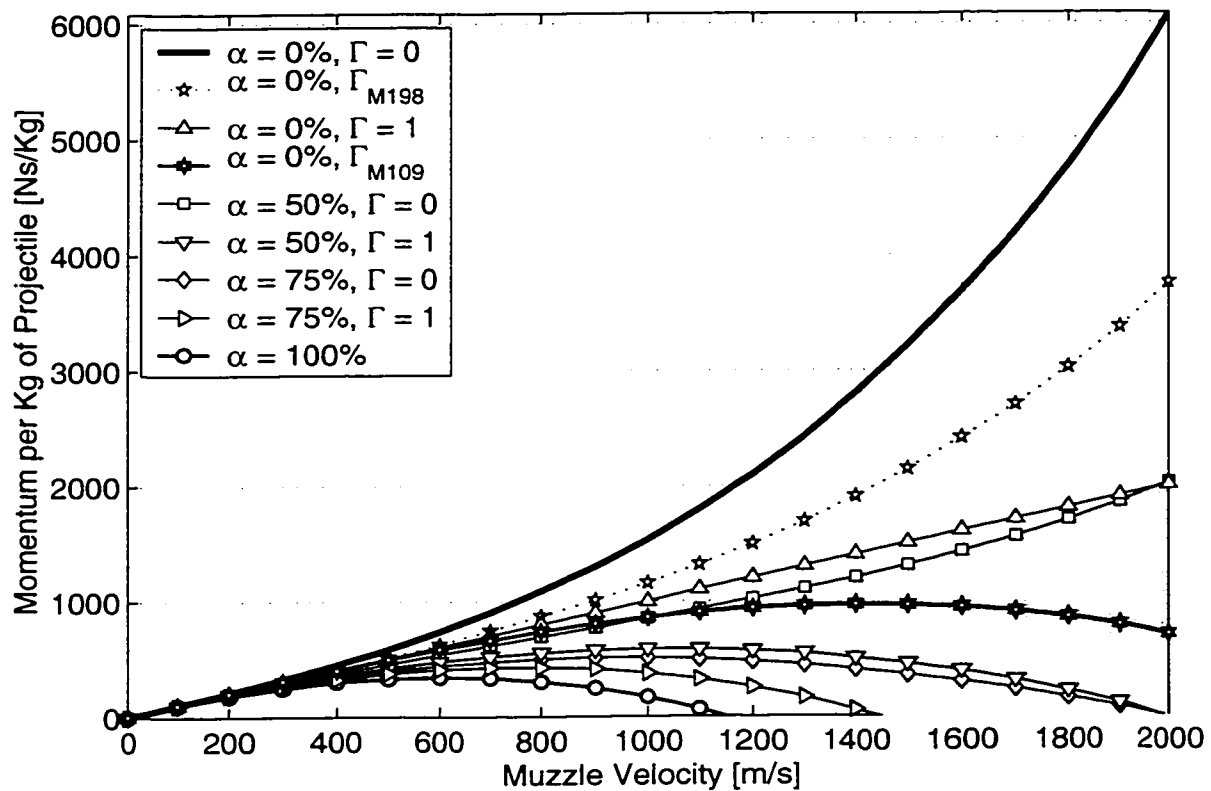


**Figure 4.2-3 Recoil Reduction Potential for Muzzle Brakes and RAVEN.**

Although the specific empirical relationships employed to develop Fig. 4.2-3 may lack fidelity, particularly at velocities in excess of 1500m/s, the general trends are clear. First, the greater the percentage of propellant gases that may be expelled rearward the better. Second, as more of the gases are being expelled rearward, there is less utility to a muzzle brake. Third, projectiles may be anticipated to achieve recoillessness as their muzzle velocity becomes high; provided sufficient propellant gas is discharged through the breech.

## **Part 5**

# **DESIGN AND DEVELOPMENT OF RAVEN 35MM TEST FIXTURE**

A bolt-action blow-back breech 35mm RAVEN was designed and constructed to experimentally determine the interior ballistic behavior of this altogether new form of gun propulsion.

### **5.1 Basic Parameters of the Fielded 35mm System**

The 35mm KD series gun and ammunition suite was originally developed by Oerlikon, Zurich, Switzerland as an anti-aircraft gun with a rate of fire in excess of 9 rounds per second [47].

#### 5.1.1 The 35mm Oerlikon KD Series Gun

Characteristics of the fielded gun system are listed in Table 5.1-1.

**Table 5.1-1: Characteristics of Oerlikon KD Series 35mm Gun [47].**

Bore Size	35mm
Muzzle Velocity	1170m/s
Barrel Length	3.15 m
Barrel Mass	140kg
Gun Mass	370kg

#### 5.1.2 The Oerlikon 35mm TP Practice Shell

The round of ammunition selected to be fired is the “Practice Shell Type UGD,” NATO designation TP. The projectile of this round is different from live shells in that the fuze is replaced by an alloy dummy, and that the shell is completely inert. Spin is imparted to the projectile by means of a soft iron rotating band that is integral with the

body of the shell. The projectile is crimped to the steel cartridge case by an eight point crimp. Characteristics of the TP round are listed in Table 5.1-2

**Table 5.1-2: Characteristics of 35mm Practice Shell TP.**

Muzzle Velocity, [48]	1175m/s
Launch Momentum <sup>†</sup>	1112Ns
Max Pressure, [48]	383MPa
Length of Round, [48]	387mm
Diameter of Case, [49]	55mm
Mass of Projectile, $m_p$ , [48]	0.550kg
Mass of Propellant, $m_c$ , [48]	0.333kg
Mass of Complete Round, [48]	1.580kg

†. Hearsay value of 250 Lb<sub>f</sub>\*sec, no reference available.

The projectile and propellant masses listed in Table 5.1-2 may be inserted into (3.2-1) to compute a predicted muzzle velocity of 1192m/s. Thus, the Ogorkiewicz formula is within 1.5% of the published velocity for this round of ammunition.

### 5.1.3 Geometry of the 35mm TP Round

A picture of the TP round and a drawing of the cartridge case [49] is included in Figure 5.1-1. The recessed band visible in the picture of the round just behind the

shoulder is for link feed guns. The round used in the testing, like the drawing of the cartridge case, did not have this recess.

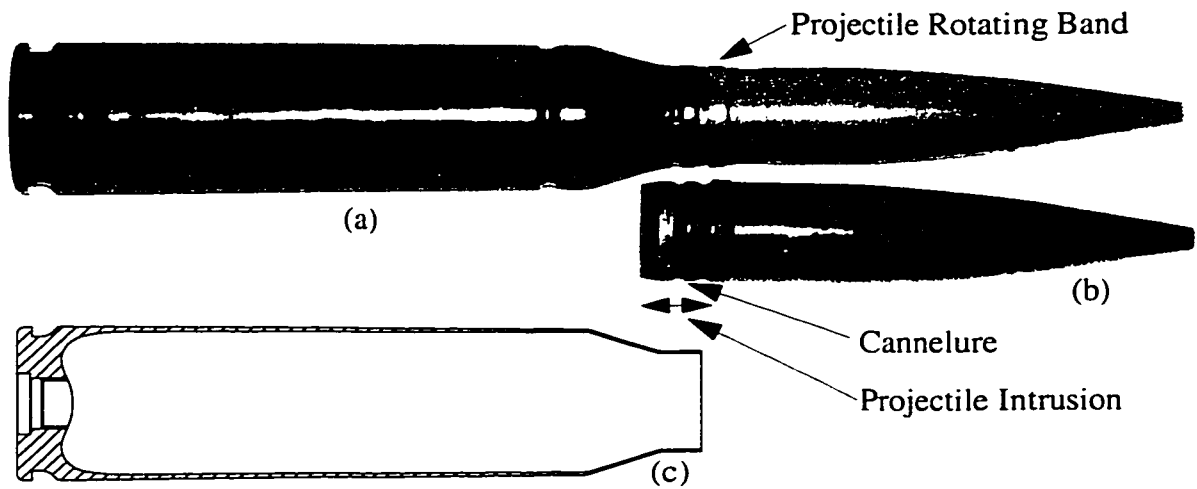


**Figure 5.1-1 35mm TP Round: Assembled Cartridge (a), Projectile (b), and Cartridge Case Drawing (c).**

The rotating band width  $b_r$  of the projectile is approximately 6.8mm with a diameter of 36.56mm.

#### 5.1.3.1 Cartridge Case Volume

The volume of the cartridge case is  $387.75 \text{ cm}^3$  not including intrusion of the projectile into the neck and for the primer in the head [49]. The intrusion of the projectile from the base of its rotating band to its rear face is 22.2mm. The intrusion volume is  $18.7 \text{ cm}^3$ . The primer intrusion may be approximated as cylinder of outer diameter 15.5mm, inner diameter of 9.8mm and length of 16mm for an intrusion volume of  $1.8 \text{ cm}^3$ . Thus, the total chamber volume is estimated at  $367.25 \text{ cm}^3$ . The primer extends rearward into

the head of the cartridge case, for an internal length of 3.1 cm and thus, a primer volume of 2.3 cm<sup>3</sup>.

#### 5.1.3.2 Length From Back of Case to Base of Projectile

The length between the rear face of the projectile and the internal face of the cartridge case head is 155mm.

#### 5.1.4 Rifling

The rifling of the barrel effects the bore area and the frictional forces during launch. The rifling cross-section of the gun is depicted in Fig 5.1-2.

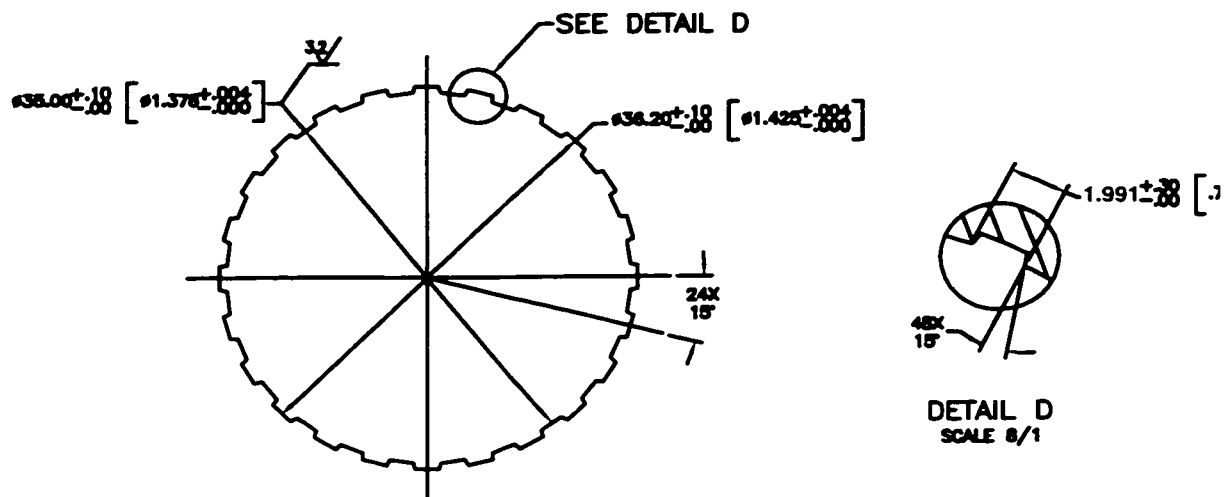


Figure 5.1-2 Cross-section of Rifling Profile [49].

Although a progressive twist was manufactured, a representative rifling twist of one turn in 28 calibers will be assumed. The rifling parameters are listed in Table 5.1-3

**Table 5.1-3: Rifling Parameters**

Number of Grooves, $n_r$	24
Groove Width, $G_w$	1.991mm
Groove to Land Ratio, GLR	0.7686
Groove Depth, $h_r$	0.6mm
Twist, $T_w$	28 Calibers per Turn

#### 5.1.5 Bullet Resistance Curve

A simple formula for the friction along the bore of the gun is [50]

$$f_{br} = \mu_o n_r h_r b_r \sigma_r, \quad (5.1-1)$$

where  $f_{br}$  is the bore friction,  $\mu_o$  is a coefficient of friction,  $n_r$  and  $h_r$  are listed in Table 5.1-3, the rotating band width  $b_r$  is listed in Section 5.1.3, and  $\sigma_r$  is the permissible surface pressure on the rotating band material. Representative magnitudes for  $\mu_o$  and  $\sigma_r$  for a soft iron rotating band are 12% to 18% and 200 MN/m<sup>2</sup> to 300 MN/m<sup>2</sup> [50]. Relative to the general guidelines for rotating band design [25] the rotating band width is short and the interference between the band outer diameter and the groove diameter is large. Therefore, the higher representative magnitudes will be used when inserting the numerical values. The resulting estimate of bore friction is 5.288 kN.

The initial engraving of the rotating band exerts a substantial resistive load between the barrel and the projectile. Robbins [51] has provided guidance for the engraving resistance of a gilding metal rotating band. Distribute 35MPa of resistance pressure as a single saw tooth curve over the first two centimeters of travel.

The shot-start pressure is related to the bullet pull force of the cartridge case. An estimate of 4.3 kN was made based upon a linear fit of bullet pull as a function of caliber for seven representative gun systems [35]. The bore resistance profile is most often represented by the equivalent pressure applied over the bore area. The results may be linearly interpolated from the values listed in Table 5.1-4.

**Table 5.1-4: Bore Resistance Profile**

Projectile Travel	Resistance Pressure
0.00m	4.48MPa
0.01m	35.0MPa
0.02m	5.5MPa
$x_p > 0.02\text{m}$	5.5MPa

#### 5.1.6 Propellant Chemical Properties

The propellant employed by the TP round is proprietary. Based upon communication with Picatinny Arsenal and Oerlikon [52], the chemical constituents of the propellant were learned to be rather similar to standard M1 propellant with an unknown

deterred layer integrated with the outer surface of the propellant grain. M1 is predominately composed of Nitrocellulose. It's properties are listed in Table 5.1-5.

The primer chemistry is unknown. Since the ratio of propellant gases that evolve from the primer relative to the main bed of propellant is very small, the ballistic solution is not particularly sensitive to this. It will be assumed that the primer volume of  $2.3 \text{ cm}^3$  determined in Section 5.1.3.1 is filled with Black Powder at a typical loading density of  $1 \text{ g/cm}^3$  for a total igniter mass of 2.3 g. It's properties are listed in Table 5.1-5.

**Table 5.1-5: Thermodynamic Properties of M1 Propellant and Black Powder.**

	M1	Black Powder
Mass in 35mm TP Cartridge	333 g	2.3 g
Adiabatic Flame Temperature	2417 K [53] <sup>†</sup>	2188 K [54]
Force	0.912 MJ/kg [53]	0.290 MJ/kg [54]
Ratio of Specific Heats	1.259 [53]	1.218 [54]
Covolume	1104 cm <sup>3</sup> /kg [53]	785 cm <sup>3</sup> /kg [54]
Grain Density	1.57 g/cm <sup>3</sup> [53]	1.97 g/cm <sup>3</sup> [54]
Burn Rate Coefficient	2.175e-3 m/s/MPa <sup>n</sup> [53]	3.65e-3 m/s/MPa <sup>n</sup> [54]
Burn Rate Exponent, n	0.710 <sup>†</sup> [53]	0.568 [54]
Computed Properties		
Heat of Explosion (3.1-6)	3.521 MJ/kg	1.330 MJ/kg
Gas Constant (3.1-1)	377.3 <sup>†</sup> J/kg/K	132.5 J/kg/K
Molecular Mass (3.1-2)	22.03 <sup>†</sup> kg/kmol	62.73 kg/kmol



- †. Ballistic matching to be presented in Section 7.2.1 will decrease the flame temperature by 9% to 2200 K and increase the burn rate exponent by 10% to 0.78. This will raise the gas constant to 414.5 J/kg/K and reduce the molecular mass to 20.06kg/kmol.

#### 5.1.7 Propellant Grain Geometry

The propellant is single perforation cylindrical geometry as in Fig. 7.1-2.f. Three representative grains were measured with a dial caliber to determine the outer diameter and length of the grains. The inner diameter of the perforation, was determined by means of a microscope. Images of the grains are included in Fig. 5.1-3. The geometry is listed in Table 5.1-6:

**Table 5.1-6: Measured Geometry of 35mm TP Propellant Grains**

Length	2608 $\mu\text{m}$
Outer Diameter	1994 $\mu\text{m}$
Perforation Diameter	250 $\mu\text{m}$

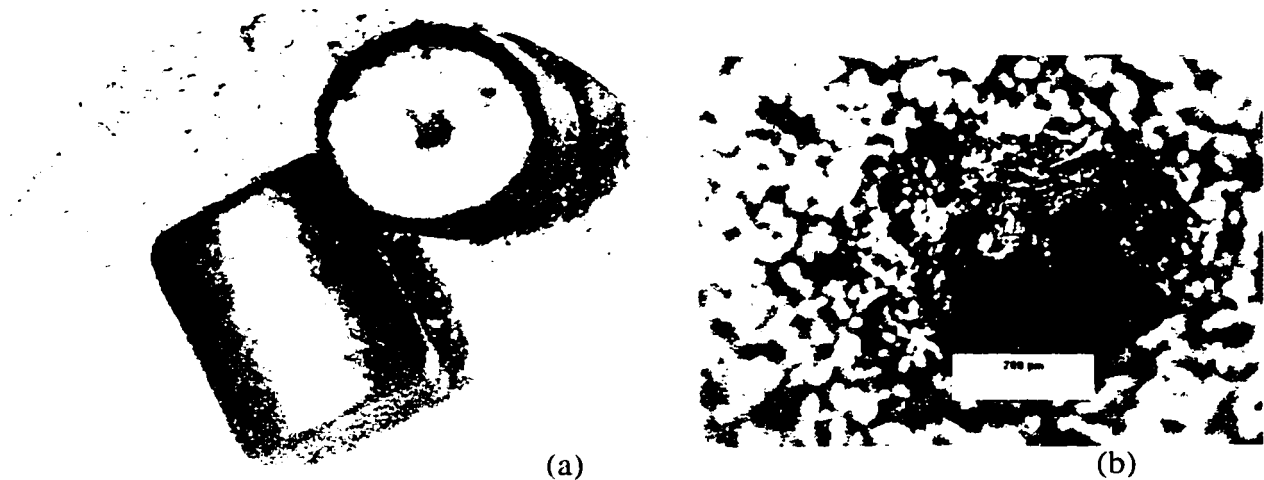


**Figure 5.1-3 Images of Propellant Grains Showing Generally Cylindrical Shape (a) and Indicating the Diameter of the Center Perforation (b).**

### 5.1.8 Interior Ballistics

The 35mm TP round is not currently used by the United States Army with the exception of the M968, which is a rarely used sub-caliber training round for the 120mm M256 cannon [30]. Therefore, modern interior ballistic data on this round was not available during the design of the test fixture. The data that was available was an engineering plot of the anticipated pressure, travel, and velocity time curves drawn in July 1975; attached here as Fig 5.1-4. Since the curves may be challenging to read, some of the pertinent data is included in Table 5.1-7.

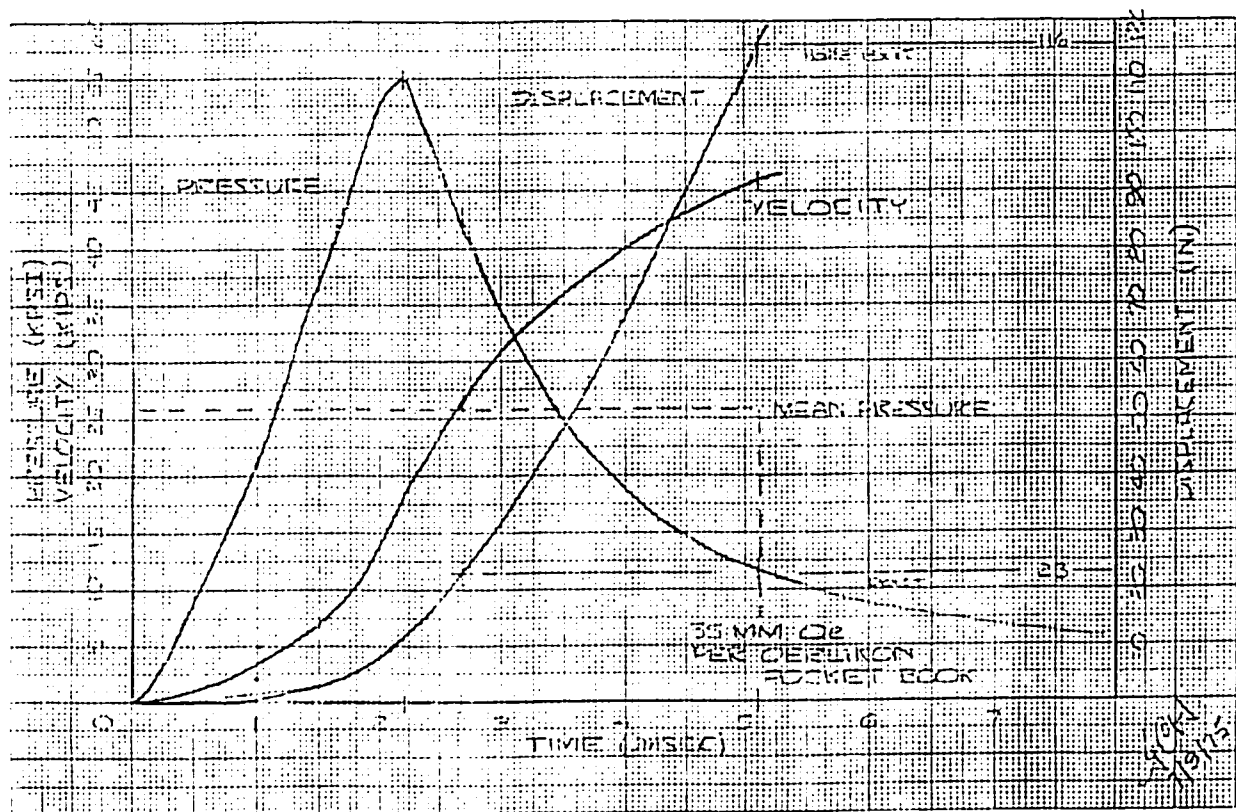


Figure 5.1-4 Pressure, Travel, and Velocity Time Curve for Gun Design [55].

**Table 5.1-7: Design Interior Ballistic Data From Fig. 5.1-4.**

Parameter	English Units	SI Units
Muzzle Velocity	46000in/sec	1168m/s
Projectile Travel	116in	2.946m
Peak Pressure	55000psi	379MPa
Exit Pressure	11500psi	79MPa
Time to Peak Pressure	2.2ms	2.2ms
Time to Shot-Exit	5.1ms	5.1ms
Velocity at 33% Travel	33000in/s	838m/s
Velocity at 25% Travel	27000in/s	686m/s

## **5.2 Mechanics of Venting**

Many methods may be conceived to cause the requisite vent timing for a RAVEN. Few of these concept methods are likely work well in practice. Fewer still will be amenable to the application of engineering principles such that a design may proceed with confidence from the computer aided design models to reliable operation without the benefit of intermediate test validation. Because of the contractual vehicle employed to construct and operate the test fixture with ARES, Inc. of Port Clinton, Ohio, it was critical that a sound design precede any testing whatsoever.

### **5.2.1 Five Principal Requirements of a RAVEN Vent**

The following qualities are highly desirable in a RAVEN vent:

#### 5.2.1.1 Reliable Vent Timing

The timing should be highly repeatable and inextricably tied into the propulsion of the projectile in a manner that is robust. The recoil reduction provided by RAVEN will enable lightweight guns and mounts that cannot tolerate venting failures that cause dramatic increases in recoil momentum relative to the intended operating momentum. Venting late, perhaps after the projectile has exited the gun, will not provide substantial recoil momentum reduction.

#### 5.2.1.2 Flow Area Comparable to Bore

When open, a RAVEN vent's minimum area of flow should be comparable to, or greater than, the bore area. A smaller flow area will result in a smaller mass fraction  $\alpha$  discharged through the recoil compensation nozzle. This will compromise recoil reduction as seen in Fig. 4.2-3. A second, more subtle impact is upon potential vent erosion as will be discussed in Section 5.2.1.4. This requirement may need to be re-evaluated as test and simulation data are generated.

#### 5.2.1.3 Swift Operation

The valve opening duration from commencement until full flow area is enabled should be swift, comparable to or less than 10% of the time from peak pressure to shot-exit. This requirement avoids effects similar to those described in Section 5.2.1.2. If the vent opens slowly, the flow is restricted; thus, limiting the mass fraction discharged through the recoil compensation nozzle.

This requirement may need to be re-evaluated as test and simulation data are generated.

#### 5.2.1.4 Erosion Tolerance

If the vent surfaces are not disposable, they should withstand the potentially erosive environment of the high-pressure propellant gas flow. One of the most powerful means to reduce the potential for erosion, is to select a venting method that opens swiftly, with a large flow area as discussed in Sections 5.2.1.2 and 5.2.1.3. This reduces erosion by minimizing the duration of high gas density flow. In different terms, the greater the flow area, the greater the mass flow rate, and the more pronounced the local gas density and temperature reduction that will be caused by the rarefaction wave.

#### 5.2.1.5 Minimize Degradation of Muzzle Velocity

Several vent techniques tap into the propellant gas energy to actuate the vent. As the propellant energy is extracted, it is not available for projectile propulsion. Thus, the actuation energy requirements may “slow down the projectile” in a manner that is totally distinct from the potential for the rarefaction wave released by the venting process to degrade ballistic efficiency.

### 5.2.2 Vent Commencement Time

The desired vent time of a RAVEN must be determined on a case-by-case basis depending upon the design objectives of the system and its interior ballistic characteristics. The results of a prior modeling effort resulted in the following vent times

to achieve synchronized timing of the base of the projectile and rarefaction wave front at the muzzle of the gun at shot-exit are presented in Table 5.2-1.

**Table 5.2-1: Synchronized Vent Timing for Guns [6,3]**

Gun/Ammo	Caliber	% Projectile Travel When Venting Commences
M242/M919	25mm	29.7%
M256/M829A2	120mm	24.2%
XM297/Zone-6	155mm	34.5%

Since the objective of the RAVEN demonstrator was to conduct research upon the interior ballistics of RAVEN, means to vary the vent timing to span an interesting design space were required. A nominal range of vent timing desirable of the RAVEN 35mm test fixture would correlate to 25% - 33% of projectile travel.

### 5.2.3 Blow-Back Recoil and the Inertial Breech RAVEN Vent

Arguably the simplest means to vent the chamber of a gun is not to screw the breech block down. Thus, rather than rely upon stresses developed within the breech block and breech ring as they strain under the pressure, the inertial resistance of the breech block to acceleration will contain the propellant gas pressure. Such a design is termed a blow-back gun [56].

Historically, blow-back operated guns that incorporate a sliding breech (but that do not vent the chamber) have been in existence since the eighteenth century. Chinn discusses the engineering of blow-back guns extensively [56]. The line drawing of Fig. 3.2-2 is actually of a blow-back operated gun with a special cartridge case head that allows

greater rearward case motion under the action of the propellant gas while still contained within the walls of the chamber. The historical challenge of blow-back operation is that the deformation of the cartridge case must be repeatable and not sufficient to allow rupture of the neck of the case from the body. Friction, in particular, is troublesome. This challenge manifests itself as very limited recoil stroke of the breech block while the chamber is under pressure.

Chinn [56] has argued that a 20mm case designed for blow-back operation should not deflect more than  $6\text{ }\mu\text{m}$  during the first 10ms. The 20mm gun reaches peak chamber pressure in 0.5ms and achieves shot-exit in 2ms [56]. Since the ballistic forces involved dwarf disturbances such as friction, the only means to keep the breech motion restricted is inertia—and lots of it: 225kg breech mass for a 0.13kg bullet with a muzzle velocity of 840m/s.

A means to avoid the excessive mass of a blow-back gun as described by Chinn [56] is to allow the cartridge case to rupture at its head (refer to Fig. 3.2-2), form a gas seal with the chamber wall, and recoil rearwards down an extended “chamber bore.” Alternatively, the cartridge case may be composed of two parts: a stub metal case with a combustible side-wall like current 120mm M256 tank gun ammunition [30]. This form of extended blow-back may be termed an inertial breech [57]. This will reduce the inertia required by elimination of the cartridge case recoil stroke limitation discussed by Chinn [56]. Thus, the inertial breech may recoil any design distance; however, the kinetic energy imparted to the breech increases with increased recoil stroke. If the mass of the sliding

breech is comparable to the recoiling mass of fixed breech gun that fires the same ammunition, and the chamber diameter is similar to the bore diameter, the recoil energy and management requirements will be similar.

Considering an inertial breech in analogy with a two stroke engine piston, the motion of the breech may expose a vent port as a function of its recoil displacement. Since the inertial breech is driven by the very same propellant gases that propel the bullet, and since this ballistic force is anticipated to be far greater in magnitude than any foreseen disturbance forces, this method of venting meets the reliable vent timing requirements of Section 5.2.1.1

Since the inertial breech is of the same diameter as the cartridge case, it may certainly expose a vent area that is greater than the bore area, meeting the requirements of Section 5.2.1.2. The greatest vent area may be opened by uncovering an exhaust port that extends a full 360 degrees —uncorking the back of the chamber into an expansion nozzle.

As the design mass of the inertial breech is increased, it will extract less energy from the propellant gases, and compromise projectile propulsion less. However, as the velocity decreases with increased design mass, it takes the breech longer to uncover an exhaust port. Thus, selection of the mass of the breech constitutes a design trade-off between Sections 5.2.1.5 and 5.2.1.3. A line drawing of an inertial breech actuated RAVEN vent based upon Fig. 3.2-2 is depicted in Fig. 5.2-1.



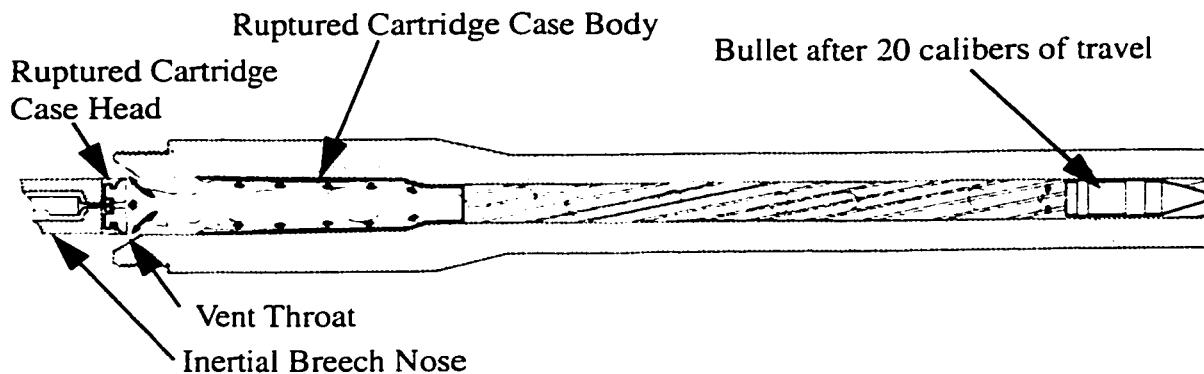


**Figure 5.2-1 Inertial-Breech Bolt-Action RAVEN Vent In Operation.**

#### 5.2.4 Cartridge Case Notch

A notch placed on the outer diameter of the cartridge case, flush with the forward face of the cartridge head is a pragmatic means to facilitate the rupture of a cartridge case. This desire drove the caliber decision for the test gun. Cartridges 35mm and larger employ a screw in primer-igniter assembly. Those that are smaller use a press fit. The screw in assembly could be safely unscrewed from a training round, the propellant downloaded, and the inert cartridge case could have a notch machined into it by means of a lathe while the inert training projectile remained crimped at the cannelure. The propellant could then be uploaded into the cartridge case and the primer screwed back into place. Since testing costs increase dramatically with caliber, the smallest screw in primer cartridge was selected, a 105mm gun being the next available cartridge in the current inventory.

In addition to the notch, the extraction rim was removed to provide a place for a nylon obturation band. These modifications to the cartridge case drawn previously in Fig. 5.1-1.c are shown in Fig. 5.2-2.

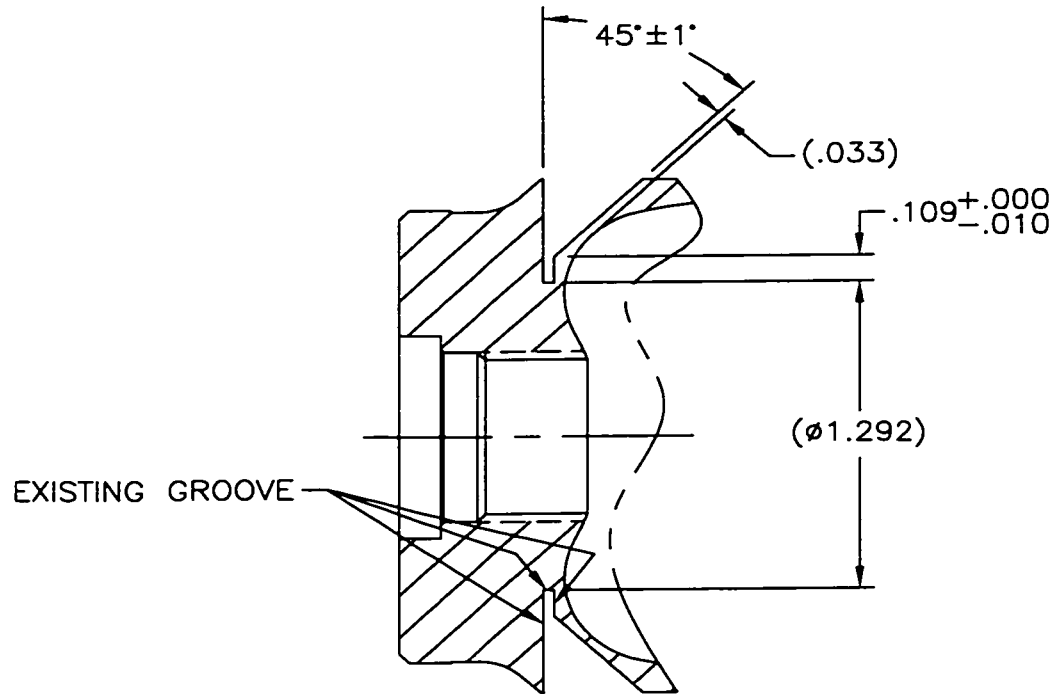


**Figure 5.2-2 Detail Modification of Drawing 31223 Showing Cartridge Case Notch and Extraction Rim Removed (English Units) [49].**

#### 5.2.5 Vent Flow Area

The flow area provided by an inertial breech with a full circumference port as shown in Fig 5.2-1 is a function of the relative position of the gun barrel and inertial breech as a function of time. Neglecting, for the moment, the taper of the expansion nozzle indicated in Fig 5.2-1, and instead assuming the rear face of the chamber is flush (a

degenerate 90 degree half-angle nozzle), when the head of the cartridge case first exposes the propellant gases to the port, the gases will tend to flow radially outward through a throat that may be described as a thin cylindrical wall as shown in Fig. 5.2-3.b.

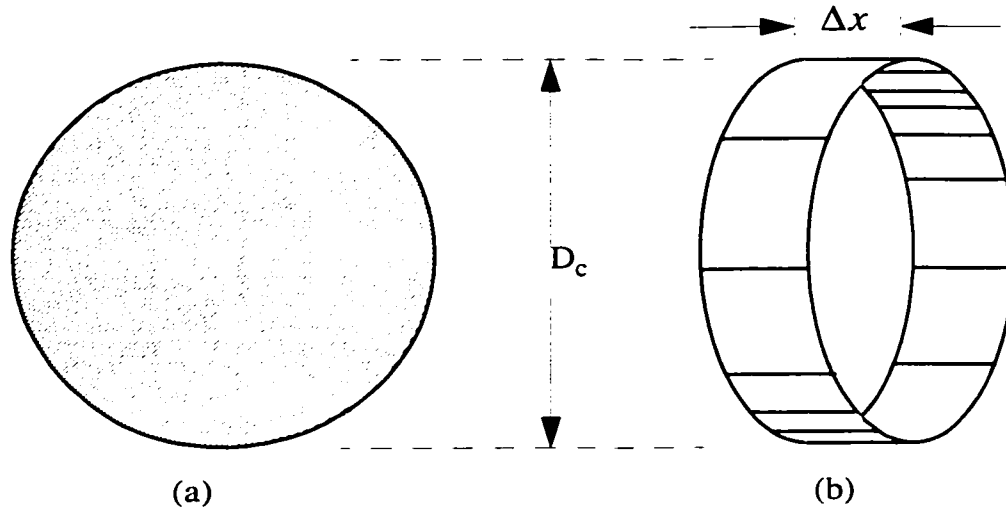


**Figure 5.2-3 Flow Area, In Circular Bore (a), Around Circumferential Port (b).**

Assuming a radial flow path, the ratio of the throat area of this expanding port relative to the cross-sectional area of the chamber bore will become unity (meeting the criteria of an open vent per Section 5.2.1.2) when

$$A_{(a)} = \frac{1}{4}\pi D_c^2 = \pi D_c \Delta x = A_{(b)}, \quad (5.2-1)$$

thus,  $\Delta x = D_c/4$ .

Thus, the inertial breech valve may be considered fully open when the breech and barrel have recoiled apart by one fourth of the chamber diameter.

### 5.2.6 Speed of Opening

To meet the criteria of Section 5.2.1.3, the speed of the inertial breech must be sufficient to traverse the relative recoil distance of (5.2-1) in 10% of the time between peak pressure and shot-exit. Using the chamber bore diameter as opposed to the gun bore as an opening criteria, the diameter to be employed in (5.2-1) is 55mm (according to Table 5.1-2). Using the timing criterion of Section 5.2.1.3 and the anticipated time between peak pressure and shot-exit presented in Table 5.1-7, the time to fully open the vent should be 10% of 5.1ms - 2.2ms or 0.29ms. This criteria will dictate the velocity of the inertial breech when venting commences as

$$v_b|_{t=t_v} = \frac{D_c/4}{(t_e - t_{pmax})/10} = \frac{(55mm)/4}{(5.1ms - 2.2ms)/10} = 47.4(m/s). \quad (5.2-2)$$

### 5.2.7 Mass of the Inertial Breech

The mass of the inertial breech will be required to achieve the velocity determined in (5.2-2) when the projectile has traversed 25% - 33% of its travel as determined in Section 5.2.2. If the diameter of the chamber and the bore were the same, the mass of the inertial breech could be computed by dividing the desired recoil velocity by the launch momentum at the desired vent times. Since the face of the inertial breech has more than double the area of the bore, the forces acting on the breech will be more than double that which would occur if it were of an area comparable to the bore.

The momentum imparted to the inertial breech face may be estimated as the launch momentum imparted to the projectile and propellant gases at the desired time of

venting, multiplied by the square of the ratio of the chamber diameter to the bore diameter. This may appear to result in more rearward momentum imparted to the system than forward momentum; however, the difference between the two is applied as forward momentum imparted to the gun barrel at the neck of the cartridge case. Such a barrel may be termed a “blow-forward” barrel [56]. Since the barrel may be assumed to have far greater mass than the inertial breech, little energy is lost to this “blow-forward” behavior. The same can be said of the inertial breech, although to a lesser extent, provided it is far more massive than the 0.555kg projectile being fired. As the inertial breech becomes lighter, more energy will be imparted to it, decrementing the propellant gas energy available for bullet propulsion. This is the subject of Section 5.2.1.5.

Accounting for the momentum imparted to the propellant gases using (4.2-24) and determining the projectile velocities when the projectile has traversed 25% and 33% of its travel from Fig. 5.1-4 as tabulated in Table 5.1-7, the momenta of the inertial breech may be computed as

$$\begin{aligned}
 I_b|_{(x_p = 25\%)} &= \left(\frac{D_c}{D_b}\right)^2 \left(m_p + \frac{m_c}{2}\right) v_p|_{(x_p = 25\%)} \\
 &= \left(\frac{55mm}{35mm}\right)^2 \left(0.550Kg + \frac{0.333Kg}{2}\right) \left(686\frac{m}{s}\right) = 1214Ns \quad , \quad (5.2-3)
 \end{aligned}$$

$$\begin{aligned}
I_b|_{(x_p = 33\%)} &= \left(\frac{D_c}{D_b}\right)^2 \left(m_p + \frac{m_c}{2}\right) v_p|_{(x_p = 33\%)} \\
&= \left(\frac{55mm}{35mm}\right)^2 \left(0.550Kg + \frac{0.333Kg}{2}\right) \left(838\frac{m}{s}\right) = 1483Ns \quad . \quad (5.2-4)
\end{aligned}$$

Combining the velocity requirement of (5.2-2) with (5.2-3) and (5.2-4), the inertial breech mass is determined to be 25.6kg and 32.3kg, respectively.

Since the mass of the inertial breech will govern vent timing, two different inertial breeches were constructed for venting, and a third for a slide breech non-venting baseline test. The masses of the configurations are listed in Table:5.2-2.

**Table 5.2-2: Inertial Breech Configurations Tested**

Description	Mass
Heavy	35.9kg
Light	20.9kg
Non-Venting	31.8kg

#### 5.2.8 Shear Plug

A means to positively secure the inertial breech to the gun until the propellant bed was ignited was desired for four reasons. (i) to provide a positive means to control head-space (between the breech face and rear of the cartridge case head) in the test fixture; (ii) to provide a closed volume for the ignition of the propellant bed that may improve repeatability; (iii) to reduce energy losses to the inertial breech early in the ballistic cycle that could result in the ejection of unburned propellant;<sup>i</sup> and (iv) to enable operation of the

test fixture as an orthodox gun by replacing the shear plug with a plug designed to withstand peak pressures.

If a shear plug is not employed, the solution to the third challenge is to reconfigure the propellant granulation to reduce the web-thickness and, thus, to engineer the propellant for the application. However, optimizing ammunition is an expensive undertaking that was directly avoided by selecting a NATO standard round. This third challenge is particularly insidious, since the ballistic performance losses associated with a poorly configured web would easily and predictably be misunderstood and attributed to venting. Therefore, programmatically, it was essential to minimize the potential for this type of performance loss.

The shear plug was simply constructed of 7178 wrought-aluminum, and integrated into the front nose of the inertial breech. The plug included an oversized circumferential band that had to shear off prior to allowing the inertial breech to recoil rearwards relative to the barrel. The diameter of the plug at the shear line was just less than the 55mm cartridge case diameter of Table 5.1-2. The original web of the band was selected to be 14mm. Thus, the circumference and web resulted in an area of  $2.42\text{e-}3\text{ m}^2$  available to shear. The tensile strength of 7178 is listed as 600MPa resulting in a shear strength of approximately 300MPa [58]. Thus, the plug would fail in shear at 726 kN. Dividing the ballistic force required by the area of the chamber results in a shear pressure

- 
- i. The recoil motion of the breech will increase the volume of the chamber effecting a minor loss in pressure. However, since the burn rate of the propellant is inextricably tied to the pressure, seemingly minor losses in pressure may cascade, resulting lower peak pressures and the potential for the propellant to fail to burn through the web prior to shot-exit.

of 305MPa, which is 80% of the anticipated maximum pressure. Pictures of failed and whole shear plugs are shown in Fig. 5.2-4. Assembly drawings including the shear plug will be appear later in Fig. 5.2-6 and Fig. 5.3-3.a.

Testing swiftly revealed that seal issues arose using this configuration, and one function test shot (1-2-2) in late October failed to shear. The web design was amenable to modification to reduce its area. The thickness of the web was reduced by means of an undermine cut to 10mm, reducing the ballistic pressure to fail in shear to 220MPa.

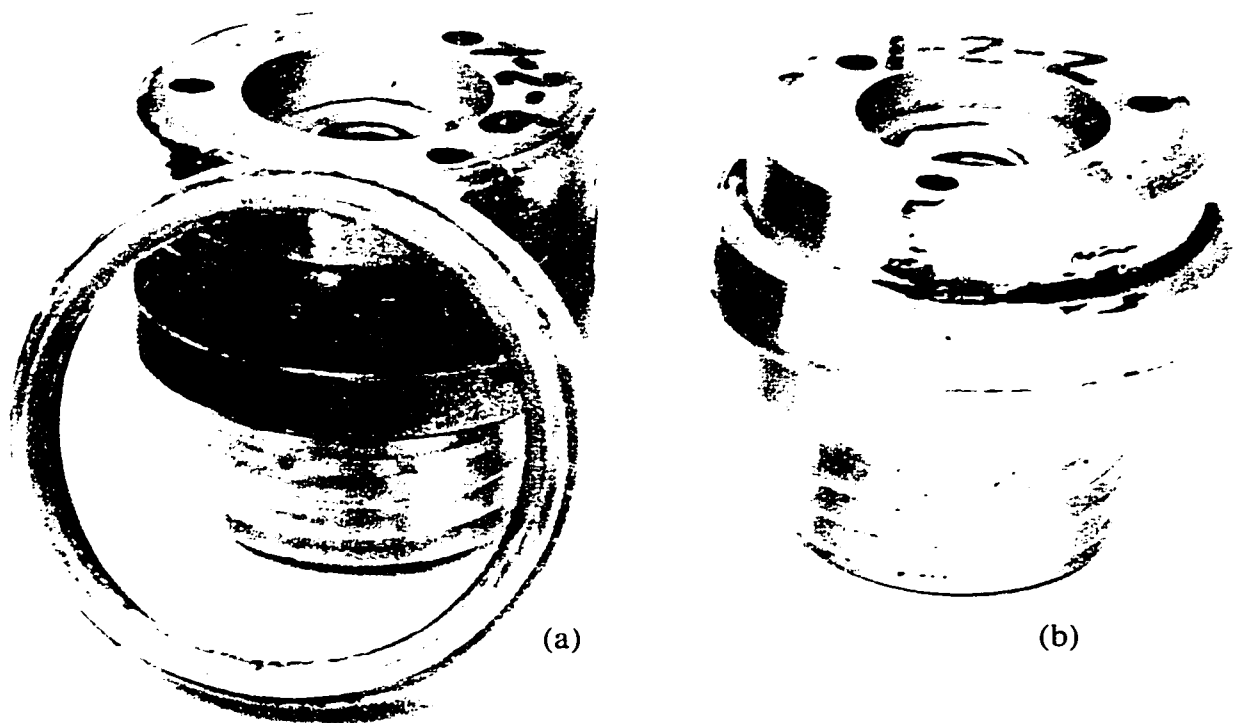


**Figure 5.2-4 Shear Plugs for the Nose of the Inertial Breech in the Sheared (a) and Un-Sheared (b) State.**



### 5.2.9 Vent Geometry

#### 5.2.9.1 Computing the Distance to the Vent Port

Clearly, the distance that a given inertial breech must recoil prior to venting the gun controls the vent timing. A simple means to estimate the travel between the barrel chamber and inertial breech before uncovering the vent port is required. Since the test fixture will incorporate means to alter the parametric configuration, fidelity is not essential.

The blow-back bolt-action Raven of Fig. 5.2-1 consists of four principal mass elements: the projectile, the propellant gas, the inertial breech, and the gun barrel. It may be reasonably assumed that external forces applied to this four mass system are small and may be neglected prior to shot-exit or venting. This is the free recoil assumption. Since the center of mass of a system of particles void of external forces cannot be accelerated, the center of mass of the blow-back bolt-action RAVEN must remain constant, i.e.,

$$m_p \Delta x_p + m_c \Delta x_c + m_r x_r + m_{gc} \Delta x_{gc} = 0, \quad (5.2-5)$$

where  $\Delta x_p$ ,  $\Delta x_c$ ,  $x_r$ , and  $\Delta x_{gc}$  are the relative motions of the projectile, propellant, inertial breech, and gun barrel following shot-start, respectively. Simply assuming a large mass for the gun barrel will not eliminate its contribution to the motion of the other parts since the gun barrel will have significant momentum.

Using the Lagrange gradient assumption, the motion of the propellant gases may be approximated as half that of the projectile in analogy with (4.2-24)

$$\Delta x_c = \frac{(\Delta x_p)}{2}. \quad (5.2-6)$$

This assumption will introduce a modest error as a result of the larger diameter of the chamber relative to the bore, but its simplicity exceeds concerns regarding fidelity.

Assuming an initial condition of rest, the rearward velocity of the breech may be computed by integration of the product of the pressure at the breech face and the area of the breech face divided by its mass

$$v_r = \frac{-A_c}{m_r} \int P_o dt. \quad (5.2-7)$$

The position may be determined by integration of the velocity in time to yield

$$x_r = \int v_r dt = \frac{-A_c}{m_r} \int \left( \int P_o dt \right) dt. \quad (5.2-8)$$

Similarly, the blow-forward motion of the gun barrel may be computed as a double integral in time of the pressure at the neck of the cartridge case

$$\Delta x_{gc} = \frac{(A_c - A)}{m_{gc}} \int \left( \int P_{gc} dt \right) dt. \quad (5.2-9)$$

The difference in pressure between the breech face and neck of the cartridge case is anticipated to be small. Therefore, the integrals in both (5.2-8) and (5.2-9) are

approximately equal. Solving (5.2-8) for the double integral, and inserting the result into (5.2-9) yields

$$\Delta x_{gc} \approx \frac{m_r}{m_{gc}} \left( \frac{A_c - A}{-A_c} \right) x_r. \quad (5.2-10)$$

This is a plausible result since differences between the chamber and bore area approach zero —a straight pipe, there is no forward motion imparted to the barrel. Similarly, as the mass of the barrel increases, its forward motion is attenuated.

Substitution of (5.2-6) and (5.2-10) into (5.2-5) results in the recoil displacement of the inertial breech as a function of projectile position as

$$x_r = \frac{(m_p + m_c/2)}{m_r} \left( \frac{-A_c}{A} \right) \Delta x_p. \quad (5.2-11)$$

It is the relative distance between the barrel and the breech that will geometrically dictate when the vent port is enabled. So the vent distance, assumed to have been zero initially, may be computed as

$$x_v = \Delta x_{gc} - x_r = \left( \frac{A_c - A}{m_{gc}} + \frac{A_c}{m_r} \right) \left( \frac{m_p + \frac{m_c}{2}}{A} \right) \Delta x_p. \quad (5.2-12)$$

**Table 5.2-3: Vent Stroke Estimates Assuming 300kg Barrel.**

Inertial Breech Used	25% Travel	33% Travel
Light (20.9kg)	65.8mm	86.8mm
Heavy (35.9kg)	39.4mm	52.0mm

The effect on vent stroke caused by the shear plug described in Section 5.2.8 is discernible but small. This may be ascertained by determining the projectile travel that is achieved prior to reaching the 220MPa shear pressure (32 ksi) using Fig. 5.1-4. This pressure is reached at 1.3ms, after the projectile has traversed just less than 50mm (2 in). Since no vent stroke is achieved prior to shearing, the recoil vent stroke computed as the projectile traverses the first 50mm of its travel should be subtracted from the vent stroke estimates of Table 5.2-3 to achieve venting at the desired percentage of projectile travel. This difference amounts to 4.4mm and 2.6mm for the light and heavy breeches respectively, assuming a 300kg barrel.

#### 5.2.9.2 Shape of the Vent Port

A first design approach for the geometry of the vent could follow that of Fig. 5.2-1 and provide for an expansion cone of reasonable included angle. As the included angle becomes smaller, the throat area assumption of Fig. 5.2-3.b becomes compromised, and in its place an annulus between the inner diameter of the nozzle and outer diameter of the nose of the inertial breech should be employed. The area of the annulus would be smaller than the cylindrical wall during the initial opening of the vent. This is not a preferred approach for swiftness in actuation as described in Section 5.2.1.3. For this

reason, an abrupt expansion into the nozzle is desired, followed by a relatively gentle radius to direct the flow into a 30 degree included angle expansion nozzle. This geometry appears in Fig. 5.2-6, Fig. 5.2-5.d., and later in Fig. 5.3-3.a.

A second consideration in the vent geometry is to provide for parametric re-configuration to facilitate research into the behavior of RAVEN under different operating conditions. Therefore, the vent defining portion of the nozzle, termed the “chamber plug,” was removable. Different configuration of the same plug could be inserted to provide for earlier porting of the propellant gases within the chamber to the expansion nozzle.

#### 5.2.9.3 Configurations Tested

The total distance to venting for the four configurations tested are listed in Table 5.2-4.

**Table 5.2-4: Recoil Distances to Vent For Different Configurations.**

Name	Drawing [49]	Distance to Vent	Radius of Transition
Early	31317-3	48.88mm	3.5mm
Nominal	31217-1	56.37mm	5mm
Intermediate	31217-2	75.31mm	10mm
Late	31317 <sup>†</sup>	94.25mm	0mm

†. Blank plug with no nozzle machined in.

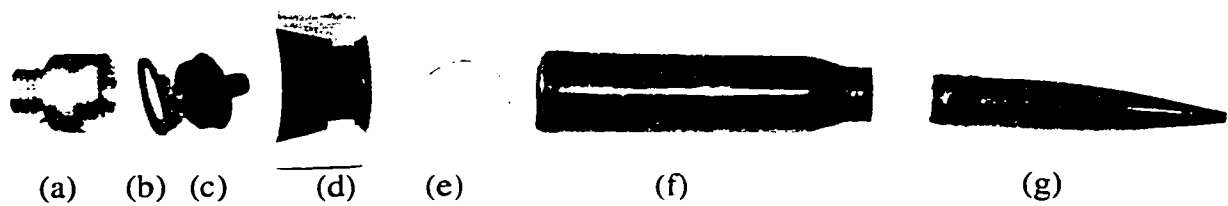


**Figure 5.2-5 View of Several Test Components: Shear Plug (Sheared) (a), Breech Obturator (b), Ruptured Cartridge Case Head (c), Chamber Plug (Nozzle) (d), Sheared Ring from Shear Plug (e), Ruptured Cartridge Case Body (f), and Projectile (g).**

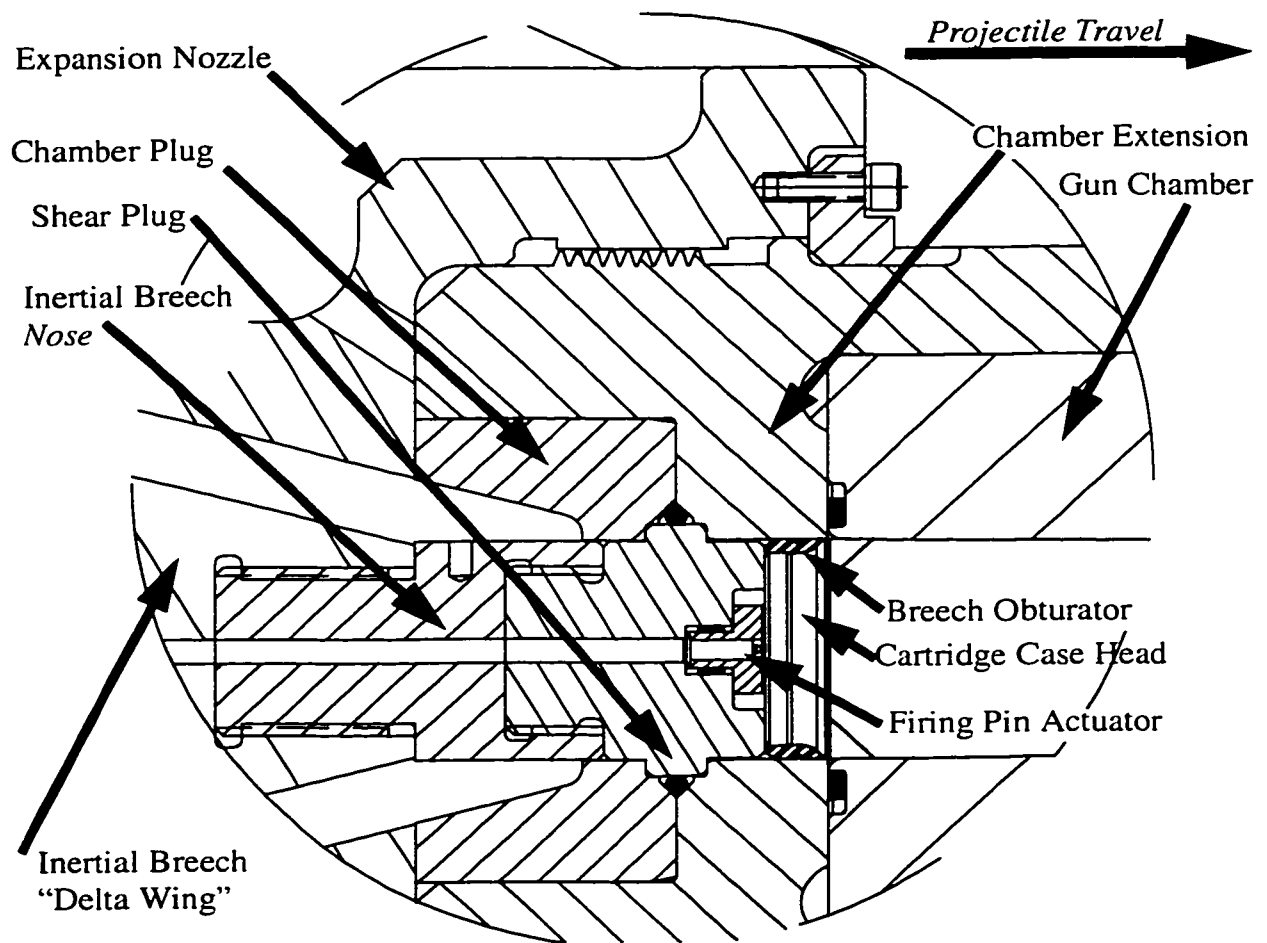


**Figure 5.2-6 Internal Working of RAVEN 35mm Test Fixture [49].**

## **5.3 Recoil Buffering**

### **5.3.1 General Approach**

The general approach taken for recoil management of the test fixture was to bring the inertial breech to rest with respect to the gun barrel, and then to bring the gun barrel to rest with respect to an inertial reference frame. Such a design is called a double recoil and was common for large railway cannons [41]. Using the standard terminology, the primary recoil brakes will bring the primary recoiling mass to rest with respect to a second (typically larger) recoiling mass. The secondary brakes then bring the combined primary and secondary mass to rest with respect to the weapon platform or ground.

The advantage of this method is that very large forces may be developed in the primary recoil brakes without exerting undue forces upon the gun mount. In this particular test fixture, this approach was an obvious path since a suitable test gun mount was already available that could be used.

Vast differences exist between the momentum and energy exchange between the primary and secondary recoil brakes. The primary recoil brakes provide an inelastic collision between the inertial breech (nominally 30kg as described in Section 5.2.7) and the barrel which may be anticipated to have a mass greater than the 140kg listed in Table 5.1-1. While momentum is conserved, energy is not. It may be shown the energy after inelastic impact relates to the energy before the impact as the ratio of the primary mass to the combined mass. Thus, if the masses were 30kg and 140kg, respectively, 82% of the recoil energy would be dissipated by the primary recoil brakes.

### 5.3.2 Primary Recoil Brakes

Imparting the full 1112Ns of momentum from Table (5.1-2) into an inertial breech correcting for its larger face diameter results in 2745Ns of momentum. Assuming no venting and no subsequent recoil reduction, endowing a 29.3kg inertial breech with 2745Ns of momentum results in a velocity of 94m/s and a kinetic energy of 130 kJ. To bring this to rest with respect to the gun barrel in one meter will require 130 kN of arresting force.

Because of the relatively high impact velocity, off-the-shelf shock absorbers are not viable. They are typically limited to impact velocities of 4m/s. The construction of a pair of custom variable orifice recoil brakes would have increased the cost of the gun fabrication project by 50%. Additionally, such fabrications often run into manufacturing delays. A simple alternative was sought.

The use of copper crush tubes as shock arrestors has a historical basis in the fatigue laboratory at Benét Labs [59]. A similar method was also employed for the landing gear of the lunar module during the Apollo program [60]. The approach is rather simple. Place a standard copper plumbing tube, size L, K, or M over a rod that allows little clearance between the rod and tube. When one end of the tube is secured to the rod by a bolt head or a nut and hardened washer, forces applied through a washer that rides the rod toward the nut may crush the copper in an accordion fashion. An example of a 3/4" Type L copper crush tube is shown in Fig. 5.3-1.



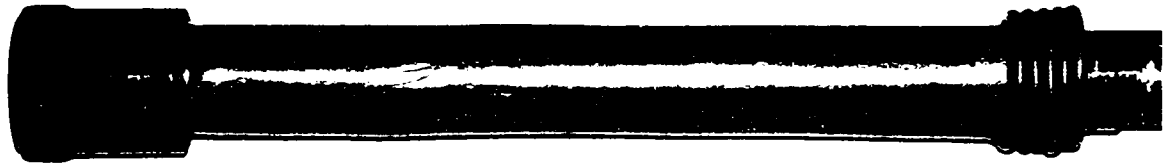


**Figure 5.3-1 Example of Copper Crush Tube Showing 5 Accordion Folds to the Right.**

A measurement was made of the force developed during crushing of a pair of coaxial 3/4" and 1" type L tubes indicated a generally constant crush load of 55 kN with a modest tendency to increase with stroke and oscillatory behavior about the mean [61]. The oscillatory behavior may be attributed to the formation of the accordion folds. The modest tendency to increase resistance load may be attributed to the binding friction developed between the crushed portion of the tube with the rod over which they must slide. As additional accordion folds are developed, the frictional contribution will increase.

This binding friction has two beneficial effects. First it minimizes the potential for any strain energy that is elastically stored within the tubes from being released after they have reached their fullest extent of crush. This should eliminate concerns of rebound [62]. Second, the recoil force generally increases until the relative motion of the components is brought completely to rest. The implication of this is that the momentum exchange duration can not exceed the magnitude of the momentum exchange divided by the initial crushing force. This is in sharp contrast to hydraulic devices whose forces fall off with decreased relative velocity.

Since the crushing is constrained by the rod, which acts as a mandrel during the crushing, the failure mode of the tubes may be considered similar to pier type crushing as opposed to buckling. Division of the crush load by the combined cross-sectional areas of the tubes ( $75.7\text{e-6 m}^2$  and  $109.0\text{ m}^2$ , respectively) results in compressive failure stress of  $298\text{ MN/m}^2$  which is 14% less than the listed yield strength of hard copper [58]. Proceeding with the measured compressive failure stress and extending to the available copper tubing geometries (english units) results in Fig. 5.3-2:

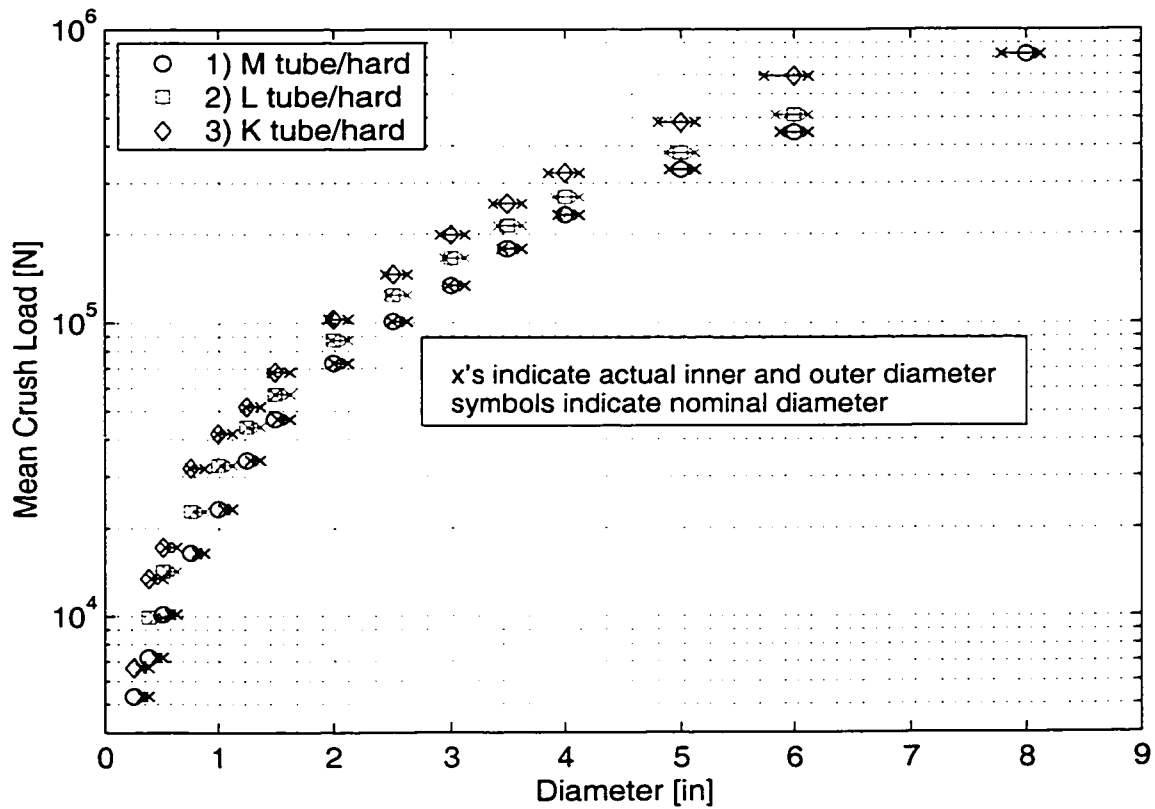


**Figure 5.3-2 Estimated Shock Arresting Loads of Off the Shelf Copper Tubing.**

The computed crush loads for 1.5" type M, L, and K are 47 kN, 57 kN, and 68 kN, respectively. Thus, a pair of type K, 1.5" copper tubes may be anticipated to bring the inertial breech to rest in 1 meter in less than 30ms, and lighter duty copper could be used as confidence was gained in the recoil arresting. The double recoil rod approach lead directly to the "delta-wing" appearance of the inertial breech shown in Fig. 5.3-3.

Because of the mass of the recoil rods, required as mandrels for the copper crushing, would have been a substantial portion of the inertial breech mass, the rods were de-coupled from the inertial breech. In an effort to bring mechanical balance to the design, the recoil rods were allowed to recoil relative to the gun barrel. Thus, copper crush tubes were applied both between the rods and the inertial breech and between the rods and the gun barrel.

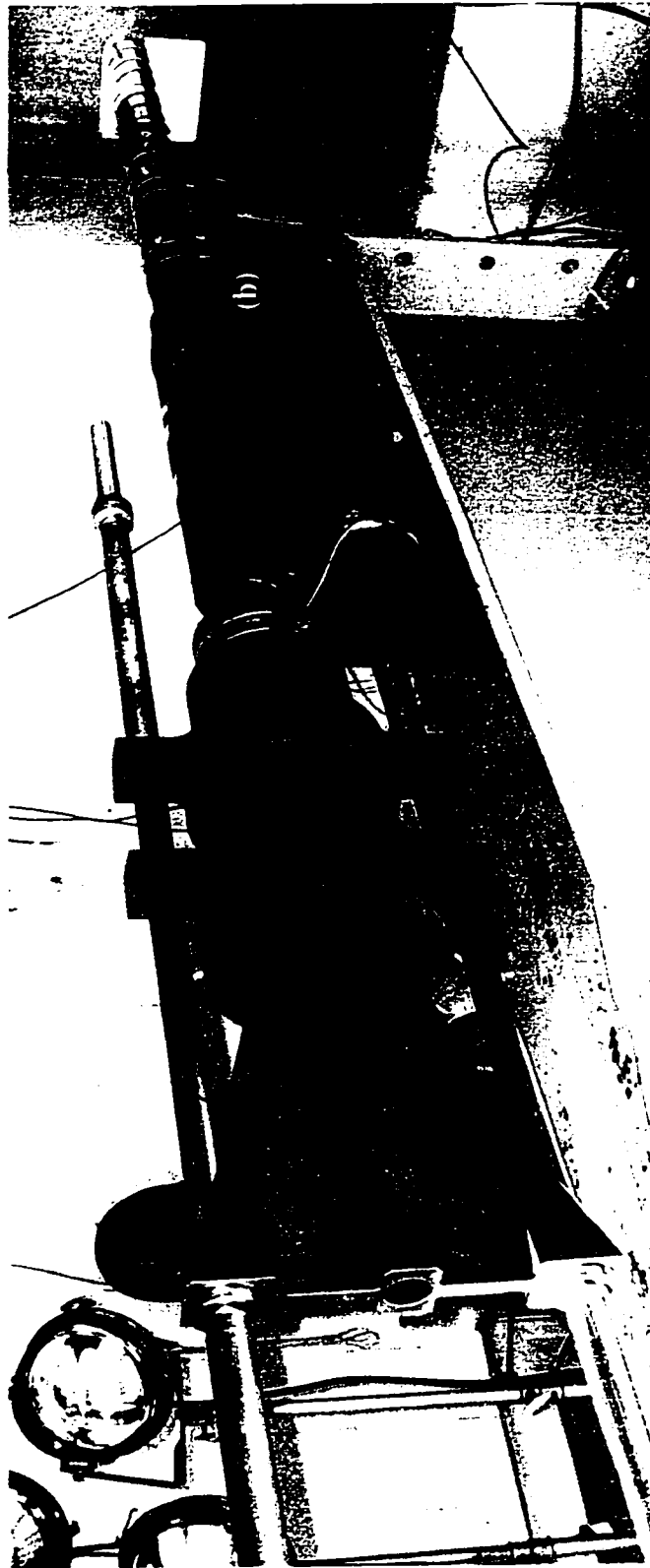
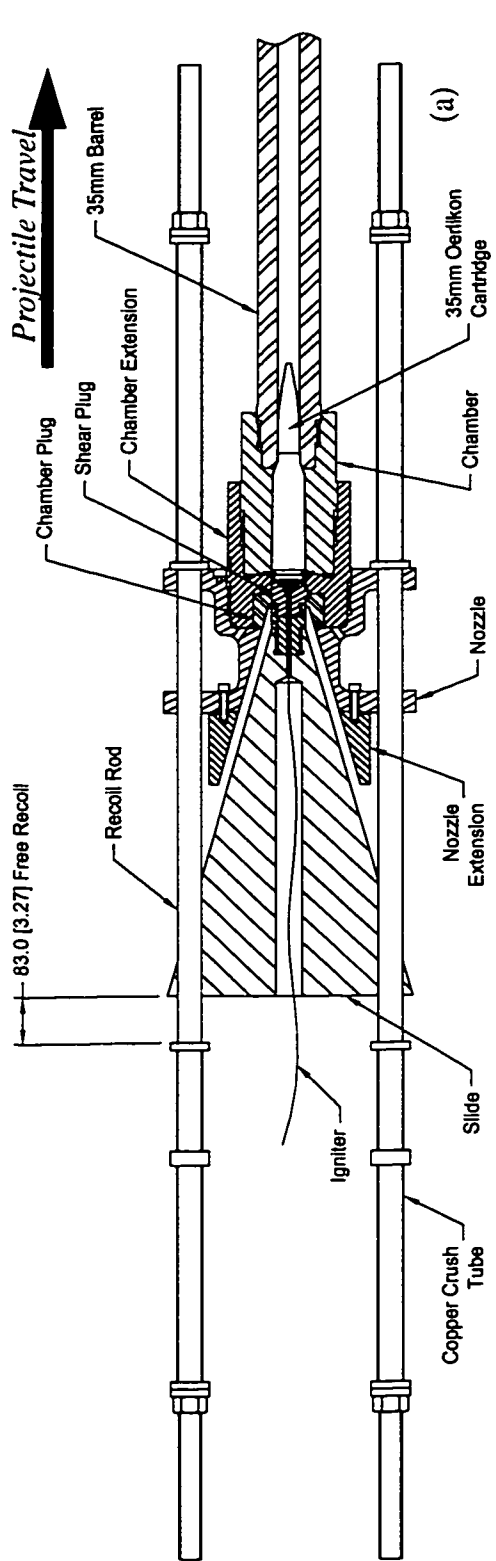
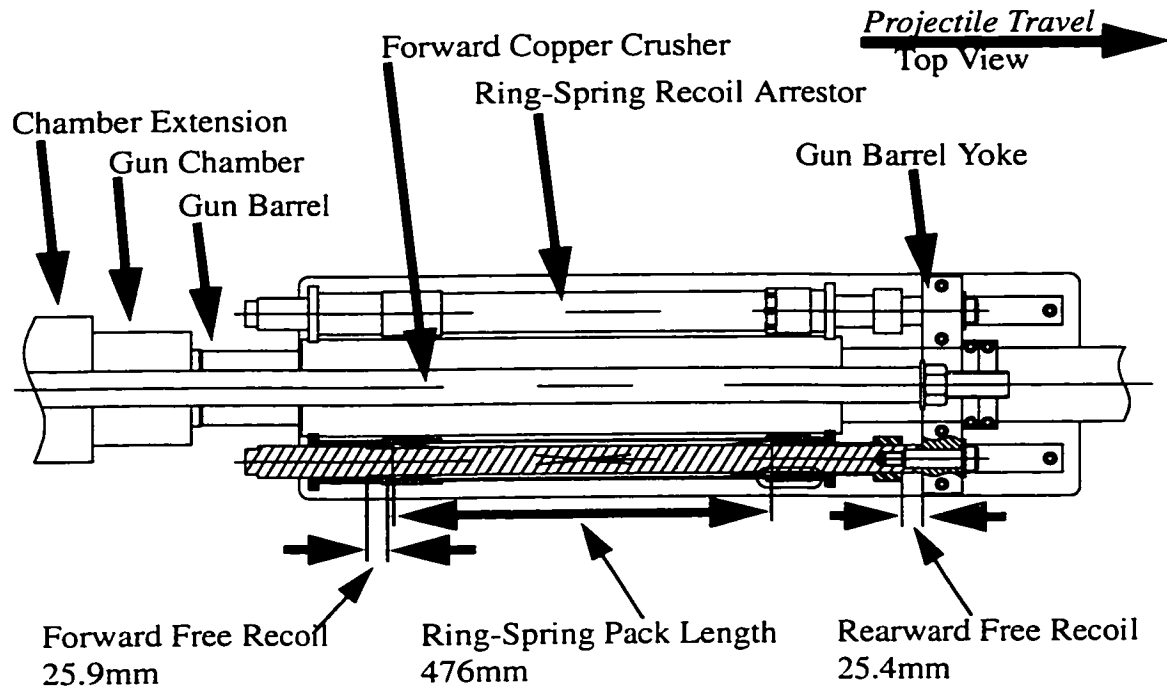


Figure 5.3-3 Raven 35 Assembly Drawing (a) and Photograph (b) [49].

### 5.3.3 Secondary Recoil and Gun Mount

The free recoil velocity was determined for every RAVEN configuration — including non-venting configurations, used in the main firing tests. This was accomplished by utilizing a free recoil mount. The mount permits, as much as possible, free recoil of the weapon during firing. The mount provided for 25.9mm and 25.4mm of free travel forwards or rearwards, respectively. A drawing of the mount pictured in Fig. 5.3-3.b is shown in Fig. 5.3-4.



**Figure 5.3-4 Free Recoil Mount and Ring-Spring Recoil Arrestors [49].**

Ring springs are a simple means to abate high force loading [62]. Ring-spring assemblies consist of a number of inner and outer closed rings contacting each other along conical surfaces. When axial force is applied, the rings telescope into one another causing compressive and tensile hoop strain for the inner and outer springs, respectively. While the springs telescope into one another, substantial friction forces are present that dissipate much of the energy imparted. Design guidance on ring-spring design is contained within [63]. A line drawing of a ring-spring pack is presented in Fig.5.3-5. The mount employed 45 matched pairs of Ringfeder® type 04800 ring springs within each of the two recoil arrestors.

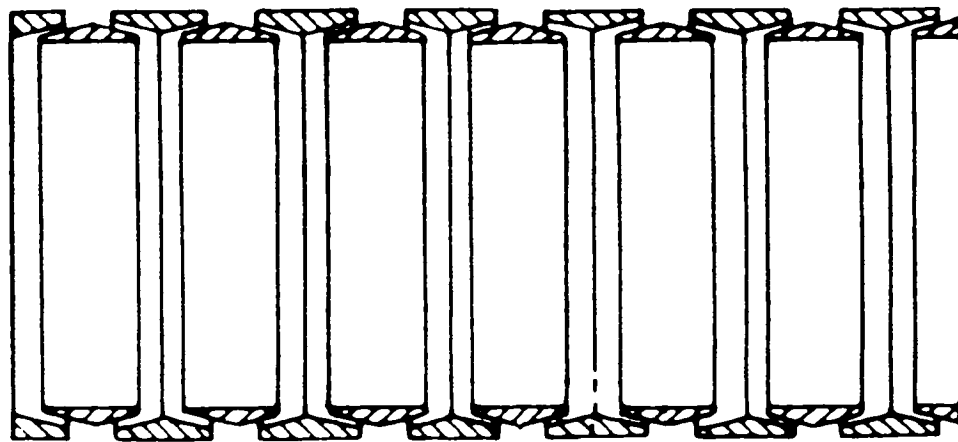


**Figure 5.3-5 Longitudinal Section of a Ring Spring Pack [63].**

#### **5.4 Non-Venting Benchmark**

Two methods were employed to provide a non-venting benchmark. The first was simply to construct a shear plug out of steel as opposed to aluminum as discussed in

Section 5.2.8. The strength of the steel was sufficient to couple the inertial breech to the gun, providing a traditional orthodox gun mode of operation. This mode of operation will simply and appropriately be termed the closed-breech mode. The second method was to mimic all of the aspects of the RAVEN test fixture described in Sections 5.2 and 5.3 with the exception that the inertial breech was designed not to vent.

A replacement of the nozzle shown in Fig. 5.3-3 with a simple closed tube and replacement of the “delta-wing” inertial breech with a “T-bar” achieves the desired effect as shown in Fig.5.4-1. The mass of this inertial breech is listed in Table 5.2-2.

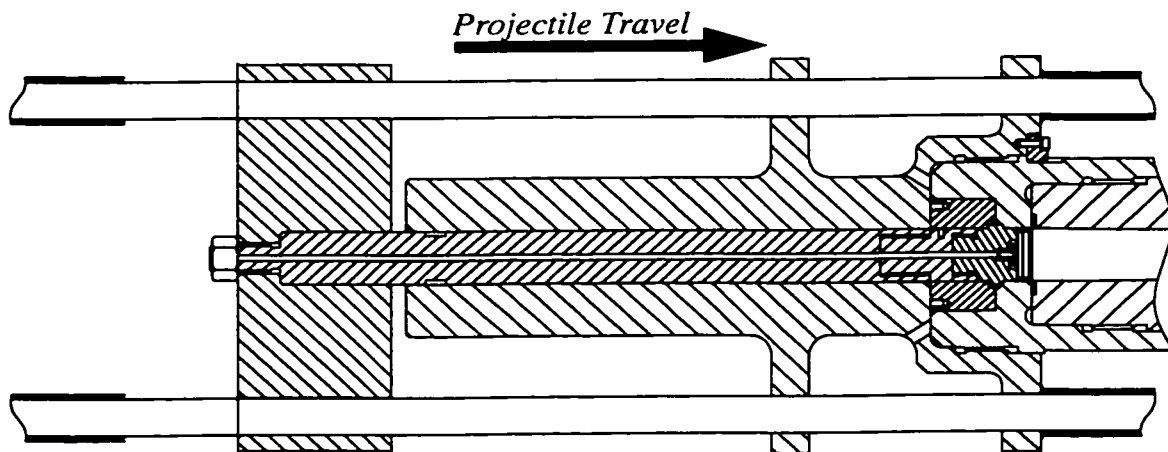


**Figure 5.4-1 RAVEN 35 Non-Venting Inertial Breech Assembly [49].**

## 5.5 Sensors Employed

The pertinent data collected included recoil motion, ballistic pressures, bore temperatures, and muzzle velocities. The majority of the data was acquired using a Nicolet Technologies Odyssey Data Acquisition System at a sample rate of 100 kHz.

### 5.5.1 Ballistic Pressure Probes.

Fourteen PCB Model 118 ballistic pressure transducers were placed along the length of the barrel from the chamber to the muzzle. Their distance is computed relative to the starting location of the front face of the cartridge case head which is effectively, the rear face of the propellant gas column. (In later ballistic modeling, the front face of the cartridge case head will be considered the front face of the breech shown in Fig. 7.1-1.)

**Table 5.5-1: Location of Barrel Pressure Probes.**

Probe #	Distance	Probe #	Distance	Probe #	Distance
P0	-0.0157 m	P5	1.3244 m	P10	2.3277 m
P1	0.0795 m	P6	1.5149 m	P11	2.5309 m
P2	0.2163 m	P7	1.7181 m	P12	2.7341 m
P3	0.5878 m	P8	1.9213 m	P13	2.9373 m
P4	0.9561 m	P9	2.1245 m	P14	3.1405 m

### 5.5.2 Thermocouples.

Four thermocouples were imbedded into the barrel to monitor heat input to the gun bore. Their placement is listed in Table 5.5-2. The thermocouples were spring loaded bayonet fitting style thermocouples, type J, Omega® part number BT-090-J-2 1/4-60-2.



The mounting hole is shown in Fig. 5.5-1. The location of the holes relative to the rifling of the bore was not determined.

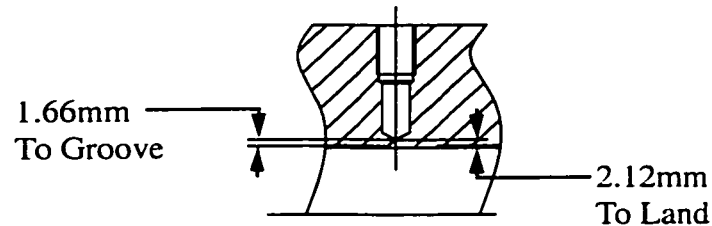


**Figure 5.5-1 Spring Loaded Bayonet Style Thermocouple Mount Hole.**

The thermocouple data was recorded on a strip-chart recorder. This was acceptable as the speed of the thermal transients is small relative to the interior ballistics.

**Table 5.5-2: Location of Barrel Thermocouples.**

Probe	Position
K1	0.3048 m
K2	1.1811 m
K3	2.2261 m
K4	3.0389 m

### 5.5.3 Recoil Motion

A Fastar® linear displacement transducer and a separate signal processor were used to measure the recoil motion of the barrel. Fastar® is a precision variable inductor. Inductance decreases linearly with insertion of an aluminum core. The processor generates a DC voltage output proportional to the change in inductance when the core is moved. This measurement was used to determine the recoil momentum by dividing the measured

velocity by the total system mass using consistent units. The recoiling masses are listed in Table 5.5-3.

**Table 5.5-3: Recoiling Masses.**

Firing Configuration	Gun Mass $m_{gc}$	Inertial Breech Mass $m_r$	Total Free Recoil Mass $m_{fr}$
Closed-Breech	297.6kg	36.4kg <sup>†</sup>	334.0kg
Light Venting	297.6kg	20.9kg	318.5kg
Heavy Venting	297.6kg	35.9kg	333.5kg
Non-Venting	405.9kg	31.8kg	437.7kg

†. The closed-breech inertial breech was the same as the heavy except that it included a steel shear plug that was designed not to release the breech.

#### 5.5.4 Muzzle Velocity

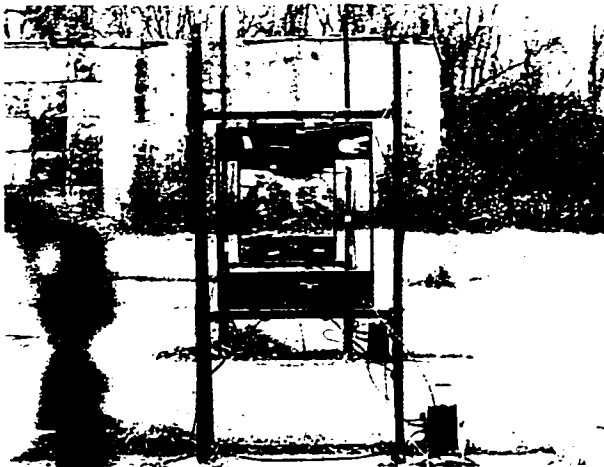


**Figure 5.5-2 Picture of Ballistic Screens Immediately Down Range of the Muzzle.**

Muzzle Velocity was recorded using MV ORDNANCE Model 6107 Ballistic screens. These screens are projectile detectors and function using a high intensity DC light source. As the projectile passes through the sensitive area, the shadow of the projectile falls on one or more of the photovoltaic

transducers creating an electrical imbalance for a period equal to the time that the projectile shadow is present. The minimum caliber projectile detected by the screen is

4.5mm and a maximum velocity of 1500m/s. The pair of screens encountered are pictured in Fig. 5.5-2.

## **Part 6**

# **EXPERIMENTAL INVESTIGATION OF RAVEN**

### **6.1 Conduct of the Experiment**

The firings were conducted at ARES, Inc., Port Clinton, OH on the Erie Proving Grounds at the medium caliber outdoor range.

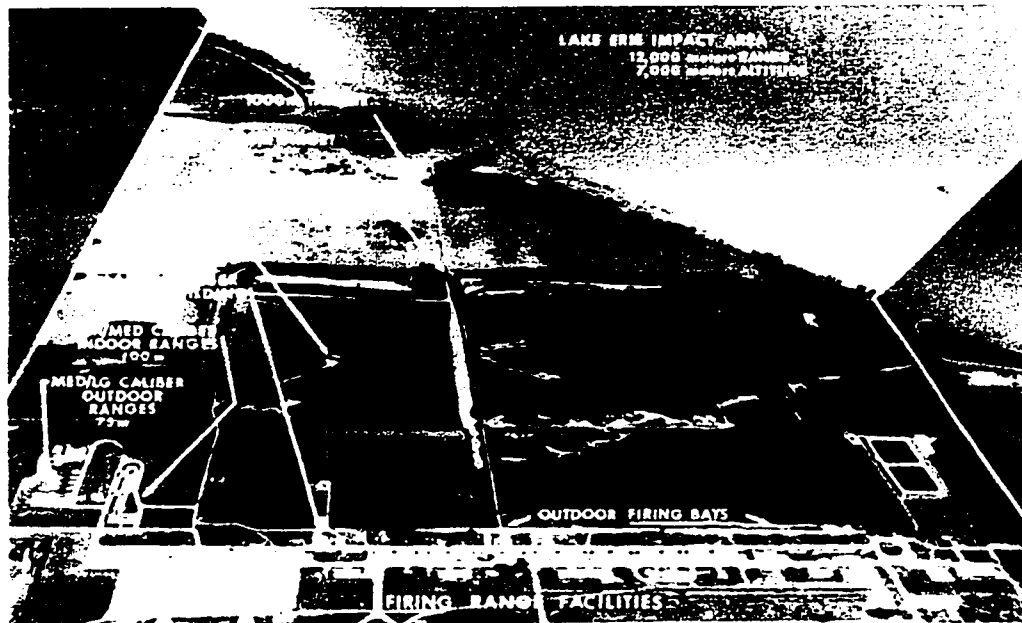


**Figure 6.1-1 ARES Test Range.**

#### 6.1.1 First Function Tests

The first function test firings began on 30 August 2001. These tests revealed a challenge with the original cartridge case notch design. The improved design is shown in Fig. 5.2-2. In the original design, only a thin groove was cut into the cartridge case (labeled “existing groove” in Fig 5.2-2). The cartridge case fired from this configuration “healed” during firing. The cause of this was a greater projected area for the rear of the wall of the cartridge case than the neck. Thus, the cartridge case was dragged rearwards, as the neck was enlarged. An image of this is included in Fig.6.1-2.

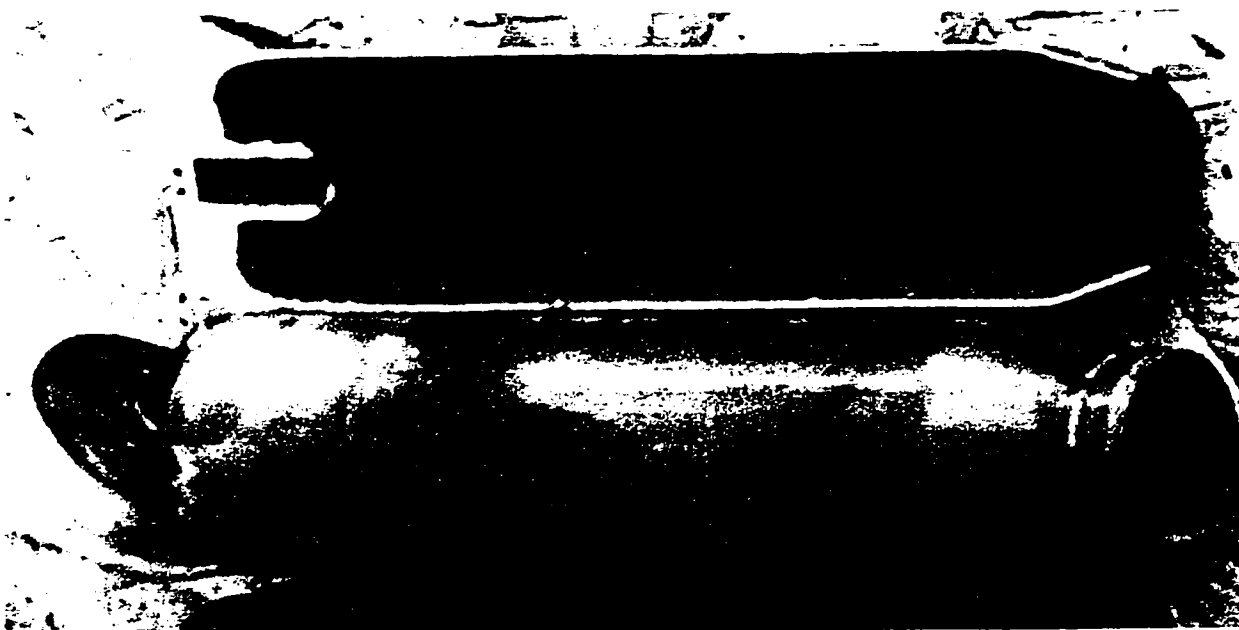


**Figure 6.1-2 Image of Cartridge Case (Split Lengthwise) That Healed Above a Properly Ruptured Case. (Note the Neck Deformation.)**

#### 6.1.2 Video of the First RAVEN firing

The final shot of this initial function test configuration successfully vented, ejecting the cartridge case from the gun. Four images of the video clip are included within Fig. 6.1-3. The frames of Fig. 6.1-3.c,d are 9 and 19 frames following Fig. 6.1-3.b respectively. Using the NTSC (National Television System Committee) standard frame rate of 30 frames per second, they may be computed to have occurred 300ms and 630ms after the firing event. The firing event from initiation to the stage shown in Fig. 6.1-3.b occurred in its entirety within the 33ms between frames. To maintain an orientation that always depicts guns with the projectile traveling to the right, a mirror image of the actual video footage is presented.

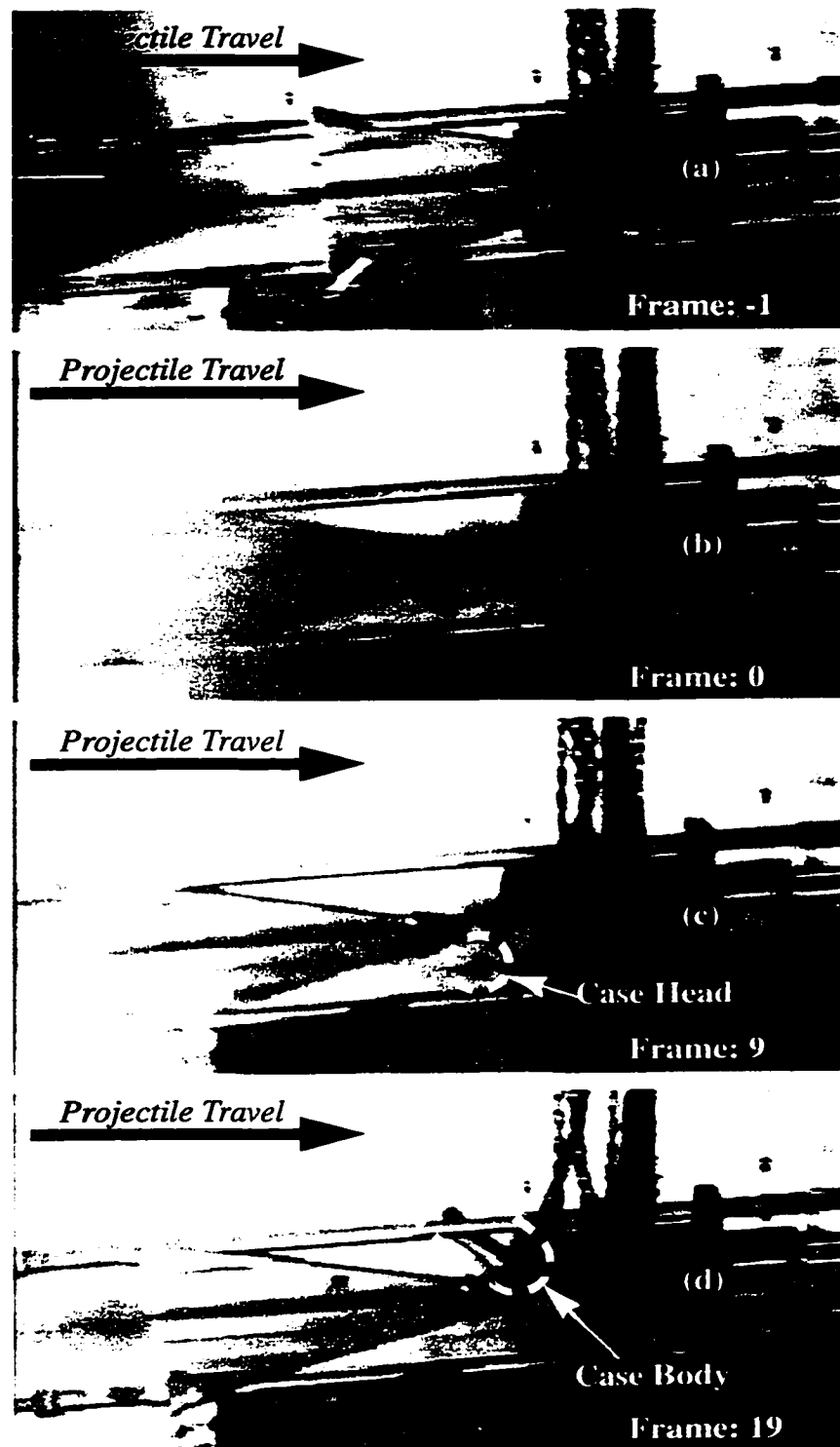


**Figure 6.1-3 Firing Video Sequence Before Firing (a) First Frame After Firing (b), Case Head Ejection (c), Case Body Ejection (d).**

When viewing the entire clip, it is clear that the rearward motion of the gun barrel following Fig. 6.1-3.b engages the secondary recoil brakes (ring-spring packs) which bring the barrel to rest about five frames (0.17 s) after Fig. 6.1-3.b. The barrel is then thrust forward by the potential energy of the rearward limiting rings-springs prior to the image of Fig 6.1-3.c. (By the design of the rings-springs, they dissipate substantial energy as they are engaged; thus, the forward speed is far lower than the initial rearward speed.) The forward velocity imparted to the barrel by the ring-springs also draws the recoil rods and inertial breech forward. About fifteen frames (0.5 s) after Fig. 6.1-3.b, the forward motion of the barrel is brought to rest by the forward ring-springs with the vast majority of the kinetic energy of the barrel absorbed by the two engagements of the springs. Since the inertial breech and recoil rods are free to slide independent of the barrel motion, the inertial breech rather gently returns to its initial “battery” position.

The forward speed of the inertial breech shown in Fig. 6.1-3.d that is asserted to be gentle, may be estimated as follows. The gap opened between the forward copper crush tubes and the gun may be visually estimated as 0.1m. This gap is a measure of the forward displacement of the inertial breech and recoil rods that occurred between the time when the gun barrel was observed to be at rest in its rearward most position and its position in Fig. 6.1-3.d. Dividing the 4 frames by the NTSC 30 frames per second, indicates the time difference to be approximately 0.133 s. Therefore, the forward speed of the inertial breech may be roughly estimated as 0.75m/s.

### 6.1.3 Pressure Data

All of the ammunition was temperature conditioned to  $70^{\circ}\text{F} \pm 5^{\circ}\text{F}$  ( $294.3\text{K} \pm 2.8\text{K}$ ) for a minimum of four hours to reduce avoidable variation in the ballistics due to the temperature of the propellant bed.

The pressure data from a closed-breech firing is plotted in Fig. 6.1-4. The pressure trace includes all 14 pressure gages along the bore. As the pressure ahead of the bullet is small, the gauges are encountered sequentially as the bullet traverses the bore. The final gage to rise is the muzzle gage, just prior to shot-exit.

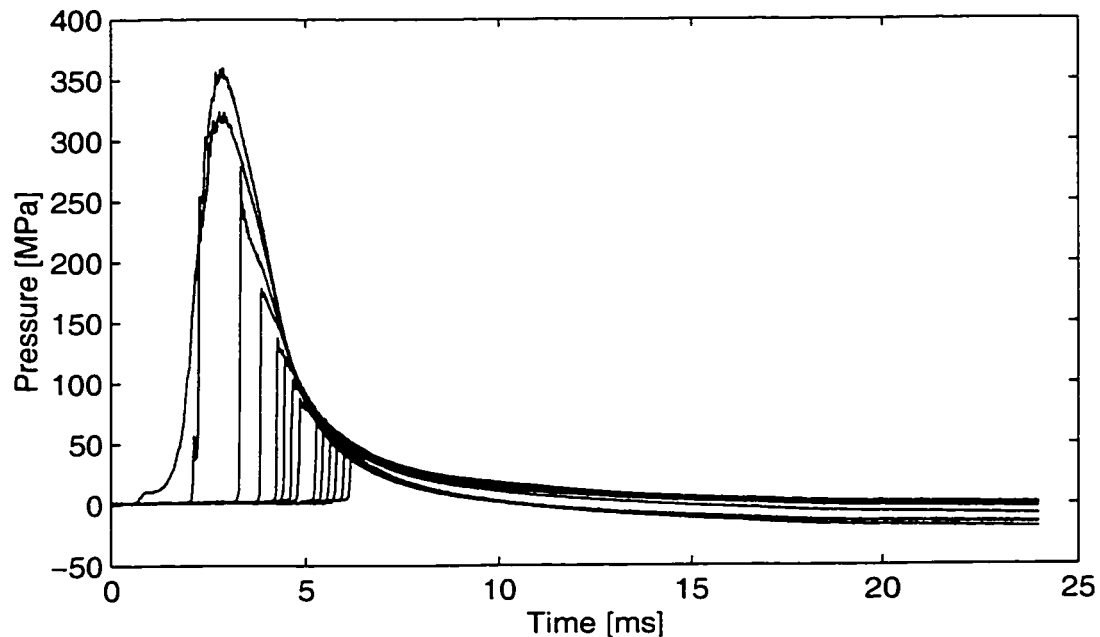


**Figure 6.1-4 Pressure Time Trace from Closed-Breech Function Test Firing 1-2-3.**

This trace indicates a problem in the tendency of the pressure reading to drift negative after firing. Further, the trace is indicating a lower pressure to the rear of the barrel than just behind the projectile preceding shot-exit.



This is not physical. Except for highly unusual circumstances the static pressure is always higher in the chamber, where the propellant gases have little velocity, than behind the projectile, where the gases have appreciable velocity. (An example of a typical pressure gradient may be seen in the model behavior to be presented later in Fig. 7.2-1 of Section 7.2.2.) The cause of this drift could be attributed to leaks in the transducer ports that could cause localized heating of the piezoelectric elements. The questionable transducers were removed and re-seated. Examination of the probes and ports for evidence of leaks was inconclusive.

The pressure data from a a vented firing using the heavy inertial breech and a late vent (see Table 5.2-4) is plotted in Fig. 6.1-5.

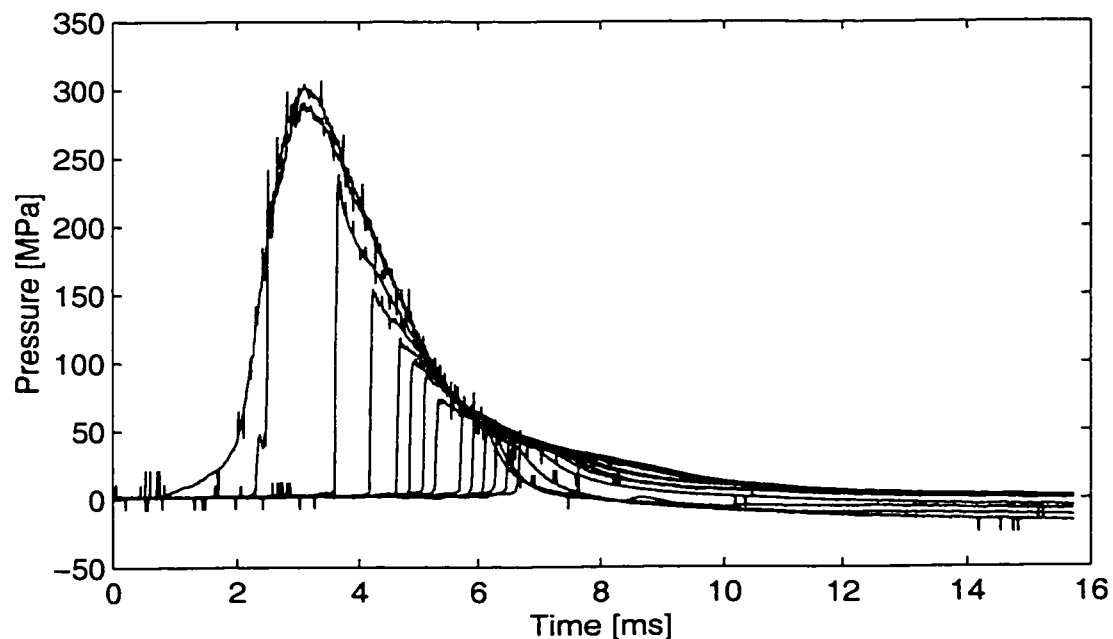


**Figure 6.1-5 Pressure Time Trace from Heavy-Late Vented Function Test Firing 1-2-6.**

This trace included substantial noise. The cause of this noise was never fully resolved; although it could be attributed to the firing circuit. The noise was amenable to removal by means of an outlier rejection algorithm. A running mean and standard deviation computation spanning five points was run through the data to reject points more than one standard deviation from the mean. This scheme worked well, rejecting outliers without distorting those data points that remained after the scheme was implemented. This is in contrast to a causal filter that would have diffused the data in an effort to reduce the effects of the noise.

#### 6.1.4 Primary Recoil Arrestors

The performance of the copper crushers was generally good with no instances of the crushers bottoming-out or otherwise failing to prevent catastrophic impact between the inertial breech, recoil rods, or gun. Examples of good behavior and poor behavior are shown in Fig.6.1-6.

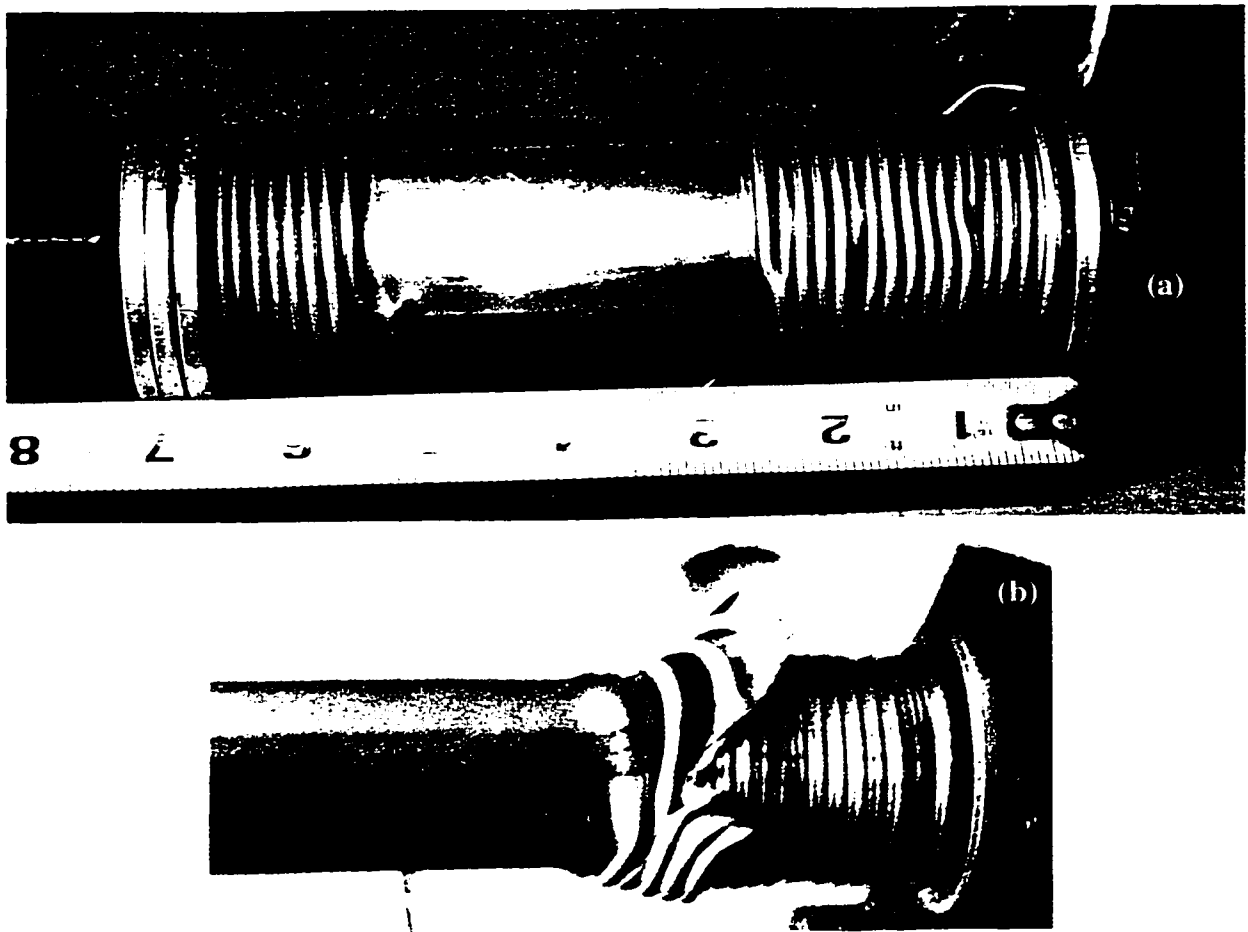


**Figure 6.1-6 Post Crushing Images of a Good Crush Tube (a) and a Ripped Crush Tube (b).**

The crushing depicted in Fig. 6.1-6.a was the result of firing the heavy inertial breech with the nominal vent chamber plug. The original length of the copper tube was 0.432m and the crushed length was 0.149 m, for a total crush length of 0.282 m. The remaining length of un-crushed tube shown in Fig. 6.1-6.a is approximately, 0.076m and of that only 0.061m could be crushed before the tube would bottom-out.

The next configuration to be fired incorporated the late vent. Since additional momentum would be imparted to the inertial breech during the additional exposure to ballistic pressures, it was decided to increase the length of the crush tubes to 0.794 m. The intent was to provide additional crush tube to avoid coming so close to bottoming-out the tubes. It was this firing configuration that resulted in the ripping shown in Fig. 6.1-6.b. It was postulated that the ripping behavior of Fig. 6.1-6.b was attributable to a combination of its length and the impact velocity. Although the inertial breech was brought to rest reasonably well despite the ripping, this failure mechanism of the crush tube could conceivably lead to a ripping of the tube off of the rod resulting in a loss of recoil arresting capability.

To reduce the propensity for future ripping failures, and to prevent such a failure from propagating down the length of a crush tube, all future vented firing configuration split the rear crush tube into two sections with a hardened washer riding the recoil rods between the two tubes. The configuration is depicted in Fig. 6.1-7.

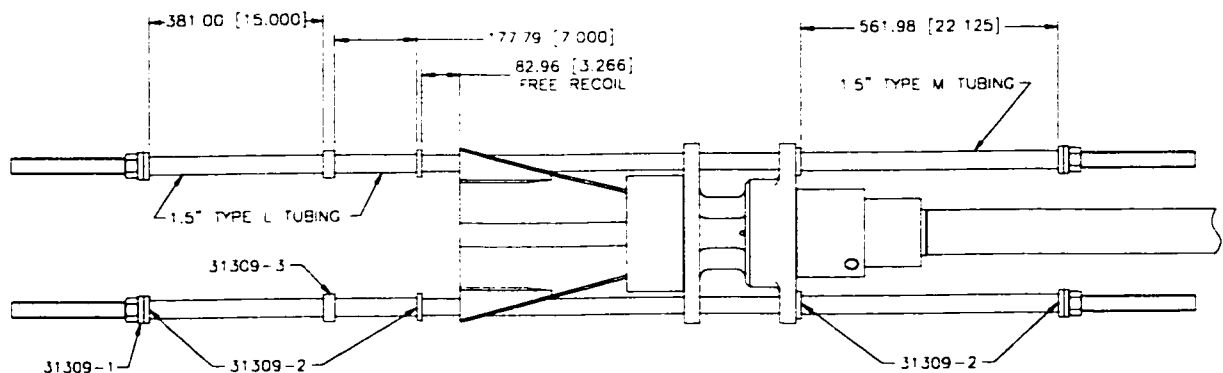


**Figure 6.1-7 Copper Tubing Setup For Final RAVEN Tests.**

### 6.1.5 Test Matrix Evaluated

A series of 30 firing tests was conducted to study the effects of different inertial breech masses and vent geometries on the interior ballistic operation of a RAVEN. The intent was to fire three shots of each configuration. A listing of the configuration of each of the shots fired, and the shot number identification convention is listed as Table 6.1-1.

**Table 6.1-1: Configuration Identification Number of Shots Fired.**

Breech Configuration		Closed-Breech	Heavy Inertial Breech			Light Inertial Breech				Non-Vent
Vent Geometry		NA	Early	Nominal	Intermediate	Early	Nominal	Intermediate	Late	NA
Shot Number	1	2-1-1	2-3-3	2-2-1	2-4-1	2-6-1	2-5-1	2-7-1	2-8-1	2-9-1
	2	2-1-2	2-3-4 <sup>†</sup>	2-2-2	2-4-2	2-6-2	2-5-2	2-7-2	2-8-2 <sup>†</sup>	2-9-2 <sup>†</sup>
	3	2-1-3	2-3-5	2-2-3	2-4-3	2-6-3	2-5-3	2-7-3	2-8-3	2-9-3
	4			2-3-1						2-9-4
	5			2-3-2						

†. Compromised Pressure Data

### 6.1.6 Corrupted or Missing Data: NaN.

With a substantial test matrix, it may be anticipated that some portion of the data to be collected will be lost or corrupted. When this occurs the listed value is the IEEE

not a number or NaN. These values are not considered for the purposes of mean and standard deviation (std) determination, polynomial fitting, nor are they plotted in the figures.

## **6.2 Measured Effect on Projectile Propulsion**

The muzzle velocity data is presented in Table 6.2-1 and illustrated in Fig. 6.2-1. The abscissa for the vented shots is a measure of the percent projectile travel down the bore of the gun when the rarefaction wave was first detected at the chamber pressure probe. (Determination of the vent time and relative projectile position at venting will be discussed in Section 6.3.7.) The two base-line configurations of Fig. 6.2-1, CB and NV are the closed-breech and non-venting inertial breech, respectively.

The very first firing of the test matrix, shot 2-1-1, indicated a muzzle velocity 18% lower than the other two of this configuration. The pressure data to be presented later in Table 6.3-1 does not support such a low muzzle velocity. This value is, therefore, considered an outlier, and was not considered further.

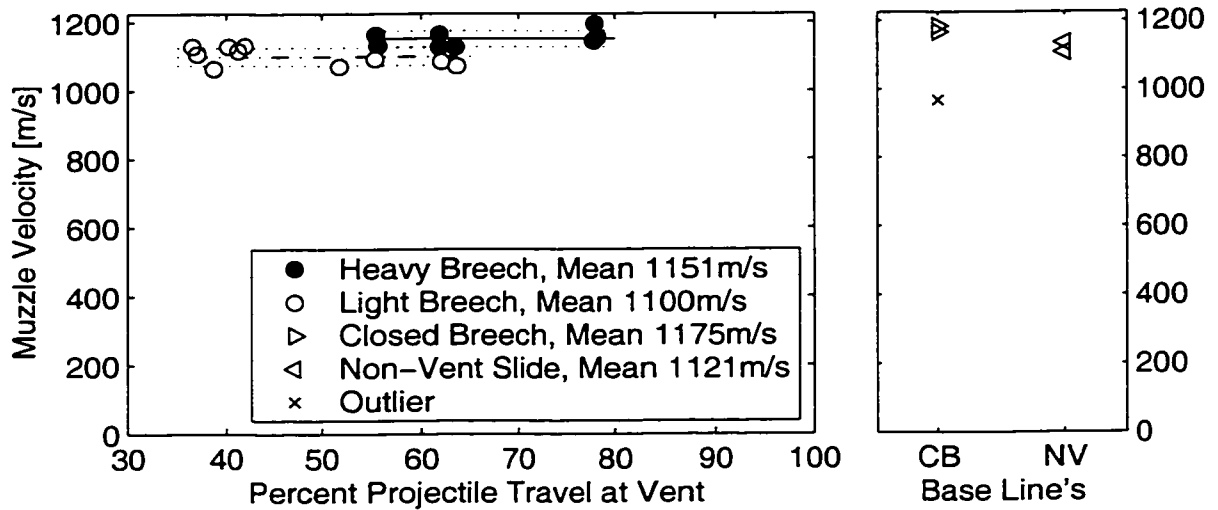


**Figure 6.2-1 Plot of Muzzle Velocity as a Function of the Percent Travel of the Projectile at Venting.**

**Table 6.2-1: Muzzle Velocities [m/s].**

Breech Configuration		Closed-Breech	Heavy Inertial Breech Mean: 1151 STD: 23			Light Inertial Breech Mean: 1100 STD: 26				Non-Vent
Vent Geometry		NA	Early	Nominal	Intermediate	Early	Nominal	Intermediate	Late	NA
Shot Number	1	968 <sup>†</sup>	1164	1128	1143	1107	1131	NaN	1085	NaN
	2	1184	NaN	1165	1155	1129	1130	1093	NaN	1106
	3	1166	1131	1128	1194	1064	1116	1070	1071	NaN
	4			NaN						1135
	5			NaN						
Mean		1175	1147	1140	1164	1100	1126	1082	1078	1121
STD		13	23	21	27	33	8	16	10	20

†. Considered an outlier and removed from the mean and standard deviation computations.

### 6.3 Measured Ballistic Pressure Data

The ballistic pressure recorded during the firing of a closed-breech configuration is plotted in Fig. 6.3-1. The tendency for the pressure readings to drift as first revealed in Fig. 6.1-4 was present throughout the test matrix.

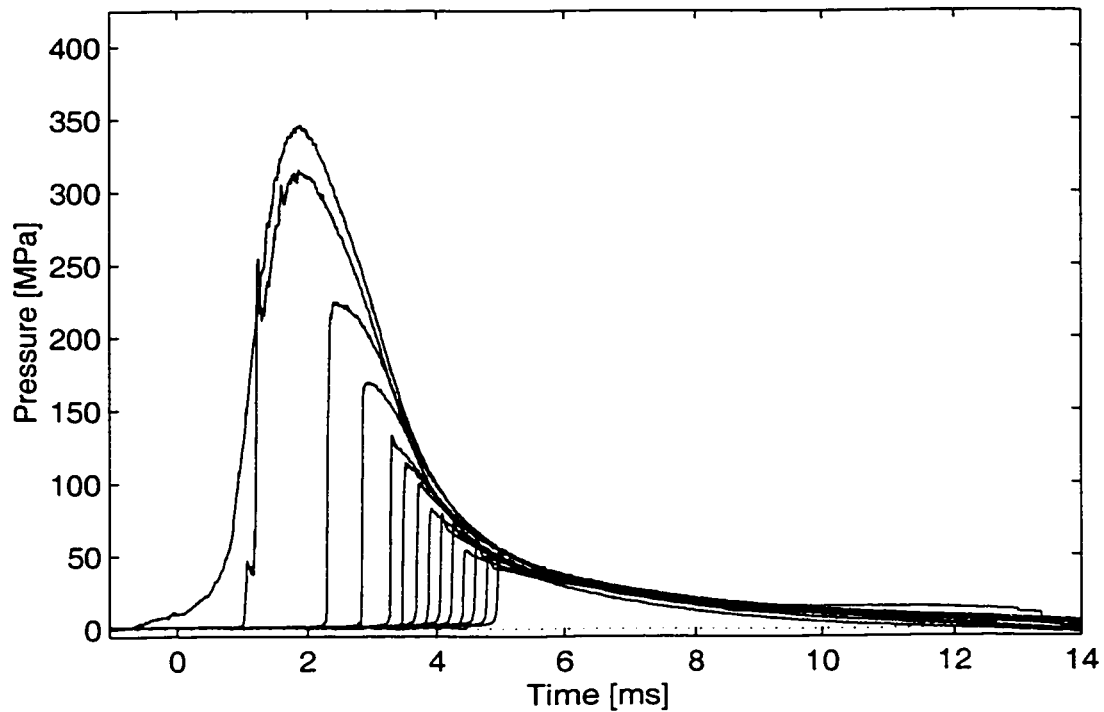


**Figure 6.3-1 Pressure Time Trace from Closed-Breech Test Matrix Firing 2-1-3.**

The pressure trace of configuration 2-9-4, a non-venting inertial breech is plotted in Fig. 6.3-2. The differences in chamber pressure will be discussed in Section 6.3.1.



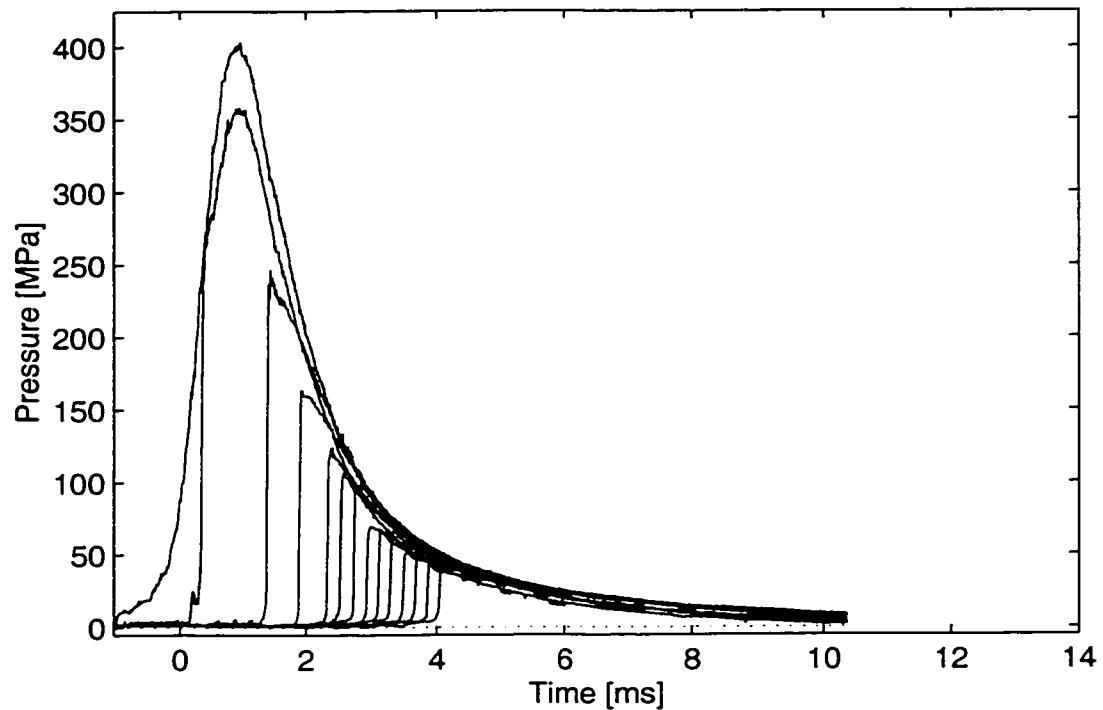


**Figure 6.3-2 Pressure Time Trace from Non-Venting Test Matrix Firing 2-9-4.**

The pressure trace of configuration 2-3-5, a heavy inertial breech firing from an early vent is plotted in Fig. 6.3-3. The pressure trace of configuration 2-5-1, a light inertial breech firing from a nominal vent, is plotted in Fig. 6.3-4. In both cases, note the dramatic loss in chamber pressure near 3ms and 2.5ms, respectively. This occurs when the rarefaction wave traverses the chamber pressure transducer.

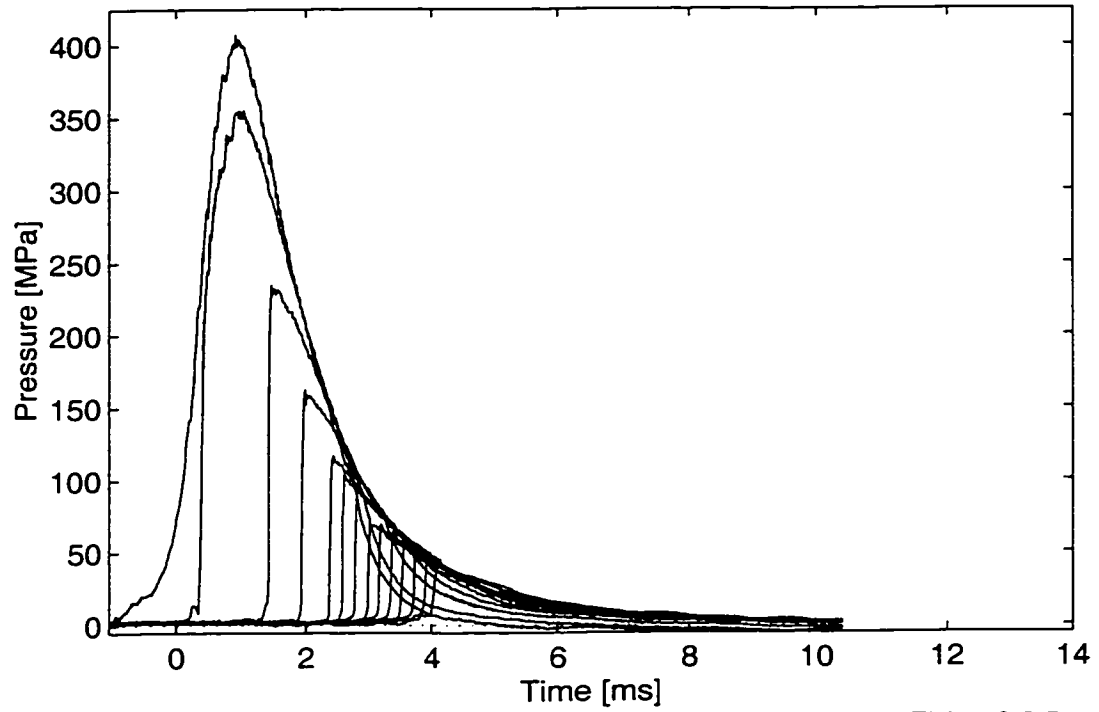


**Figure 6.3-3 Pressure Time Trace from Heavy-Early Vent Test Matrix Firing 2-3-5.**

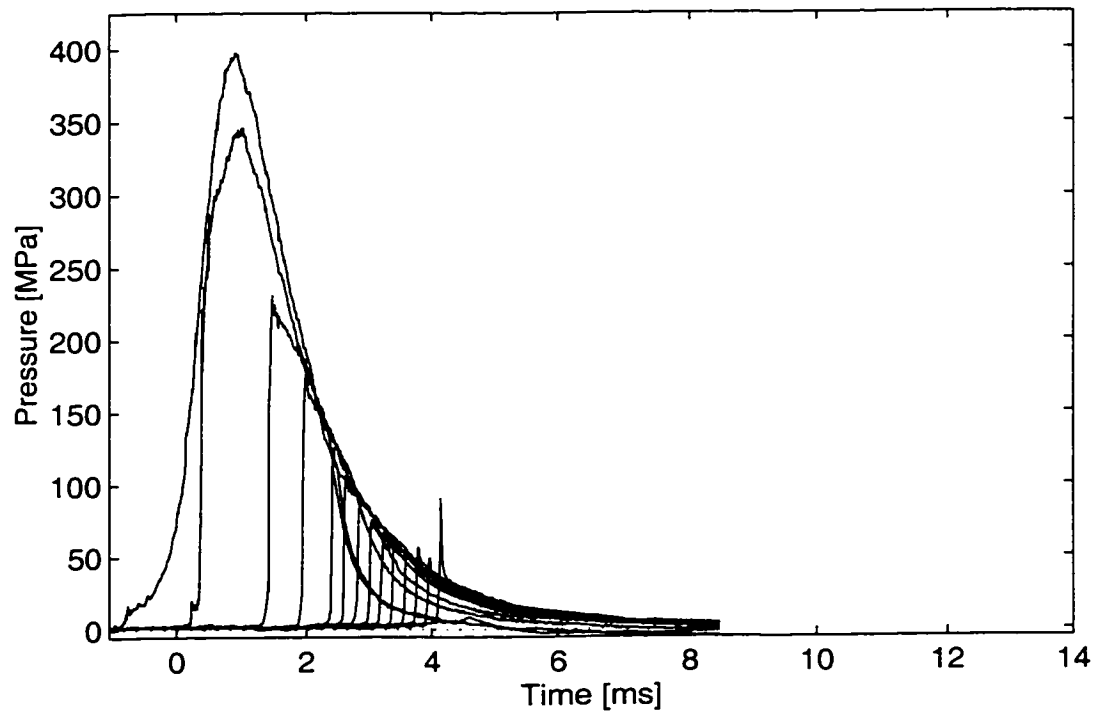


**Figure 6.3-4 Pressure Time Trace from Light-Nominal Test Matrix Firing 2-5-1.**

### 6.3.1 Effect on Peak Pressure

For the inertial breech gun configurations, the peak pressure followed a logical pattern. The greater the inertia of the breech the greater the peak pressure. The closed-breech gun configurations exhibited lower pressures but produced generally higher muzzle velocities. Therefore, the closed-breech peak pressures are suspect.

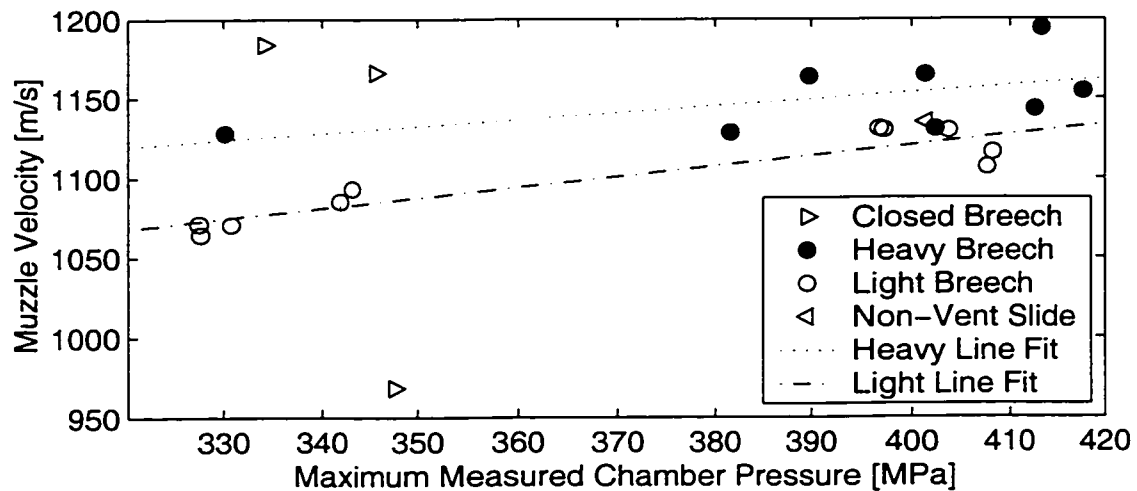


**Figure 6.3-5 Distribution of Muzzle Velocity as a Function of the Maximum Measured Chamber Pressure.**

**Table 6.3-1: Peak Pressure [MPa].**

Breech Configuration		Closed-Breech	Heavy Inertial Breech Mean: 390 STD: 34			Light Inertial Breech Mean: 367 STD: 35				Non-Vent
Vent Geometry		NA	Early	Nominal	Intermediate	Early	Nominal	Intermediate	Late	NA
Shot Number	1	348	390	382	413	408	397	340	342	350
	2	334	319	401	418	404	397	343	385	NaN
	3	346	402	330	413	328	408	331	328	337
	4			409						401
	5			409						
Mean		342	370	386	415	380	401	338	352	363
STD		7	45	33	3	45	6	6	30	34

### 6.3.2 Juxtaposition of Venting to Non-Venting Cases

A clear indication of the effect of the venting may be achieved by superimposing the chamber pressure traces of a venting and non-venting configuration. This is done for two venting configurations: heavy-early 2-3-5 and light-nominal 2-5-1 relative to the non-venting configuration 2-9-4. For all three shots, the measured chamber pressure and muzzle velocity are within 1% of each other. The results are plotted in Fig. 6.3-6 and Fig. 6.3-7.

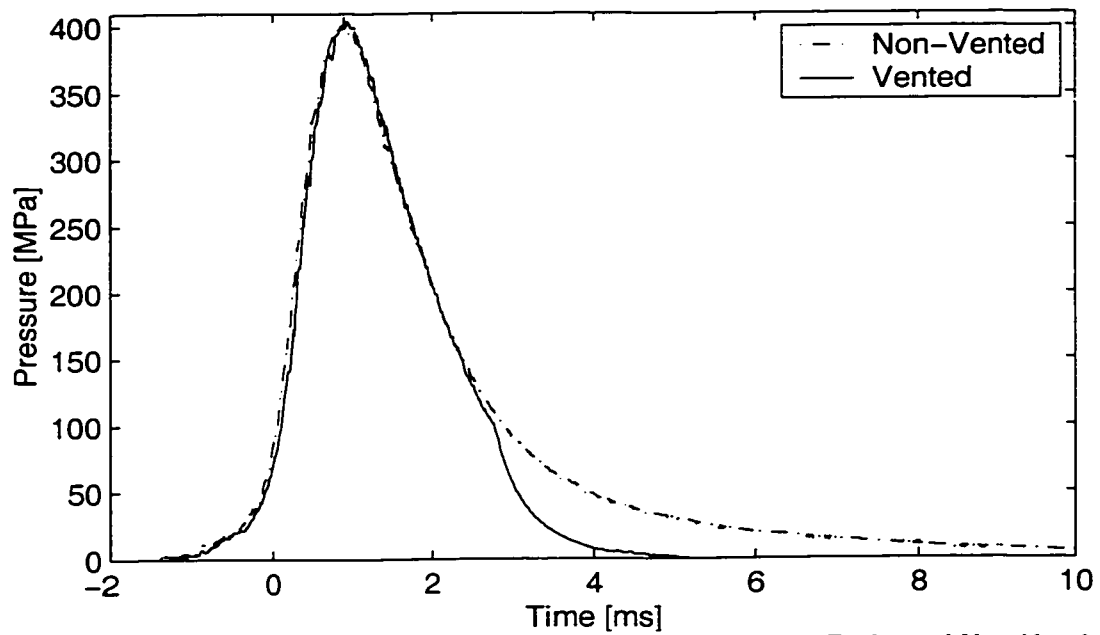


**Figure 6.3-6 Juxtaposed Plot of Chamber Pressure for Heavy-Early and Non-Venting.**

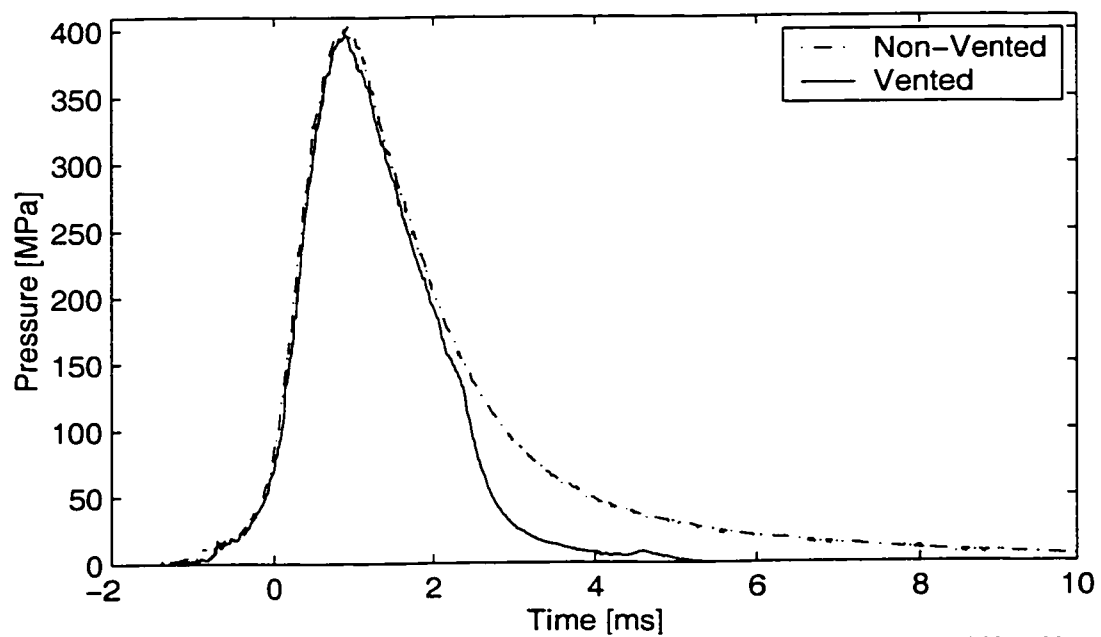


**Figure 6.3-7 Juxtaposed Plot of Chamber Pressure for Light-Nominal and Non-Venting.**

### 6.3.3 Determination of Projectile Traverse

A straightforward means to determine the projectile travel within the gun was to examine the pressure time curves at the 13 pressure ports down-bore of the chamber. When the pressure reached one half the maximum pressure for the trace, the base of projectile was considered to be at the axial position of the port. Since the geometry of the ports are known (Table 5.5-1), the time and position of the projectile may, thus, be determined.

### 6.3.4 Determination of Rarefaction Wave Front Traverse

As clearly visible in Fig. 6.3-6 and Fig. 6.3-7, a substantial discontinuity in the slope of the pressure time curve occurs at the head of the rarefaction wave. Noting the exponential decay behavior of the curve in the region of interest, the  $\log_{10}$  of the curve should indicate a relatively constant slope prior to and following the passage of the wave head. The first derivative should be characterized by a nearly discontinuous reduction at the time of the passage of the wave head. The local minimum of the second derivative of the curve will, therefore, be indicative of the time of passage of the rarefaction wave head.

Implementation of this technique required smoothing of the data vectors after differentiation. A fifty point running average was implemented to achieve this along the first derivative of the data that were collected at 100 kHz; thus, the running average spanned 0.5ms. Differentiation was estimated by assembling a vector of the differences between adjacent elements, and multiplying by the sampling rate. A ten point running average was then used after the second derivative was taken.

For identification of the first passage of the rarefaction wave front past the P1 chamber pressure port, the range of data examined for the local minimum spanned the data between one and three milliseconds following the peak pressure. This captured the rarefaction wave head for all venting cases except shots 2-3-4 and 2-8-2 whose pressure data was compromised as listed in Table 6.1-1. The reason for examining a limited range of data is that the second derivative has other local minima which must be avoided. This method is depicted in Fig. 6.3-8 which includes the chamber pressure trace of configuration 2-5-1 plotted in Fig. 6.3-4.

The concern with this method is that the smoothing of the data could introduce an error shift in the passage time identification. Therefore, this method was used as a predictor to enable the construction of a pair of exponential polynomial fits to the data over a limited locus of pressure data points either side of the predicted slope discontinuity. The intersection of the two exponential fits then constitute the estimated time of passage of the rarefaction wave head.

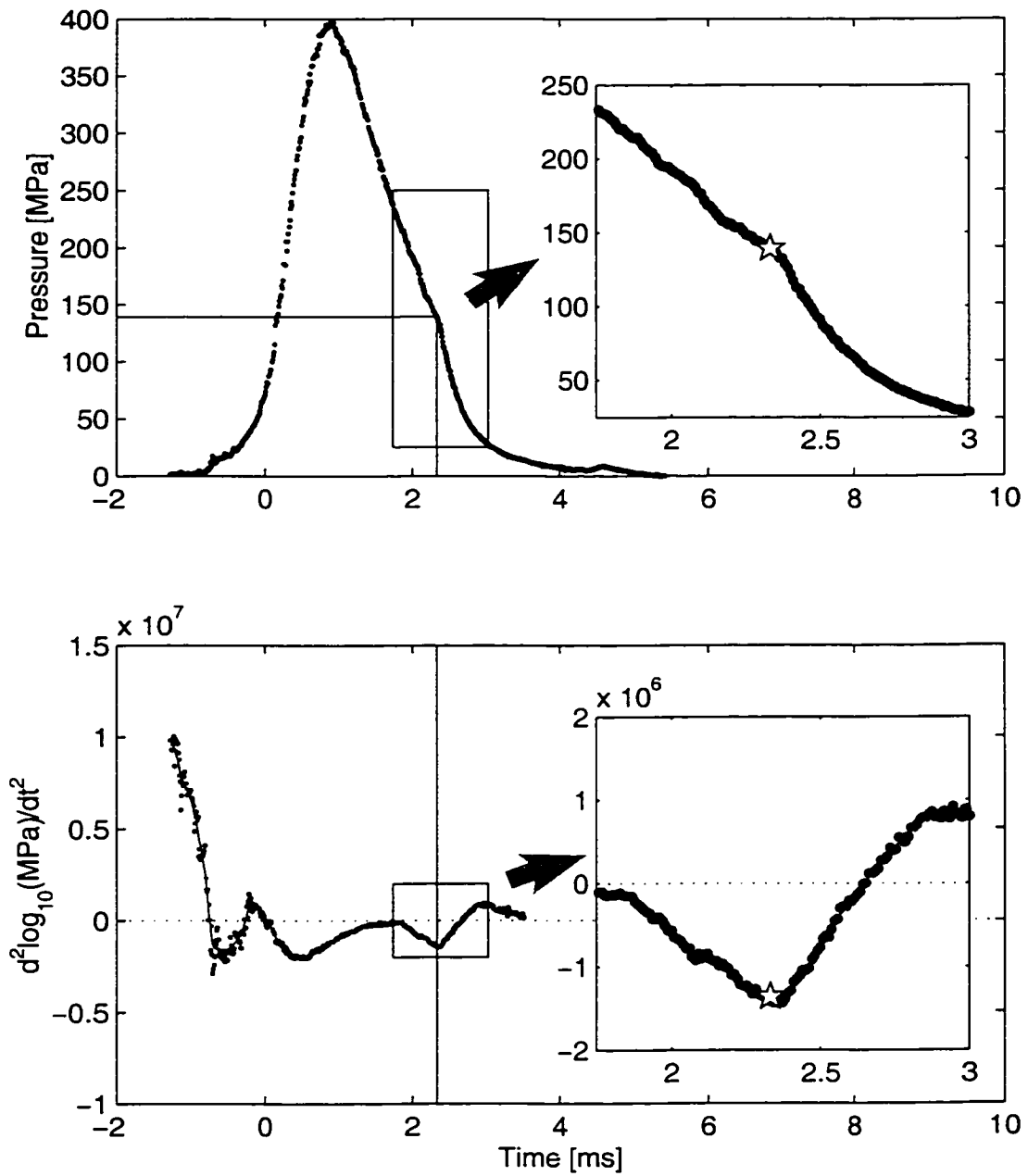


**Figure 6.3-8 Identification of Rarefaction Wave Head By Means of Local Minimum of Second Derivative of the Logarithm.**



The locus of data points employed by the curve fit to the data following passage of the rarefaction wave head (downside) was established as from 7 to 60 points to the right of the predicted intersection. The first six points were not included to avoid contaminating the downside polynomial fitting with data that preceded the passage of the wave head (upside) data points in the event the predicted intersection was in error by as much as six points. The upper-side locus was established as from 4 to 30 points from the predicted intersection. In general, the behavior of the pressure curve prior to the rarefaction wave was not as well behaved as the downside; thus, it was desirable to better localize it near to the predicted intersection. This method is depicted in Fig. 6.3-9.

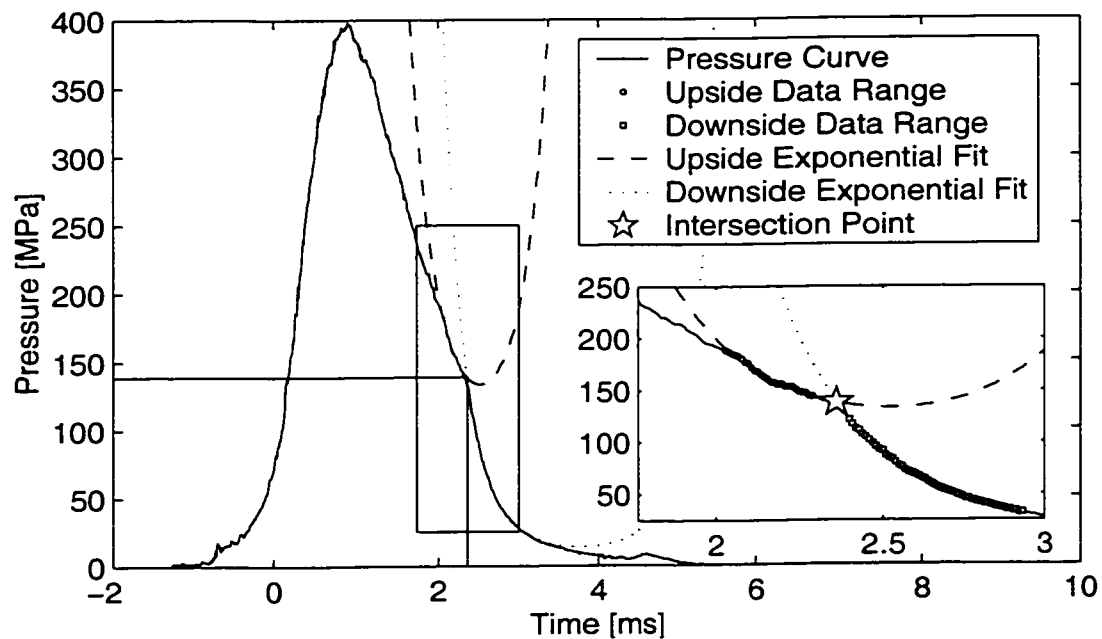


**Figure 6.3-9 Identification of Rarefaction Wave Head By the Intersection of Exponential Curve Fits to the Data Adjacent to the Predicted Point.**

Three methods were used to reject poor estimates. First, if the exponential fits didn't cross, no real root exists in the determination of the intersection and the estimate is rejected. Second, if the right most point of the downside was within four confidence levels of the upside exponential fit, the point was rejected of concern the two exponential curves were too tangent. This would indicate an absence of a true discontinuity of slope. Similarly, if the left-most point of the upside was within two confidence intervals of the downside exponential fit, the point was rejected. Third, if the wave was identified in front of the projectile, it was rejected. If the rarefaction wave was not identified at a given pressure port, no further estimations were made for later ports.

Following the first pressure port, the same technique was applied for the remainder of the ports. First, bracket the anticipated range for the passage. Second, identify the minimum of the second derivative of the logarithm of the pressure in that range. Third construct a pair of exponential curve fits and identify the intersection.

For pressure ports P2 - P4, the range of data examined was bracketed by identification of the prior wave head passage time, and the minimum speed that a rarefaction wave could be anticipated to travel between the prior port location and the current port. This speed was set to 400m/s, less than half the anticipated sonic velocity. An example of a fit to a later P4 port is plotted in Fig. 6.3-10.

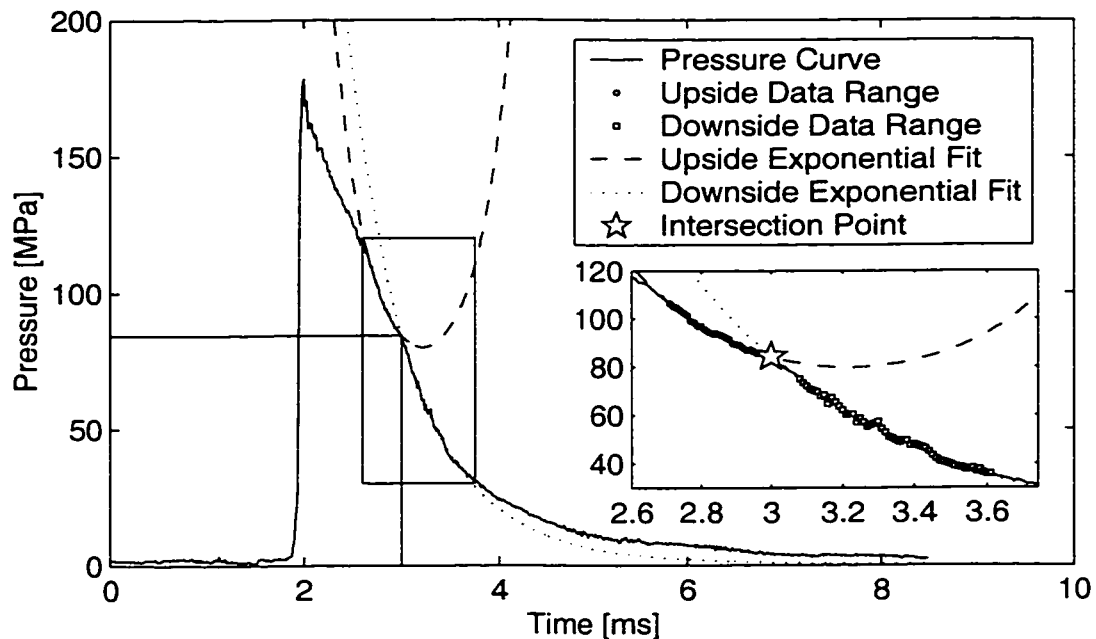


**Figure 6.3-10 Identification of Rarefaction Wave Head at the P4 Probe.**

For the subsequent ports, it was found that any overestimation of the time of wave front passage would “ratchet” the remaining ports to an incorrect solution. Therefore, a new method was employed to identify a range. A second order polynomial fit was applied to the prior passage times. Projecting this solution forward to the current probe, an estimated time for the rarefaction wave head passage was determined. The range was set to twice the confidence interval of the polynomial fit. An additional constraint rejected points within 0.45ms of the projectile. (The inflection of the pressure curve at the projectile crossing and the transient behavior exhibited by some shots near the muzzle (see Fig. 6.3-4 for example) would confound the predictor if this step was not taken.)

The process continued until all 14 ports were identified, or until one of the rarefaction wave head's could not be identified. For two thirds of the vented guns with valid pressure data, this method resolved the first 8 ports. For one configuration, the rarefaction wave was tracked at all 14 ports, and for four others, to 13 ports.

The result of this procedure was a series of port crossing times that, when combined with the port locations listed in Table 5.5-1, provided a measure of the rarefaction wave head traversal through the bore of the gun. A second-order polynomial fit of this measurement could then be applied to estimate the position of the rarefaction wave head at any time during its traversal of the bore.

#### 6.3.5 Spatial Pressure Gradient

For a vented firing, the pressure behind the rarefaction wave head will be lower than an orthodox gun as a result of the expulsion of propellant gases from the chamber. The experimental results are plotted for the same three systems considered in Section 6.3.2 in Fig. 6.3-11 and Fig. 6.3-12. The rarefaction wave head location at shot-exit was estimated using a second-order polynomial fit of the rarefaction wave head measurement discussed in Section 6.3.4.

Due to the pressure transducer drift, the measurement of this gradient was impaired with the measured pressure for the non-venting configuration exhibiting a modest gradient reversal for pressure ports P1 - P3. (An example of a theoretical pressure gradient is presented later in Fig. 7.2-2 which indicates a slight gradient with higher pressure at the breech than the muzzle.) Nevertheless, the dramatic reversal of the pressure

gradient achieved by the rarefaction wave is clear. It is worth restating that the peak chamber pressure and muzzle velocities were within 1% for all three of these configurations.

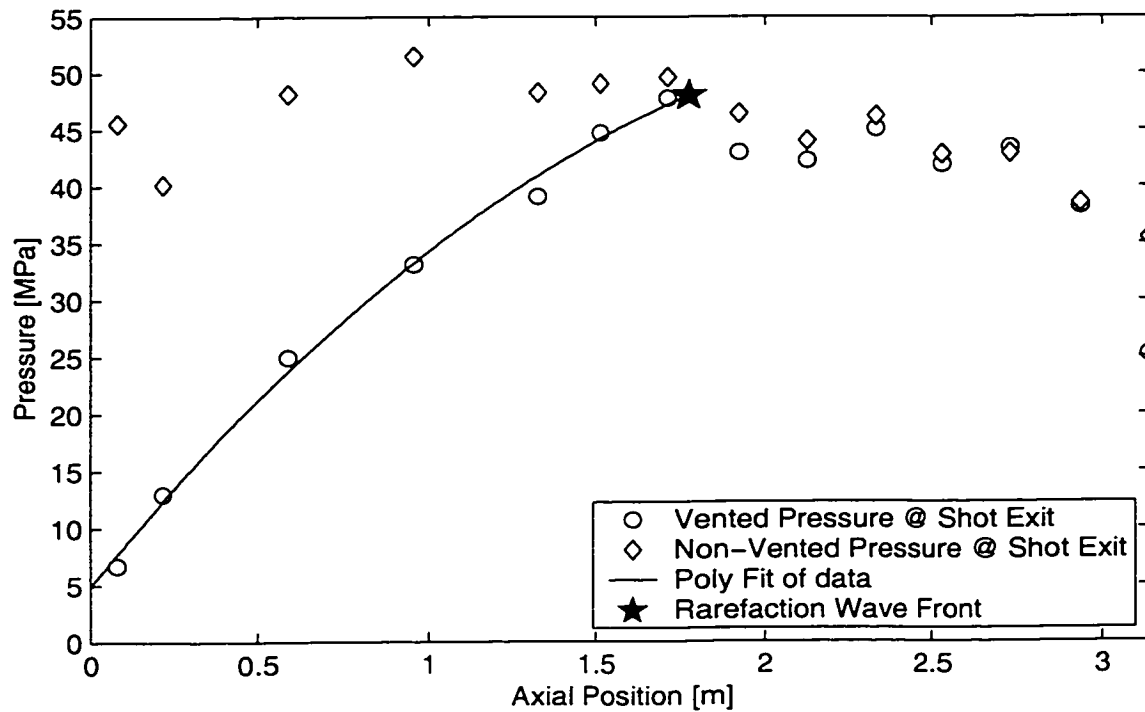


**Figure 6.3-11 Spatial Gradient of Pressure Within Gun at Shot-Exit for Non-Venting Versus a Heavy-Early Vent.**

The muzzle pressure transducer is subject to a substantial transient upon shot-exit. Thus, the seemingly low pressure of the vented shot depicted in Fig. 6.3-11 is readily explained. Similarly, the muzzle pressure of the vented shot depicted in Fig. 6.3-12 is off the scale as may be appreciated from Fig. 6.3-4.

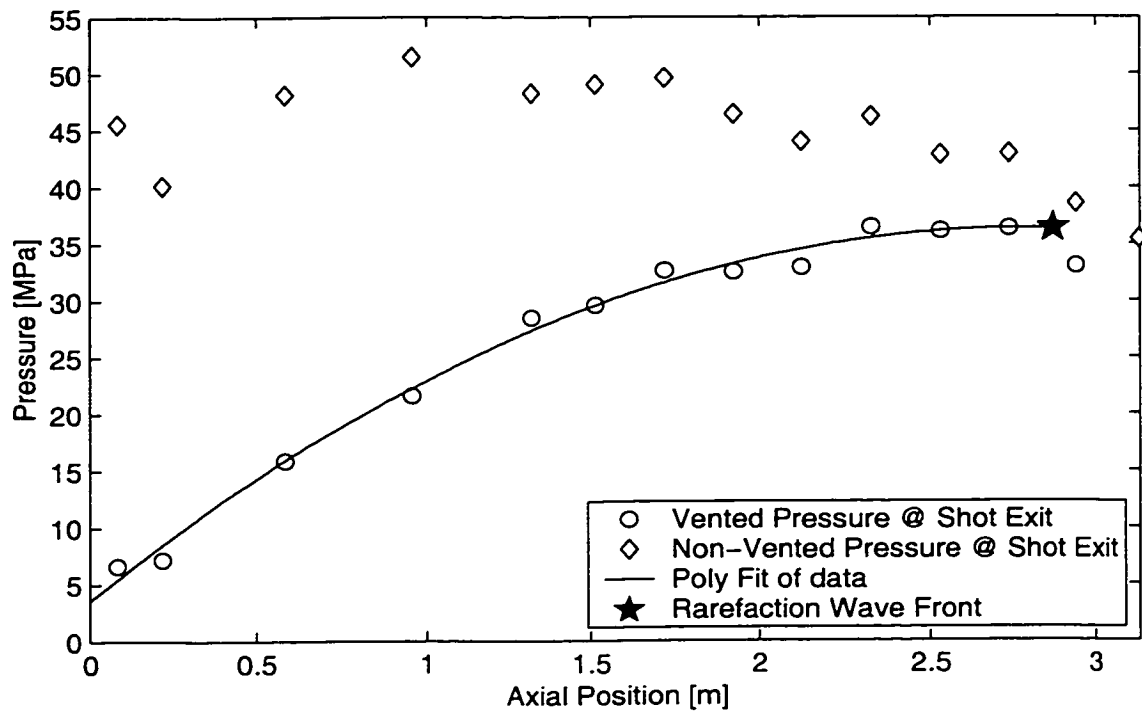


**Figure 6.3-12 Spatial Gradient of Pressure Within Gun at Shot-Exit for Non-Venting Versus a Light Nominal Vent.**

#### 6.3.6 Combined Pressure Travel Time Curves

Presentation of the combined pressure, projectile travel, and rarefaction wave front propagation appears in the following Figures:

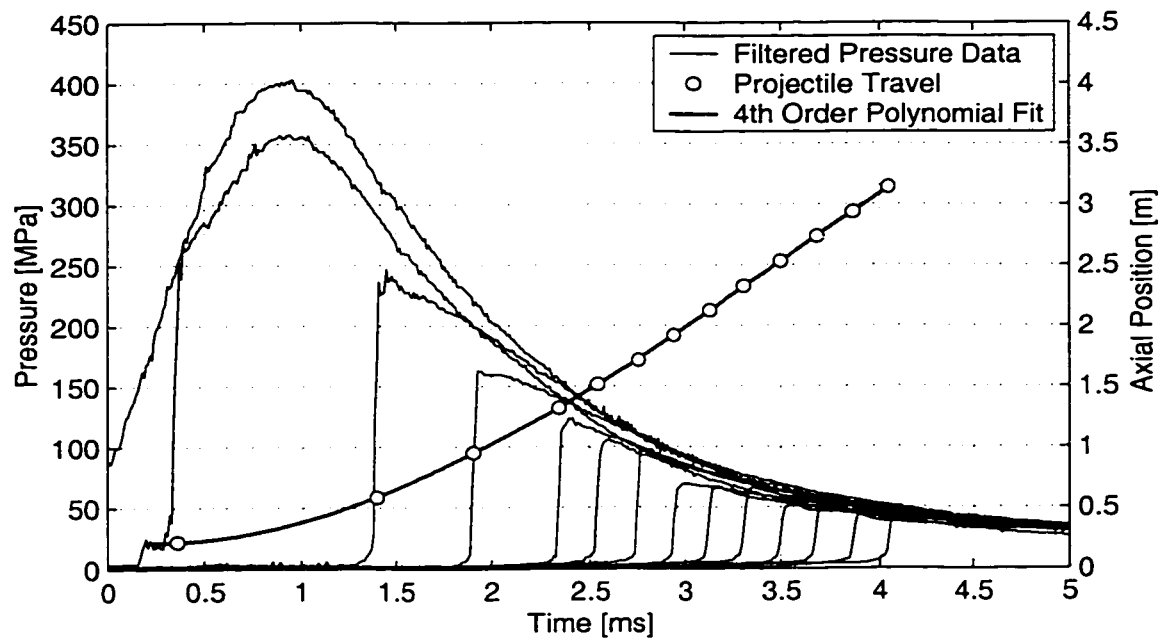


**Figure 6.3-13 Integrated Pressure Travel Time Curve for the Non-Vented configuration Shot 2-9-4.**

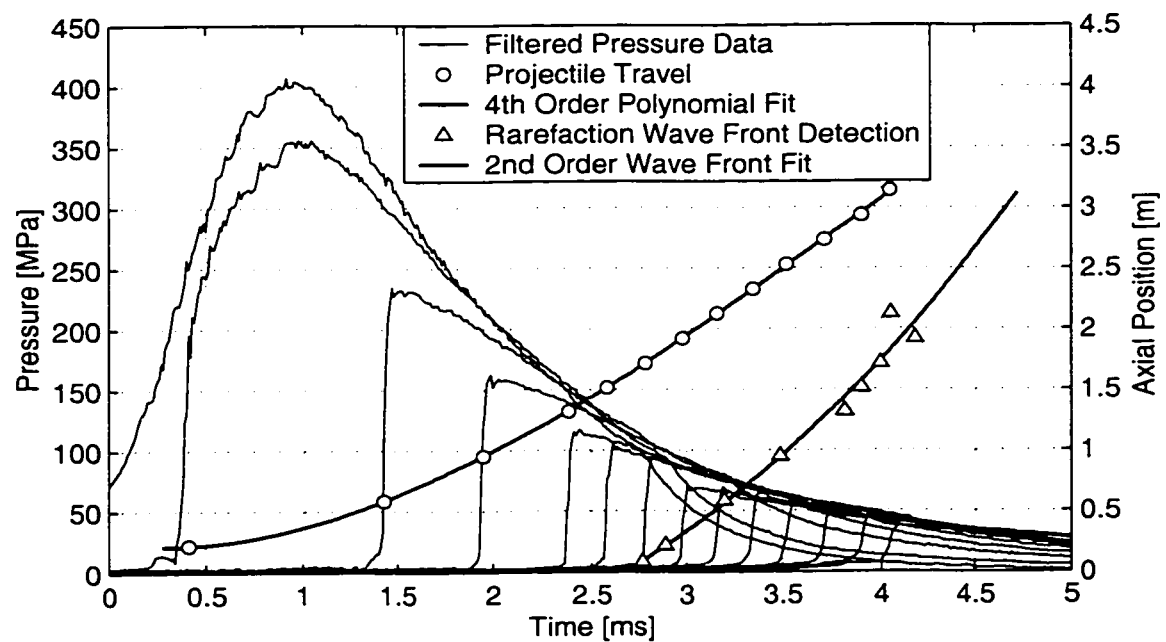


**Figure 6.3-14 Integrated Pressure Travel Time Curve for the Heavy-Early configuration Shot 2-3-5.**

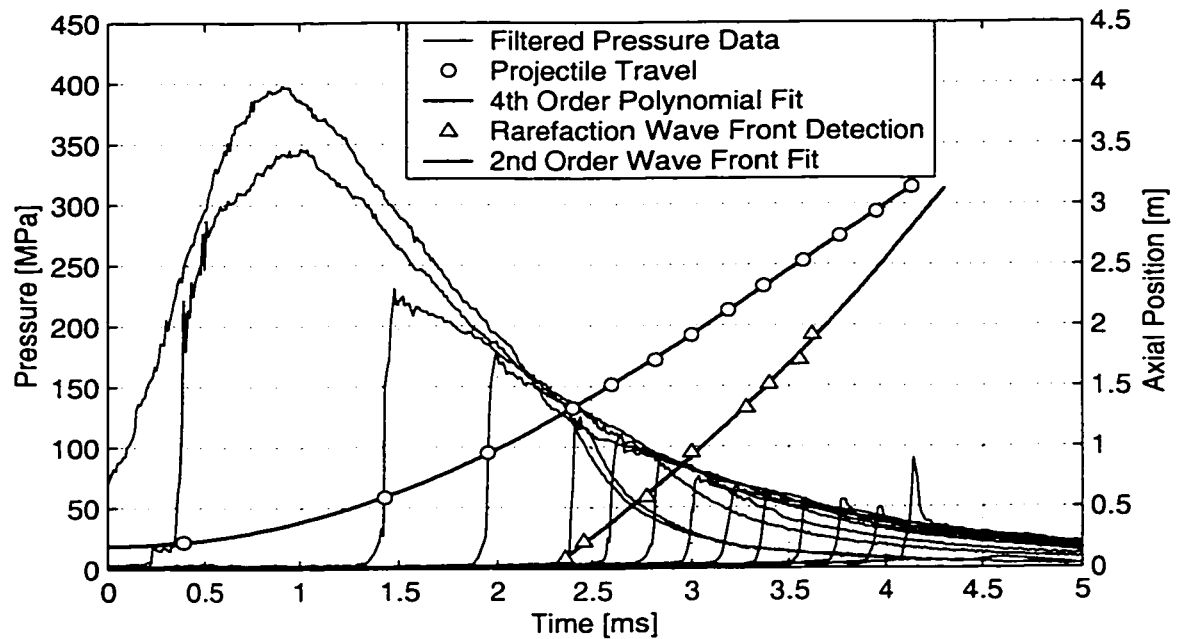


**Figure 6.3-15 Integrated Pressure Travel Time Curve for the Light-Nominal configuration Shot 2-5-1.**

#### 6.3.7 Measured Vent Time and Relative Projectile Travel

The duration during which propellant gas is being expelled from the back of the gun, while the bullet is still in-bore is of interest. The measured time between when the rarefaction wave head is detected traversing the chamber pressure port P1 and at shot-exit is a close approximation that does not account for the time it takes to traverse the chamber. (The rarefaction wave head will take nominally a tenth of a millisecond to traverse the 110mm from the vent to the chamber pressure port.) Similarly, the percent of the 2.963m travel length of the barrel that projectile has traversed when the rarefaction wave head is detected at the chamber port is of interest. Both of these are presented in Table 6.3-2 and shown in Fig. 6.3-16.



**Table 6.3-2: Duration of Concurrent Venting and Propulsion and Percent Projectile Travel at Venting [ms/%].**

Breech Configuration		Closed-Breech	Heavy Inertial Breech			Light Inertial Breech				Non-Vent
Vent Geometry		NA	Early	Nominal	Intermediate	Early	Nominal	Intermediate	Late	NA
Shot Number	1		1.58 55.5	1.36 61.9	0.94 77.8	2.16 37.0	2.02 42.0	1.67 54.5	1.40 62.0	
	2		NaN NaN	1.39 61.8	0.95 78.3	2.15 36.5	2.06 40.2	1.62 55.4	NaN NaN	
	3		1.52 55.7	1.41 63.5	0.94 78.0	2.29 38.7	2.02 41.3	1.77 51.8	1.33 63.6	
	4			1.36 62.2						
	5			1.35 63.5						
Mean			1.55 55.6	1.37 62.6	0.94 78.0	2.20 37.4	2.03 41.2	1.69 53.9	1.37 62.8	
STD			0.04 0.2	0.03 0.8	0.01 0.2	0.08 1.2	0.02 0.9	0.08 1.9	0.05 1.1	

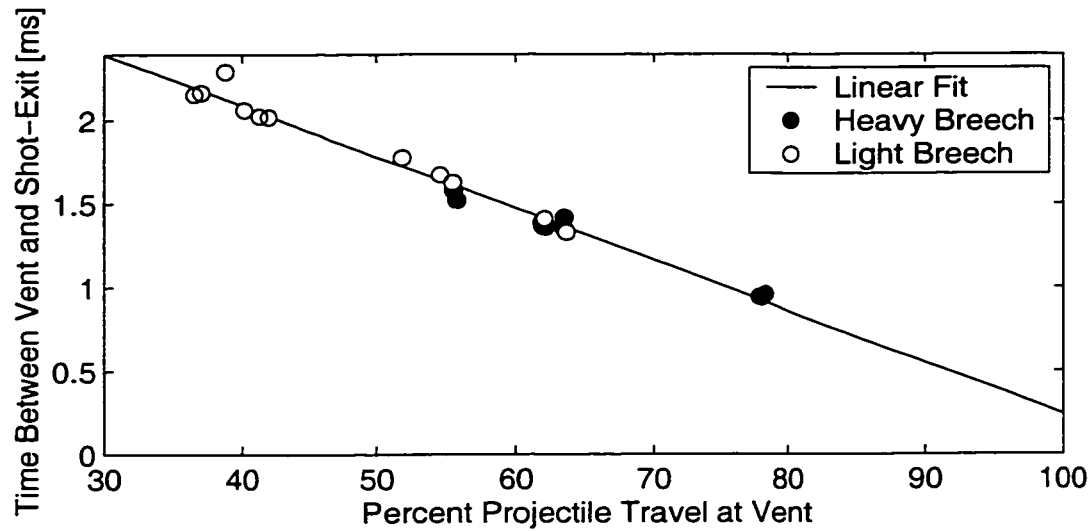


**Figure 6.3-16 Duration of Concurrent Venting and Projectile Propulsion Versus Percent Projectile Travel at Venting.**

#### 6.3.8 Integrated Chamber Pressure Impulse

For an orthodox gun, the recoil momentum is often inferred by integration of the chamber pressure projected upon the bore cross-sectional area over the duration of the firing event. This may be termed the chamber pressure impulse. (This is a reasonable measure, but it neglects the nozzle effect at the neck of the cartridge case for guns with a larger chamber diameter than bore diameter. This effect may add an additional 8% to the measured momentum.) For a RAVEN, the chamber pressure impulse should provide an upper bound as it neglects two basic contributions to recoil reduction. The first and smaller effect is the pressure gradient between the vent and the chamber port. When venting first commences, the measured chamber pressure will be far higher than the vent chamber for a brief period of time.

The second effect is the potential to generate forward thrust by means of a rearward directed expansion nozzle. As discussed in Section 4.2.2 following (4.2-20), those propellant gases that are expelled rearward have the potential to reach nominally 2,000m/s. If 60% of the 333g of propellant used in the 35mm TP round (See Table 5.1-2) are vented in this manner, 400Ns of forward momentum may be anticipated to be imparted to the launcher.

The integrated pressure data is shown in Fig. 6.3-17 and presented in Table 6.3-3. Each of the data vectors was truncated to 10ms. No effort was made to eliminate pressure drift from the data.

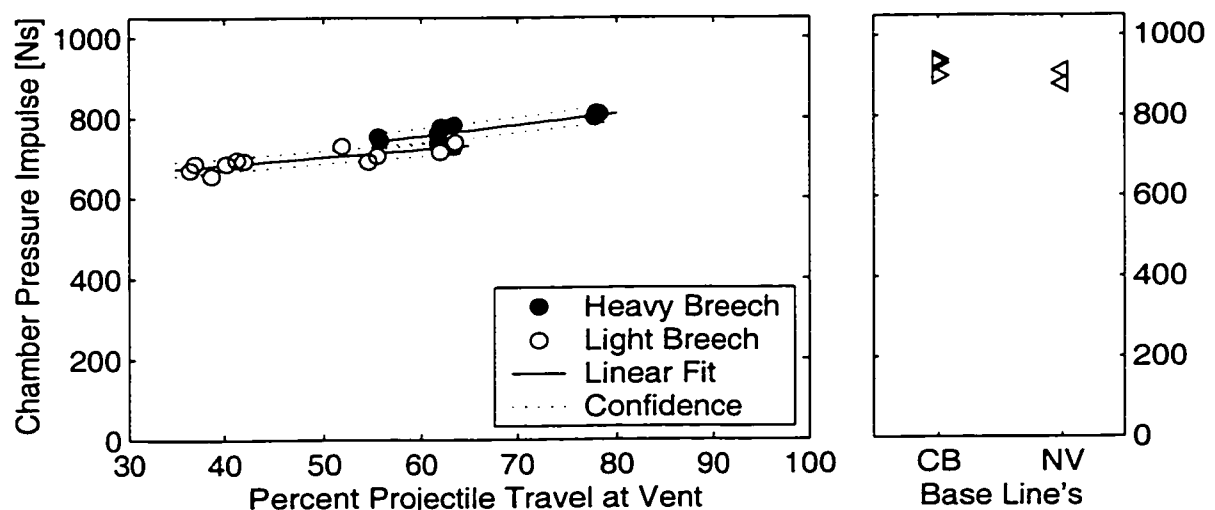


**Figure 6.3-17 Integrated Chamber Pressure Impulse as a Function of the Projectile Travel at the Commencement of Venting.**

The quality of this data has been called into question by the tendency of the pressure transducers to drift negative. If one were to assume that the drifting occurs

gradually over the interior ballistic event, the readings collected are lower than they should be for later times. Thus, the findings presented are likely to be lower than actually occurred. Further, since the data is likely to suffer a greater skew to the later times, and since RAVEN achieves all of its recoil reduction after peak pressure, it may be anticipated that the skew introduced will reduce the chamber pressure impulse computations for the non-vented and closed-breech guns more so than for the vented configurations.

**Table 6.3-3: Integrated Chamber Pressure Impulse [Ns].**

Breech Configuration		Closed-Breech	Heavy Inertial Breech			Light Inertial Breech				Non-Vent
Vent Geometry		NA	Early	Nominal	Intermediate	Early	Nominal	Intermediate	Late	NA
Shot Number	1	938	753	737	801	687	693	691	715	882
	2	898	NaN	762	811	670	687	705	NaN	NaN
	3	930	744	728	811	656	697	730	738	877
	4			777						911
	5			782						
Mean		922	748	757	807	671	692	709	727	890
STD		21	7	24	6	15	5	20	16	18

## **6.4 Measured Recoil Results**

The preferred method to determine the recoil momentum of a RAVEN is to measure the free recoil velocity of the launcher.

### **6.4.1 Challenges to Achieve Free Recoil**

As discussed in Section 5.3.3, the recoil momentum is to be inferred from the free recoil velocity of the entire gun after firing and before the gun has traversed nominally 25mm to impact the ring-spring recoil arrestors. There are three principal concerns with this approach.

#### **6.4.1.1 Premature Engagement of the Secondary Recoil Brakes**

If the gun impacts a recoil arrestor prior to achieving its full free recoil velocity, the free-recoil assumption is violated and the data is corrupted. This concern is readily addressed by examination of the recoil data. If the highest rearward free recoil speed was not attained prior to reaching the ring-springs, then the data was compromised. If the measured speed reached a maximum, as may be inferred by a horizontal trace, the data is not corrupted.

#### **6.4.1.2 Incomplete Primary Braking**

Second, if the primary recoil brakes have not successfully brought the inertial breech to rest with respect the cannon barrel prior to the gun impacting the recoil arrestors, the data is corrupted. This concern may be addressed by two means. First, the primary recoil arrestor crush tubes have a fast action (less than 30ms) with little propensity for rebound as discussed in Section 5.3.2. If the ring-springs are not impacted prior to this time, the data is not corrupted. The second method is to examine the recoil data. If the

recoil speed is accelerated to its free recoil velocity prior to engagement with the ring-springs, the speed may be anticipated to remain generally constant with perhaps some modest frictional losses prior to engagement.

#### 6.4.1.3 Friction

Friction can not be eliminated. Thus, it is known that the free recoil velocity measured will be effected by friction. This concern is challenging to quantify. For a closed-breech gun, however, the barrel will slide rearward within the mount prior to engagement with the ring springs. Thus, the effect of friction will be to reduce the free-recoil speed: the friction forces will only be applied in a forward direction resisting the recoil motion. This will manifest itself as an apparent reduction in the measured launch momentum. The magnitude of the reduction remains illusive, but not its sign.

For a blow-back inertial-breech and blow-forward barrel this argument is lost. For such a configuration, the barrel is first blown forward, by the axially projected area of the cartridge case neck (also known as the chambrage of the gun). For the 35mm test gun, the cartridge case diameter is 55mm while the bore is 35mm (see Tables 5.1-1 and 5.1-2). The resulting axially projected area (annulus between 55mm and 35mm) is nearly 50% more than the projected area of the bore. Thus, the gun is blown forward with greater force than an orthodox closed-breech gun is blown-back. This initial motion is swiftly reversed as the primary recoil brakes (see Section 5.3.2) bring the inertial breech to rest with respect to the rest of the gun.

This blow-forward behavior can be a challenging concept to accept. The line drawing of Fig. 3.2-2 depicts the pressure acting at the neck of the cartridge case with an axial component. Further discussion will be made in Section 7.1.2 and depicted in Fig. 7.1-1. (If referring to Fig. 7.1-1, imagine the chamber pressure pushing forward on the modeled gun chambrage.)

During this initial motion of the barrel, within the gun mount, friction will resist the forward velocity and apply a rearward directed force. This will manifest itself as an apparent increase in the measured launch momentum. As the primary recoil brakes engage the gun, the forward motion will be brought to rest at its maximum forward intrusion and subsequently impart rearward motion. The friction of the mount will then change sign, resisting the rearward motion of the barrel. This portion of the friction will manifest as an apparent decrease in the measured launch momentum.

#### 6.4.2 Phase-Plane Representation of Recoil Motion

It is important to consider the extent or stroke of the recoil motion to ascertain when engagement with the ring-spring secondary recoil brakes are encountered. It is also important to examine the velocity of the gun to gain confidence that free-recoil has been achieved by observing a period of free recoil velocity prior to engagement with the recoil arrestors. The ideal format to present this information is a phase-plane with the recoil stroke and velocity represented by the abscissa and ordinate, respectively.

The data collected consisted of position measurements sampled at 100 kHz. Two filtering levels were applied. A coarse filter consisting of a 50 point running average

that spanned half a millisecond and a smooth filter using a 300 point running average that spanned three milliseconds.

Velocity was estimated by assembling a vector of the differences between adjacent elements of the position data and multiplying by the sampling rate. Both the coarse and smoothed data were used to provide two different estimates of the velocity. The coarse and smooth filters were then applied to the result. The smooth velocity data was used to determine the free recoil velocity.

The phase plane recoil response of the third closed-breech shot 2-1-3 is depicted in Fig.6.4-1.

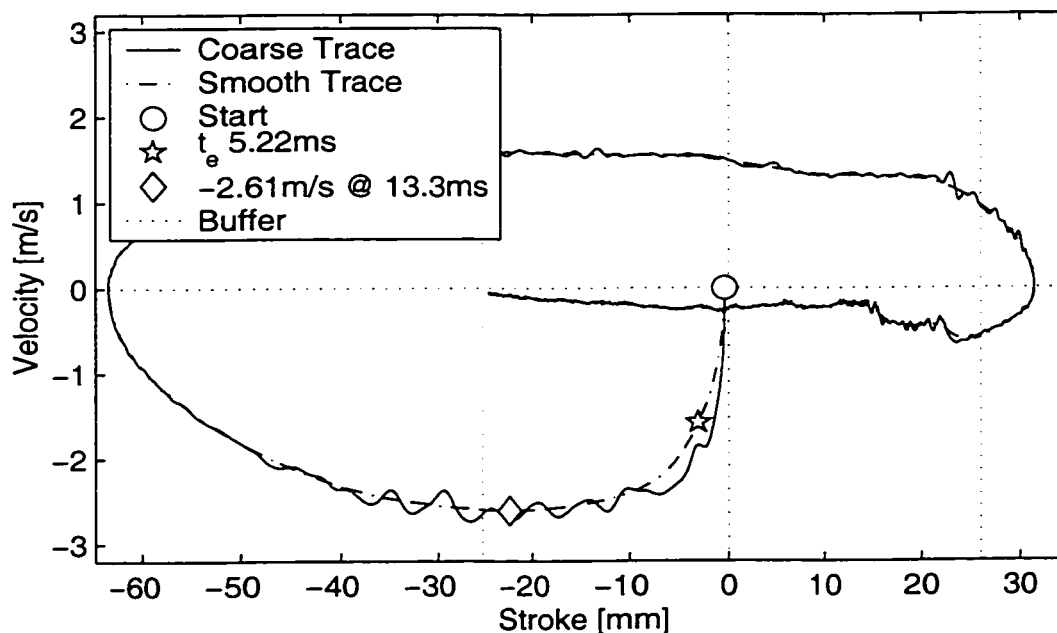


**Figure 6.4-1 Recoil Phase Plane Response of the Third Closed-Breech Shot.**



Since the gun is at rest prior to firing the trajectory begins at the origin. For this orthodox configuration the gun recoils rearwards with a negative velocity of increasing magnitude. Thus, the trajectory in the phase plane travels into the third quadrant. It then rebounds forward and back again, coming to rest at -25mm. (This rebounding behavior was observed in the video clip described in Section 6.1.2.)

An oscillatory dynamic may clearly be seen in the coarse trajectory. It's frequency is nominally 2kHz. This frequency may be speculated to be attributed to transducer mount structural dynamics, or a transducer dynamic such as stick-slip friction of the internal components. It is also possible that this motion could be attributable to a chattering motion [62] of the 334kg gun mass through the gun mount. Regardless, this motion has little to do with this analysis other than confounding potential efforts to model friction.

The free recoil velocity of -2.61m/s was reached at 13.3ms after shot-start using the smooth trace. The free recoil velocity is reached at a point suspiciously close to the recoil buffer zone; however, it is reached after the blow-down has been progressing half again as long as the action time of the gun with the bullet in-bore. Thus, there is little if any recoil momentum remaining to be imparted at this time. Unfortunately, examination of Fig. 6.3-1 indicates a negative chamber pressure at this time due to the transducer drift, rendering verification of this inconclusive.

For a blow-forward configuration the gun will recoil forward with an increasing positive velocity and stroke. Thus, it will initially follow a trajectory into the

first quadrant. Upon reversal of its velocity by the primary recoil brakes, the trajectory will pass into the forth quadrant, and subsequently the third quadrant. This is shown in Fig. 6.4-2 for the fourth shot of the non-venting configuration 2-9-4.

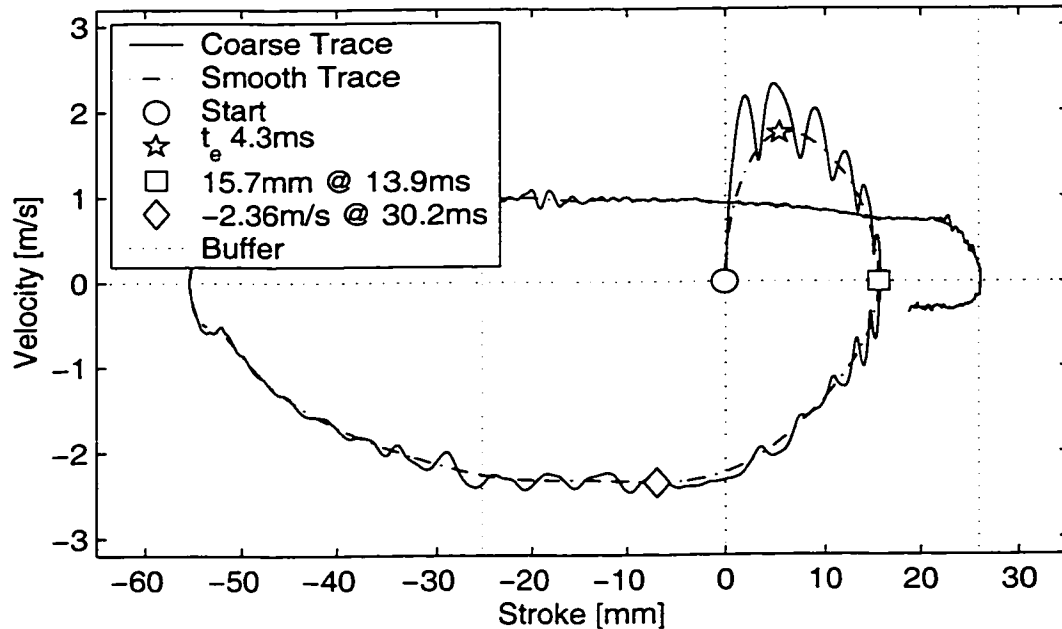


**Figure 6.4-2 Recoil Phase Plane Response of Fourth Non-Venting Shot.**

Examination of Fig. 6.4-2 reveals that the forward buffer was not encountered prior to achieving its free recoil velocity. The barrel intruded a maximum extend to 15.7mm forward, coming to rest temporarily 13.9ms after shot-start. The free recoil velocity was achieved 30.2ms after shot-start. This configuration was subject to forward motion friction for the first 13.9ms followed by rearward motion friction for 16.3ms prior to arriving at its free recoil velocity.

The primary recoil braking occurred within the 30ms estimate of Section 5.3.2. (A short 83mm span was provided for the inertial breech to traverse prior to engaging the primary recoil rods as depicted in Fig. 6.1-7. This was to allow all the vent configurations except the late vent of Table 5.2-4 to occur prior to engagement of the primary recoil rods. Thus, the primary recoil brakes were not engaged for a few milliseconds.)

By inspection of the phase plane after it reached its free recoil velocity (to the left of the diamond) the gradual loss in recoil speed may be attributed to friction.

Figure 6.4-3 is the phase-plane of the third heavy-early shot 2-3-5. The magnitude of its free recoil velocity is less than the prior non-venting guns. The free recoil velocity is reached while the trajectory is still in the right-half plane.

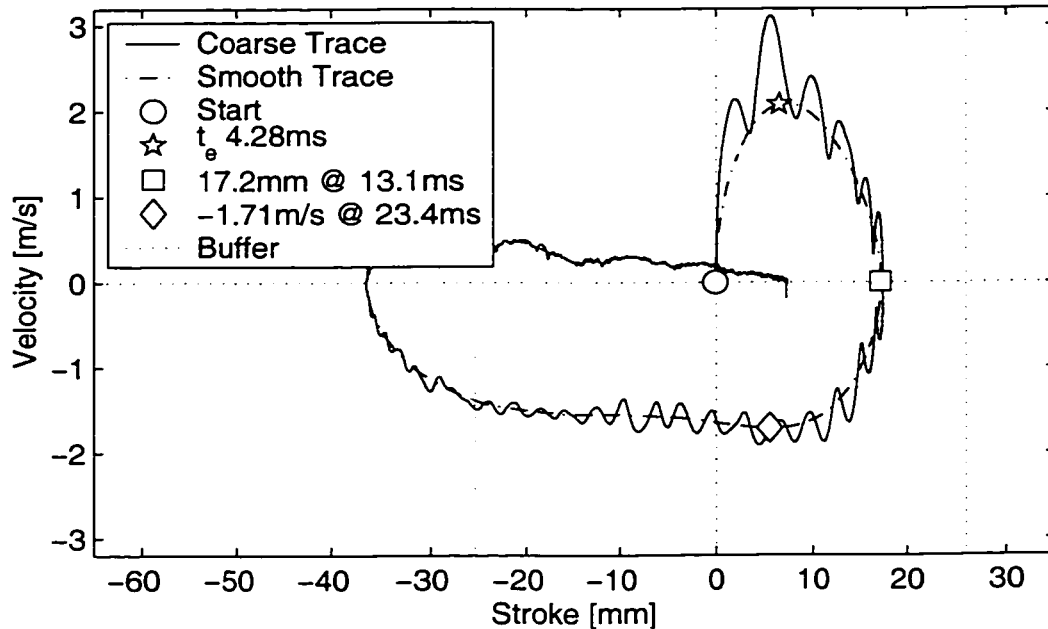


**Figure 6.4-3 Recoil Phase Plane Response of Heavy-Early Shot 2-3-5.**

This configuration was subject to forward motion friction for the first 13.1ms followed by rearward motion friction for 10.3ms prior to arriving at its free recoil velocity.

Figure 6.4-4 is the phase-plane of the first light-nominal shot 2-5-1. Note that the magnitude of its free recoil velocity is less than any of the prior guns. This configuration was subject to forward motion friction for the first 10.1ms followed by rearward motion friction for 7.8ms prior to arriving at its free recoil velocity.

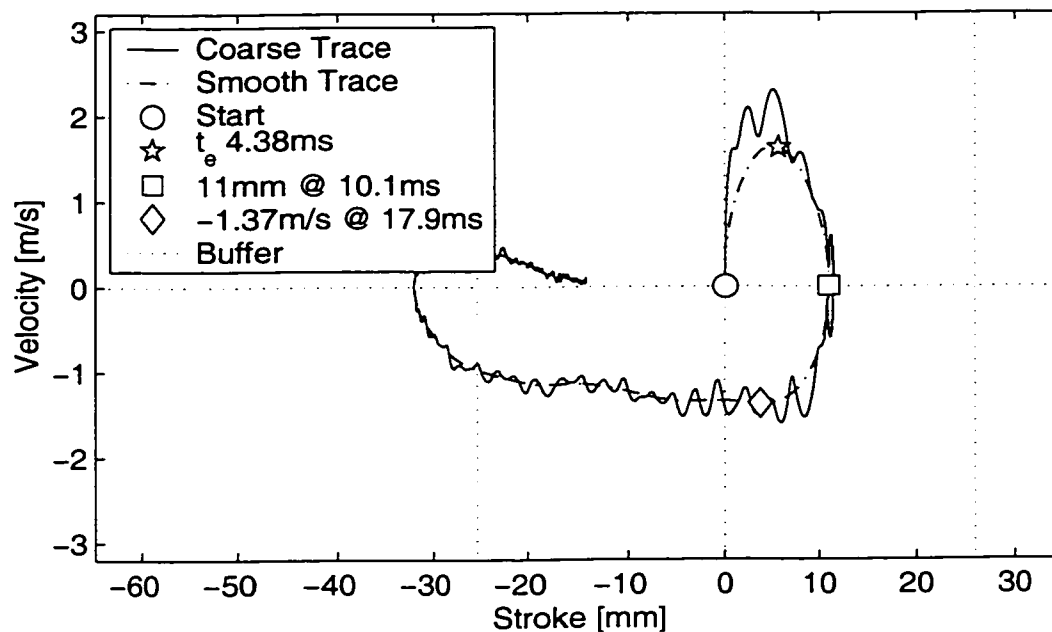


**Figure 6.4-4 Recoil Phase Plane Response of Light-Nominal Shot 2-5-1.**

#### 6.4.3 Determination of Measured Recoil Momentum

The free recoil velocity was determined for each configuration fired with the exception of configuration 2-9-2 which suffered an unknown data problem. With the recoil velocities determined, the momentum is inferred by multiplication of the total recoil mass from Table 5.5-3. The results are presented in Table 6.4-1 and depicted in Fig. 6.4-5.

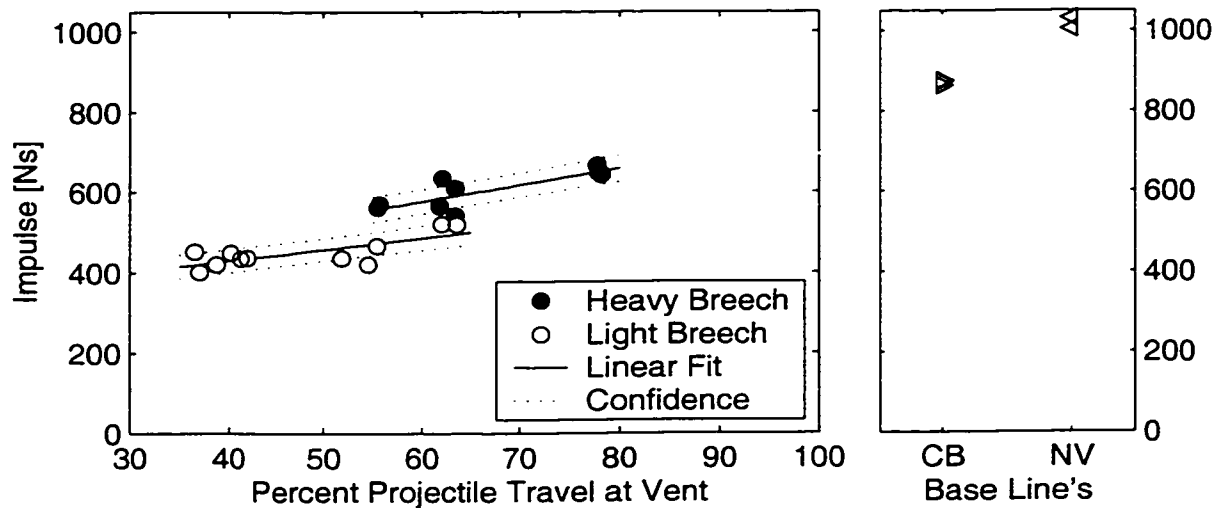


**Figure 6.4-5 Plot of Measured Launch Momentum (Impulse) as a Function of the Percent Travel of the Projectile at Venting.**

**Table 6.4-1: Measured Momentum [Ns].**

Breech Configuration		Heavy Inertial Breech				Light Inertial Breech				Non-Vent
Vent Geometry		NA	Early	Nominal	Intermediate	Early	Nominal	Intermediate	Late	NA
Shot Number	1	863	562	567	667	402	436	421	521	NaN
	2	875	560	565	643	453	449	467	509	NaN
	3	872	570	542	650	421	436	436	519	1004
	4			635						1031
	5			609						
Mean		870	564	584	653	425	440	441	517	1018
STD		6	5	38	13	26	8	23	6	19

## 6.5 Effect on Barrel Heating

The expulsion of hot propellant gases from behind the projectile while it is being propelled down the bore reduced the heat transfer to the bore of the gun. The peak temperature excursion at each of the four thermocouples K1-K4 was recorded. Each of the collected data points are displayed in the figures that follow. The mean of the peak temperature excursions for each probe during the firing of each configuration is listed in Table 6.5-1, along with the standard deviation. The mean difference over all four probes is listed at the bottom as an indicator of overall heat transfer reduction. The earliest venting reduced total heat transfer by 40%, the latest reduced it by over 20%.

**Table 6.5-1: Max Bore Temperature Change (Mean/Std.) [K]**

Breech Configuration		Closed-Breech	Heavy Inertial Breech			Light Inertial Breech				Non-Vent
Vent Geometry		NA	Early	Nominal	Intermediate	Early	Nominal	Intermediate	Late	NA
Thermocouple	K1	4.89 0.10	4.06 0.10	4.64 0.43	4.13 0.18	3.53 0.67	4.15 0.26	4.06 0.10	4.14 0.20	5.46 0.34
	K2	3.00 0.06	2.35 0.06	2.14 0.12	2.39 0.24	2.03 0.12	1.78 0.10	2.35 0.14	2.53 0.27	3.47 0.16
	K3	4.09 0.14	2.24 0.17	2.97 0.35	1.31 0.08	1.50 0.24	1.19 0.25	1.57 0.06	1.69 0.12	2.24 0.19
	K4	2.33 0.29	1.78 0.06	1.50 0.39	2.04 0.16	1.44 0.08	1.69 0.03	1.59 0.27	1.83 0.08	3.29 0.09
Mean		3.58	2.61	2.81	2.47	2.13	2.20	2.39	2.55	3.61

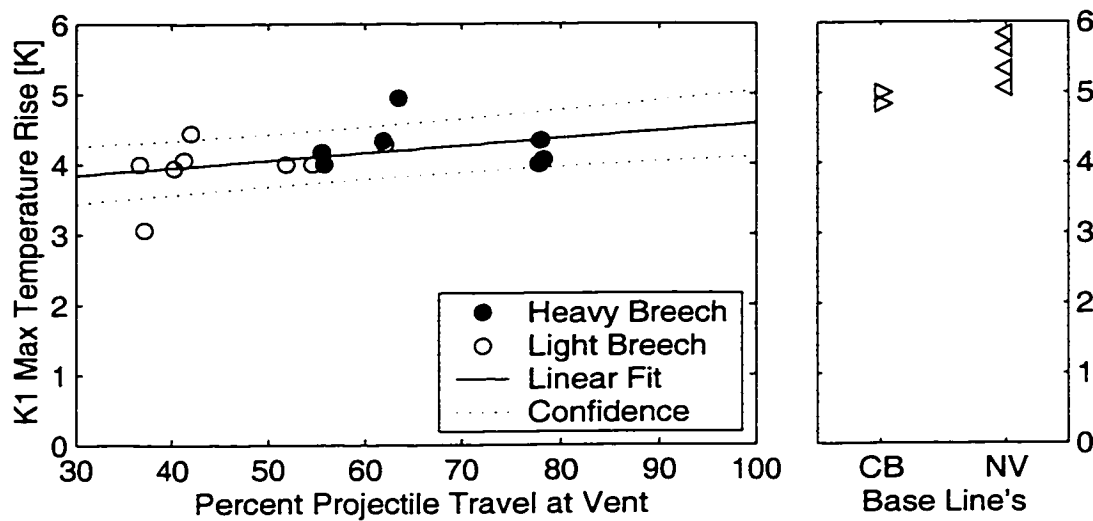


**Figure 6.5-1 Plot of Thermocouple K1 Max Temperature Rise as a Function of the Percent Travel of the Projectile at Venting.**

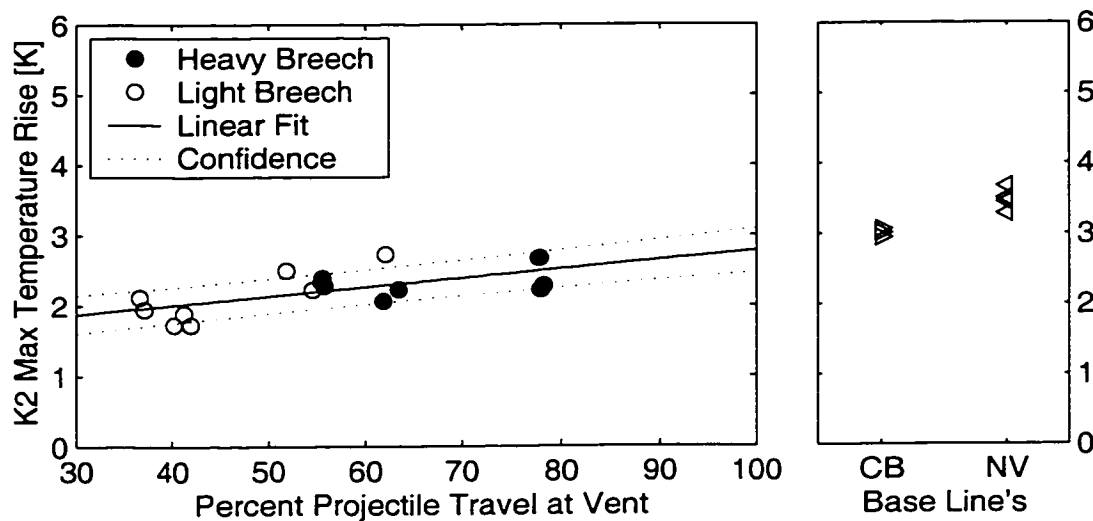


**Figure 6.5-2 Plot of Thermocouple K2 Max Temperature Rise as a Function of the Percent Travel of the Projectile at Venting.**



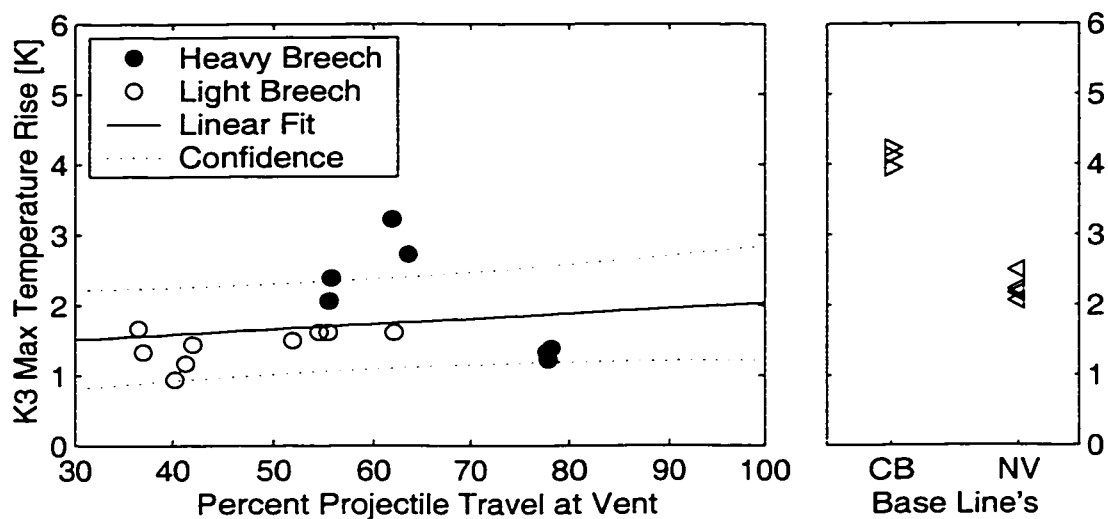


**Figure 6.5-3 Plot of Thermocouple K3 Max Temperature Rise as a Function of the Percent Travel of the Projectile at Venting.**

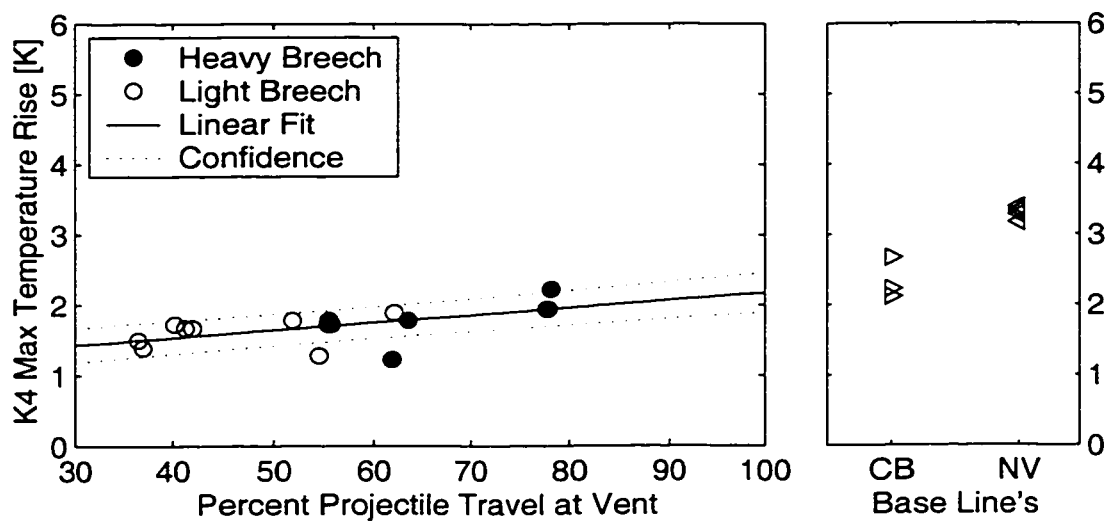


**Figure 6.5-4 Plot of Thermocouple K4 Max Temperature Rise as a Function of the Percent Travel of the Projectile at Venting.**

## **Part 7**

### **THEORY**

#### **7.1 Lumped Parameter Interior Ballistics Model**

A lumped parameter interior ballistics model code implemented in Matlab® is included in the appendix based upon two prior well documented models by Vottis [19] and Robbins [39]. Additional discussion on lumped parameter modeling of interior ballistics is provided by Krier and Adams [64]. The development of this model of gun behavior has been written to remain compatible with the lumped parameter interior ballistics model adopted by The Technical Cooperation Program (TTCP) Technical Panel on Propulsion (WTP-4) of the North Atlantic Treaty Organization (NATO) in the late 1980's [39]. The model will be compatible when the specialized chamber geometry, to be presented in Fig. 7.1-1, is replaced by a bore diameter chamber of equivalent volume with the breech securely fixed to the barrel.

##### 7.1.1 Equation of Motion for the Projectile

Assuming the projectile to be rigid and of fixed mass, the equation of motion of the projectile is governed by Newton's second law accounting for the relevant forces:

$$\dot{v}_p = A(P_b - br - P_g)/m_p, \quad (7.1-1)$$

where  $m_p$  is the mass of the projectile,  $\dot{v}_p$  is the time rate of change of projectile velocity (acceleration),  $A$  is the axially projected area of the projectile (bore area),  $P_b$  is the pressure on the base of the projectile,  $br$  is the bore resistance or friction between the

projectile per unit area of projectile to enable it to be cast as a pressure, and  $P_g$  is the pressure of the gases in front of the projectile.

The bore area for a rifled barrel may be computed as

$$A = \frac{\pi}{4} D_b^2, \quad (7.1-2)$$

where  $D_b$  is the effective diameter of the bore

$$D_b = \sqrt{\left( \frac{R_{GL} D_G^2}{R_{GL} + 1} + \frac{D_L^2}{R_{GL} + 1} \right)}, \quad (7.1-3)$$

where  $R_{GL}$  is the groove to land ratio of the rifling,  $D_G$  is the diameter of the grooves, and  $D_L$  is the diameter of the lands. ( $D_L$  defines the caliber.)

Assuming the projectile to have been at rest prior to shot-start, the velocity of the projectile may determined as

$$v_p = \int_0^t \dot{v}_p dt. \quad (7.1-4)$$

Similarly, the travel displacement of the projectile,  $x_p$  from its starting point relative to an inertial reference frame is

$$x_p = \int_0^t v_p dt. \quad (7.1-5)$$

The 0.550kg projectile mass, rifling geometry, and bore resistance curve are listed in Tables 5.1-2, 5.1-3, and 5.1-4, respectively.

When the gun is operated in a blow-back breech and blow-forward barrel configuration, to be discussed in Section 7.1.2.4, the potential exists for the barrel to begin to blow-forward prior to the pressure in the chamber becoming sufficient to achieve shot-start. In this event, the projectile will be constrained to move with the barrel prior to shot-start. In this configuration, (7.1-1) remains true; however, the sign of the bore resistance is reversed. The impact upon the computations are essentially trivial for all but the most unrealistic of gun parametric configurations. However, failure to explicitly tie the projectile to the barrel in this configuration will result in rearward traverse of the projectile relative to the barrel, confounding numerical implementation of the bore resistance profile of Table 5.1-4. This operation condition will be explicitly formulated in (7.1-14) of Section 7.1.2.5.

### 7.1.2 Equation of Motion for the Recoiling Mass

The equation of motion for a recoiling blow-back gun is more complicated than for a fixed breech gun. As described in Sections 5.2.3 and 5.2.9.1, the barrel motion of a gun, such as that depicted in Fig. 5.2-1, will include the blow-forward motion of the barrel and the blow-back motion of the inertial breech. The blow-forward motion is

imparted to the gun barrel by the chamber pressure acting upon the axially projected area of the “chambrage” cone at the neck of the cartridge case. (After venting, additional blow-forward motion may be imparted by the thrust generated by the expansion nozzle.) A simplified chamber geometry is presented in Fig 7.1-1 that also defines the projectile  $x_p(t)$ , gun chambrage  $x_{gc}(t)$ , and inertial breech  $x_r(t)$ , positions relative to an inertial reference frame that is coincident with the initial location of the inertial breech face. (Relative to Fig. 5.2-1 and Fig. 5.2-2, the face of the inertial breech is actually the front face of the cartridge cases head.)

The mass of the inertial breech and gun barrel configurations modeled for the 35mm demonstrator were listed in Table 5.5-3.

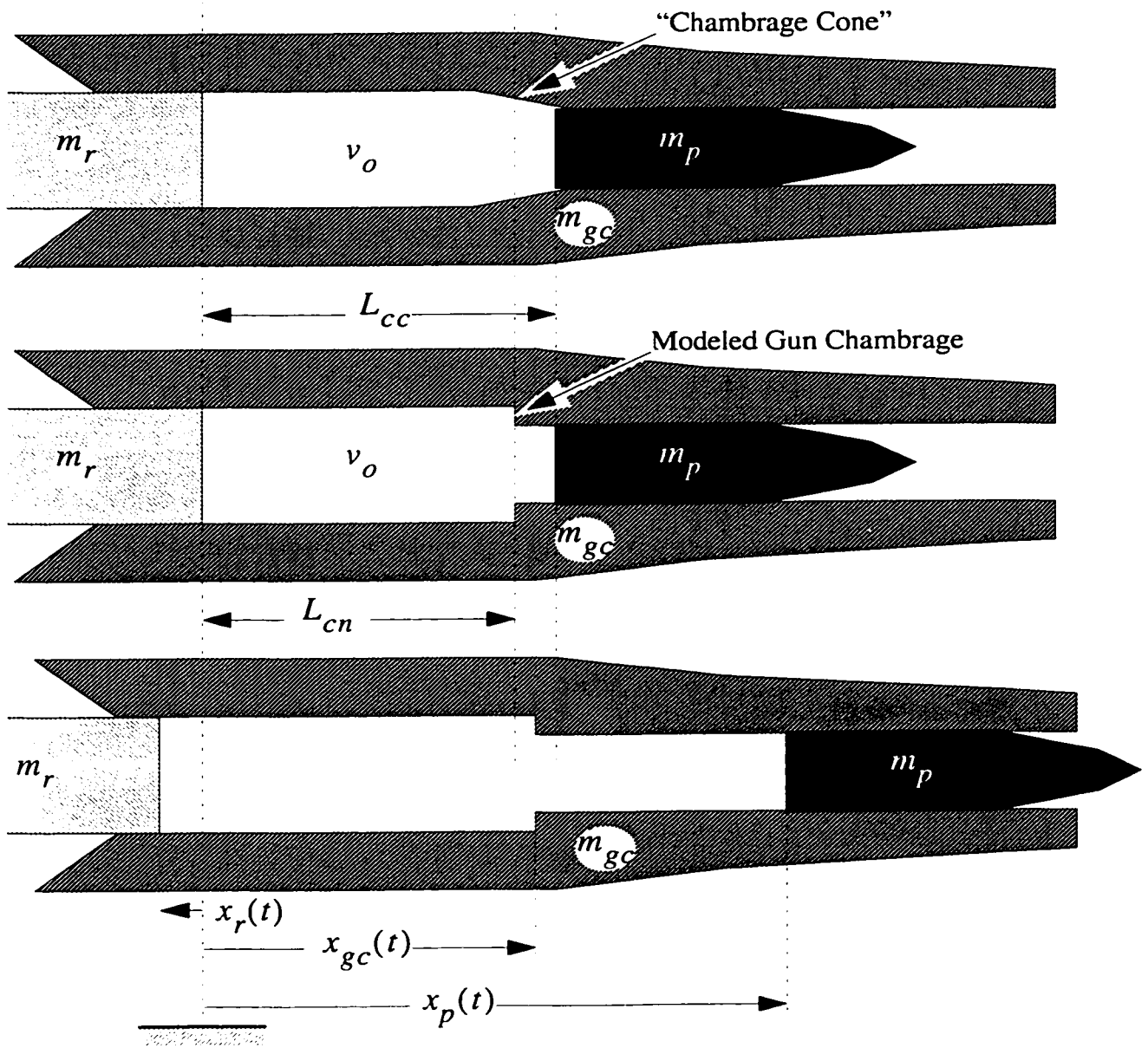


**Figure 7.1-1 Simplified Chamber Geometry and Inertial Reference Position Definitions**

The initial projectile and gun chambrage locations are defined by the cartridge case length  $L_{cc}$  and an equivalent length to the cartridge case neck  $L_{cn}$ . The length to the cartridge case neck is computed by matching the chamber volume as

$$L_{cn} = \frac{v_o - AL_{cc}}{A_c - A}, \quad (7.1-6)$$

where  $v_o$  is the chamber volume and the cross-sectional area  $A_c$  may be computed from the chamber diameter  $D_c$  as

$$A_c = \frac{\pi}{4} D_c^2. \quad (7.1-7)$$

The volume of the 35mm TP cartridge case is 367.25 cm<sup>3</sup> with a cartridge case length of 155mm as discussed in Section 5.1.3. The 55mm diameter of the cartridge case is listed in Table 5.1-2.

#### 7.1.2.1 Forces Applied to the Gun Barrel

The chamber pressure at the chambrage  $P_{gc}$  acting upon the projected annular area is the principal force applied to the gun barrel. Three frictional forces may also be present. Each of these forces will be normalized by the bore or chamber area so that they may be presented as equivalent pressures. First, the frictional bore resistance between the gun and bullet will pull the cannon barrel forward as the bullet is propelled

forward. Second, a recoil brake force  $F_{brake}$  may be included to maintain compatibility with Robbins [39] that will also generally apply a forward force. Third, a chamber/inertial breech resistance load  $F_{ib}$  may be developed between the chamber and the sliding inertial breech that will generally pull the barrel rearwards. Thus,

$$F_{gc} = P_{gc}(A_c - A) + (br + F_{brake})A - F_{ib}A_c. \quad (7.1-8)$$

The actual magnitudes for the breech resistance curve will be presented in Section 7.2.1.1.

#### 7.1.2.2 Forces Acting on the Breech

The forces applied to the breech result from the chamber pressure at the breech face, acting on the chamber area  $A_c$ , and the frictional load between the breech and the gun chamber. Thus,

$$F_r = -P_o A_c + F_{ib} A_c. \quad (7.1-9)$$

The actual magnitudes for the breech resistance curve will be presented in Section 7.2.1.1.

#### 7.1.2.3 Closed-Breech Recoil

When the gun is operated in a closed-breech mode, the breech and barrel are constrained to move with each other. In this case, the barrel chambrage forces and breech forces may be summed and divided by their common mass to compute the rearward recoil acceleration as

$$\dot{v}_r = \dot{v}_{gc} = (F_r + F_{gc}) / (m_r + m_{gc}). \quad (7.1-10)$$



Including the pressure gradient within the chamber between  $P_o$  and  $P_{gc}$  produces a minor enhancement to the recoil behavior of the gun relative to prior models [19,39]. To maintain absolute compatibility with these prior codes, the chamber diameter must be set equal to the effective diameter of the bore and the cartridge case length modified to match the chamber volume. This will eliminate the contribution of  $P_{gc}$  to the recoil motion.

#### 7.1.2.4 Blow-Back Recoil

When the breech and gun barrel are free to move independently, their accelerations may be computed as

$$\dot{v}_r = F_r/m_r, \quad (7.1-11)$$

$$\dot{v}_{gc} = F_{gc}/m_{gc}. \quad (7.1-12)$$

#### 7.1.2.5 Transitional Recoil

Shot-start is a reference to the minimum pressure at the base of the bullet required to overcome the bore resistance profile and commence acceleration of the projectile. For the 35mm TP cartridge this value has been presented as 4.48MPa in Table 5.1-4. Breech-start is a reference to the minimum pressure at the face of the breech required to overcome the breech resistance profile and commence rearward acceleration of the breech (blow-back) and forward acceleration of the barrel (blow-forward). The pressure required to initiate motion of the breech for the 35mm RAVEN demonstrator is

governed by the shear plug, which is designed to shear at 220MPa as discussed in Section 5.2.8.

If neither shot-start nor breech-start have occurred, all of the pressure forces developed within the chamber are in equilibrium. In this case, the accelerations of the components are

$$\dot{v}_p = \dot{v}_{gc} = \dot{v}_r = 0. \quad (7.1-13)$$

To provide for general operation of the model, an additional provision must be included when the breech-start pressure occurs prior to shot-start. In this configuration, the projectile is constrained to move with the barrel as discussed in Section 7.1.1. Thus,

$$\dot{v}_{gc} = \dot{v}_p = \frac{P_{gc}(A_c - A) + (P_b + F_{brake} - P_g)A - F_{ib}A_c}{m_p + m_{gc}}. \quad (7.1-14)$$

The appropriate equations for the four possible operational configurations are listed in Table 7.1-1.

**Table 7.1-1: Shot-Start and Breech-Start Configurations and Equations of Motion.**

Achieved Shot-Start?	Achieved Breech-Start?	Projectile Acceleration	Breech Acceleration	Gun Barrel Acceleration
No	No	(7.1-13)	(7.1-13)	(7.1-13)
Yes	No	(7.1-1)	(7.1-10)	(7.1-10)
No	Yes	(7.1-14)	(7.1-11)	(7.1-14)
Yes	Yes	(7.1-1)	(7.1-11)	(7.1-12)

### 7.1.3 Propellant Burning Rate

In general, a mixture of  $n$  propellant gases will occur within a gun. The atmospheric air within the cartridge case in and around the propellant grains prior to firing may be included [19], although it is often neglected as a small effect. For the model of the 35mm RAVEN demonstrator, two propellant gases will be included, the igniter and main propellant bed.

For the bed of propellant, a straight line fit of log burning rate versus log pressure results in a burn rate equation for the  $i^{\text{th}}$  propellant that may be considered reasonable for interior ballistic modeling [19,39,65,64]

$$\dot{r}_i = \beta_i \bar{P}^{\alpha_i} , \quad (7.1-15)$$

where  $\dot{r}_i$  is the regression velocity of the grains of the  $i^{\text{th}}$  propellant as driven by the space mean pressure  $\bar{P}$  and the burning rate coefficient and exponent are  $\beta_i$  and  $\alpha_i$  for the  $i^{\text{th}}$  propellant, respectively.

For modeling the 35mm TP round, the propellant bed burning rate coefficient and exponent are  $2.175\text{mm/s/MPa}^{0.78}$  and 0.78 respectively after ballistic matching as listed in Table 5.1-5.

Assuming a uniform density of each propellant grain, the mass fraction burning rate of the  $i^{\text{th}}$  propellant is

$$\dot{Z}_i = \frac{S_i \dot{r}_i}{V_{g_i}}, \quad (7.1-16)$$

where  $\dot{Z}_i$  is the mass fraction burning rate of the  $i^{\text{th}}$  propellant,  $S_i$  is the instantaneous value of the surface area of a grain of the  $i^{\text{th}}$  propellant, and  $V_{g_i}$  is the initial volume of a grain of the  $i^{\text{th}}$  propellant.

The fraction of mass burned of the  $i^{\text{th}}$  propellant may be integrated as

$$Z_i = \int_0^t \dot{Z}_i dt. \quad (7.1-17)$$

The depth of burn of the  $i^{\text{th}}$  propellant may be integrated as

$$r_i = \int_0^t \dot{r}_i dt . \quad (7.1-18)$$

#### 7.1.3.1 Propellant Ignition

Ignition of the propellant bed is achieved by a complete combustion of the igniter materials, commonly black powder, at the commencement of the interior ballistic model. The igniter may be considered the first of  $n$  propellant gases that occur within the gun. Thus, the mass fraction of the igniter burned,  $Z_1 = 1$  at the start of the interior ballistic model.

Successful ignition of the propellant bed is assumed by this burn model. As long as the propellant bed is exposed to finite pressure provided by the igniter, the bed will burn. Clearly, this is not physical, the outer surface of the grains must have reached a sufficient temperature for combustion to initiate. Modeling ignition is achieved through more advanced interior ballistic models, most notably the NOVA series authored by Gough [7]. The challenges of igniter design should not be underestimated. For the current effort, a standard ammunition cartridge was employed; therefore, it is known that ignition will reliably occur.

#### 7.1.4 Propellant Progressivity

It is often desirable to deter the peak pressure from occurring within the gun until after the projectile has begun traveling down the bore (see Section 3.2.1). As the projectile moves through the bore it increases the volume available for the propellant gases by  $x_p A$ . From the equation of state, to be presented later as (7.1-58), the projectile travel will tend to lower the pressure. The reduction in pressure will subsequently tend to decrease the burning rate (7.1-15). As the burning rate decreases, the projectile continues to gain speed, which tends to reduce the propellant gas pressure and burn rate further. Therefore, it is highly desirable to develop means that may tend to increase the rate of burning as the interior ballistics progress. There are two principal means to achieve this: grain geometries that increase surface area as they burn, and chemical inhibitors that slow burning through the outer layer of the grains.

##### 7.1.4.1 Form Function for Propellant

Propellant grain geometry can provide a favorable increase in exposed surface area as the grain is burned to mitigate the tendency for the mass fraction burn rate (7.1-16) to slow with projectile travel. Propellant grains that are engineered to cause burn rate to increase as the depth of burn increases are termed “progressive,” those that decrease burn rate with depth of burn are termed “digressive,” and propellant grains that maintain a constant burn rate with depth of burn are “neutral.”

Several grain geometries are depicted in Fig. 7.1-2.

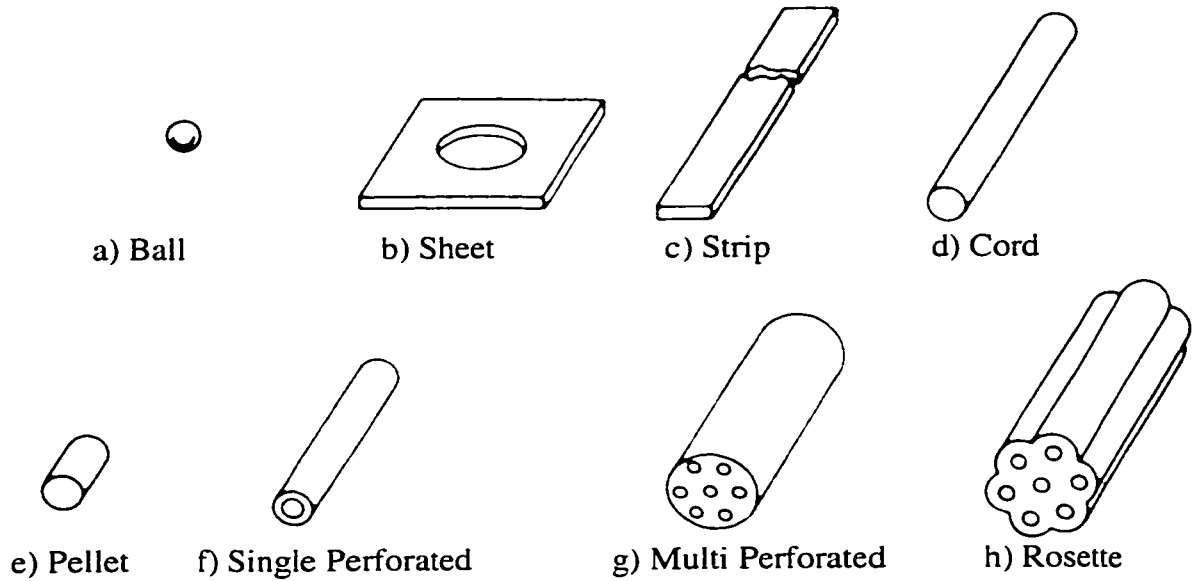


**Figure 7.1-2 Typical Shapes of Propellant Grains [21].**

The grain geometries of Fig. 7.1-2.a,c,d,e are digressive; that in Fig. 7.1-2.b is essentially neutral; and those in Fig. 7.1-2.f,g,h are progressive. For a cylindrical grain with a single perforation down the center, as depicted in Fig. 7.1-2.f, the following volume and surface area formulae result:

$$V_g = (L_g - 2r) \left( \frac{\pi}{4} [(d_o - 2r)^2 - (d_i + 2r)^2] \right), \quad (7.1-19)$$

$$S = (L_g - 2r) (\pi [(d_o - 2r) + (d_i + 2r)]) + 2 \left( \frac{\pi}{4} [(d_o - 2r)^2 - (d_i + 2r)^2] \right), \quad (7.1-20)$$

where  $V_g$  is the remaining grain volume; and  $L_g$ ,  $d_o$ , and  $d_i$  are the original length, outer diameter, and inner perforation diameter of the grain prior to the commencement of the burn, respectively, and  $r$  is the total depth of the burn (7.1-18).

The web of the grain is the dimension corresponding to the thinnest portion of the grain where burn surfaces intersect during a uniform burn. For ball, sheet, strip, cord, and pellet grains shown, respectively, in Fig. 7.1-2.a-f, the entire grain is consumed when the web is burned through. For these grains the web is the ball diameter, sheet thickness, strip thickness, cord diameter, pellet diameter, and for the single perforated grain it is the difference between the outer radius and inner radius.

The most common multi-perforated propellant geometry is that shown in Fig. 7.1-2.g, the seven perforation grain. The form function for this geometry becomes more complicated after “splintering.” This occurs when the depth of burn from the inner perforation and the outer diameter meet causing the cylindrical grain to break up into 12 smaller pieces. Note, since maximum progressivity is attained prior to splintering, virtually all multi-perforation grains incorporated equal distances between perforations and the outer surface such that major and minor splintering occur at the same time as depicted in Fig. 7.1-3. The intent behind the rosette geometry of Fig. 7.1-2.h is to eliminate the major splinters, although no major U.S. gun systems have incorporated such a grain geometry.



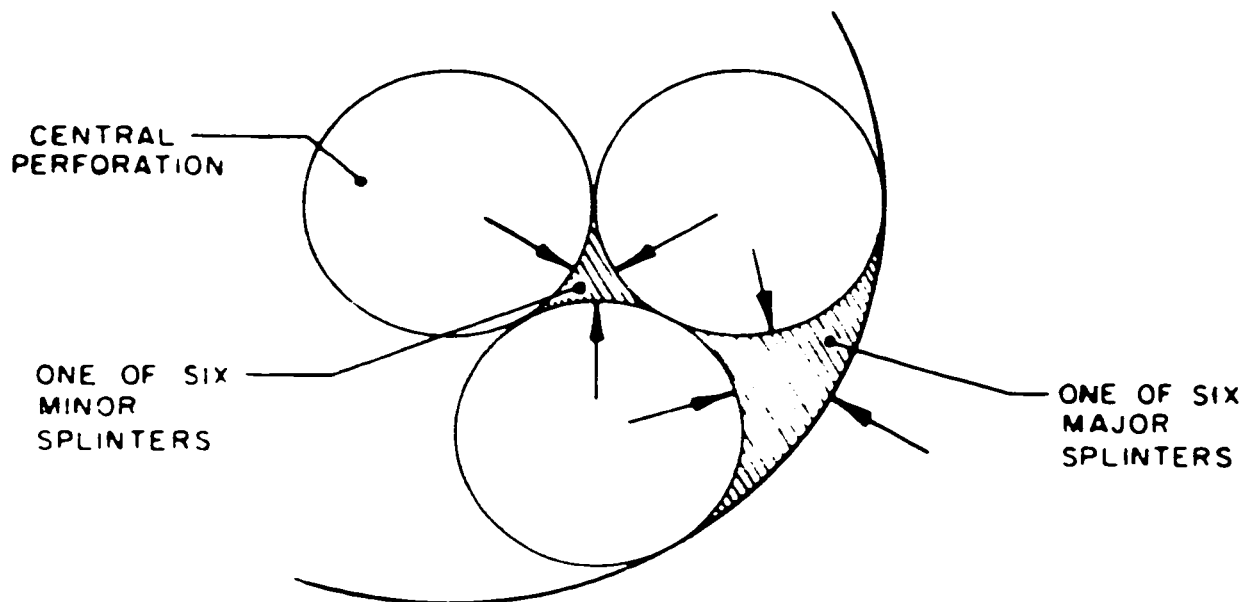


**Figure 7.1-3 Splinters Resulting From a Seven Perf Grain [19].**

#### 7.1.4.2 Inhibited Propellants

An alternative to controlling the burn rate by means of propellant grain geometry is to manufacture propellant grains whose burn rate is a function of burn depth [66]. Typically applied during the manufacture of a single perforation grain, the outer diameter of the grain will be endowed with a deeper deterrent depth than the inner diameter of the grain. Combustion gases evolve from the deterred layer with somewhat less energy than the remainder of the propellant grain. However, the deterrent's dominate role is one of slowing the burn rate, until the deterred layer is burned through.

Stiefel conducted a systematic study of deterred propellants, cataloging their effects [23]. As most propellant manufacturers maintain the exact characteristics of their

propellants proprietary this information is of value for the current objective of modeling the deterred Oerlikon proprietary propellant used by the 35mm TP round. Although the Oerlikon propellant was not included, a similar geometry grain, IMR 5010, was included. This propellant had a deterred depth of approximately 130  $\mu\text{m}$  on the outer diameter and half that on the inner perforation. The adiabatic flame temperature was decremented from 3094K to 2593K. A relation between burn rate and flame temperature indicated a 25% reduction in burn rate.

The effect may be modeled by simply slowing the burn rate of (7.1-15) by the ratio of the inhibited to non-inhibited burning rate coefficient. Since this model does not include the loss in chemical energy of the inhibited layer, some compensation may be achieved by decreasing the burn rate slightly more, perhaps to 70% of the undeterred rate. If this model is employed a modified form function may account for the inhibited layer.

First, assume the burn rate may be decremented by pre multiplication by some value  $\phi$  such as 70%. Further assume that the deterrent depth  $p_d$  on the inner diameter of the perforation and the ends is half that of the outer diameter  $y_d$ . This is in keeping with the experimental findings of Stiefel [23]. A means to account for the decreased rate of burning, is to decrement the total depth of burn  $r$ . Define the reciprocal of the burn rate decrement as

$$\alpha = \frac{1}{\phi}. \quad (7.1-21)$$

The depth that an undeterred propellant grain would have made in the same time it takes to burn through the deterred layer is

$$r_{od} = \alpha p_d, \quad (7.1-22)$$

$$r_{id} = \alpha y_d. \quad (7.1-23)$$

The actual depth of burn on the outer diameter of the grain prior to burn through is

$$p = \begin{cases} \varphi r, & \text{if } p < p_d \\ r - (\alpha - 1)p_d, & \text{if } p \geq p_d, \end{cases} \quad (7.1-24)$$

$$y = \begin{cases} \varphi r, & \text{if } y < y_d \\ r - (\alpha - 1)y_d, & \text{if } y \geq y_d, \end{cases} \quad (7.1-25)$$

$$Vg = (L_g - 2p) \left( \frac{\pi}{4} [(d_o - 2y)^2 - (d_i + 2p)^2] \right), \quad (7.1-26)$$

$$S = (L_g - 2p) (\pi [(d_o - 2y) + (d_i + 2p)]) + 2 \left( \frac{\pi}{4} [(d_o - 2y)^2 - (d_i + 2p)^2] \right). \quad (7.1-27)$$

As discussed, the propellant grains for the 35mm TP round will be modeled by means of this deterred layer model using an outer deterrent depth of 130  $\mu\text{m}$  and a burning rate in the deterred layer that is 70% of the value for the bulk material.

#### 7.1.5 Gas Property Gradient Model

Most lumped parameter interior ballistic codes are based on a formulation due to Lagrange in 1873 [22]. The gas velocity at any position of the expanding gas column during interior ballistics is equal to the projectile velocity multiplied by the ratio of gas behind the position in question and the total volume behind the projectile. As a special case of this formulation, it is assumed that no axial density gradient exists within the gas column. It is further assumed that the gases at the back of the gun have no recoil velocity.

It is remarkable, that this formulation has remained the back-bone of most interior ballistic codes until quite recently when the ratio of propellant to projectile mass approached and exceeded unity for current high-performance 120mm tank gun ammunition. For such applications, modifications to the classic Lagrange assumption have been called for [67] and created [68,69]. In addition, higher fidelity codes using finite volume techniques have been developed. Most notable among these are NOVA [70,7] and NGen [71]. Due the simplicity and utility of the Lagrange gradient, it will be used in this research as was done by Krier [64], Robbins [39], and Vottis [19].

It is desirable to alter the assumption often employed with the Lagrange gradient, that a chamber of greater diameter than the bore should be approximated as an elongated chamber of equal volume and bore diameter. This added chamber length will

impair the model fidelity of the right running rarefaction waves released by RAVEN venting. To this end, the volume behind the projectile and points along the gun will be used. Defining  $\Omega_p$  to be the total volume between the breech face and base of the projectile available for the gas column and  $\Omega(x)$  to be the volume between the breech face and an axial location  $x$  along the bore of the gun that is of interest, the ratio of volume behind  $x$  to that behind the projectile is

$$\eta|_x = \frac{\Omega(x)}{\Omega_p}. \quad (7.1-28)$$

Two other volumes of interest are the volume occupied by the unburned propellant grains, and that allocated to the co-volume of the gases. Recalling that in general, a mixture of  $n$  gases will occur within a gun

$$\Omega_{grains} = \sum_{i=1}^n \frac{(1 - Z_i)m_{ci}}{\rho_i}, \quad (7.1-29)$$

where  $\rho_i$ ,  $m_{ci}$ , and  $Z_i$  are the propellant grain density, total mass, and mass fraction burned for the  $i^{\text{th}}$  propellant, respectively. Density and mass values for the primer and propellant of the 35mm cartridge are listed in Table 5.1-5. The volume allocated to the co-volume may be determined as

$$\Omega_{co-volume} = \sum_{i=1}^n Z_i b_i m_{ci}, \quad (7.1-30)$$

where  $b_i$  is the co-volume of the  $i^{th}$  propellant. Co-volume and mass values for the primer and propellant of the 35mm cartridge are listed in Table 5.1-5.

#### 7.1.5.1 Pressure Gradient

The pressure distribution is [22]

$$P|_x = P_b + \frac{m_c}{2m_p} \left( 1 - \eta|_x^2 \right) (P_b - br - P_g). \quad (7.1-31)$$

In particular, the mean pressure of the gas column is [22]

$$\bar{P} = P_b + \frac{m_c}{3m_p} (P_b - br - P_g). \quad (7.1-32)$$

#### 7.1.5.2 Propellant Gas Density

Since the Lagrange gradient assumption assumes no spatial gradient in the density

$$\rho_g = \frac{\left( \sum_{i=1}^n Z_i m_{ci} \right)}{\Omega_p - \Omega_{grains}}. \quad (7.1-33)$$

### 7.1.5.3 Temperature Gradient

The distribution of the temperature of the gases may be computed by the equation of state, to be presented later as (7.1-59), using mass averaged gas properties

$$T|_x = \frac{\left(\frac{1}{\rho_g} - \bar{b}\right)P|_x}{\bar{R}}. \quad (7.1-34)$$

The mass-average properties require the determination of the mass of gas liberated from the propellant burn, which is

$$m_g = \sum_{i=1}^n Z_i m_{ci}. \quad (7.1-35)$$

Several mass-averaged properties may now be computed as follows:

$$\bar{b} = \left( \sum_{i=1}^n Z_i b_i m_{ci} \right) / m_g, \quad (7.1-36)$$

$$\bar{R} = \left( \sum_{i=1}^n Z_i R_i m_{ci} \right) / m_g, \quad (7.1-37)$$

$$\bar{\gamma} = \left( \sum_{i=1}^n Z_i \gamma_i m_{ci} \right) / m_g. \quad (7.1-38)$$

Property values for the primer and propellant of the 35mm cartridge are listed in Table 5.1-5.

#### 7.1.5.4 Sonic Speed Gradient

The local sonic velocity may be computed from the local temperature and the mass-averaged gas properties. Using the Nobel-Abel equation of state (7.1-59), the co-volume term may be incorporated as follows [22]:

$$c|_x = \frac{\sqrt{\bar{\gamma} \bar{R} T|_x}}{1 - \bar{b} \rho_g}. \quad (7.1-39)$$

#### 7.1.5.5 Velocity Gradient

By the Lagrange assumption, the velocity gradient increases from zero at the breech face, to projectile velocity at the base of the projectile, linearly with the volume ratio. This assumption ignores the recoil motion of the gases at the front face of the recoiling breech. The error in neglecting this term is small, considering recoil velocities are much smaller than projectile velocities.

It will prove convenient to assume a linear velocity gradient with respect to volume fraction from the recoiling breech velocity to the projectile velocity. To be accurate, the pressure gradient should be recomputed, based upon this rearward motion of



the gases next to the breech. However, the inaccuracies introduced into the kinetic energy estimation of the gas column are small, even for a relative fast inertial breech with a design velocity of 21.5m/s (5.2-2). This velocity is dwarfed by the muzzle velocity of 1175m/s listed in Table 5.1-2. If one were to try to model a Davis gun, however, the pressure gradient and kinetic energy of the gas computations would need to be modified. The velocity gradient is

$$v|_x = v_r + (v_p - v_r)\eta|_x. \quad (7.1-40)$$

#### 7.1.5.6 Mapping Axial Position to Volume

Using the chamber model of Fig. 7.1-1, the volume as a function of an inertial reference frame axial position may be computed. There are two factors, first the geometric volume available and second, the volume occupied by unburned propellant grains. Inherent in a lumped parameter model is the assumption that the gases are well mixed [64], including the propellant grains. Therefore, their contribution will cancel from the above gradient equations and it may be ignored.

The geometric considerations are driven by the nonlinearity of the assumed form of the chambrage. One could call the volume behind the chambrage the “chamber volume;” however, this would inevitably result in confusion with the cartridge case volume, therefore it will be awkwardly termed the “chamber-bore” volume. Since rearward recoil is negative, the distance from the chambrage to the front face of the breech is determined by subtracting the negative recoil stroke from the position of the chambrage to obtain

$$\Omega_{cb} = A_c(x_{gc} - x_r), \quad (7.1-41)$$

$$\Omega(x) = \begin{cases} A_c(x - x_r), & \text{if } x \leq x_{gc} \\ \Omega_{cb} + A(x - x_{gc}), & \text{if } x > x_{gc} \end{cases}, \quad (7.1-42)$$

$$\Omega_p = \Omega_{cb} + A(x_p - x_{gc}). \quad (7.1-43)$$

#### 7.1.6 Heat Transfer to Gun and Bullet

Heat transfer from the propellant gas by means of convective and conductive heating must estimate the temperature difference between the wall and the gas. The temperature rise of the surface of the bore is substantial during firing; thus, to model this energy exchange, an estimate of the wall temperature must be maintained.

A simplified model of the heat transfer from the propellant gases to the wall of the barrel may be made as follows: First, assume that only a thin portion of the inner wall is heated during the firing  $\tau_w$  and neglect the radial temperature gradient that may be anticipated in this thin wall. Second, assume the chamber geometry of the extended Lagrange chamber of bore area cross-section. Third, assume that no axial temperature gradient exists between within the fictitious thin-walled cylinder behind the projectile. Fourth, make the same approximation to the breech face area and projectile base area. Further, assume that the thermal properties of the projectile base are identical to that of the barrel wall. A typical value for  $\tau_w$  is 114.3  $\mu\text{m}$  for a 127mm gun [39]. (When modeling

the 35mm gun this value will be decremented to 82.9 $\mu$ m to reflect its smaller size and swifter firing.)

The total surface area presented for heat transfer from the propellant gases under these assumptions is [51]

$$A_w = 2A + \pi D_b \left( x_p - x_r + \left( \frac{A_c - A}{A} \right) (x_{gc} - x_r) \right). \quad (7.1-44)$$

Once again, rearward recoil is negative; therefore, the recoil motion of the breech increases the volume. The difference between the chamber diameter and the bore diameter results in the annular volume contribution between the gun chambrage and front face of the breech as depicted in Fig. 7.1-1.

The temperature of this wall at any point in time may be related to the combined thermal heating of the wall and the portion of the frictional energy imparted to the wall (and not the projectile), divided by its thermal capacity as

$$T_c = \frac{(E_h + fE_{br})}{C_{pw}\rho_w A_w \tau_w}. \quad (7.1-45)$$

where  $E_h$  and  $E_{br}$  are the integrated energies at any given time imparted by means of heat transfer (7.1-56) and bore resistance (7.1-52), respectively, and  $f$  is the ratio of bore resistance friction manifest as barrel heating. Vottis [19] presents an interesting method to estimate  $f$  based upon the shear moduli of the rotating band and barrel. Since the band

properties are unknown, and the ballistic solution is insensitive to this result, a value of one half was chosen for the 35mm RAVEN demonstrator.

The heat transfer coefficient is determined by means of a method attributed to Nordheim and Soodak [72,21,51]. As presented by Robbins [51], the heat transfer coefficient may be computed using mass averaged gas properties as

$$h = \lambda \overline{C_p} \bar{\rho} \bar{v} + h_o, \quad (7.1-46)$$

where  $h_o$  is an unknown coefficient of unknown derivation with a typical value of 11.35 J/(m<sup>2</sup>Ks) (which will be employed by the 35mm RAVEN demonstrator model) and  $\lambda$  is an empirical friction factor that may be computed as [21,51]

$$\lambda = (13.2 + 4 \log(D_b))^{-2}. \quad (7.1-47)$$

where  $D_b$  is the magnitude of the bore diameter expressed in meters. The heat transfer rate may now be expressed as

$$\dot{Q} = A_w h (\bar{T} - T_c). \quad (7.1-48)$$

The total heat transfer to the wall will be integrated in time in (7.1-56) of Section 7.1.7.8.

#### 7.1.7 Energy Sinks

The interior ballistic model presented by Robbins [51] numerically computes the interior ballistic state of launch by separating the chemical energy released by the

progress of the propellant burn to all of the energy sinks of the system. The thermal energy remaining in the gas after accounting for each of the sinks and the chemical source may be used to determine the mass average temperature of the gases. This may then be inserted into the equation of state (7.1-59) to determine the mean pressure within the total volume behind the projectile  $\Omega_p$ , which is known by (7.1-42).

#### 7.1.7.1 Energy Lost to Projectile Translation

The kinetic energy of the projectile may be expressed as

$$E_{pt} = \frac{m_p v_p^2}{2}. \quad (7.1-49)$$

#### 7.1.7.2 Energy Lost to Projectile Rotation

Approximating the rotational inertia as that of a uniform solid cylinder

$I = (m_p D_b^2)/8$  and recognizing that the angular rate of spin in radians is  $(2\pi v_p T_w)/D_b$ , the rotational energy may be computed as

$$E_{pr} = m_p \left( \frac{\pi v_p T_w}{2} \right)^2. \quad (7.1-50)$$

#### 7.1.7.3 Energy Lost To Kinetic Energy of Propellant.

Using the Lagrange gradient, without the special chamber geometry of Fig. (7.1-1), subject to the same small errors discussed in Section (7.1.5.5), the kinetic energy

of the propellant gas and entrained unburned propellant grains may be computed as [39,51]

$$E_p = \frac{m_c v_p^2}{6}. \quad (7.1-51)$$

#### 7.1.7.4 The Energy Lost to Projectile Friction

The energy lost to the forces generated between the projectile and bore due to engraving and friction may be integrated as

$$E_{br1} = A \int_0^t v_p b_r dt. \quad (7.1-52)$$

#### 7.1.7.5 The Energy Lost to Breech Friction

The energy lost to the forces generated between the breech and gun chamber due to friction may be integrated as

$$E_{br2} = A_c \int_0^t (v_{gc} - v_r) F_{ib} dt. \quad (7.1-53)$$

#### 7.1.7.6 The Energy Lost to Recoil Kinetic Energy

The kinetic energy of recoil may be attributed to both the inertial breech and gun barrel as

$$E_r = \frac{1}{2}m_r v_r^2 + \frac{1}{2}m_{gc} v_{gc}^2. \quad (7.1-54)$$

Note that if the gun is operated as an orthodox closed-breech gun, the gun and breech will recoil together which may be modeled as a single combined recoil mass recoiling at one velocity. However, (7.1-54) remains true regardless.

#### 7.1.7.7 Energy Lost to Air Resistance

If included in the model, the energy lost pushing the ambient gas ahead of the projectile may be expressed as

$$E_d = A \int_0^t v_p P_g dt. \quad (7.1-55)$$

#### 7.1.7.8 Energy Lost to Heat Transfer

The integral of the heat transfer from the hot propellant gases to the wall is

$$E_h = \int_0^t \dot{Q} dt. \quad (7.1-56)$$

#### 7.1.7.9 Sum of Energy Sinks

Summation of the energy sinks results in:

$$E_{snk} = E_{pt} + E_{pr} + E_p + E_{br1} + E_{br2} + E_r + E_d + E_h. \quad (7.1-57)$$

### 7.1.8 Equation of State

Due to the extremely high operating pressure of many modern guns (500MPa), the ideal gas equation of state is insufficient for accurate modeling of the gas dynamics. The Nobel-Abel equation of state is most often used in its place [19,39,64]. This equation of state modifies the ideal gas law by the inclusion of a co-volume term that is intended to correct for the volume occupied by the propellant gas molecules. The Nobel-Abel equation of state is equivalent to using the second virial coefficient [19]. It is also equivalent to using the van der Waals equation of state, neglecting the forces of intermolecular attraction [40]. (The van der Waals intermolecular attraction forces are of interest for rarefied gas dynamics that are decidedly not present within a gun.) Thus, pressure is determined by an equation of state in the form of:

$$P(V - b) = RT. \quad (7.1-58)$$

where  $P$  is the gas pressure,  $V$  is the mass specific volume available for the gases,  $b$  is the covolume term,  $R$  is the gas constant per unit mass for the gas in question, and  $T$  is the temperature.

In general, a mixture of  $n$  gases will occur within a gun, each independently obeying the equation of state. Using the gun volume definitions of (7.1-29), (7.1-30), and (7.1-43) results in



$$\bar{P} = \frac{\left( \bar{T} \sum_{i=1}^n R_i m_{ci} \right)}{\Omega_p - (\Omega_{grains} + \Omega_{co-volume})}, \quad (7.1-59)$$

where  $\bar{P}$  is the space-mean pressure,  $\bar{T}$  is the mean temperature of the mixture, and  $R_i$ ,  $m_{ci}$ , and  $b_i$  are the mass specific gas constant, mass, and co-volume of the  $i^{\text{th}}$  propellant gas, respectively.

The mass specific gas constant for the  $i^{\text{th}}$  gas may be determined by dividing the universal gas constant  $R_u$  with an accepted value of 8,314 J/kmol/K by the molecular mass  $m_{mi}$  of the  $i^{\text{th}}$  gas

$$R_i = \frac{R_u}{m_{mi}}. \quad (7.1-60)$$

The molecular mass of common propellants is near 25kg/kmol as listed in Table 3.1-1. The gas properties for the igniter and propellant to be used in the modeling of the 35mm demonstrator are listed in Table 5.1-5.

#### 7.1.9 Determination of Mean Temperature

The mean propellant gas temperature may be determined by an energy balance of the chemical energy liberated and the distribution of this energy to the various energy

sinks of Section 7.1.7. The difference between the two will manifest as heat developed within the gases themselves.

The total energy liberated,  $E_{chem}$  by burning may be computed as the product of the mass fraction of propellant burned using (7.1-17) and its specific chemical energy using (3.1-6)

$$E_{chem} = \sum_{i=1}^n (U_{oi} Z_i m_{ci}) = \sum_{i=1}^n \left( \frac{F_i}{\gamma_i - 1} Z_i m_{ci} \right). \quad (7.1-61)$$

The temperature may be determined by dividing the chemical energy released (7.1-61) minus the sum of the energy sinks (7.1-57) by the mass averaged constant volume heat capacity and the mass of propellant gas liberated (7.1-35). The mass averaged constant volume heat capacity may be determined by combining (3.1-4), (7.1-37), and (7.1-38) to obtain

$$\bar{T} = \frac{E_{chem} - E_{snk}}{\left( \frac{\bar{R}}{\gamma - 1} \right) m_g}. \quad (7.1-62)$$

#### 7.1.10 Integration

Execution of the interior ballistic code formulated above may be achieved through a simple incremental time marching solution using Euler's method [19,39]. A step size of 5  $\mu s$  provides ample numerical stability.

Integration is continued as long as the projectile remains within the launcher. Once the projectile has left the muzzle and the integration is terminated. The projectile is within the launcher provided

$$x_p - x_{gc} \leq L. \quad (7.1-63)$$

#### 7.1.11 Determination of Right Running Characteristics

Right and left running characteristics travel at the local gas velocity plus or minus the sonic speed for an inviscid flow as governed by the Euler equations [4]. Of principal interest to RAVEN is the right running characteristic released by the chamber venting. The velocity and position of the rarefaction wave front may be computed after first determining the volume of propellant gas behind it (7.1-42) as

$$\Omega_{rwf} = \begin{cases} A_c(x_{rwf} - x_r), & \text{if } x_{rwf} \leq x_{gc} \\ \Omega_{cb} + A(x_{rwf} - x_{gc}), & \text{if } x_{rwf} > x_{gc} \end{cases}, \quad (7.1-64)$$

and then its ratio to the volume behind the projectile (7.1-28) as

$$\eta_{rwf} = \frac{\Omega_{rwf}}{\Omega_p}. \quad (7.1-65)$$

The sonic speed at the wave front may be determined from (7.1-31), (7.1-33), (7.1-34), and (7.1-39) as

$$c_{rwf} = \frac{\sqrt{\bar{\gamma}(\rho - \bar{b}) \left( P_b + \frac{m(1 - \eta_{rwf}^2)(P_b - br - P_g)}{2m_p} \right)}}{(1 - \bar{b}\rho)}. \quad (7.1-66)$$

Combining the sonic and gas velocity contribution, the velocity of the right running characteristic may be computed as

$$v_{rwf} = c_{rwf} + v_r + \eta_{rwf}(v_p - v_r). \quad (7.1-67)$$

The location of the rarefaction wave front may be integrated as

$$x_{rwf} = \int_{t_v}^t v_{rwf} dt + x_r(t_v),$$

where  $t_v$  is the time at which the venting commences.

## 7.2 Modeling the 35mm Test Fixture

The parameters used in the interior ballistic simulation have already been presented in the preceding tables and text. In particular, in each Section of the model development the parameters were identified or earlier tables were referenced.

### 7.2.1 Ballistic Matching

As mentioned in the footnote of Table 5.1-5, the adiabatic flame temperature, and burn rate exponent have been slightly altered to achieve ballistic matching. In

addition, the wall thickness for heat transfer was reduced as discussed in Section 7.1.6. This topic is discussed at length by Baer [65].

The interior ballistic model is intended to model the inside of the gun and enable interpolation and extrapolation of the sensor data collected from the firings. From this model we may compute the rarefaction wave speed within the gun, despite our lack of temperature and gas velocity sensory information.

When developing a new gun and ammunition system it is, of course, desirable to achieve predictive capability with the model. In the case at hand, the unknown chemical composition of the proprietary propellant chemistry and deterred layers simply introduce too many degrees of freedom. As with any form of extrapolation, the fidelity of the model may be anticipated to remain high for parametric configurations similar to the test gun and decline as the parametric configurations diverge from the tested system.

The model was ballistically matched by considering two performance factors: the muzzle velocity and the maximum chamber pressure. In addition, an effort was made to limit the number of parameters considered for adjustment and attention was paid to ensure that the results were plausible.

To match the model to the experiment, the flame temperature was reduced by 9% and the burn rate was increased by nearly 10%. In addition, the wall thickness of the bore for the heat transfer computation was reduced by 27% from 114.3  $\mu\text{m}$  for a 127mm gun to 82.9  $\mu\text{m}$  for the 35mm gun as discussed in Section 7.1.6. Adjusting the burn rate is

very common as the burn law of (7.1-15) and experimental means to determine the parameters are both suspect [65]. There is some reason to believe that the flame temperature may be high as the limited communication on the Oerlikon propellant did indicate lower energy by a little under 10% than that of M1 Propellant [52]. However, to reduce the chemical energy would require either the force to be reduced or the ratio of specific heats to be increased, neither of which was done. The consequence of this fitting is a molecular mass of 20.1 kmol/kg. This is low. A non-public domain reference to M1A1 propellant indicates similar thermodynamic properties to the matched propellant with a molecular mass of 21.8 [54]; thus, the fitted value is low by about 8%. This is sufficiently close to a realistic value for the intent of this modeling.

The major results of the model are presented in Table 7.2-1.

**Table 7.2-1: Results of Closed-Breech Interior Ballistic Model.**

Muzzle Velocity	1175m/s
Max Chamber Pressure	425MPa
Time of Inner Deterred Layer Burn Through	1.19ms
Time of Outer Deterred Layer Burn Through	1.61ms
Time of Propellant Burn-Out	3.58ms

Relative to the expectations of Table 5.1-2, the muzzle velocity has been matched but the pressure is 11% high. The peak pressure is subject to greater error as it is very sensitive to the burning model of the deterred grain, which, as stated earlier, is oversimplified and lacking accurate thermo-chemical properties [65]. Also, the measured

pressures from the testing were often higher than the value listed in Table 5.1-2 and subject to test variation of approximately 10%. Thus, there is uncertainty regarding both the magnitude of the model parameters that effect the peak pressure and the peak pressure that should be attained. Therefore, continued tuning of the model in an attempt to better match the anticipated peak pressure is not warranted.

The time of propellant burn-out is listed to confirm that the propellant did burn out. (It is not uncommon when ballistically matching to get otherwise acceptable results with unburned propellant ejected from the gun. While such a design could occur in practice, it would clearly be suboptimal.) The propellant burnout and deterred layer burn through times are also of interest to explain seemingly anomalous behavior in the plots of the interior ballistics at these times. When the deterred layers are burned through, the power of the burn instantaneously increases resulting in an increase of the pressure time slope that is often discernible. Similarly, when the cylindrical grains burn through their web, the power loss is very abrupt as the substantial surface area exposed for burning vanishes, resulting in a discernible reduction in the pressure time slope.

#### 7.2.1.1 Matching Vent Time

To accurately mimic the vent timing of the RAVEN test demonstrator, a very simple inertial breech resistance curve was empirically developed. Examination of the sheared off web of the shear plugs reveals that the shearing action is not “clean.” Therefore, a simple linear ramp of friction as a function of displacement was applied over the 10mm width of the shear web. It was found that ramping from an initial value of 64%

of the 220MPa shear force (expressed as an equivalent pressure) determined in Section 5.2.8 to zero over the 10mm stroke was sufficient to match the results. It is also a plausible, albeit simplified, model of what is actually occurring.

### 7.2.2 Pressure Time and Pressure Travel Curves

The pressure time curve of Fig 7.2-1 depicts pressure at various location per the left ordinate, and the position of the projectile base versus time per the right ordinate. The pressure curves include all of the barrel pressure probe locations outlined in Table 5.5-1. The magnitudes of the pressures of the probes ahead of the projectile remain zero until the projectile passes. Only the chamber probe has finite magnitude from the start of the ignition process. Thus, beginning with the chamber probe as P1 per the nomenclature of Table 5.5-1, the next probe is P2, and so on until P13 is reached. P14 is not displayed because the projectile exits the muzzle at that probe, and the model ceases to continue at shot-exit. The double hump behavior near peak pressure is caused by the burn through of the outer deterred layer of the propellant grains. Once through this layer, the burn rate increases substantially; with the model indicating that prior to burning through the layer, the rate of energy expended by the gas expansion was exceeding the rate of energy introduced by burning.



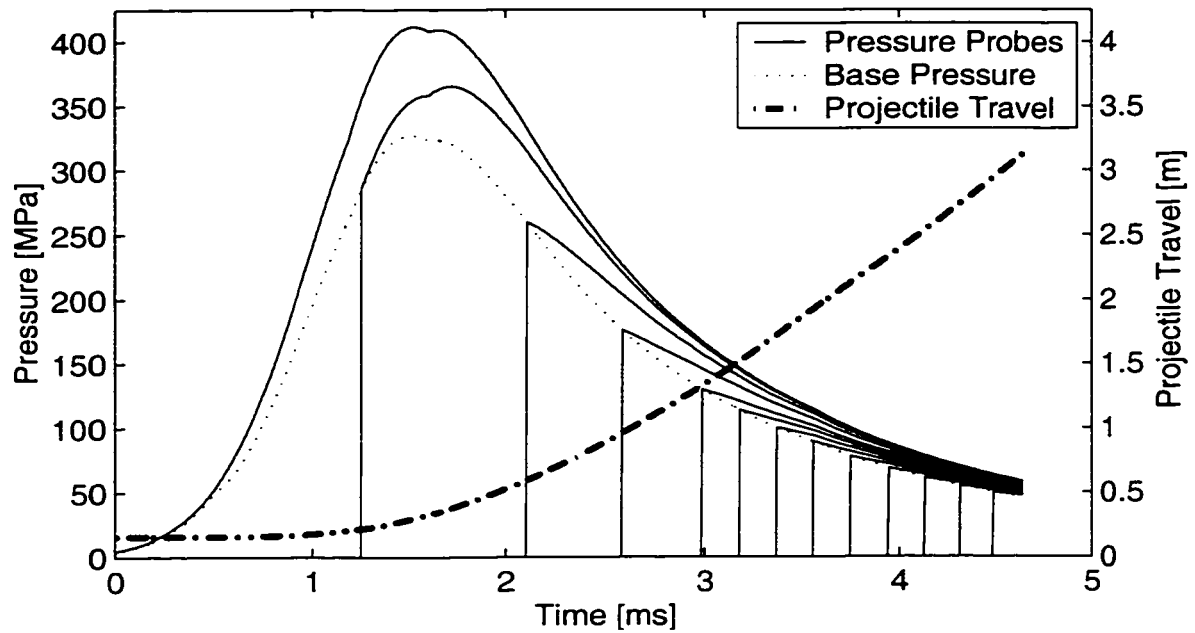


**Figure 7.2-1 Pressure and Travel Versus Time for 35mm Closed-Breech Gun.**

One may consider a pressure time plot to be the momentum domain where areas under the curve correspond to area specific momentum. An alternative view is the pressure travel plot, where the pressure is plotted as a function of projectile translation. Thus, this may be interpreted as an area specific energy domain.

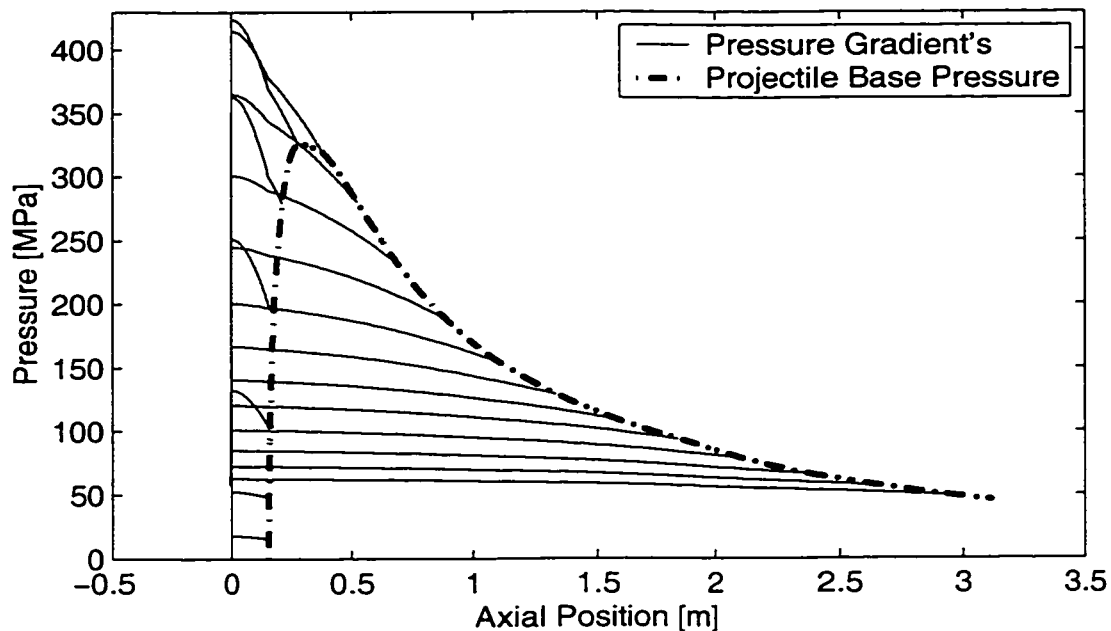


**Figure 7.2-2 Pressure and Travel Plot for the 35mm Closed-Breech Gun.**

The spatial pressure gradient is clearly depicted in Fig. 7.2-2. The increased gradient within the gun chamber results from mapping of the Lagrange pressure gradient of (7.1-31) to volume (7.1-42) by means of the approximated chamber geometry of Fig. 7.1-1. Since the barrel is massive, it doesn't move appreciably relative to the plot of Fig. 7.2-2. The gradient is most pronounced when the bullet (and propellant gas column) is subject to the greatest acceleration.

### 7.2.3 Energy Considerations

As is typical of any dynamic simulation, the best location to look for unrealistic model behavior is by tracking the energy. A table of typical values for a medium caliber gun based upon a Navy manual from the early 1960's is included within

[64]. The values of this table are listed with values generated by the interior ballistic model presented.

**Table 7.2-2: Relative Magnitudes of Model Energy Sinks**

Energy Sink / Total Chemical Energy	Typical	Model
Projectile Translation, $E_{pt}$	32.00%[64]	32.30%
Projectile Rotation, $E_{pr}$	0.14% [64]	0.20%
Projectile Friction, $E_{br}$	2.17% [64]	1.38
Recoil Energy, $E_r$	0.12% [64]	0.11
Propellant Motion, $E_p$	3.14% [64]	6.56
Ratio of Thermal Loss To Projectile Energy, $\Upsilon$	30% (Table 4.2-1)	23.17

The disparity in the energy expended upon propellant motion may be readily explained. The 35mm TP round is faster than the “typical” medium caliber gun. Anti-Aircraft guns are typically of higher performance than standard guns. Therefore, it has a greater ratio of propellant to projectile mass. Using the arguments of Section 7.1.7.3, it may be estimated with reasonable confidence that the difference in propellant to projectile mass ratio for the two guns is equal to  $E_p$  for the two systems. Thus, the tabulated gun has about half the propellant of the 35mm TP round. Using the Ogorkiewicz relation of (3.2-1), we may anticipate the tabulated gun to have approximately half the muzzle energy of the 35mm TP round with a predicted muzzle velocity of 864m/s. This value is 4%

higher than the value listed for Navy Guns such as the MK1 and MK2 based upon a 20mm Oerlikon design [73]. This also explains the disparity in friction. Since friction is not supposed to increase substantially with velocity, the energy lost to friction from a fast gun should be comparable to that of a slower gun. Since the kinetic energy of 35mm TP round gun is nearly double, the ratio of friction to projectile kinetic energy may be anticipated to be half.

#### 7.2.4 Determination of Right Running Characteristics

Using the relations developed in Section 7.2.4, the propagation of rarefaction wave fronts within the gun tube may be computed. An interesting vent timing is achieved when the rarefaction wave front released from the breech of the gun just reaches the base of the bullet as the bullet exits the muzzle. Such a timing may be termed “synchronized.”

Determination of the synchronized rarefaction wave front may be made by back-propagation of the wave from the muzzle (backwards in time) until it reaches the front face of the breech. Thus, the integration method of Section 7.1.10 may be run in reverse. The result of this computation for the closed-breech gun is depicted in Fig. 7.2-3.

The model indicates that a rarefaction wave released after the projectile has only traversed 35.3% of its travel will not catch the bullet prior to shot-exit. This continues to be an astonishing result.

As discussed in Section 7.1.11, the speed of the rarefaction wave front is determined by a summation of the local gas velocity and the local sonic velocity. These are depicted in Fig. 7.2-3.b. The gas velocity contribution begins at the rearward velocity

of the breech face, about  $-2.3\text{m/s}$  in this case, per (7.1-40). It rapidly rises through the chamber. Since the smooth chambrage of the actual gun was approximated as an abrupt contraction as shown in Fig. 7.1-1, the gas velocity contribution abruptly changes slope as the chambrage is traversed. The gas velocity contribution to the rarefaction wave front continues to rise until it reaches the projectile velocity at the muzzle.

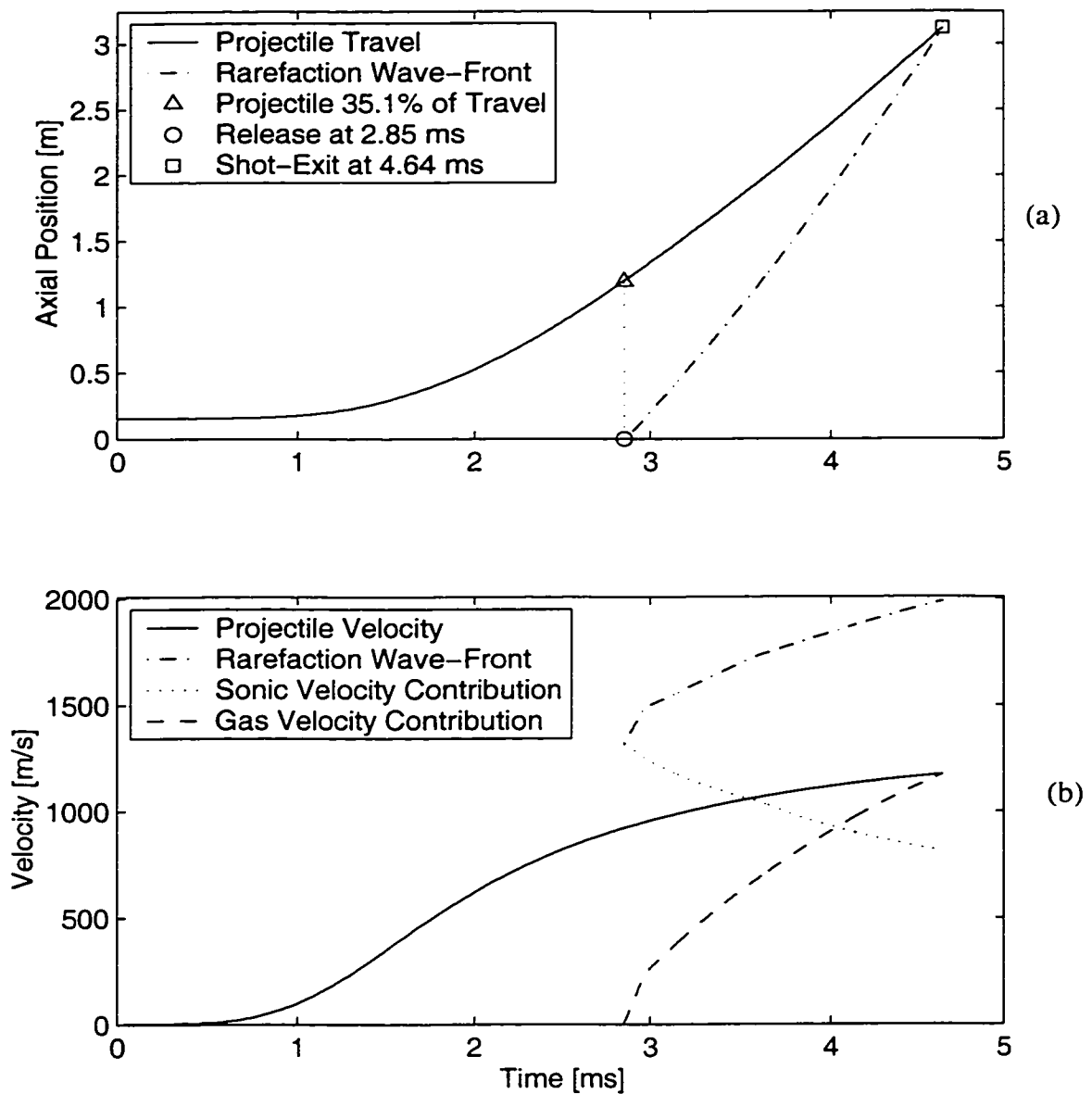


**Figure 7.2-3 Synchronized Rarefaction Wave Front Propagation (a) and Velocity Contributions (b).**

The sonic velocity contribution reflects the general trend of expansion cooling of the propellant gases. The abrupt change in the sonic velocity gradient at the mid-way

point is due to the sudden burnout of the propellant grains at this time as listed in Table 7.2-1.

### 7.2.5 Inertial Breech Behavior

The recoil motion of the blow-back inertial breech and blow-forward barrel was explicitly included in the interior ballistic model. The rearward recoil of the inertial breech is much more substantial than the closed-breech gun. This may be illustrated by examination of the pressure and travel plot for the light inertial breech operated gun.

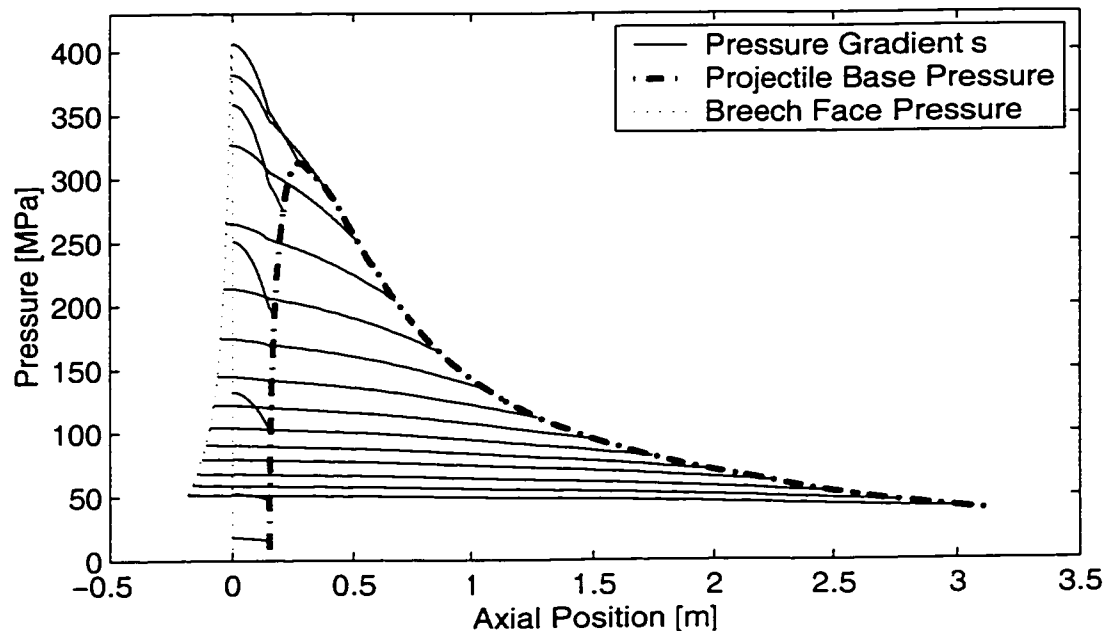


**Figure 7.2-4 Pressure and Travel Plot for the 35mm Light Venting Breech RAVEN.**

Note that the blow-back breech actually travels sufficiently to be discernible in the plot. The product of the integral under the breech face pressure curve and the chamber area constitutes the ballistic energy imparted to the recoil of the breech.

It is of particular interest to examine the behavior of the breech and barrel before and after the shear plug releases the breech. The recoil strokes are plotted in Fig. 7.2-5, while the recoil velocity is plotted in Fig. 7.2-6. It is clear that the barrel is first dragged rearwards by the close-breech behavior of the gun prior to the shearing. Once released, the breech swiftly accelerates rearwards, while the barrel accelerates forwards.



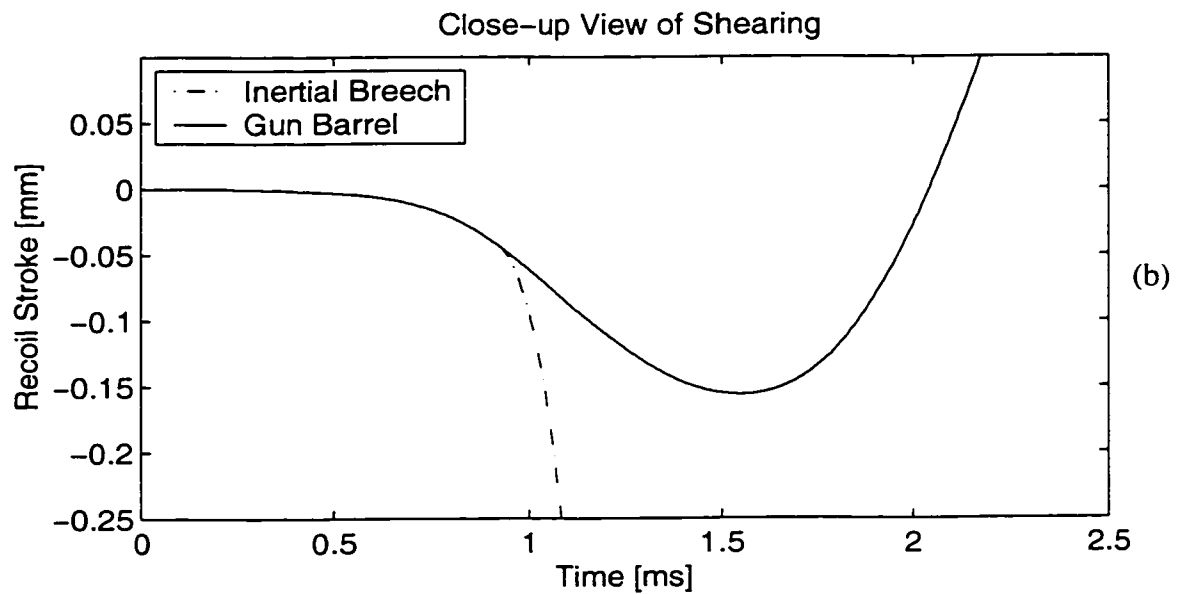
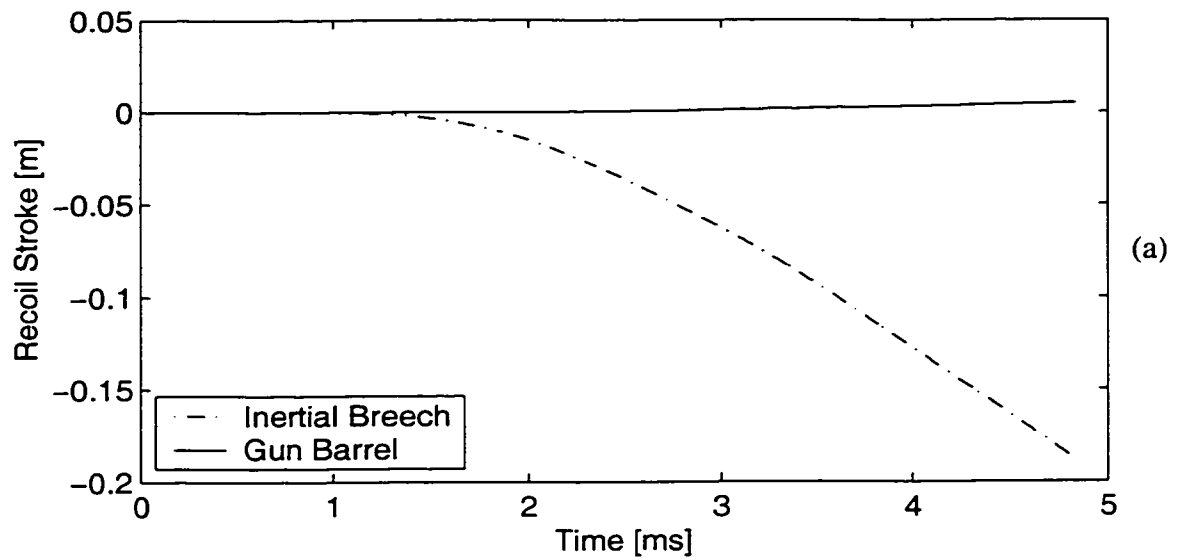


**Figure 7.2-5 Recoil Motion of Light Inertial Breech and Gun Barrel (a) and Close-up of the Shearing Action (b).**

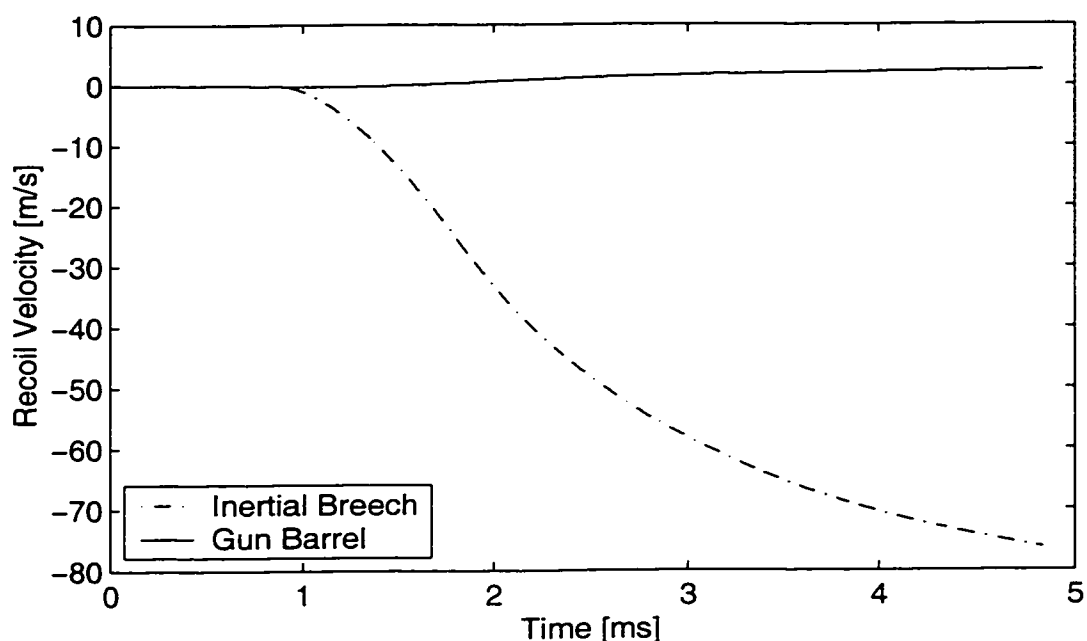


**Figure 7.2-6 Recoil Velocity of Light Inertial Breech and Barrel.**

The loss in muzzle velocity and maximum pressure that may be anticipated to occur with an inertial breech gun relative to that of a closed-breech gun are listed in Table 7.2-3.

**Table 7.2-3: Modeled Muzzle Velocity and Pressure For Inertial Breech Configurations.**

Configuration	Muzzle Velocity	Maximum Chamber Pressure
Closed-Breech	1175m/s	425MPa
Heavy Venting	1130m/s	414MPa
Light Venting	1095m/s	406MPa
Non-Venting	1124m/s	413MPa

## **Part 8**

# **DISCUSSION OF RESULTS**

Despite challenges in collecting data devoid of imperfections, the experimental results clearly verify the fundamental precepts of RAVEN. Recoil momentum imparted to the launcher was dramatically reduced without measurable reduction in muzzle velocity (non-venting inertial breech gun baseline). The magnitude of the reduction was consistent with the level of recoil reduction anticipated. The rarefaction wave was identified within the gun concurrently with the projectile. A dramatic reversal of the pressure gradient with the gun was detected behind the rarefaction wave front. Finally, the heating of the bore of the gun was substantially reduced.

### **8.1 Muzzle Velocity**

The measured muzzle velocities of Table 6.2-1 were in agreement with the anticipated muzzle velocity of the Oerlikon 35mm TP round listed in Table 5.1-2 and the lumped parameter model predictions of Table 7.2-3.

The experimental results included only one outlier, and otherwise resulted in a standard deviation of nominally 2%. No correlation could be drawn between geometric vent timing and muzzle velocity. Since it was the light inertial breech that provided the earliest venting, it would be the one most likely to suffer a reduced muzzle velocity as a result of the rarefaction wave overtaking the base of the projectile prior to shot-exit. Table 6.2-1 indicates the lowest muzzle velocity configuration for the light breech was the

intermediate vent. However, the slowest round was fired by the earliest vent configuration; thus, additional scrutiny is warranted and will be discussed in Section 8.7.

Since the lumped parameter model was ballistically matched to the orthodox configuration, the model's behavior for the inertial breech configurations relative to the orthodox configuration is of interest. The model indicated a muzzle velocity loss of 45m/s, 80m/s, and 51m/s for the heavy, light, and non-venting inertial breechs, respectively. The measured loss was 24m/s, 75m/s, and 54m/s. The trend was correct in all cases, and the prediction was very accurate for the later two breech configurations.

## **8.2 Peak Pressure**

Experimental results of peak pressure are questionable; particularly for the closed-breech configuration. As shown in Fig. 6.3-5, the measured muzzle velocity for the closed-breech was lower with increased measured peak pressure. This is not physical and may be attributed to instrumentation challenges in muzzle velocity measurement, pressure measurement, or both.

The experimental results for the inertial breech configurations was better behaved, with a positive relation between peak pressure and muzzle velocity. However, the standard deviations of nominally 10%, listed in Table 6.3-1, seem rather high.

It is surprising that seven of the configurations recorded a peak pressure in excess of 400MPa with the design pressure for the round listed as 383MPa in Table 5.1-2.

As discussed in Sections 6.1.3 and 6.3 the pressure data was subject to a downward drift that is not consistent with recording higher than actual pressures.

It is also interesting to note that no systems recorded a peak pressure between 350MPa and 380MPa. This is indicative of a different process occurring between the high pressure and low pressure shots as opposed to a normal distribution uncertainty.

### **8.3 Rarefaction Wave Traverse Tracking**

The projectile position and rarefaction wave front locations determined experimentally may be juxtaposed with the interior ballistic model by means of a time correlation to shot-exit. In the Figures that follow, the experimentally determined projectile passage times and rarefaction wave front passages for all of the shots of each configuration are presented. Thus, for a typical configuration, three sets of projectile travel and three sets of rarefaction wave passage are juxtaposed over the lumped parameter model.

Since the experimental results are discrete, corresponding to the axial location of the gauge, they will be plotted using “o’s” and triangles. The model results are plotted using lines, to distinguish them from the experimental results. This may cause confusion with the earlier experimental results presented in Section 6.3.6 that included polynomial fits to the experimental points. In the plots that follow, the lines are the model. That they may appear to be polynomial fits bodes well for their fidelity.

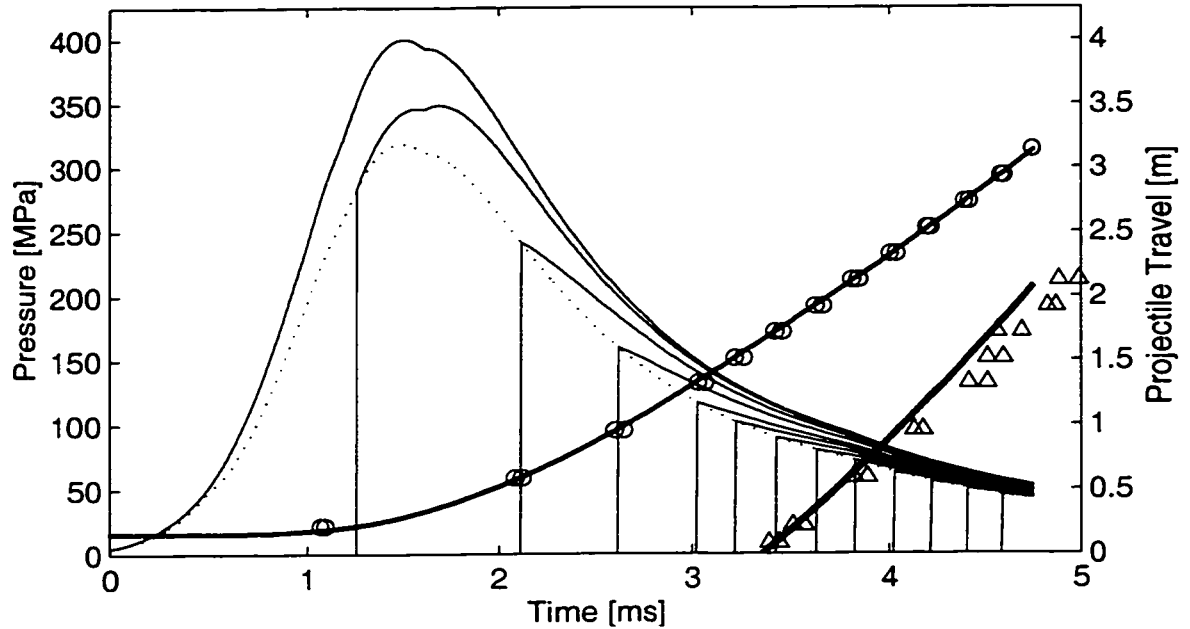


**Figure 8.3-1 Juxtaposition of Model and Experimentally Inferred Projectile and Rarefaction Wave Progression for the Heavy/Early Configuration.**

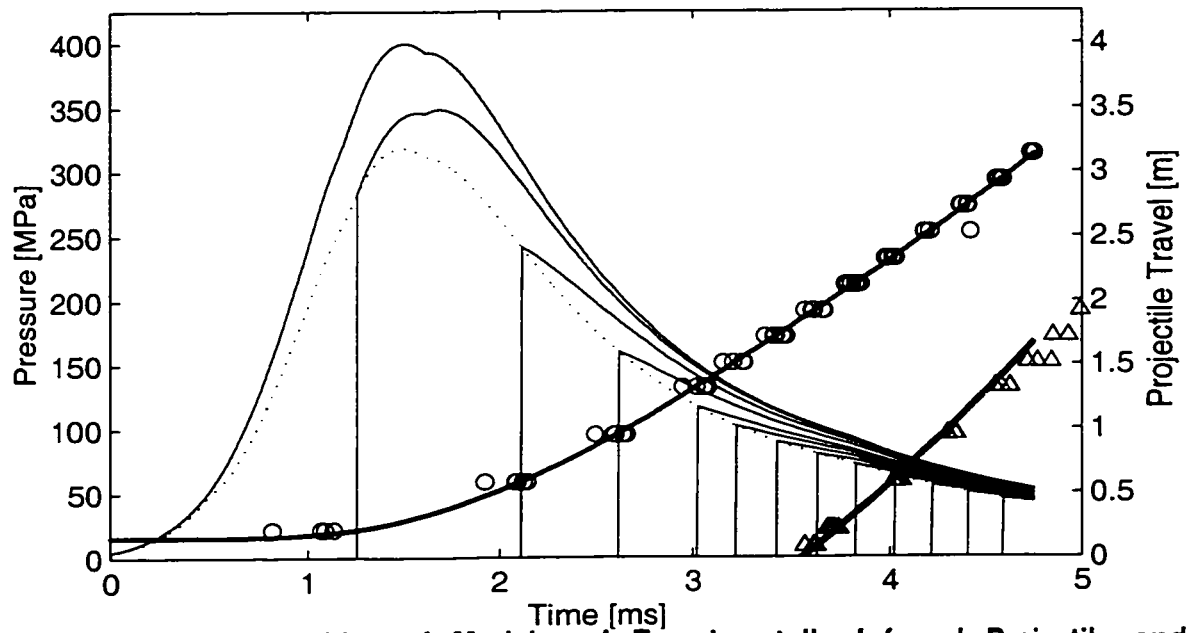


**Figure 8.3-2 Juxtaposition of Model and Experimentally Inferred Projectile and Rarefaction Wave Progression for the Heavy/Nominal Configuration.**

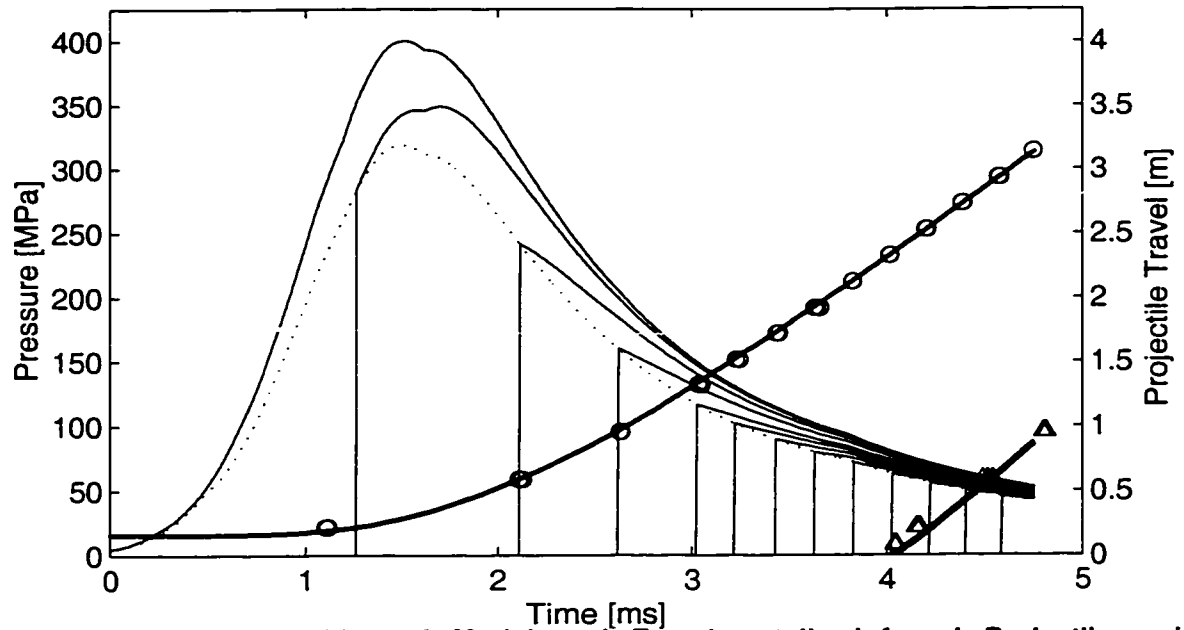


**Figure 8.3-3 Juxtaposition of Model and Experimentally Inferred Projectile and Rarefaction Wave Progression for the Heavy/Intermediate Configuration.**

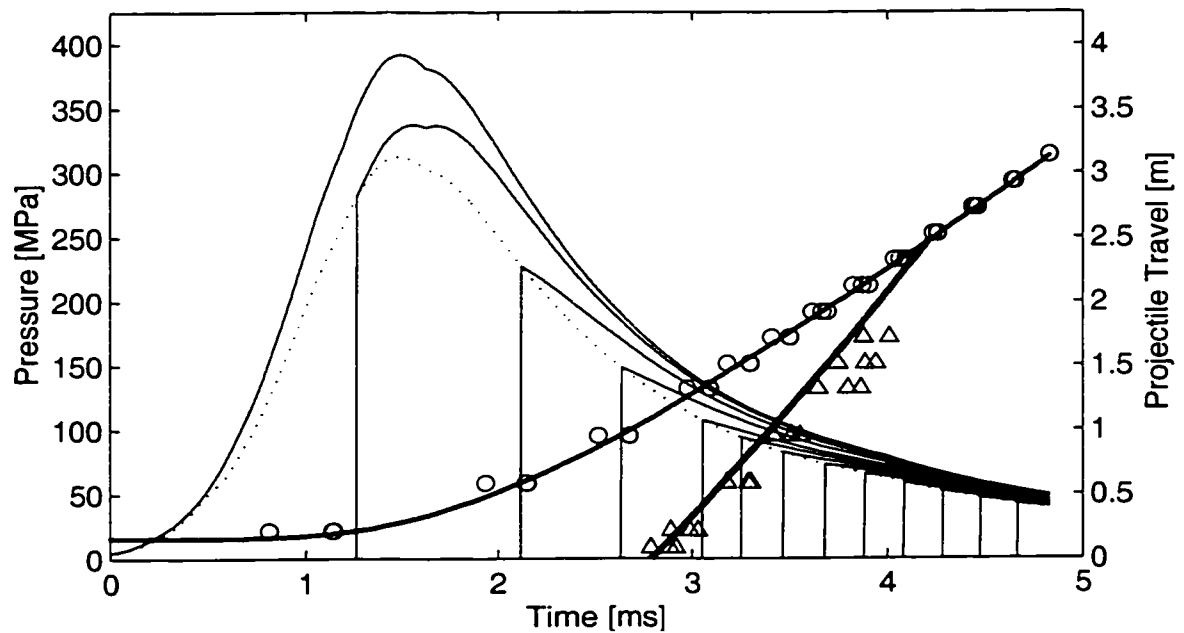


**Figure 8.3-4 Juxtaposition of Model and Experimentally Inferred Projectile and Rarefaction Wave Progression for the Light/Early Configuration.**

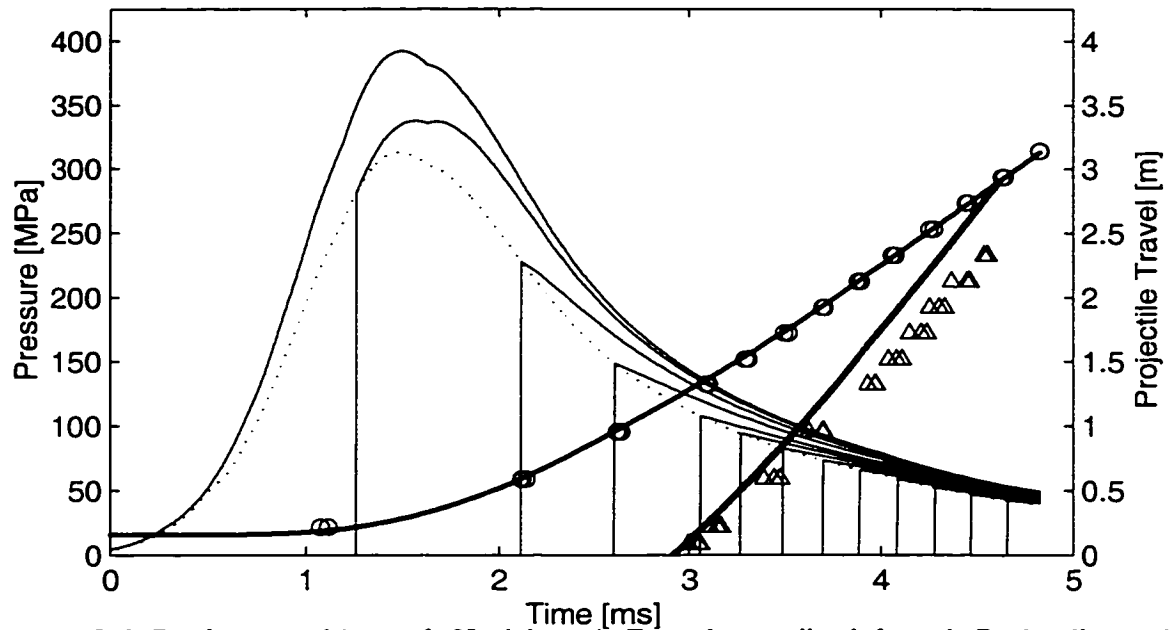


**Figure 8.3-5 Juxtaposition of Model and Experimentally Inferred Projectile and Rarefaction Wave Progression for the Light/Nominal Configuration.**

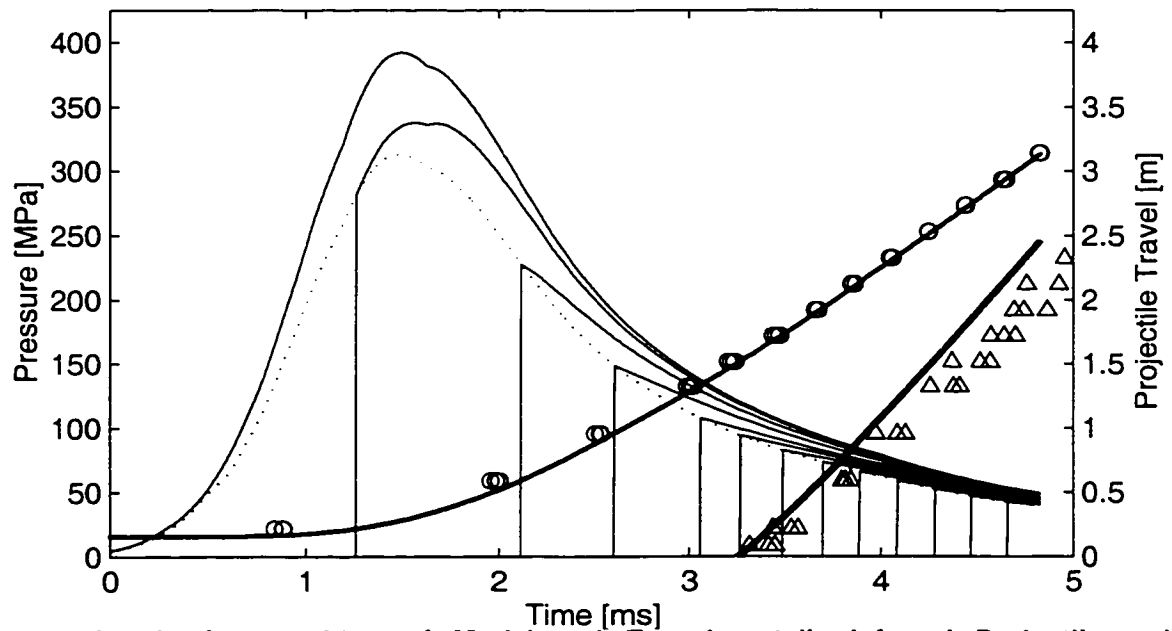


**Figure 8.3-6 Juxtaposition of Model and Experimentally Inferred Projectile and Rarefaction Wave Progression for the Light/Intermediate Configuration.**



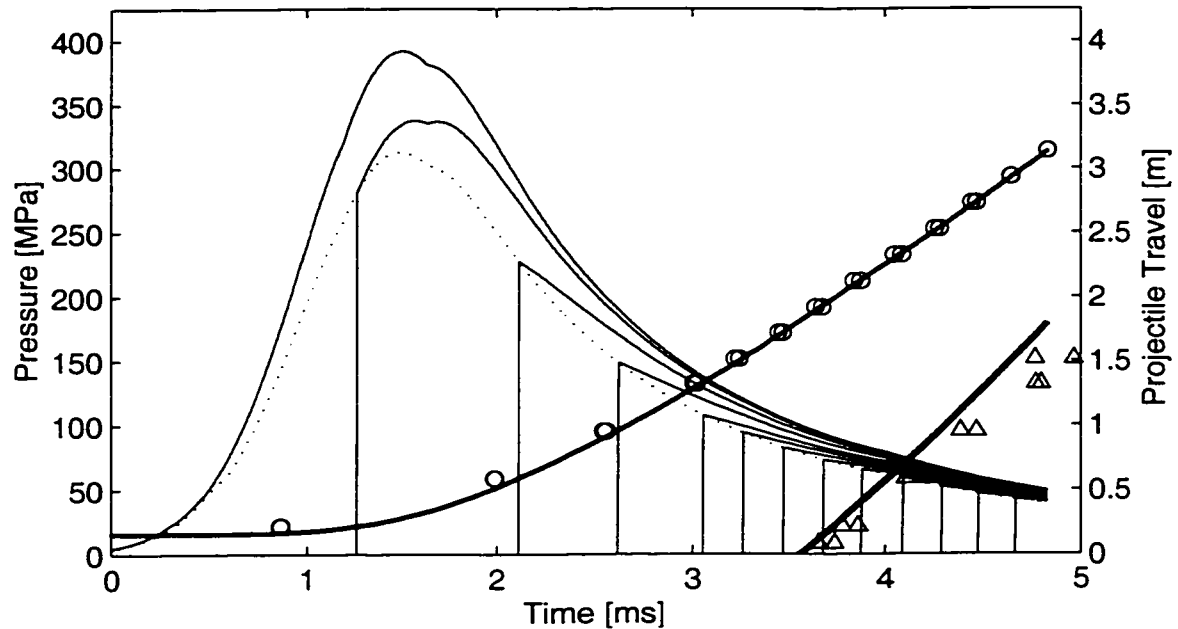


**Figure 8.3-7 Juxtaposition of Model and Experimentally Inferred Projectile and Rarefaction Wave Progression for the Light/Late Configuration.**

### 8.3.1 Vent Time

The vent release time determined by the ballistic model mimicked very well the actual test results. The incorporation of the custom chamber geometry of Fig. 7.1-1 appear to have worked well. While the vent release time was ballistically matched as discussed in Section 7.2.1.1, the matching was achieved by altering a single resistance parameter, relating to the friction of the shearing action. Two inertial breech's were matched at four geometric vent times. Thus, if the model was not soundly based upon the underlying physics, it would be unlikely that a single empirical correction term would successfully match such disparate parametric configurations.

The repeatability of the vent timing (the concern of Section 5.2.1.1) was high with no instance of a significant departure in timing. The average standard deviation vent

time as related to the percent projectile travel for the three heavy breech configurations was 0.63%. The light breech did not fair as well, with a 2.5% standard variation.

It may be speculated that disturbance forces have less of an effect on the increased inertia of the heavy breech. Alternatively, it may be speculated that the higher acceleration of the lighter breech increased its receptance to structural dynamics that increased the variation in disturbance forces. For example, a dynamic behavior similar to the oscillatory behavior indicated in the recoil phase-plane plots of Section 6.4.2 could have increased the effect of disturbances on the light breech.

### 8.3.2 Right Running Characteristics

In general, the slope of the modeled rarefaction wave front progression is in good agreement with the experimental results. However, as the wave progresses down the bore the model would appear to be overestimating the wave speed.

As was discussed in the ballistic matching Section 7.2.1, the flame temperature of the propellant was reduced, which would tend to lower the sonic velocity. However, as a consequence of not tuning the force, the molecular mass declined which increases the sonic velocity; thus, the sonic velocity was largely unaffected. The potential exists to enhance the results by explicitly including the sonic velocity in the ballistic matching process. (I.e., also tune the force.)

It is also possible that the temperature of the down bore gases are more sensitive to the inaccuracies of the Lagrange assumption of uniform gas density described

in Section 7.1.5 than are traditional gun performance issues such as muzzle velocity and pressure.

Examination of Fig. 8.3-4 indicates that the model is predicting the rarefaction wave to reach the base of the projectile prior to shot-exit for the light-early vent configuration. The experimental results are inconclusive, but certainly do not support the intersection of the rarefaction wave front with the base of the projectile 20% prior to shot-exit, but 10% is plausible. This will be elaborated upon in Section 8.7.

## **8.4 Chamber Pressure Impulse**

The chamber pressure impulse results plotted in Fig. 6.3-17 of Section 6.3.8 indicate the anticipated trends. The heavier inertial breech does not open as swiftly as the light breech; therefore, it does not achieve as much of a pressure reduction as its lighter counterpart that vents at the same time. This is the concern raised in Section 5.2.1.3. Similarly, the earlier the venting, the lower the measured impulse. The results are rather well behaved in this respect as indicated by the linear fits to the data and the close proximity of the confidence intervals to the data in Fig. 6.3-17.

By this metric of recoil reduction, the closed-breech and non-venting configurations are rather comparable with the non-venting measuring 3.5% less chamber impulse than the closed-breech per Table 6.3-3.

As was elaborated in Section 6.3.8, all of the pressure data is suspect, so conclusions based upon this data must be tempered.

## **8.5 Measured Recoil Velocity**

The principal means by which recoil momentum of the gun was determined was by measuring the velocity of free recoil within the mount. The validity of this data must be called into question because of the wide disparity between the measured recoil momentum between the closed-breech and non-venting inertial breech configuration. The mean results for the closed-breech configuration are 6% below that of the integrated chamber pressure impulse while the non-venting configuration exceeds its mean integrated chamber pressure impulse by 16%.

A plausible explanation for this imbalance in measured recoil momentum was made in Section 6.4.1.3. The friction of the mount behaves differently for blow-forward guns, predictably increasing the recoil momentum inferred from the recoil velocity subject to friction. This argument is sound, but the required force to explain the discrepancy is large.

If one assumes a constant level of friction, regardless of whether the friction is opposing forward or rearward motion, the magnitude of the friction required to explain the discrepancy may be evaluated. (Note, this model of friction is over simplified, and intended only to provide perspective.)

Inspection of Fig. 6.4-1 reveals that closed-breech shot 2-1-3 experienced an exposure to a forward directed friction force for 13.3ms prior achieving its recoil velocity. The non-venting configuration 2-9-4 experienced rearward directed friction for 13.9ms prior to having its forward intrusion reversed. It then experienced forward directed friction

for 16.3ms as it recoiled rearwards through the gun mount. Thus, it was exposed to a net forward friction force for 2.4ms, 10.9ms less than its closed-breech counterpart. The disparity in recoil momentum for these configurations reflected in Table 6.4-1 is 159Ns. Thus, a friction force of 14.6 kN would be required to explain the difference. Although plausible, this seems high for a lubricated mount. If this value were accurate, it would imply that the non-venting inertial breech actually incurred an additional 35Ns of rearward momentum during its 2.4ms of exposure to forward friction forces.

The potential for the gun to be chattering as it traverses the mount may explain a high level of friction. This postulate is supported by the oscillatory behavior of the phase plane response of Section 6.4.2.

An alternative source for a large friction discrepancy would occur if the mount friction is increased when the outer diameter of the bore is dilated by the internal propellant gas pressures. Thus, the closed-breech gun would experience this higher friction as a forward force opposing its rearward motion. The blow-forward barrel would experience the higher friction as a rearward force opposing its forward intrusion into the mount. This is a plausible explanation that lacks supporting evidence.

For the vented configurations, the duration of exposure to rearward directed frictional forces as a result of the forward motion exceeds the duration of the forward directed forces that result after the forward motion of the gun is reversed. The difference is 2.8ms and 2.3ms for the heavy-early configuration plotted in Fig. 6.4-3 and the light-nominal configuration plotted in Fig. 6.4-4, respectively. If the 14.6 kN friction force is

true, the measured impulse for these configurations is high by 41Ns and 34Ns, respectively.

It is also possible that the closed-breech configuration did engage the secondary recoil brakes (ring-springs) prior to attaining its free recoil velocity.

## 8.6 Measured Recoil Momentum

The measured recoil reductions of Fig. 6.4-5 are substantial. They may be placed into perspective by reconsidering the parametric study of Section 4.1.4, as applied directly to the 35mm demonstrator using the ballistically matched propellant properties listed in Table 5.1-5 and ammunition parameters listed in Table 5.1-2. The results applied to the 1175m/s muzzle velocity are depicted in Fig. 8.6-1.

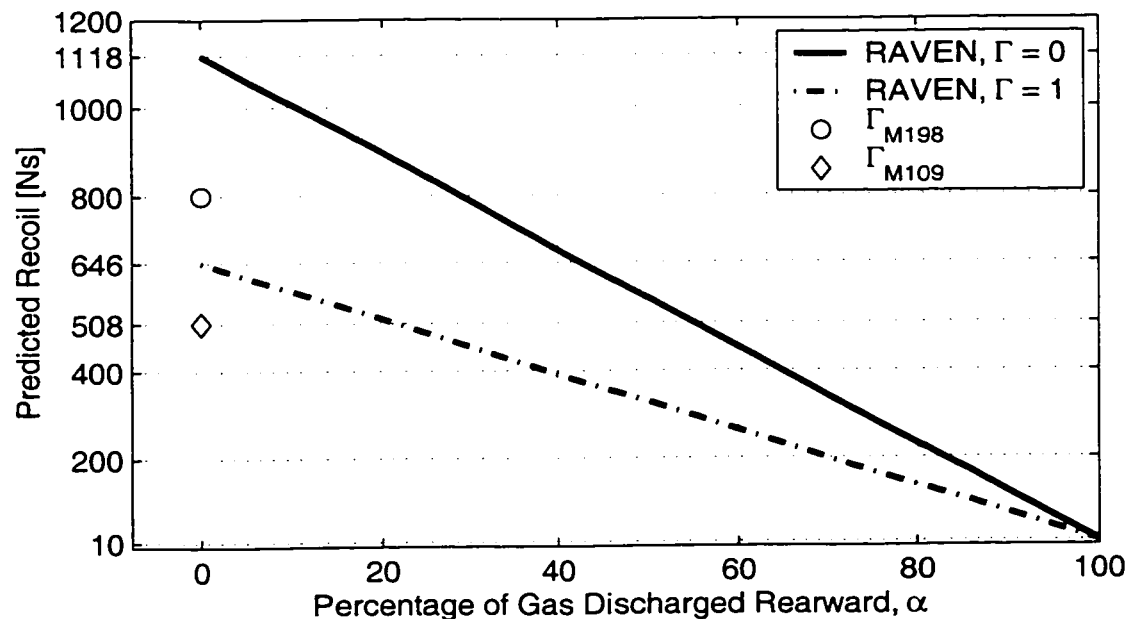


**Figure 8.6-1 Predicted Recoil Performance for 35mm RAVEN and Muzzle Brakes.**

The recoil momentum prediction of (4.2-25) is 10% higher than the 1018Ns of measured recoil momentum for the non-vented inertial breech. Note that the momentum imparted to the 0.55kg projectile at a muzzle velocity of 1175m/s is 646Ns. Therefore, the 1118Ns prediction assumes 42.2% of the recoil to be manifest in the propellant gas momentum.

By means of its ability to reverse the exit velocity of the propellant gases, the M109 double baffle brake may reduce the imparted impulse below that of the projectile alone to 508Ns.

The light-early measured momentum of Table 6.4-1 constitutes a 42% reduction relative to the non-venting configuration. Scaling this result to the slightly higher predicted momentum of Fig. 8.6-1 results in recoil estimate of 467Ns. The estimated percentage of gas discharged rearward may be estimated as 59% or 0.196kg at the intersection of the bare muzzle,  $\Gamma = 0$ , RAVEN performance line with 467Ns of momentum. Extending down the chart, it is estimated that a  $\Gamma = 1$  muzzle brake would effect a further reduction to 272Ns.

The estimated discharge velocity,  $v_c$  of (4.2-18) for the propellant properties listed in Table 5.1-5 and the ammunition configuration listed in Table 5.1-2 is 1912m/s. Thus, 375Ns of forward momentum may be generated by the 0.196kg of vented propellant gas. Subtracting this momentum from the integrated chamber impulse of 671Ns listed in Table 6.3-3 results in 296Ns which is about 30% when compared to the measured

momentum of 425Ns for the light-early RAVEN configuration. However, the known inaccuracies of the pressure readings discussed in Section 6.3 and the issues of gun mount friction discussed in Section 8.5 will both tend to improve the correlation. Since there was no measurable reduction in muzzle velocity, greater recoil reduction may be possible.

### **8.7 Scrutiny of Light-Early Shot 2-6-3**

As discussed in Section 8.1, the slowest accepted velocity was that of early shot 2-6-3. Further, examination of Table 6.3-2 reveals that it was effectively the earliest venting, with detection of the rarefaction wave at the chamber pressure port P1 2.29ms prior to shot-exit.

Reviewing Table 6.3-1 and Fig. 6.3-5, it may be seen that this round recorded the lowest measured peak chamber pressure of the entire test. Since the rarefaction wave was released well past peak pressure, it could not have caused the reduction in peak pressure. While confidence in the pressure gage data cannot be considered high, its relative correlation to muzzle velocity was reasonably well behaved for the light breech configuration as indicated by the line-fit plotted in Fig. 6.3-5. Thus, it is likely the projectile was going slow when the venting first occurred. This would explain the long duration of concurrent venting and propulsion. The bullet took additional time to traverse the remainder of the bore.

This does not rule out the possibility that the rarefaction wave front reached the base of the projectiles fired in the light-early configuration. However, if the rarefaction wave did reduce their velocity, the reduction was well below that measurable in this



limited data set. Bear in mind, the mean velocity of the light-early configuration was higher than either of the two latest vent geometries for the light breech.

## **8.8 Reduction in Barrel Heating**

The measurements of barrel temperature conclusively revealed a reduction in the heating of the gun when firing vented shots. Strong correlation was drawn as indicated in the linear fits of the peak temperature rise to the percentage of projectile travel at the time of the venting.

Reduction of barrel heating by 40%, as was achieved during the earliest vented shot, is dramatic with profound implications on the design of direct fire weapons. Direct fire weapons are engineered to manage the thermal energy imparted to the barrel during rapid firing by the thermal mass of the barrel. The rate of heat input during rapid fire is higher than could be abated by known practicable heat sinks, other than barrel mass. Thus, it is not uncommon for gun barrels to have a much greater wall ratio than required for pressure containment alone. This is particularly true for down-bore locations such as the muzzle where pressure containment requirements are substantially reduced.

Alternative technologies to reduce bore heating include the application of wear reducing additives to the propellant bed [74]. The additive may include ablative materials to impair heat transfer to the wall during early phases of the interior ballistics. Clearly such techniques are compatible with RAVEN.

To place this result into perspective, Bracuti [74] discusses a threshold at about  $350 \text{ J/mm}^2$  below which barrel erosion is minimal for the 105mm M68 gun under consideration. (This gun is about to be fielded in a new mobile gun system combat vehicle designed by General Dynamics for the Army's Interim Brigade Combat Team.) Bracuti further describes efforts to reduce the heat input from  $449 \text{ J/mm}^2$  to values as low as  $348 \text{ J/mm}^2$ , a reduction of 22.5% to improve barrel life. Reduction of the temperature at the earliest temperature probe, K1 (approximately three calibers down bore) was 28% relative to the closed-breech case.

## **Part 9**

# **CONCLUSIONS**

A new form of gun propulsion was conceived, formulated, and experimentally evaluated.

The basic premise of rarefaction wave gun propulsion was that a delayed venting of the chamber could develop a rarefaction wave that would propagate down the bore of the gun, following the projectile, without slowing it down. Figure 6.3-11 graphically depicts pressure reductions of an order of magnitude in the chamber of a vented gun versus an orthodox gun with no discernible reduction in pressure between the rarefaction wave front and the base of the projectile.

The major advantages of RAVEN were clearly demonstrated. Recoil reductions of more than 50% were demonstrated as listed in Table 6.4-1. An overall bore heating reduction of 40% was demonstrated as listed in Table 6.5-1. Both the recoil and temperature reductions were found to be enhanced by earlier venting, thus, demonstrating consistency with the predicted effects.

### **9.1 Recommendation for Future Investigation**

Because of the fundamental new and unprecedented contribution of RAVEN, the recommendations for future investigation may be divided into several broad categories.

### 9.1.1 Performance

The parametric study of synchronized RAVEN operation conducted in Section 4.2.4 lacks experimental validation, and is likely inaccurate in its predictions (but not its trends). A blend of interior ballistic modeling and experimental testing would be of great value. Particular points of interest include:

#### 9.1.1.1 Recoilless Synchronized RAVEN

Achieving synchronized venting timing with zero net recoil momentum may be expected to occur for projectile velocities less than 2000m/s per Fig. 4.2-3, provided a muzzle brake is employed. What velocity is required to achieve recoillessness without resorting to a muzzle brake? What is the lowest velocity that may achieve recoillessness with an aggressive muzzle brake?

#### 9.1.1.2 High Efficiency Recoilless RAVEN

If reduced ballistic efficiency is tolerable, what will be the ballistic efficiency of a recoilless RAVEN relative to the prior art recoilless rifles? How close to the Ogorkiewicz line can the Olcer and Levin recoilless curve fit of Fig.3.6-1 be raised? How much can a muzzle brake help?

#### 9.1.1.3 Near Synchronized RAVEN

It is not anticipated that projectile propulsion will be greatly attenuated if the rarefaction wave front reaches the base of the projectile shortly prior to shot-exit. Quantification of this, so an appropriate engineering trade-off can be made, would prove of great utility, both for recoil reduction and heat reduction.

#### 9.1.1.4 Lowest Heat Launcher

Recognizing the RAVEN gets the hot erosive propellant gases from behind the bullet prior to shot-exit, it may be appreciated that the earlier the venting occurs, the greater this effect will be—to a point. As the ballistic efficiency of launch is reduced by early venting, more propellant is required to achieve the desired muzzle velocity. What are the bounds and behavior of this parametric concern. What is the lowest heat configuration of propellant to projectile mass ratio and vent timing to achieve a desired muzzle velocity?

#### 9.1.2 Blast

RAVEN introduces back blast as an inescapable consequence of its operation. In general, back blast is bad. It does, however, offer an interesting potential to reduce muzzle blast and the obscuration of targets while they are engaged.

##### 9.1.2.1 Blast Characterization

The dynamic processes of a RAVEN venting is extremely transient, an order of magnitude swifter than prior art recoilless rifles. How does this blast behave? What are the extents of the danger zone?

##### 9.1.2.2 Blast Mitigation

What can be done to reduce the back-blast danger zone? What can be done to inhibit secondary flash? Can thrust vectoring break-up undesirable blast patterns?

### 9.1.3 Venting Mechanics

#### 9.1.3.1 Alternatives to the Inertial Breech

The inertial breech method of venting developed in Section 5.2 worked well for a test fixture to prove the concept. It may work well as an objective design, but there are alternatives including mechanical valves, and single use detonation devices.

#### 9.1.3.2 Transients Immediately Following Venting

The behavior of the propellant gases first vented out of the gun is of interest. They are manifest with the greatest stagnation properties of any of the subsequent flow. What are the implications of this highly transient flow on nozzle efficiency, on pressure containment requirements, on the developed blast field? Would the method of Bulman, described in Section 2.6, to preemptively establish a “plume within a plume” be of advantage?

#### 9.1.3.3 Heat Transfer and Erosion at the Vent

The heat transfer of a RAVEN vent, when it first commences its opening may be anticipated to be dramatic, but drop off very swiftly as the rarefaction wave progresses through the chamber. What are the implication on heating and erosion of the vent material? What materials would perform well in this application? Would ablatives be of utility?

## **Part 10**

### **Literature Cited**

1. Kathe, E., "Sonic Rarefaction Wave Recoilless Gun System," U.S. Patent Application 09/631,142, filed 02 August 2000 and Provisional Patent Application 60/152,217 filed 03 September 1999.
2. Anderson, J. D. Jr., Modern Compressible Flow, with Historical Perspective, McGraw-Hill, 1990.
3. Kathe, E. L. and Dillon, R., "Sonic Rarefaction Wave Low Recoil Gun," AIAA 01-0743, 39th Aerospace Sciences Meeting and Exhibit, Reno, NV, January 2001. Also available as ARDEC Technical Report ARCCB-TR-02001, January 2002.
4. Anderson, J. D. Jr. Computational Fluid Dynamics, the Basics with Applications, McGraw-Hill, 1995.
5. Coffee, T., "RAVEN Simulations," Army Research Laboratory, presented at RAVEN Meeting, Picatinny Arsenal, NJ, 27 June 2000.
6. Kathe, E., Dillon, R., Sopok, S., Witherell, M., Dunn, S., and Coats, D., "Rarefaction Wave Gun Propulsion," Presented at 37th JANNAF Combustion Meeting, Monterey, CA 12-17 November 2000. Also presented at the 50th JANNAF Propulsion Meeting, Salt Lake City, Utah, 11-13 July 2001.
7. Gough, P. S., "The XNOVAKTC Code," Portsmouth, NH, 1990.
8. Headquarters, U.S. Army Materiel Command, "Recoilless Rifle Weapon Systems," AMCP 706-238, Washington, 1976.
9. The Franklin Institute, "Muzzle Brakes, Volume I, History and Design," Philadelphia, 1949.
10. The Franklin Institute, "Recoilless Weapons, Volume I, The Recoilless Principle," Philadelphia, 1948.
11. Hatcher, J. S., Hatcher's Notebook, Third Edition, The Stackpole Company, Harrisburg, Pa, 1962.
12. Cook, C. J., "Non-Recoil Gun," U.S. Patent 1,380,358, Issued 7 June, 1921.
13. Studler, R., "Recoilless Rifles," Army Ordnance Magazine, v29, n152, Sep-Oct 1945.

14. Armour Research Foundation of Institute of Technology, "Development of Battalion Anti-Tank Weapons," Office of Chief of Ordnance RRDTS Project No. TS4-4020, Chicago, November 30, 1952.
15. Ashley, E., "105-MM Recoilless Guns for Firing Guided Projectiles," Contract Report DAAA22-77-C-0240, Watervliet Arsenal, Watervliet, NY 12189, January 1978.
16. Bulman, M. J. and Graham, A. R., "Liquid Propellant Gun (Recoilless Regenerative Piston)," U.S. Patent 4,043,248, Issued 23 August 1977.
17. Bulman, M. J., Private Communication, 30 July 2001.
18. Czysz, P. A., "Solid Propellant 75MM Recoilless Gun System for Airborne Applications," Contract Report DAA# 30-01-M-1348, Benét Laboratories, Watervliet, NY 12189, 30 January 2002.
19. Vottis, P., "Digital Computer Simulation of the Interior Ballistic Process in Guns," Technical Report WVT-6615, Benét Laboratories, Watervliet Arsenal, NY, October 1966.
20. Ogorkiewicz, R. M., Technology of Tanks: Volumes I and II, Jane's Information Group, Surrey, UK, 1991.
21. Headquarters, U.S. Army Materiel Command, "Interior Ballistics of Guns," AMCP 706-150, Washington, 1965.
22. Corner, J., Theory of the Interior Ballistics of Guns, Wiley, New York, 1950.
23. Stiefel, L. "Thermochemical and Burning Rate Properties of Deterred US Small Arms Propellant," ARDEC Technical Report ARSCD-TR-80005, Picatinny Arsenal, NJ, June 1980.
24. Headquarters, U.S. Army Materiel Command, "Elements of Armament Engineering: Part Three, Weapon Systems and Components," AMCP 706-108, Washington, July 1963.
25. Headquarters, U.S. Army Materiel Command, "Ammunition Series: Section 4, Design for Projection," AMCP 706-247, Washington, July 1964.
26. Stiefel, L., "Pressure-Time-Velocity-Travel Relationship in Typical Gun Systems," in Gun Propulsion Technology, Steifel, L. Ed., AIAA, Washington, 1988.



27. Kroeger, W. J. and Musser, C. W., "The Design of Recoilless Infantry Weapons, Report No. R-727, Ordnance Laboratory, Frankford Arsenal, Philadelphia, PA, June 1946.
28. The Franklin Institute, "Recoilless Weapons, Volume IV, Description of Weapons," Philadelphia, 1949.
29. Headquarters, U.S. Army Materiel Command, "106-MM Recoilless Rifle M40A2," FM 23-82, Washington, 1973.
30. Headquarters, Department of the Army, "Army Ammunition Data Sheets, Artillery Ammunition; Guns, Howitzers, Mortars, Recoilless Rifles, Grenade Launchers, and Artillery Fuzes," Technical Manual TM-43-0001-28, Washington, April 1994.
31. Love, E. H. and Pidduck, F. B., "Lagrange's Ballistic Problem," Phil. Trans. Roy. Soc., 222, 1922.
32. May, I. W. and Horst, A. W., "Charge Design Considerations and Their Effect on Pressure Waves in Guns," in Interior Ballistics of Guns, Krier and Summerfield (Ed), AIAA, 1979.
33. Duncan, W. E., "105MM Davis Type Gun Design Test Report," Technical Note 3015-011, Naval Weapons Center, China Lake, CA, 1972.
34. Sanford, M. J., Crabtree, L. E., Ellis, R. L., and Cahill, J. F., "Recoilless and gas-free projectile propulsion," U.S. Patent 5,952,601, Issued 14 September 1999.
35. Munitions and Weapons Division, "Artillery Ammunition Master and Reference Calibration Chart," Report No. 1375, 39th Revision, June 2000, Material Test Command, U.S. Army Yuma Proving Ground, Az (Distribution Limited).
36. Germershausen R. and Melchior, E. "Internal Ballistics," in Handbook on Weaponry, First English Edition, Rheinmetall GmbH, Düsseldorf, 1982.
37. Dunn, S., Private Communication, Subject: RAVEN Analysis, 21 April 2000.
38. Dunn, S., French, J., Coats, D., Kathe, E., Dillon, R., Sopok, S., and Witherell, M., "Internal Ballistics Analysis for the RAVEN Propulsion System," 10th US Army Symposium on Gun Dynamics, Austin Texas, 23-26 April 2001.
39. Robins, F. W., "A Lumped Parameter Interior Ballistic Computer Code Using the TTCP Model," Ballistic Research Laboratory Memorandum Report BRL-MR-3710, Aberdeen Proving Ground, MD, November 1988.

40. Van Wylen, G. J. and Sonntag, R. E., "Fundamentals of Classical Thermodynamics, 3rd Ed." Wiley, 1985.
41. Headquarters, U.S. Army Materiel Command, "Recoil Systems," AMCP 706-342, Washington, 1963.
42. Headquarters, U.S. Army Materiel Command, "Muzzle Devices," AMCP 706-251, Washington, 1968.
43. Dillon, R. E. Jr., "A Method of Analyzing Perforated Muzzle Brake Performance," Ph.D. Thesis, Rensselaer Polytechnic Institute, Troy, NY, May 1983.
44. Schmidt, E. M., "Recoil Characteristics of Electromagnetic Cannon," Shock and Vibration, v8, n3-4, pp. 141-146, 2001.
45. Boutteville, S. V., "Gun Mechanics," in Handbook on Weaponry, First English Edition, Rheinmetall GmbH, Düsseldorf, 1982.
46. Hammer, E. W., Jr., Muzzle Brakes, Volume I, History and Design, The Franklin Institute, Philadelphia, 1949.
47. Chinn, G. M., The Machine Gun, Volume V, Edwards Brothers Publishing, Ann Arbor, MI, 1987.
48. Oerlikon, "Oerlikon 35mm Ammunition," Machine Tool Works Oerlikon-Bührle Ltd., Publication WWW 400101 E 1978, Zurich, Switzerland, 1978.
49. Kertis, A. J. Jr., "Demonstrator, RAVEN 35MM," Drawing Set, Ares, Inc., Port Clinton, OH, 2001.
50. Romer, R., "Ammunition," in Handbook on Weaponry, First English Edition, Rheinmetall GmbH, Düsseldorf, 1982.
51. Robins, F. W., "Interior Ballistics, Theories, Models and Computer Codes: A Seminar," Fre-Lin Associates, Havre de Grace, MD, Held at Watervliet Arsenal, NY, 24-26 October 2000.
52. Wetzel, J. E., Private Communication, subj: Oerlikon 35mm TP propellant properties, 23 March 2001.
53. Stiefel, L., "Gun Propellants," in Interior Ballistics of Guns, Krier and Summerfield. Ed., AIAA, Washington, 1979.

54. O'Hara, G. P., Private Communication, subj: Thermochemical Properties of Propellants, 1999.
55. Kertis, A. J. Jr., Private Communications, 2001.
56. Chinn, G. M., The Machine Gun, Volume IV, Department of the Navy, Washington, 1955.
57. Kathe, E., "Inertial Breech Gun System," U.S. Patent Application Serial Number 09/363,700, filed 16 July 1999.
58. Avallone, E. A. and Baumeister, T. III, Mark's Standard Handbook for Mechanical Engineers, Ninth Edition, McGraw-Hill, New York, 1987.
59. Brown, B. B., "Hazards and Safeguards of High Pressure Hydraulic Fatigue Testing," in High Pressure Engineering Technology, PVP-Vol. 125, ASME Book No G00371, ASME Press, New York, 1989.
60. Flaherty, J., Private Communication, 13 April 2002.
61. Olmstead, V., Private Communication, subj: Copper Crush Shock Arresting, August, 2000.
62. Harris, C. M., Shock and Vibration Handbook: Fourth Edition, McGraw Hill, New York, 1995.
63. Headquarters, U.S. Army Materiel Command, "Carriages and Mounts Series: Recoil Systems," AMCP 706-342, Washington, 1969.
64. Krier, H. and Adams, M. J., "An Introduction to Gun Interior Ballistics and a Simplified Ballistic Code," in Interior Ballistics of Guns, Krier and Summerfield. Ed., AIAA, Washington, 1979.
65. Baer, P. G., "Practical Interior Ballistics of Guns," in Interior Ballistics of Guns, Krier and Summerfield. Ed., AIAA, Washington, 1979.
66. Goldstein, S., "Interior Ballistic Modeling Applied to Small-Arms Systems," in Interior Ballistics of Guns, Krier and Summerfield. Ed., AIAA, Washington, 1979.
67. Robins, F. W. and Keller, G. E., "Studies Supporting Development of a Modified Gradient Equation for Lumped-Parameter Interior Ballistic Codes," Ballistic Research Laboratory Memorandum Report BRL-MR-3678, Aberdeen Proving Ground, MD, July 1988.

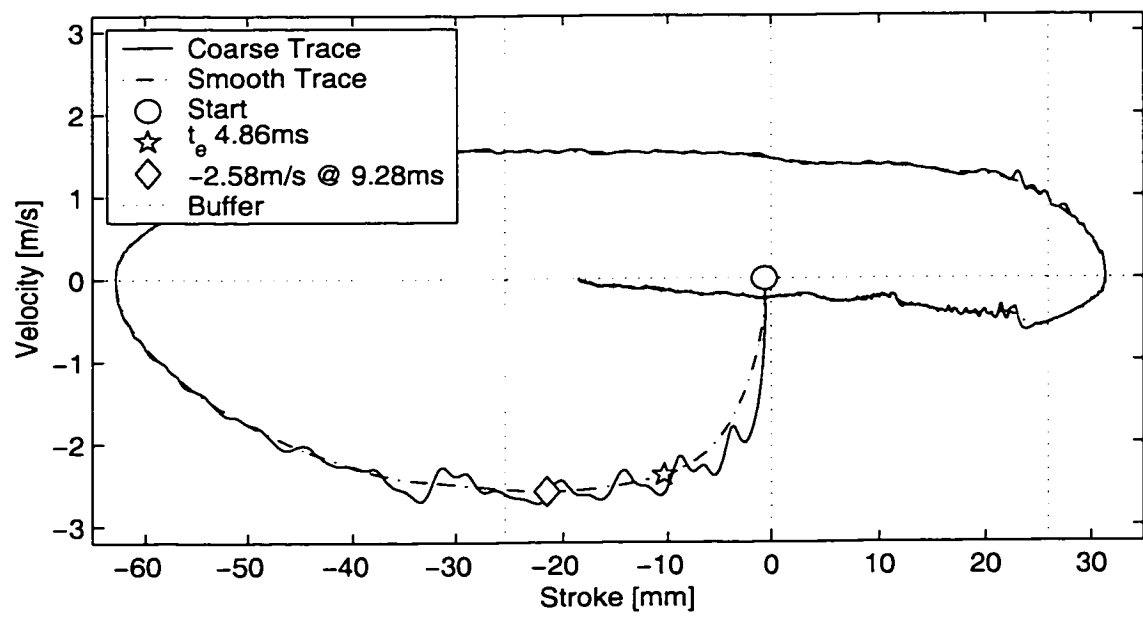
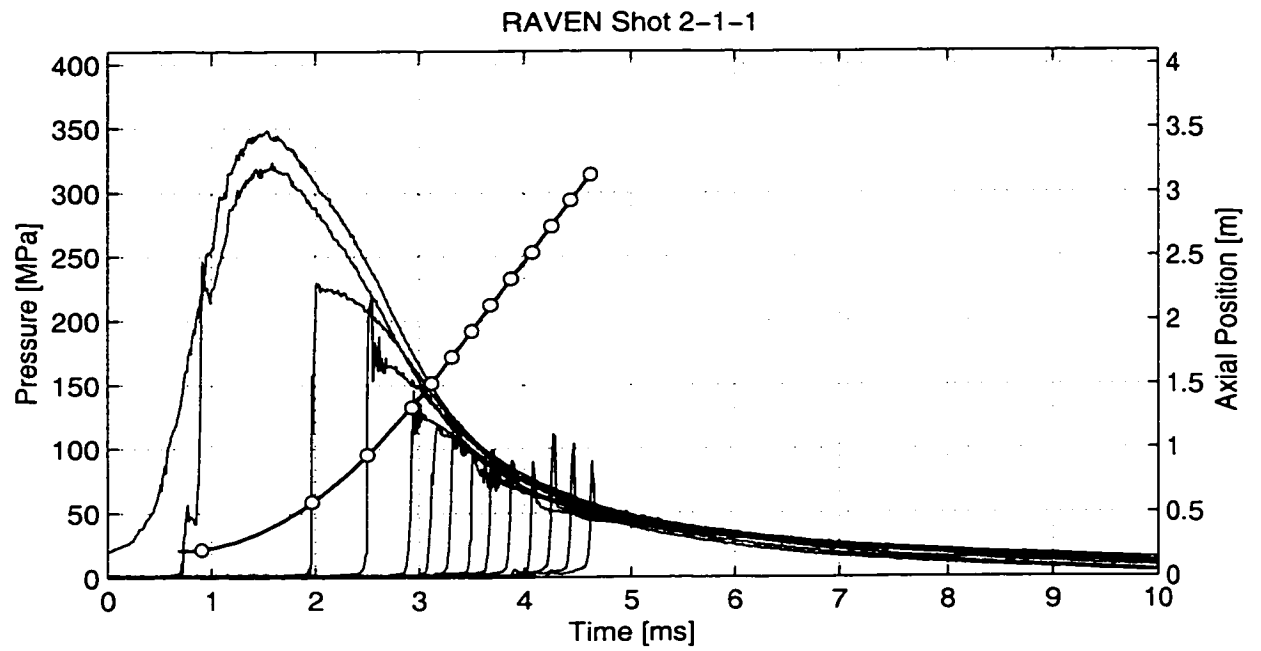
68. Robins, F. W., Anderson, R. D., and Gough, P. S., "New Pressure Gradient Equations for Lumped Parameter Interior Ballistic Codes," Ballistic Research Laboratory Technical Report BRL-TR-3097, Aberdeen Proving Ground, MD, 1990.
69. Gough, P. S., "Interior Ballistics Modeling: Extensions to the One-Dimensional XKTC Code and Analytical Studies of Pressure Gradient for Lumped Parameter Codes," Army Research Laboratory Contractor Report ARL-CR-460, Aberdeen Proving Ground, MD, February 2001.
70. Gough, P. S., "Fundamental Investigation of the Interior Ballistics of Guns: Final Report," Indian Head Contractor Report 74-1, Naval Ordnance Station, Indian Head, MD, 13 July 1974.
71. Nusca, M. and Conroy, P. J., "Multiphase CFD Simulations of Solid Propellant Combustion in Gun Systems," AIAA Paper 2002-1091, Journal of Propulsion and Power, June 2002, in-press.
72. Nordheim, L. W., Soodak, H., and Nordheim, G., "Thermal Effects of Propellant Gases in Erosion Vents and in Guns," National Defense Research Committee Report A-201, 1944.
73. Armour Research Foundation Technology Center, "Survey of Automatic Cannon Mechanisms, Volume I," Office of Chief of Ordnance, Ordnance Research and Development Division, Project No. TR 1-1026A, Chicago, July 1947.
74. Bracuti, A. J., "Wear-Reducing Additives—Role of the Propellant," in Gun Propulsion Technology, Steifel, L. Ed., AIAA, Washington, 1988.

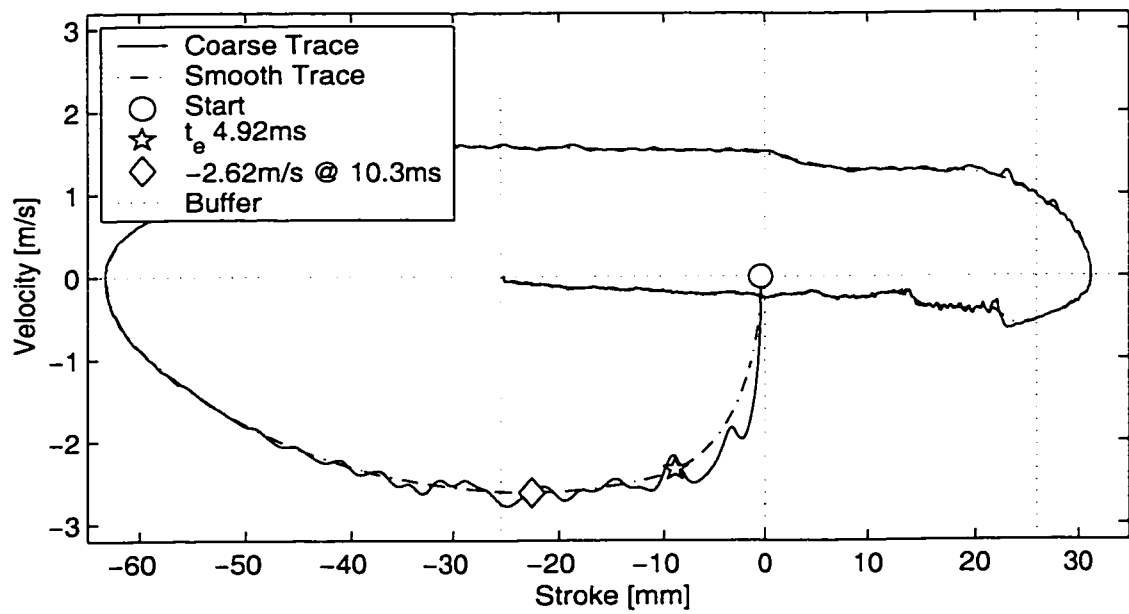
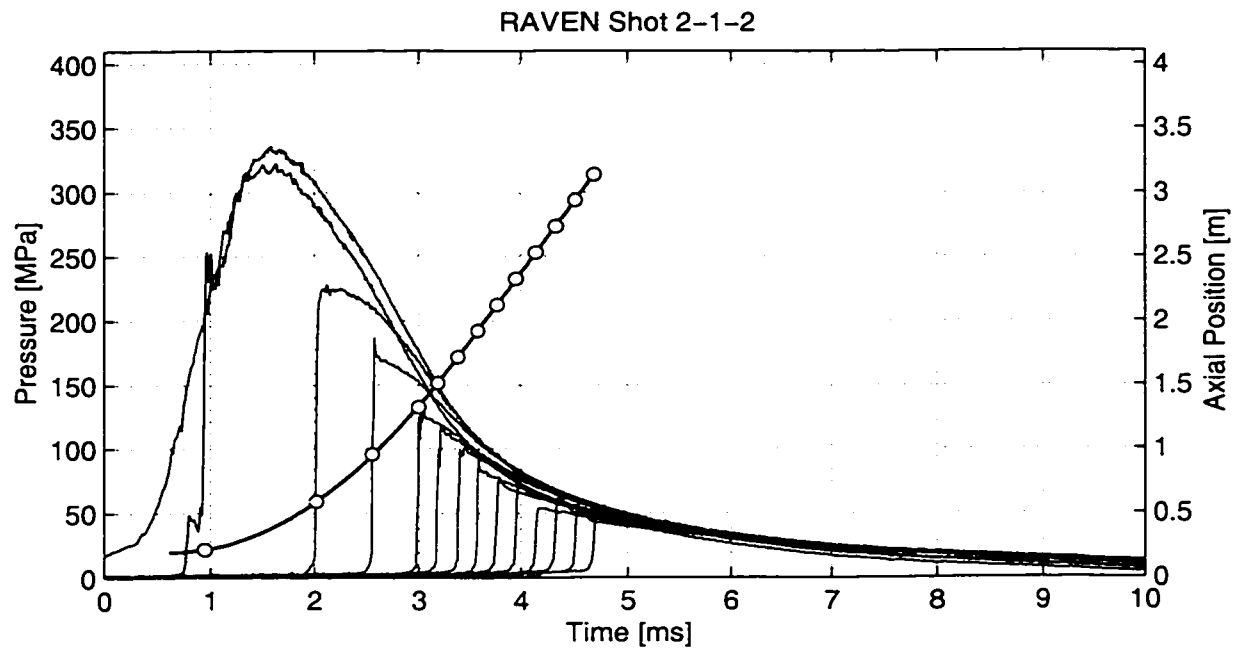
## **APPENDIX A DATA COLLECTED**

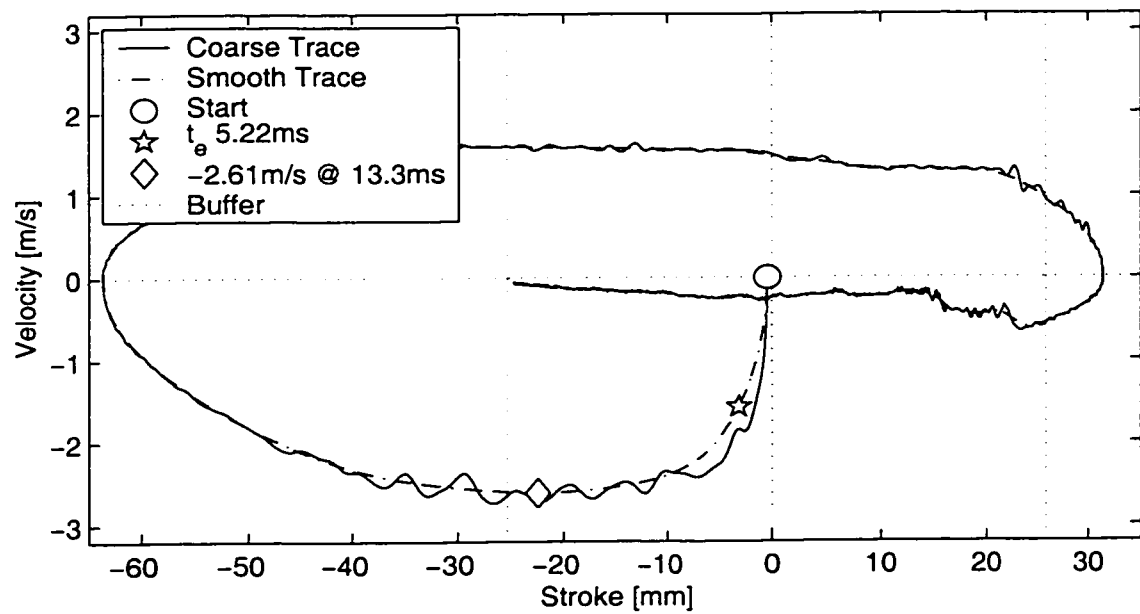
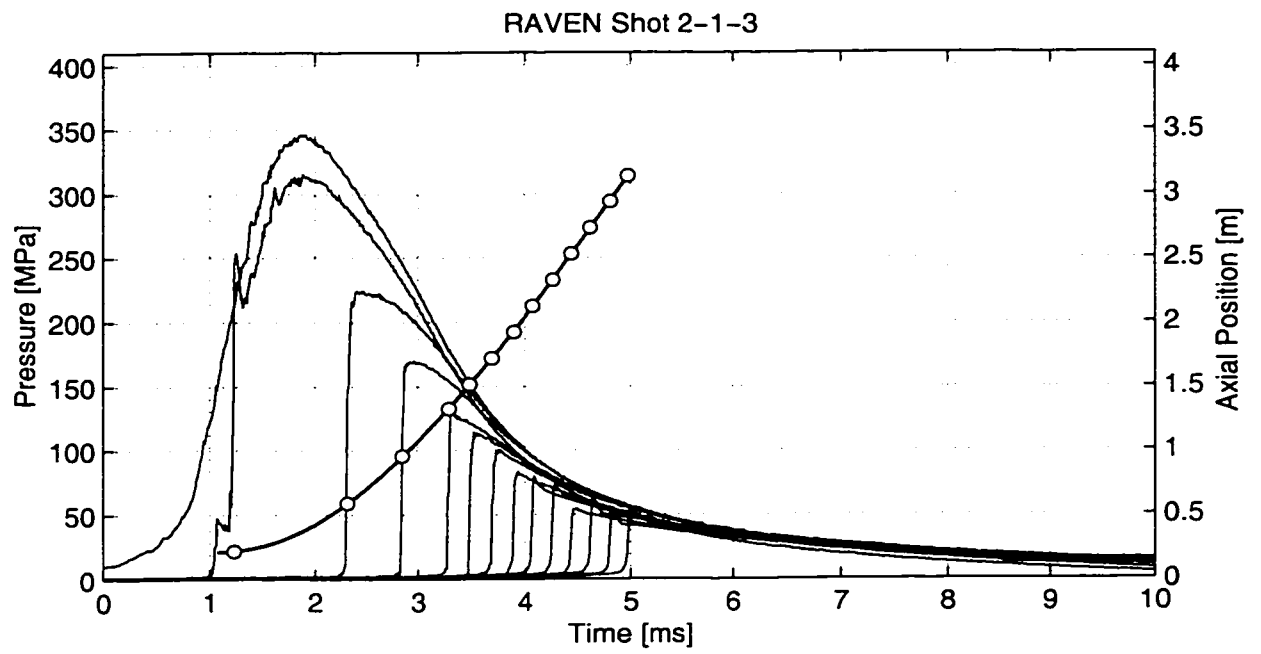
This Section includes a plot of the combined pressure, projectile travel, and rarefaction wave front propagation curves for each shot. The legend was removed to simplify the presentation. In addition, a plot of each recoil phase plane is included for each shot. Consult Section 6.3.6 and 6.4.2 respectively for guidance on interpreting these figures.

The configurations of each of the shots is recorded in Table 6.1-1. Three of the shots exhibit particularly strong pressure anomalies (as indicated in Table 6.1-1) whose source is unknown but not physical. (E.g., there is no source of energy to cause the late high pressure of shot 2-3-4 and no increase in the muzzle velocity that would have resulted.) Similarly, the recoil data for shots 2-9-1 and 2-9-3 are corrupt for reasons that remain unknown.

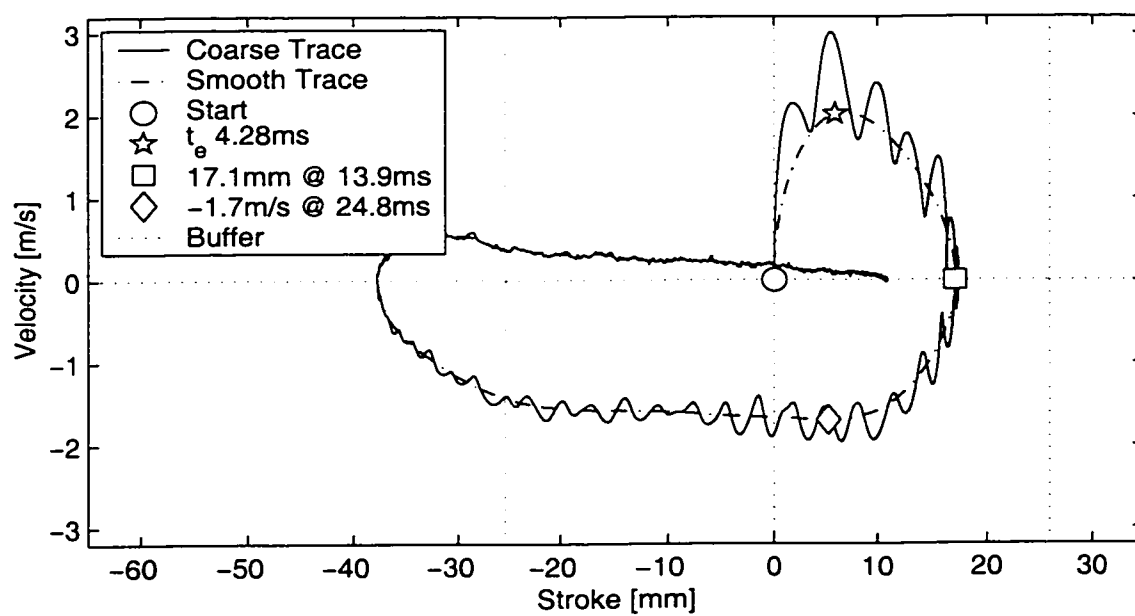
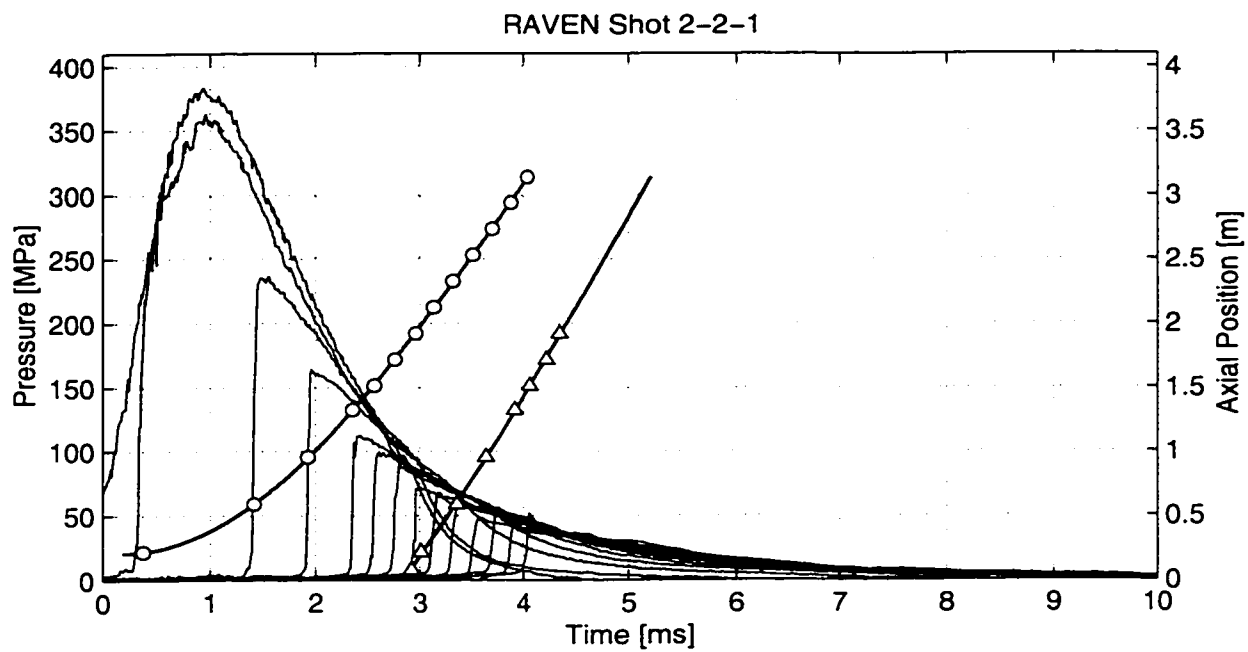
The polynomial fits to the rarefaction wave fronts are also subject to occasional erroneous behavior including negative curvature (e.g., shot 2-3-1) and plotting of the fit at times prior to venting (e.g., shot 2-6-1).

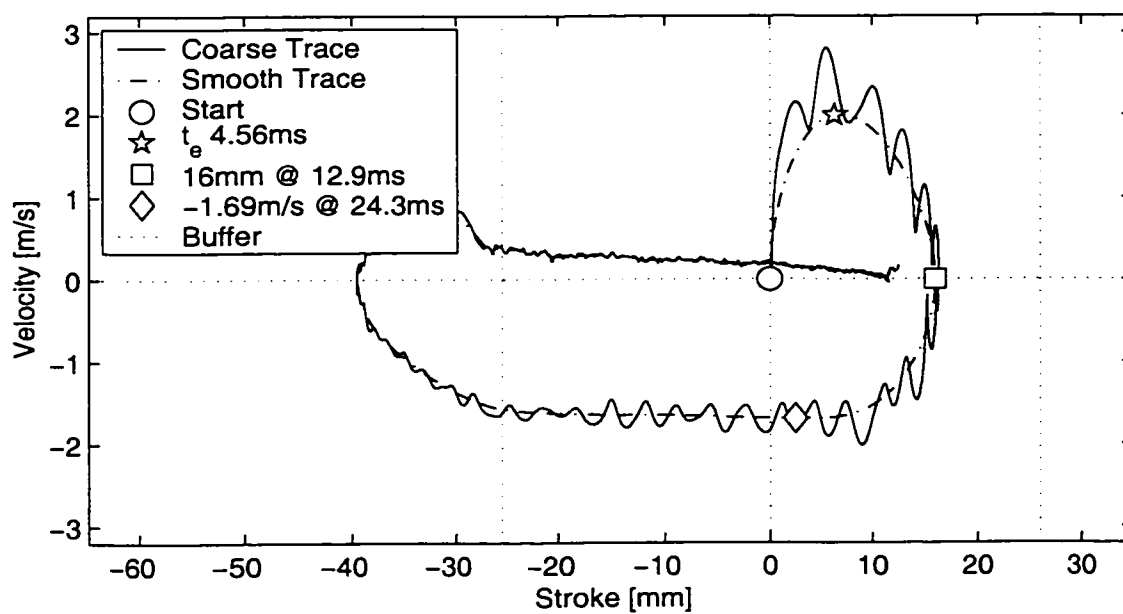
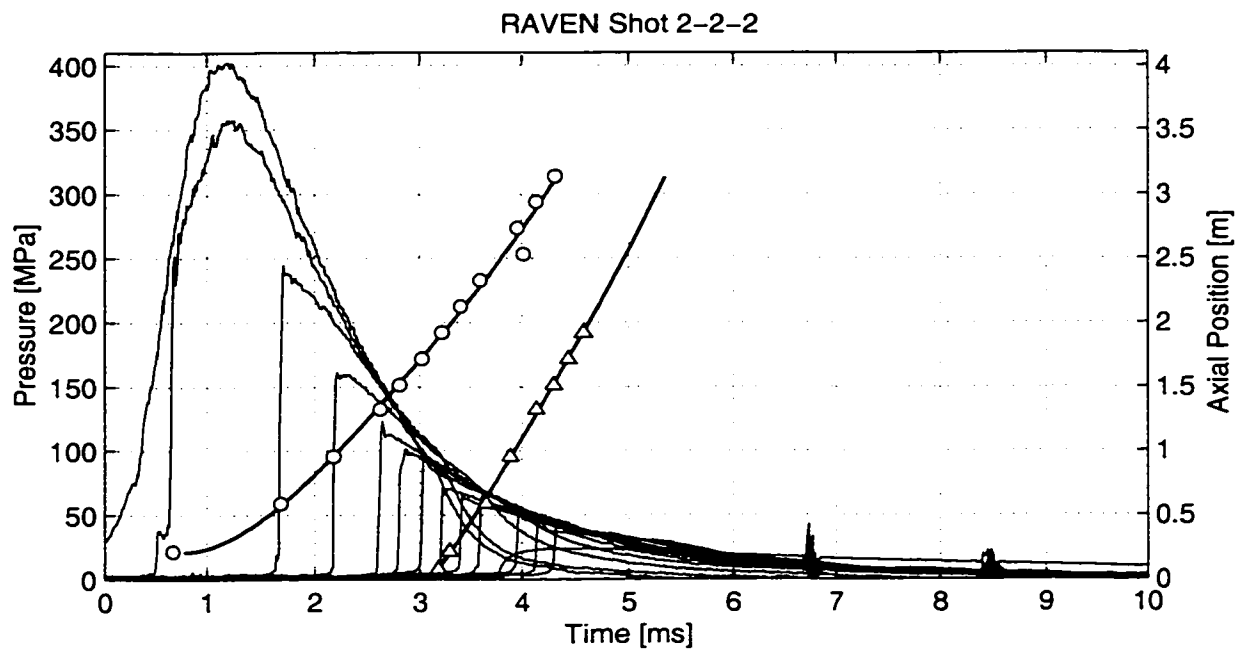


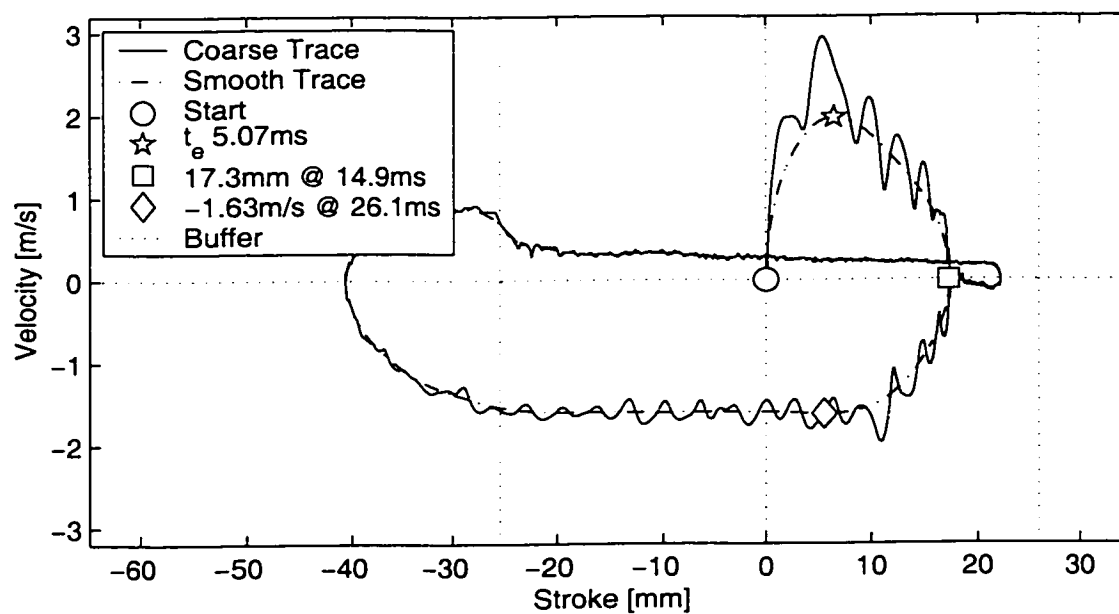
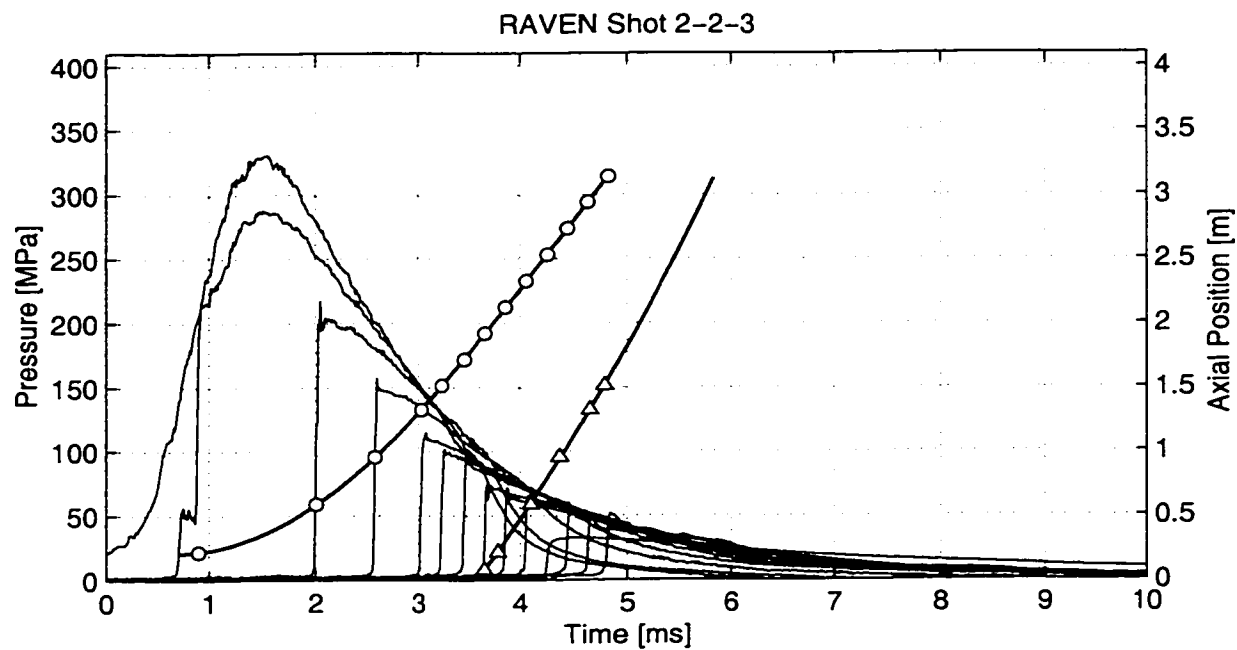


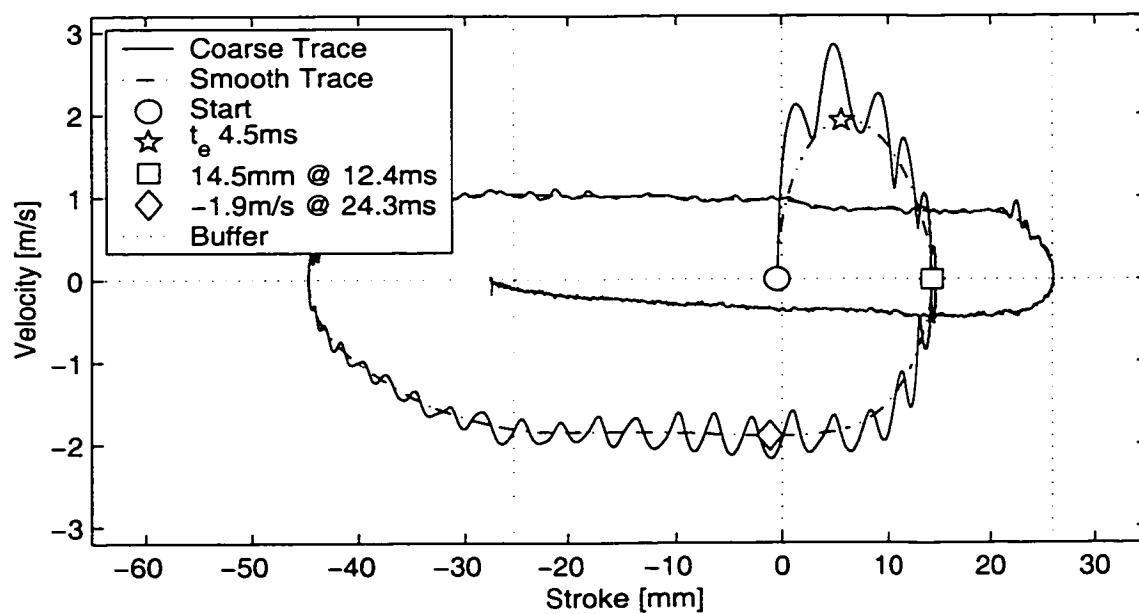
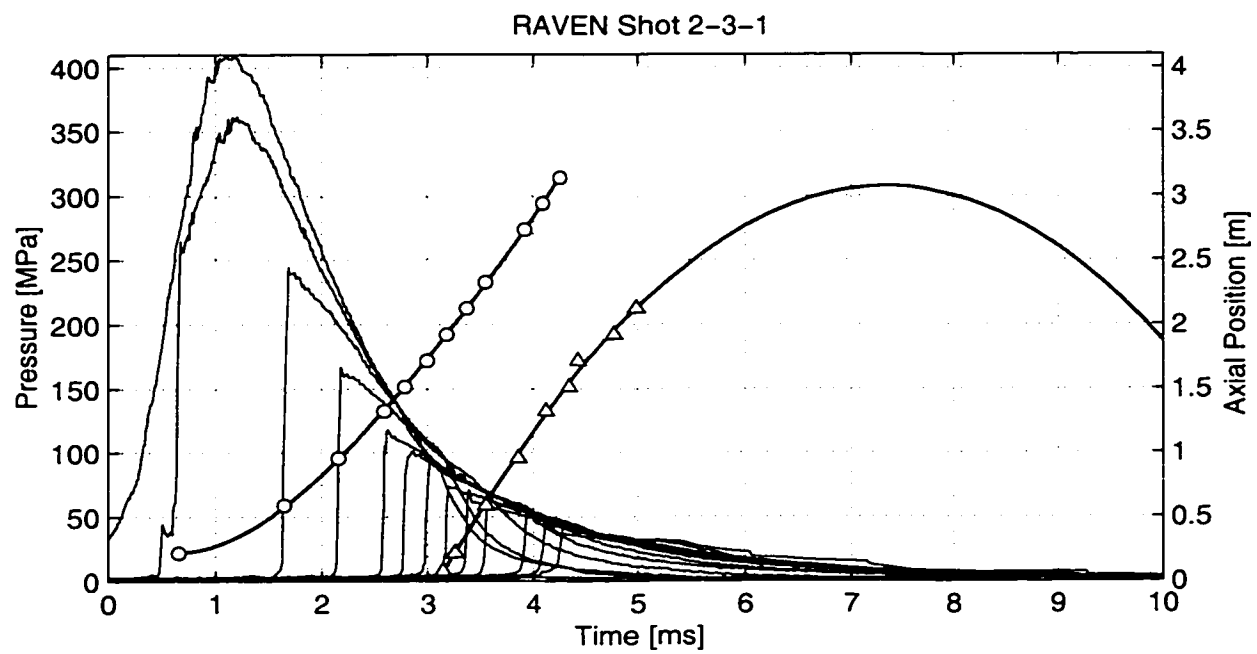


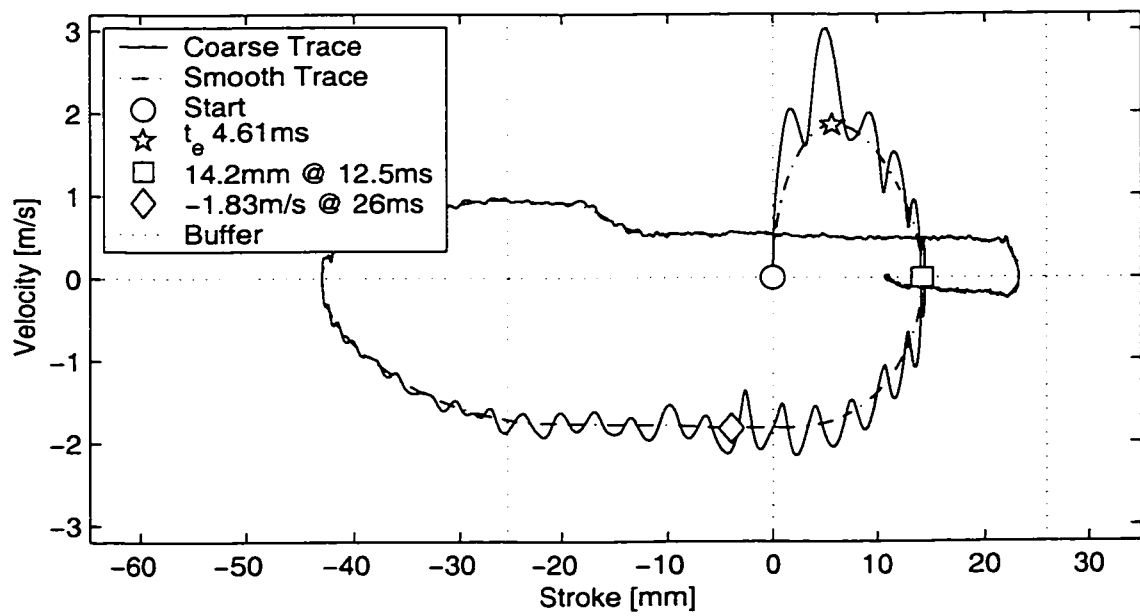
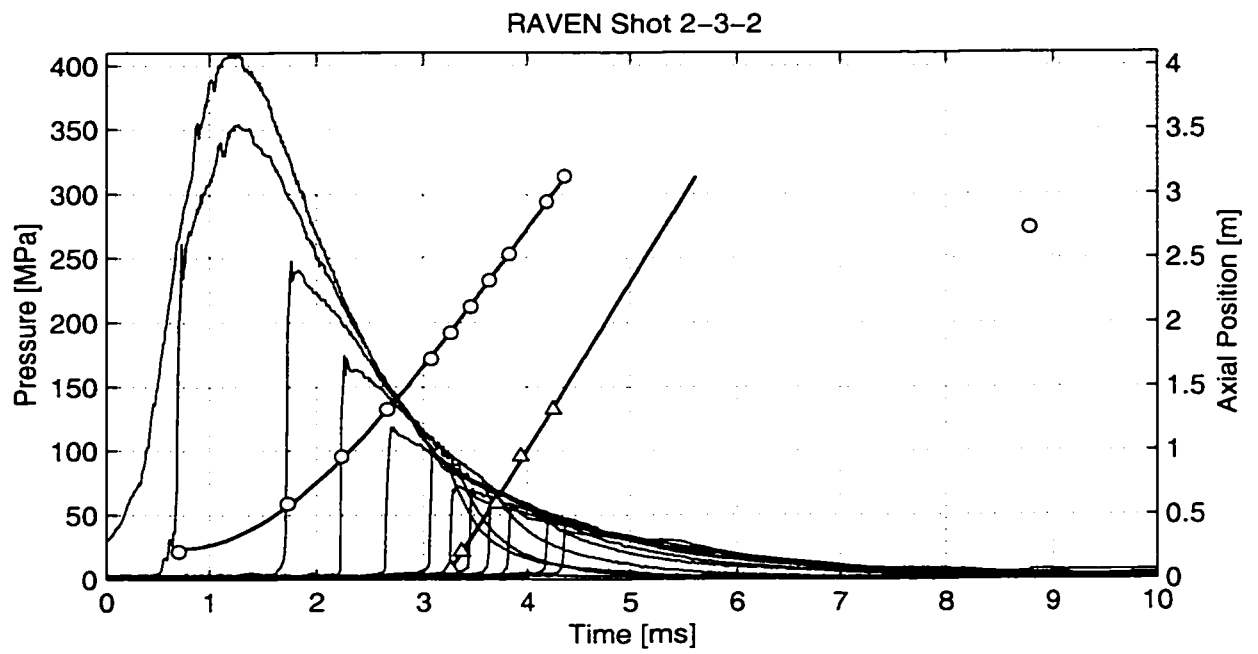


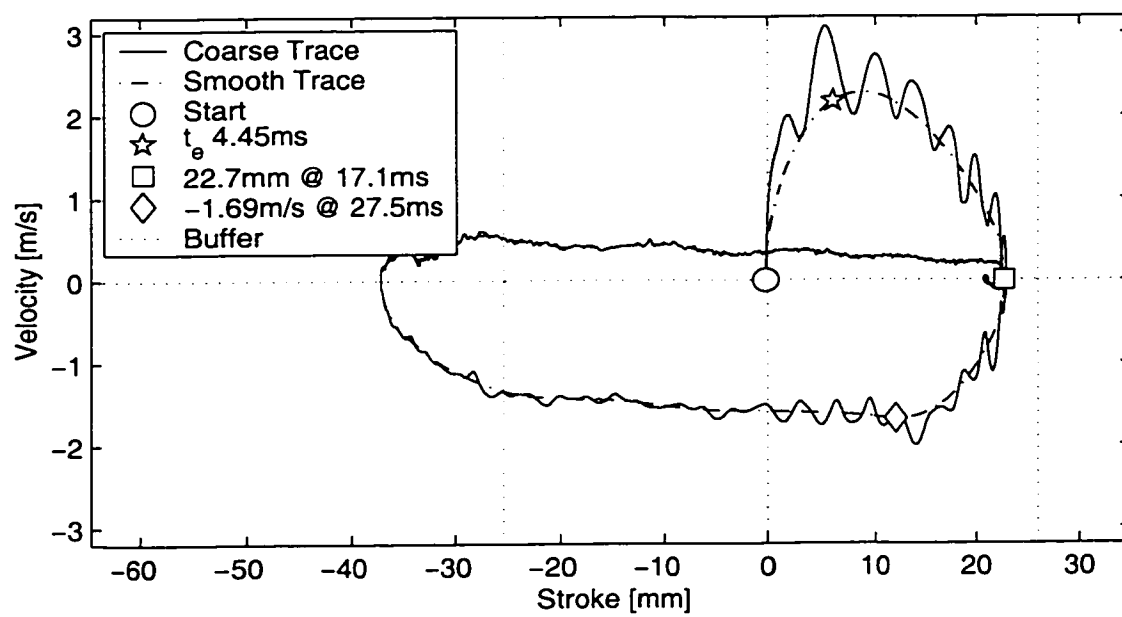
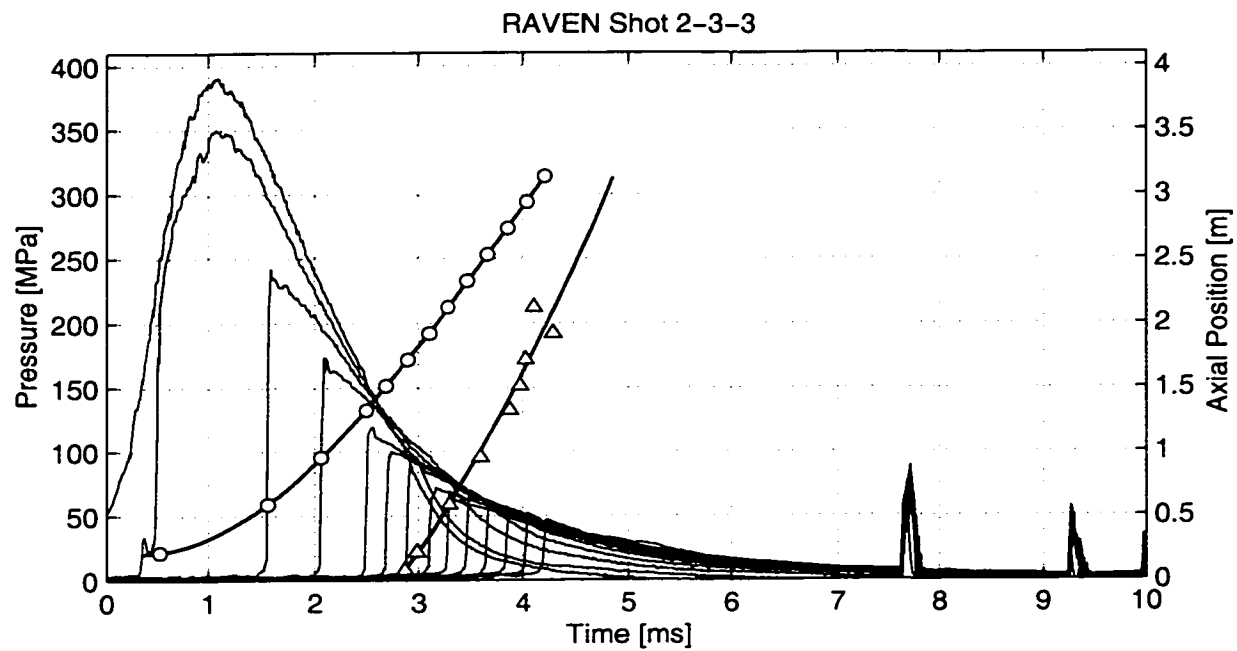


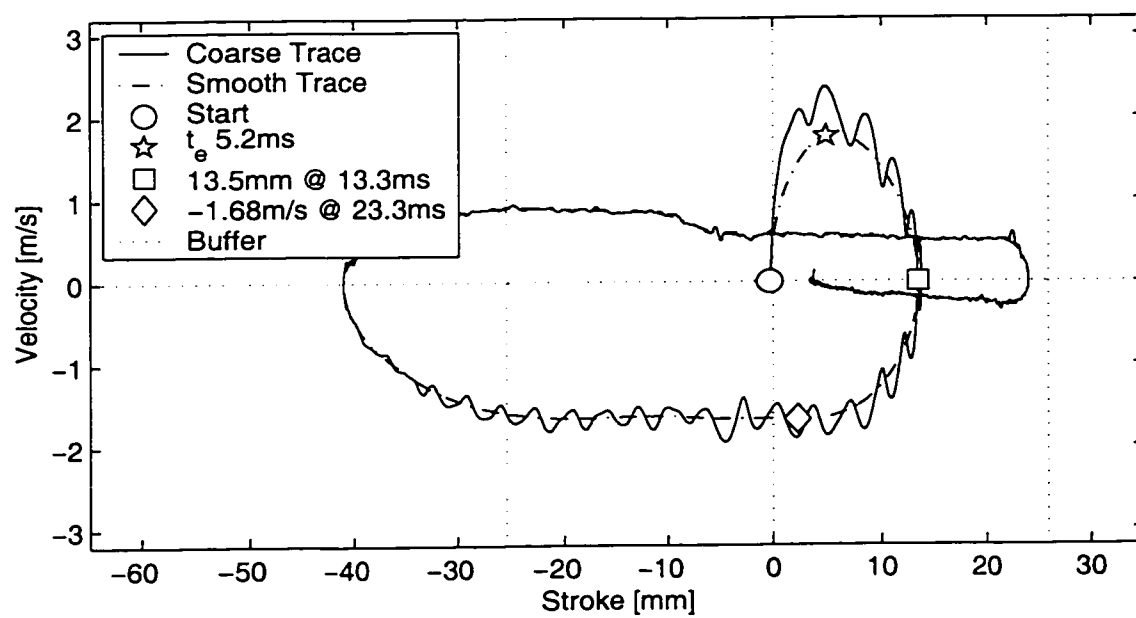
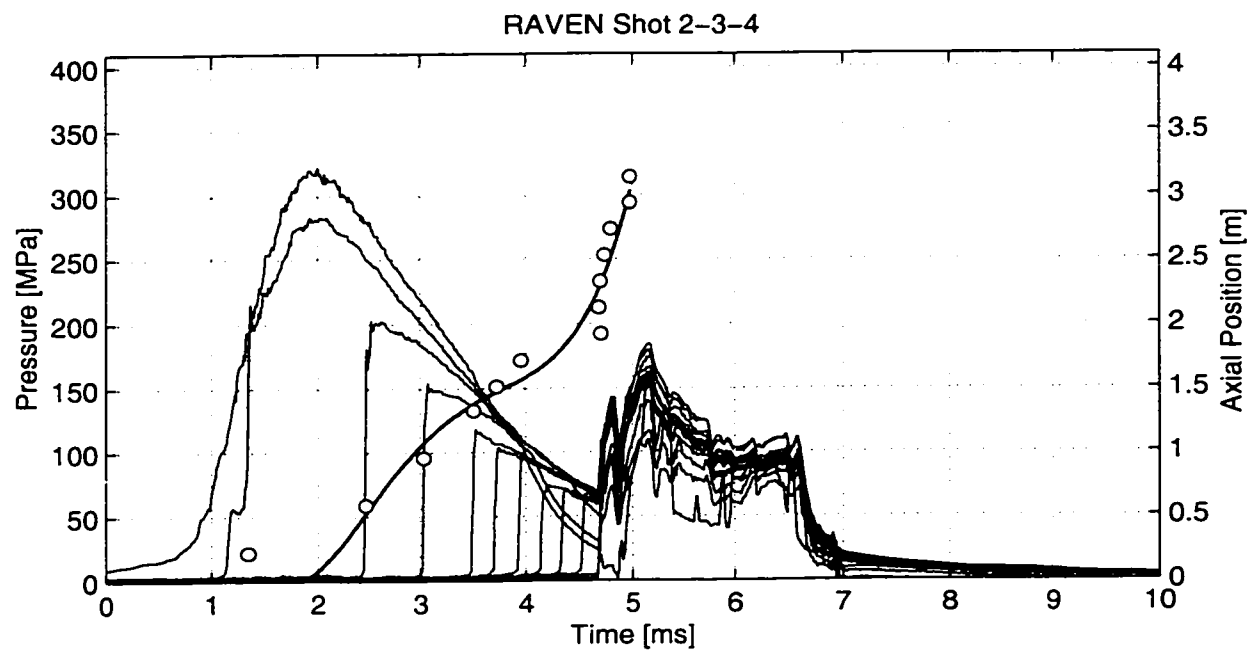


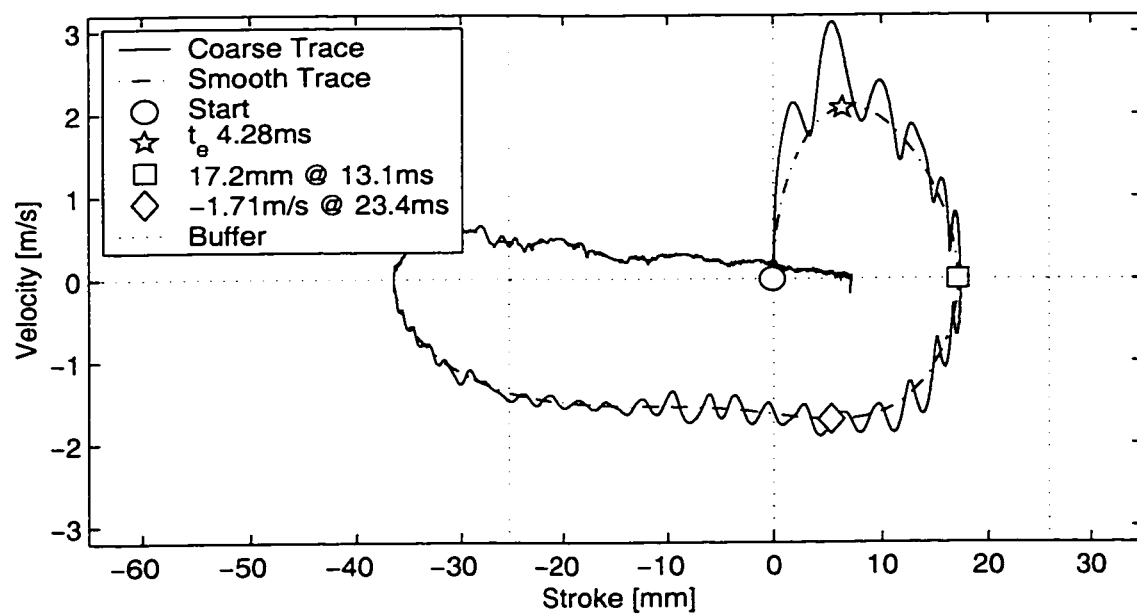
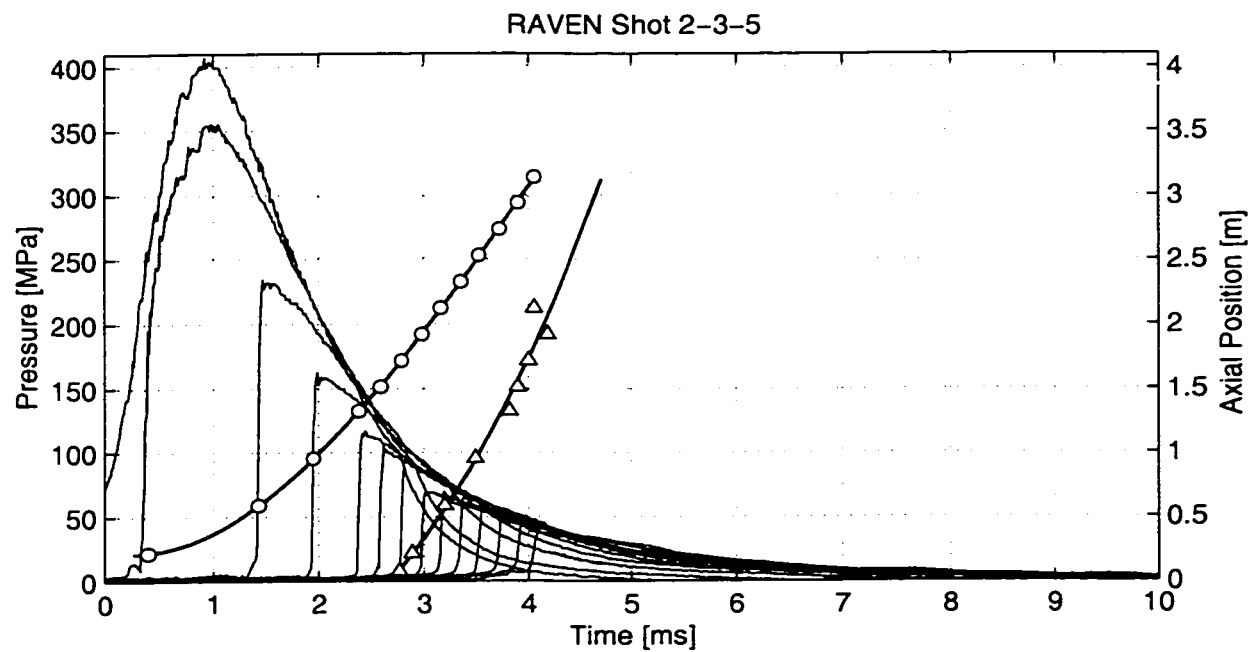




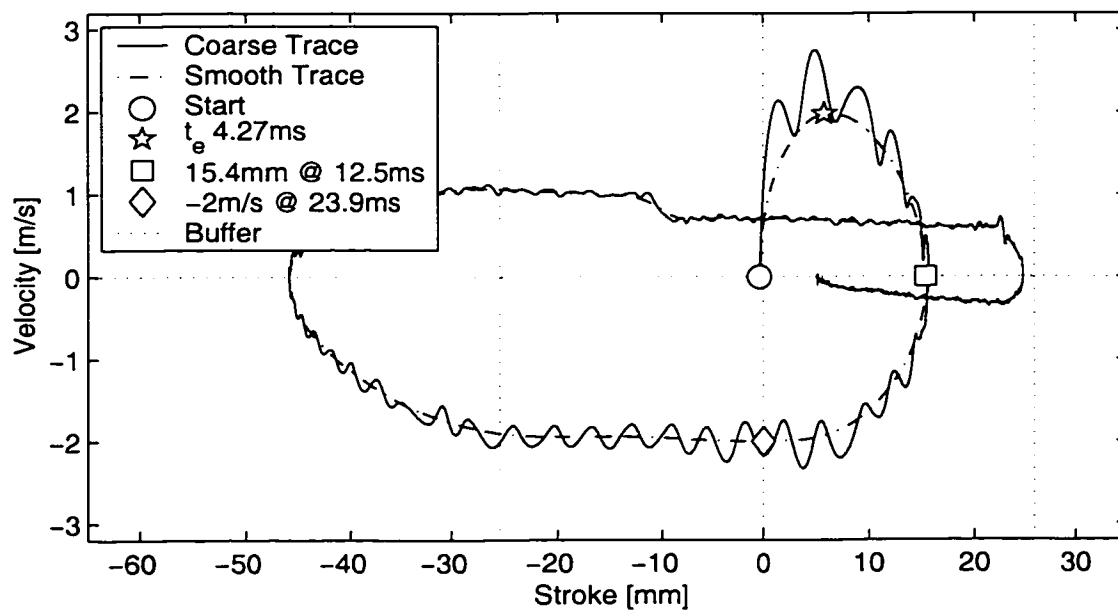
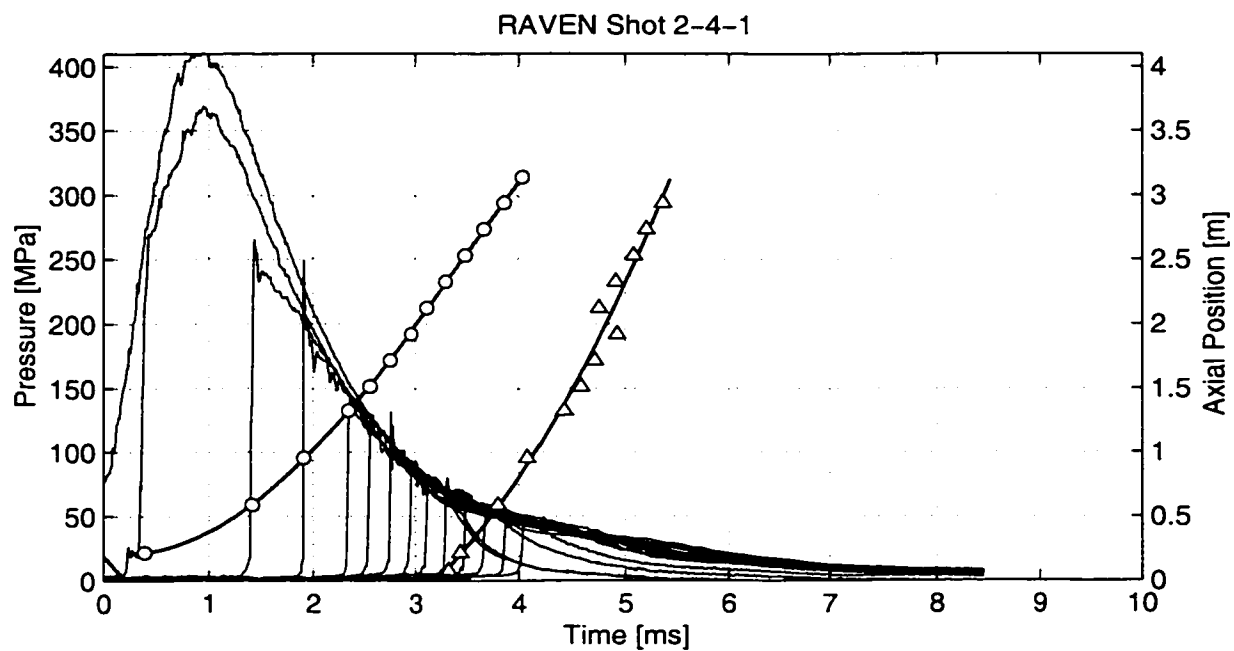


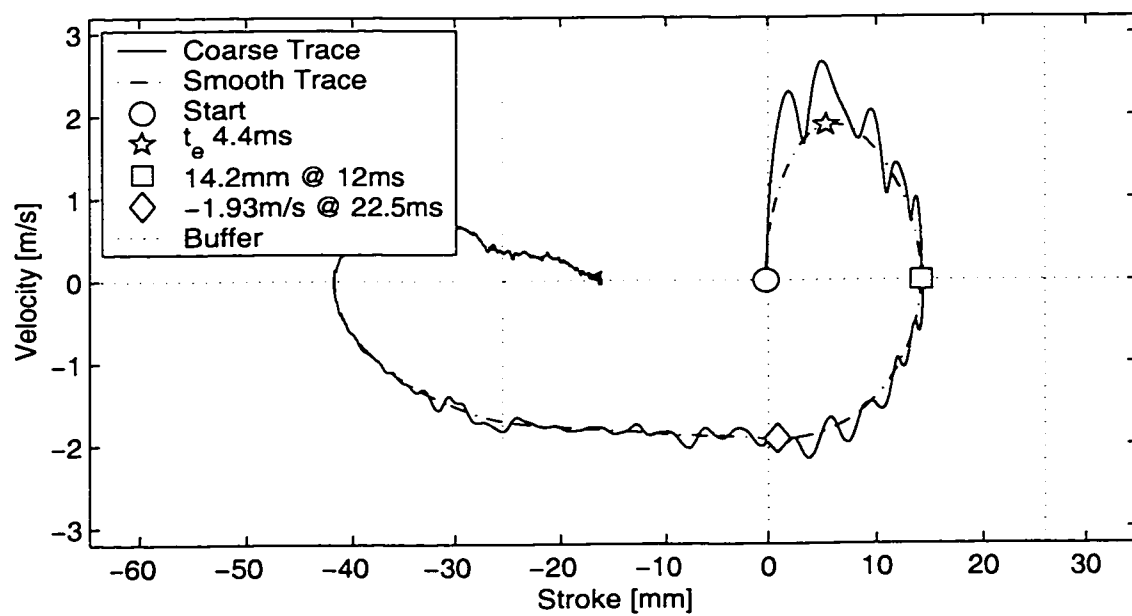
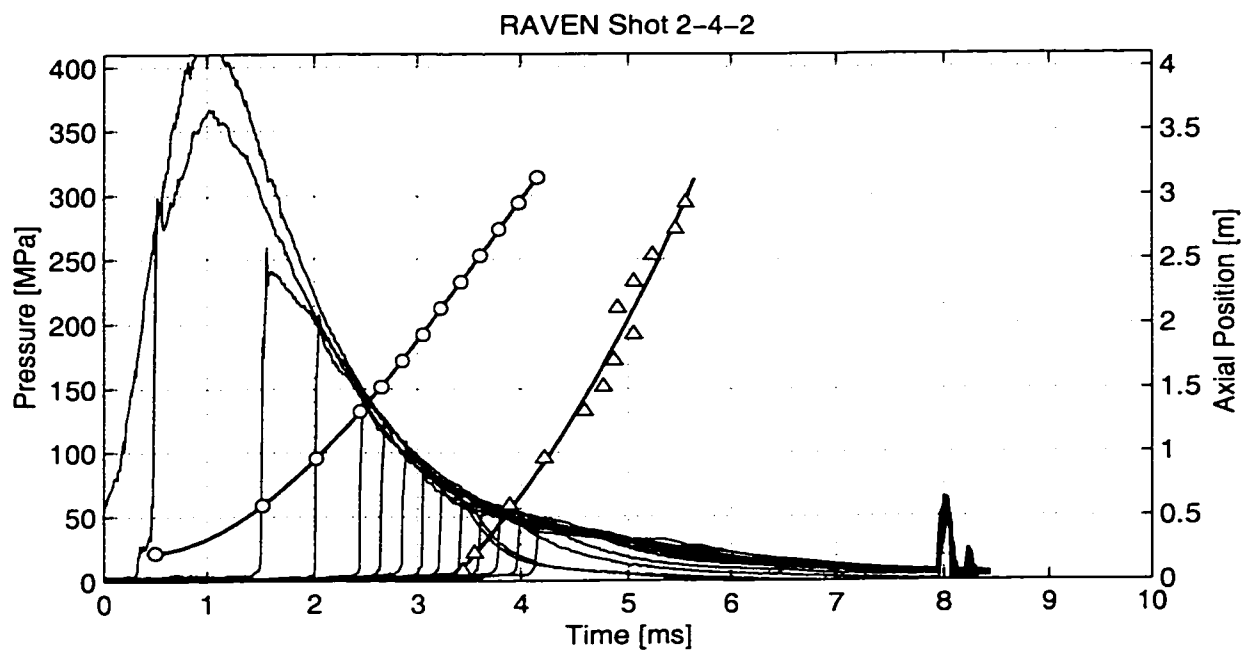


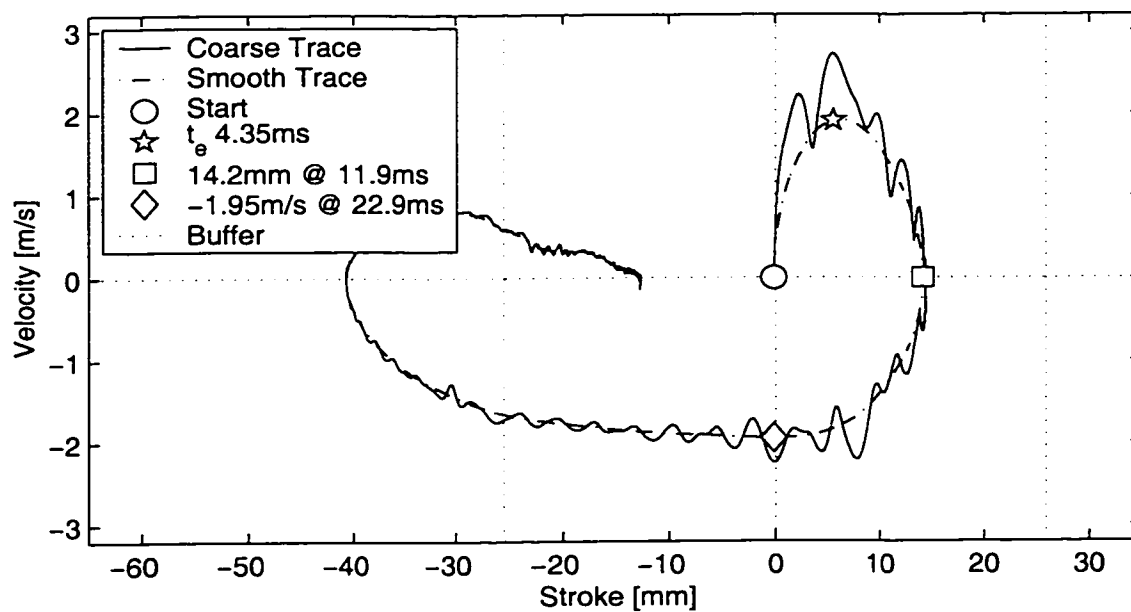
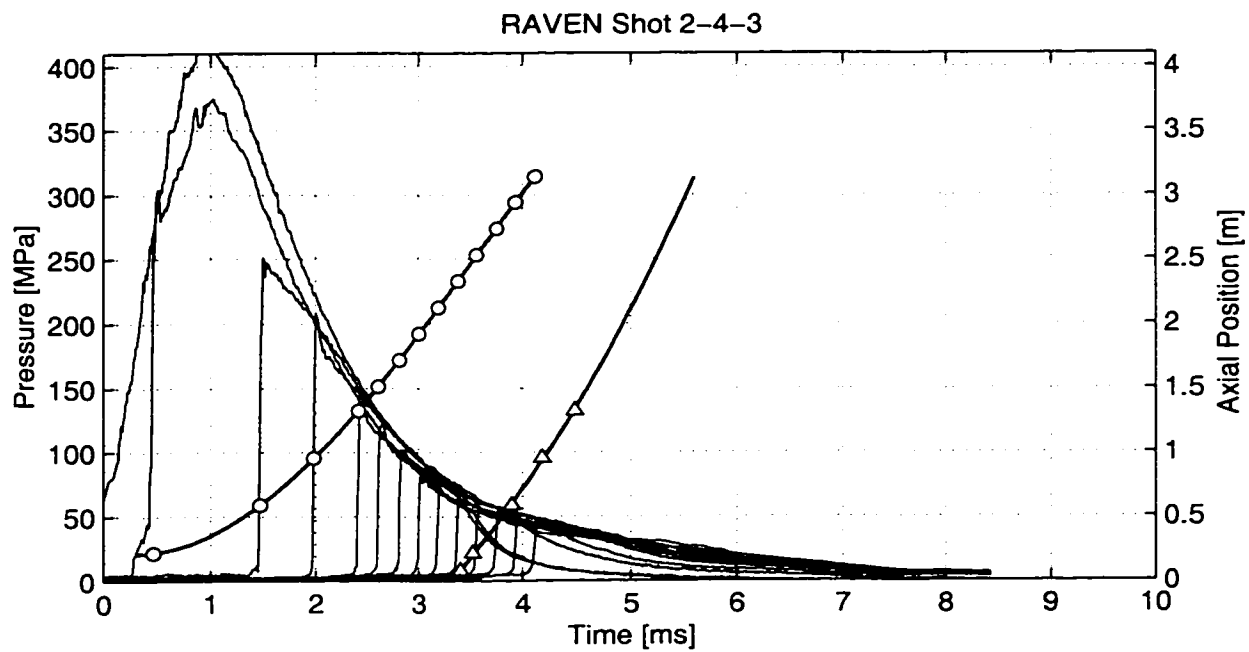


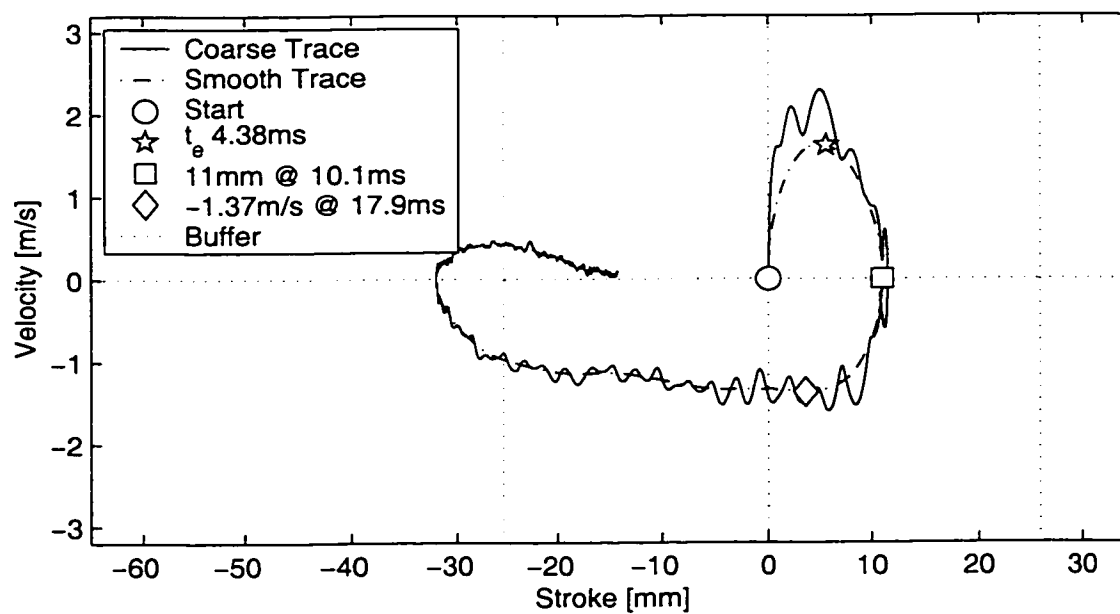
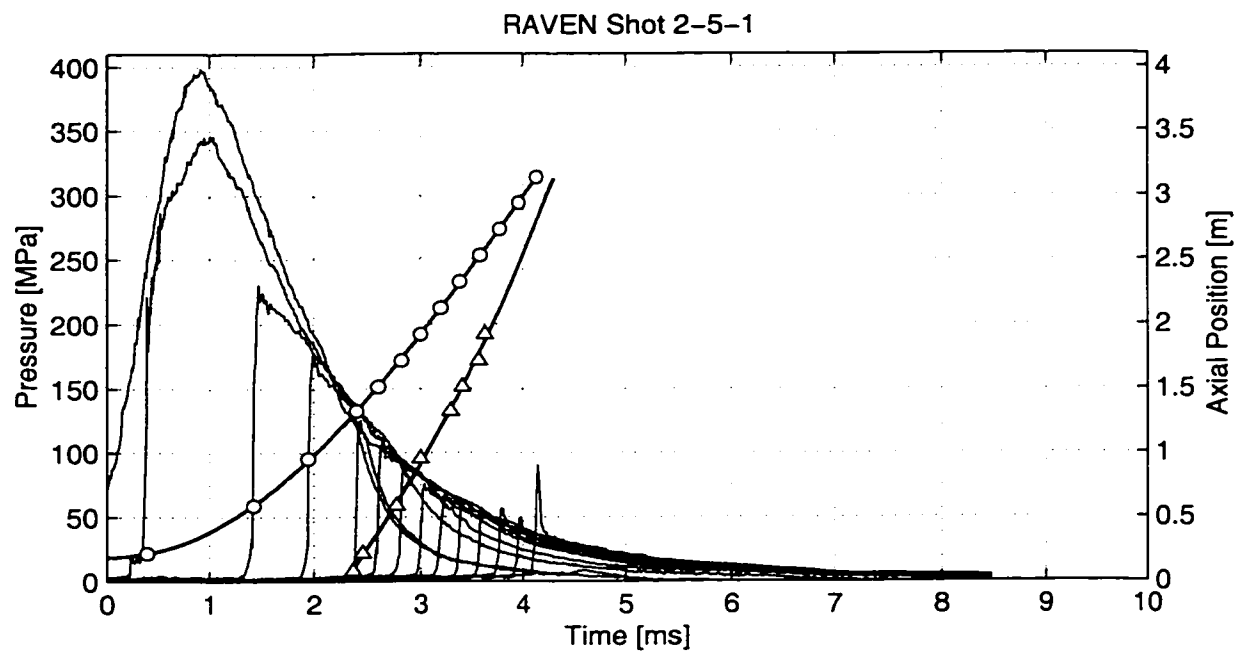


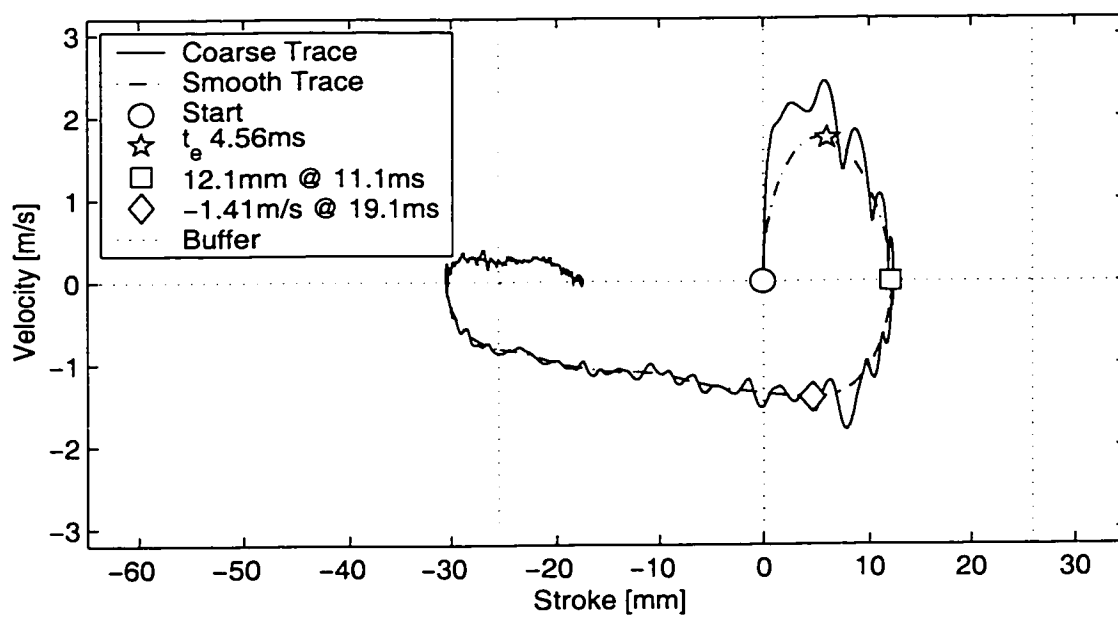
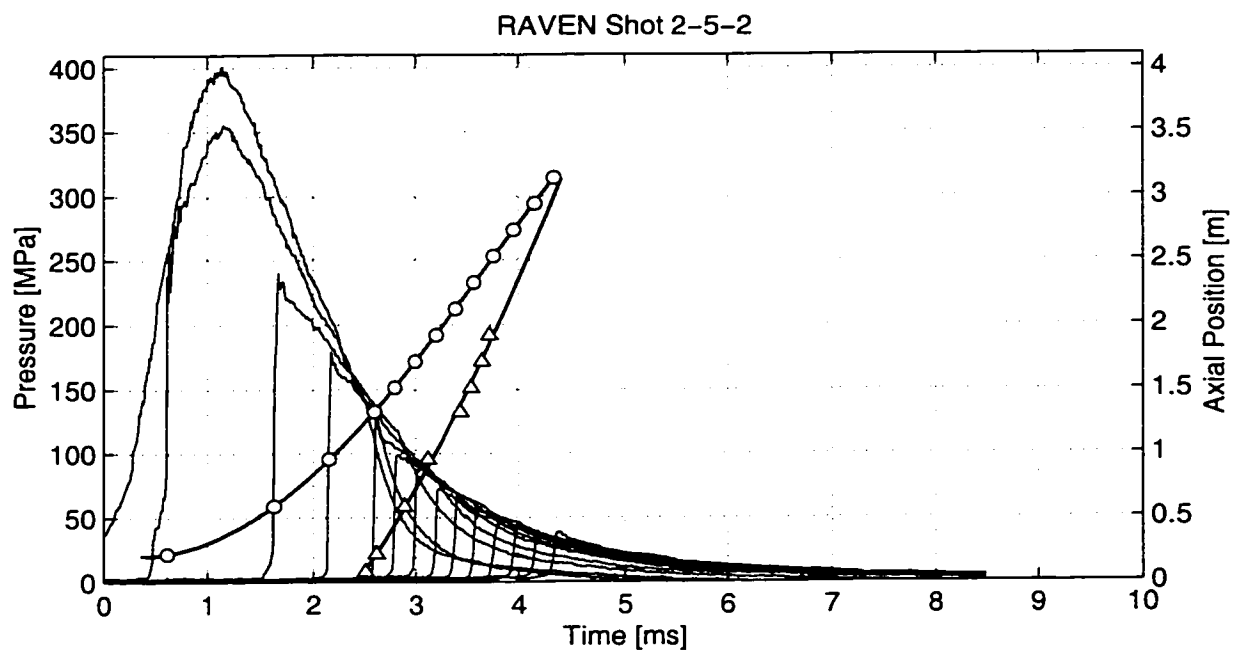


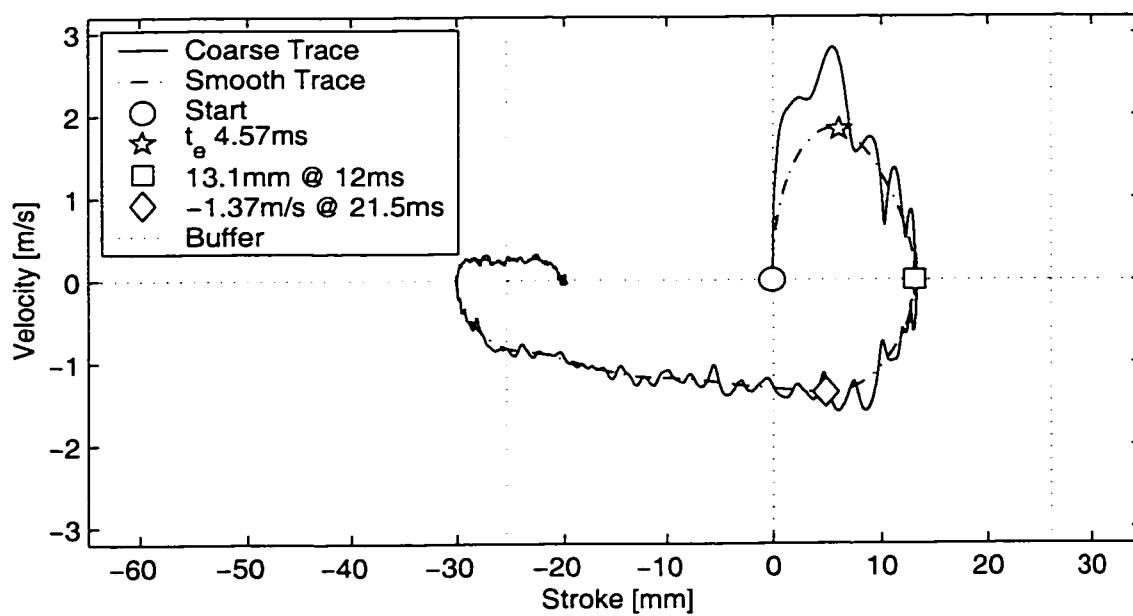
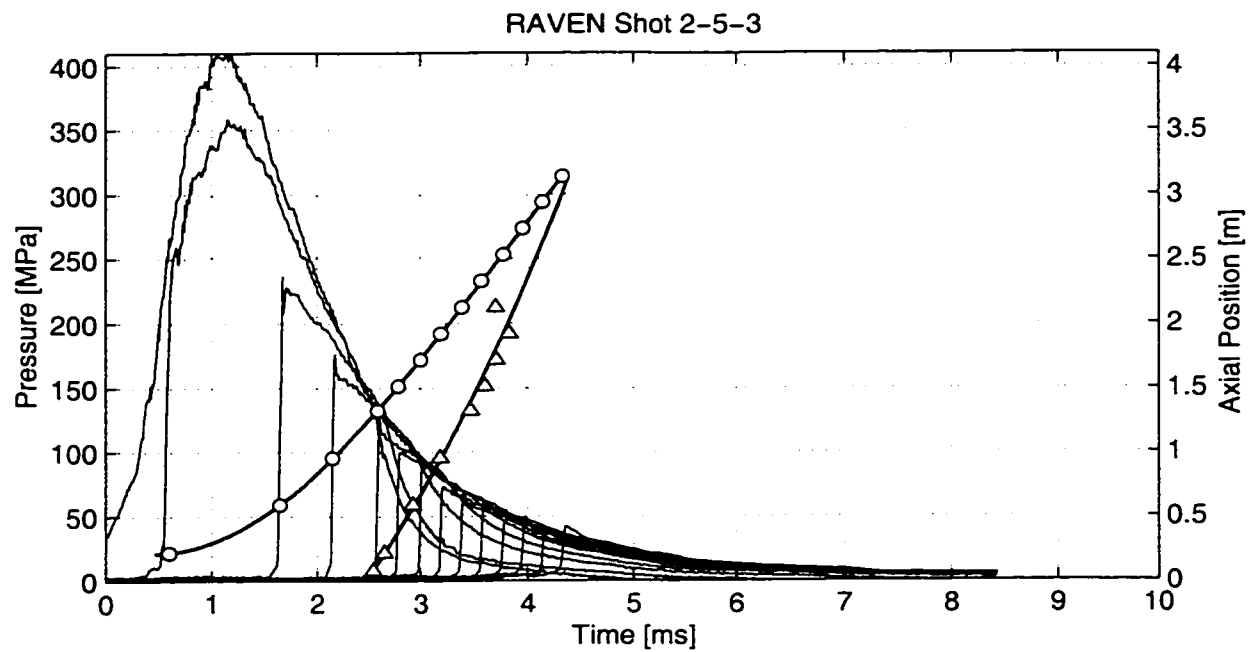


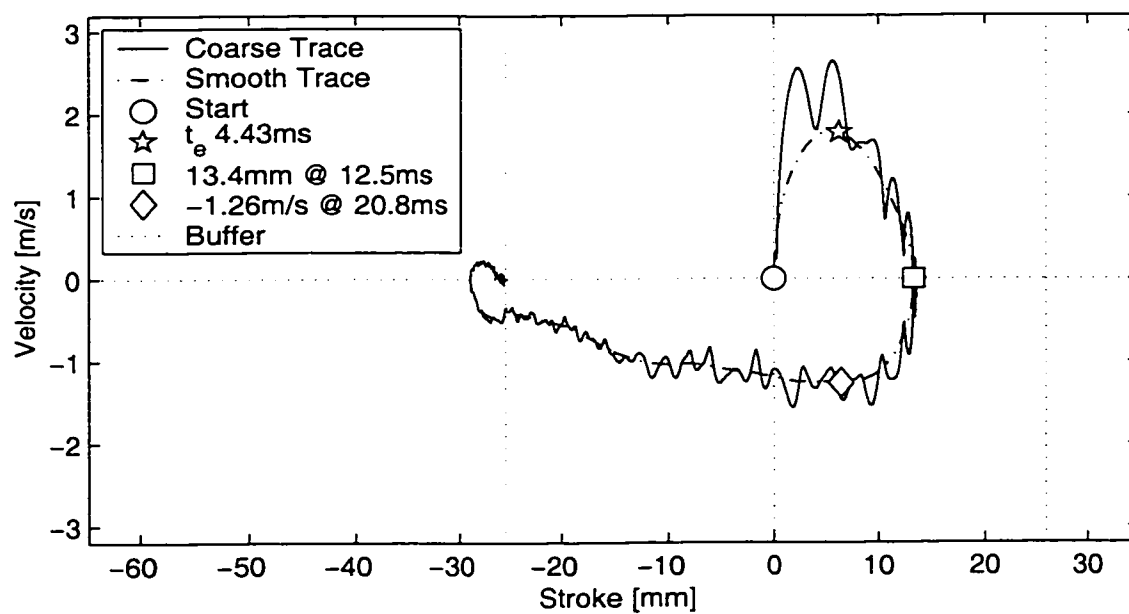
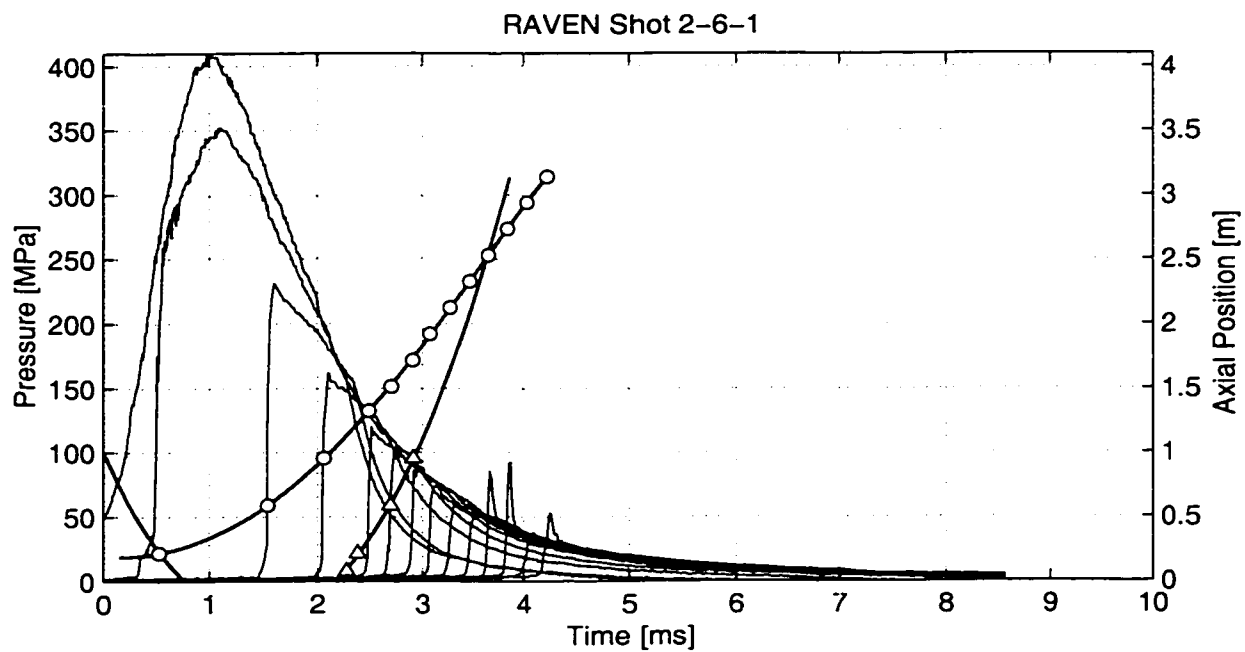


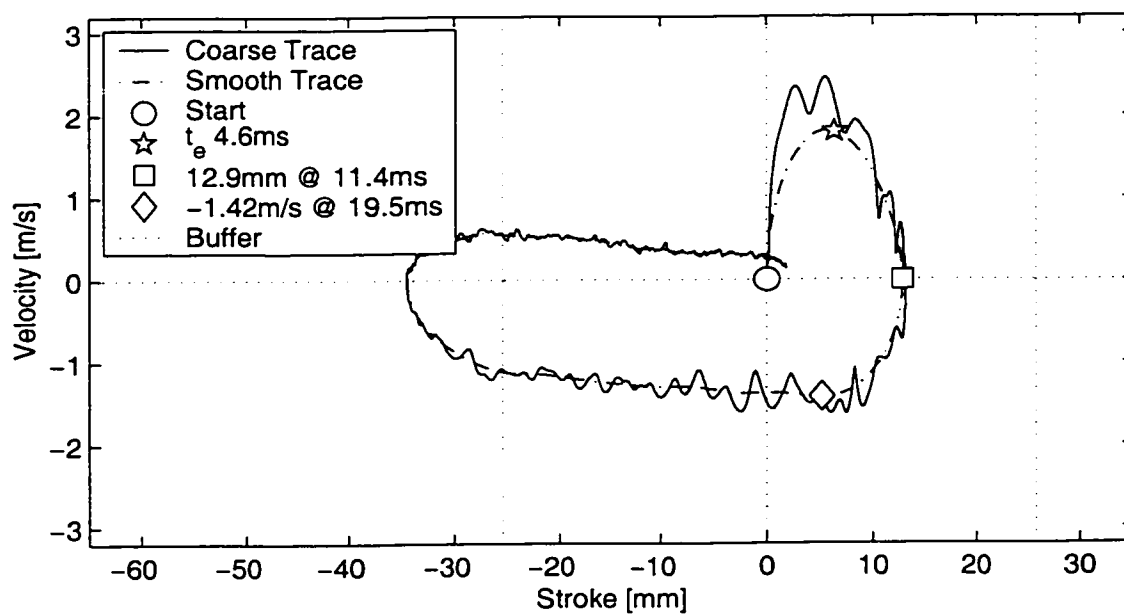
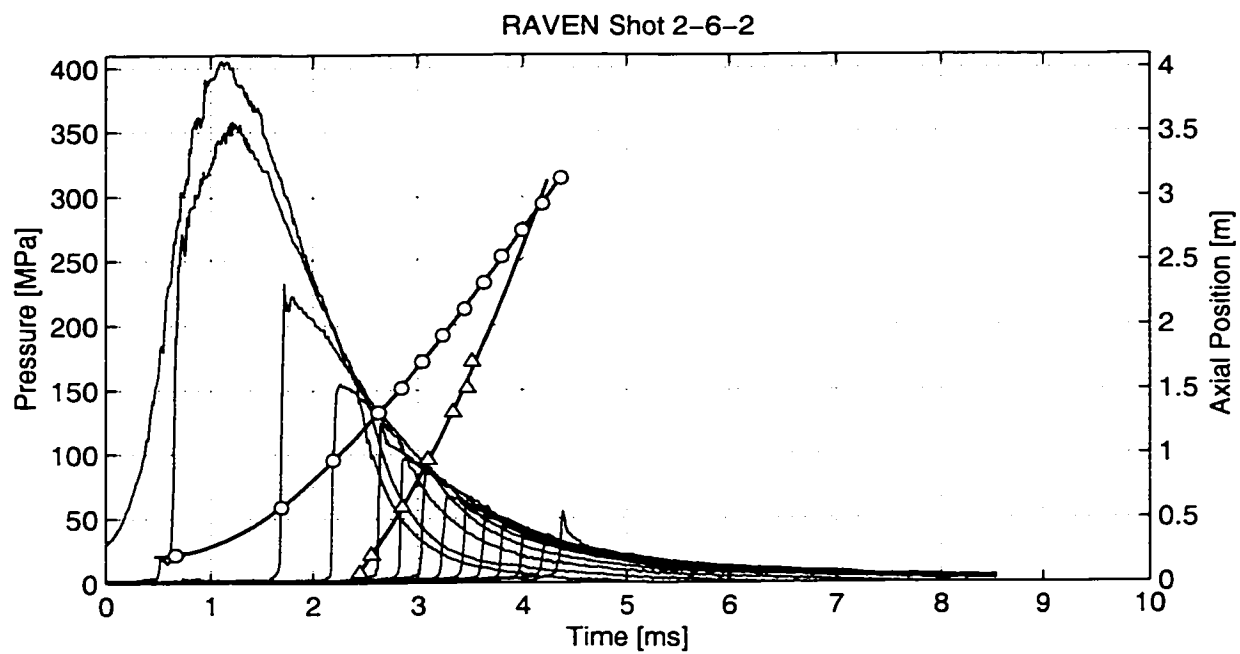




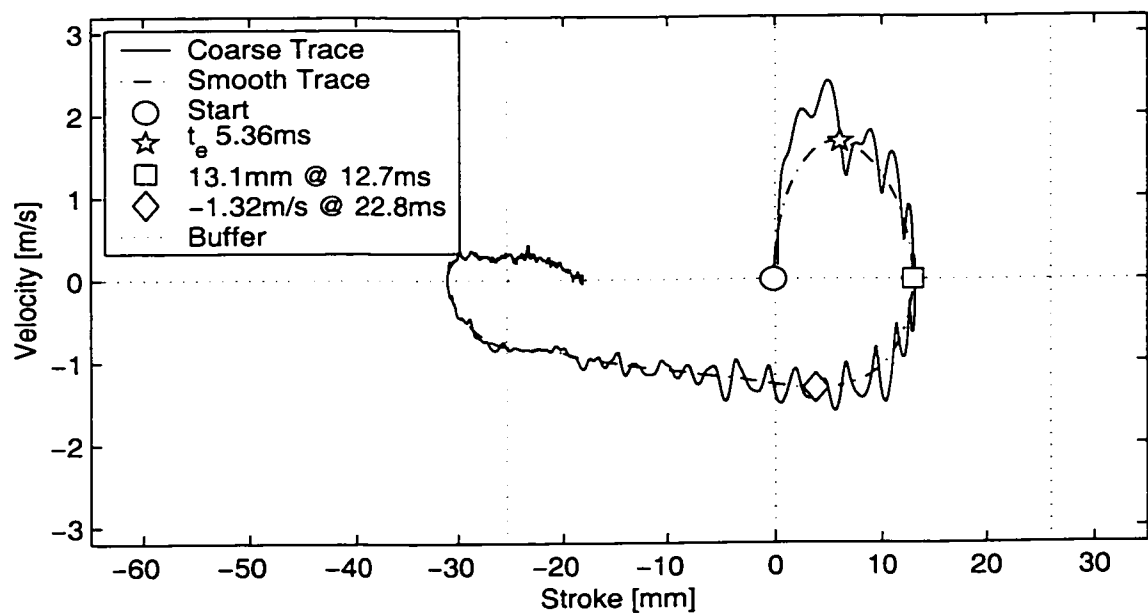
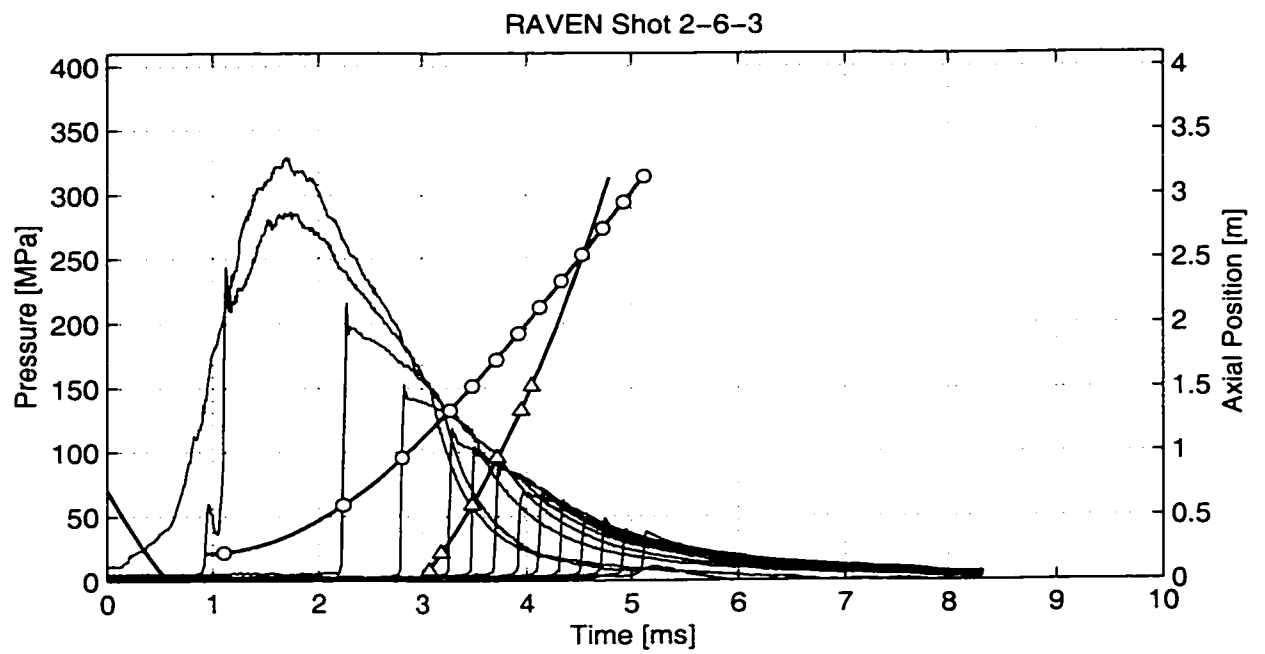


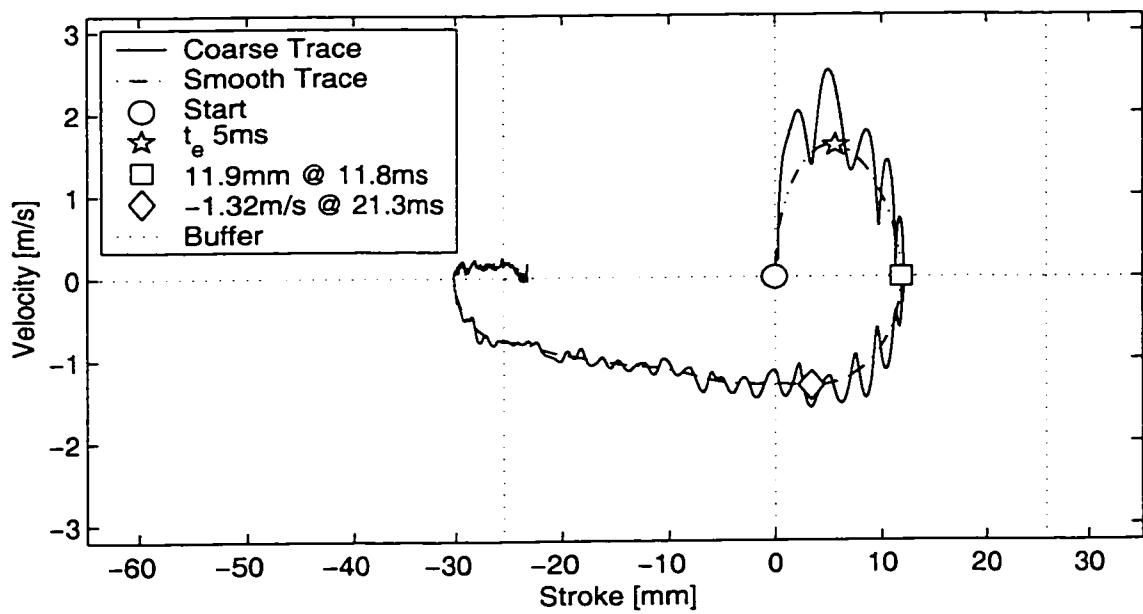
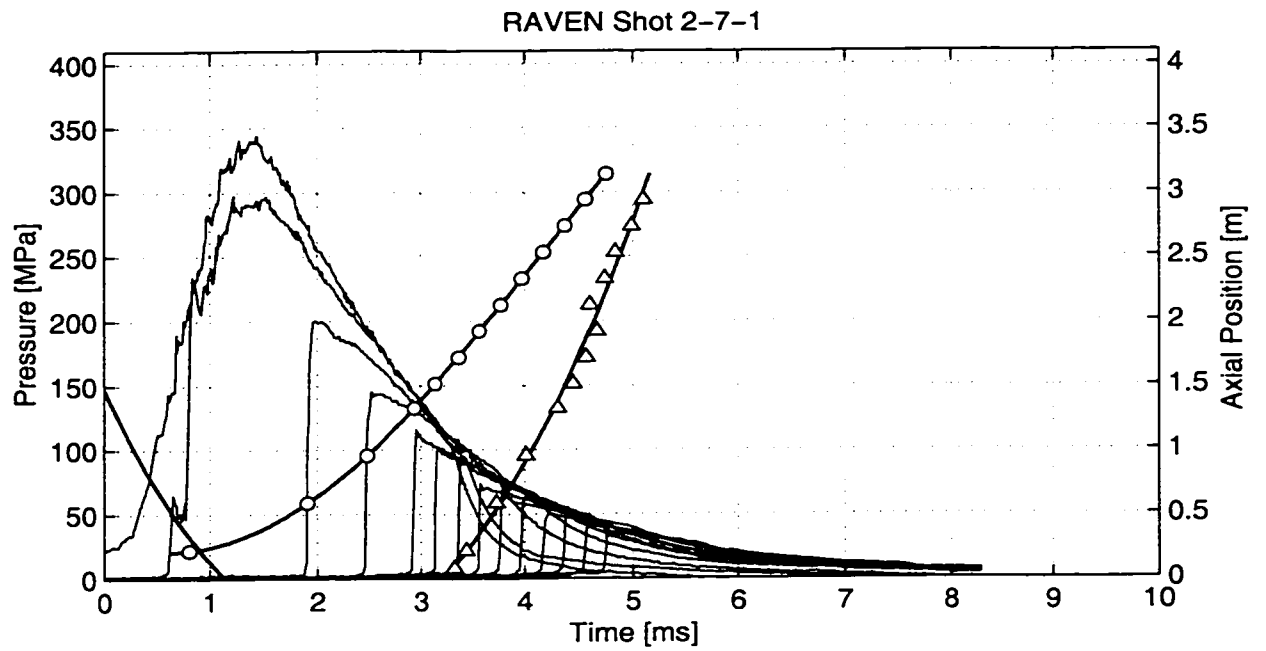


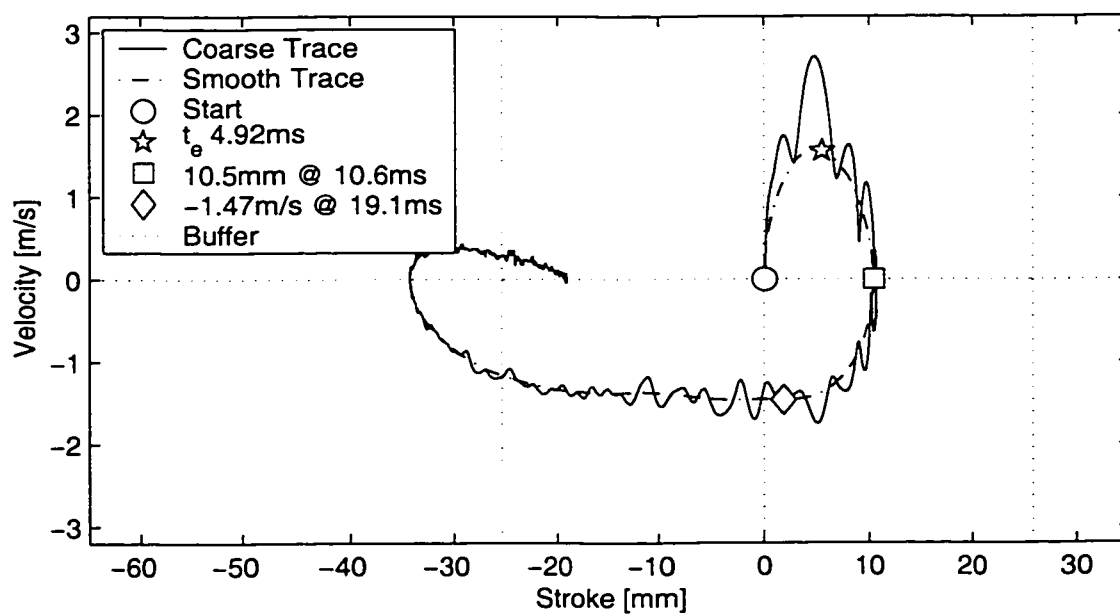
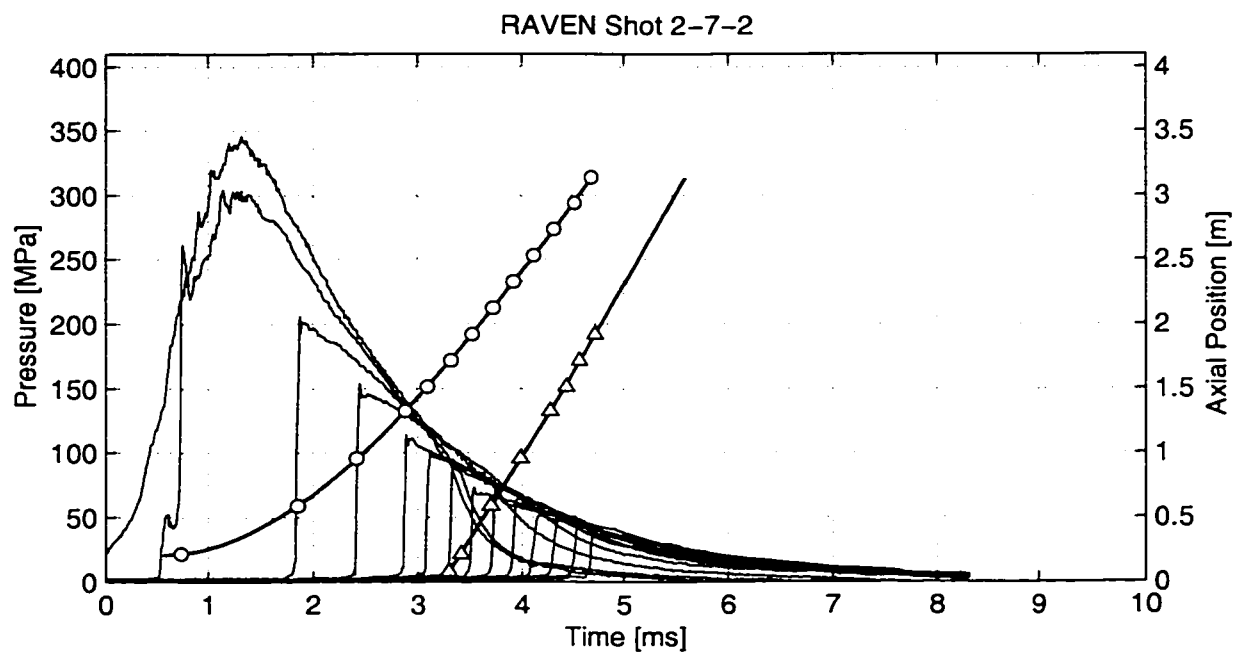


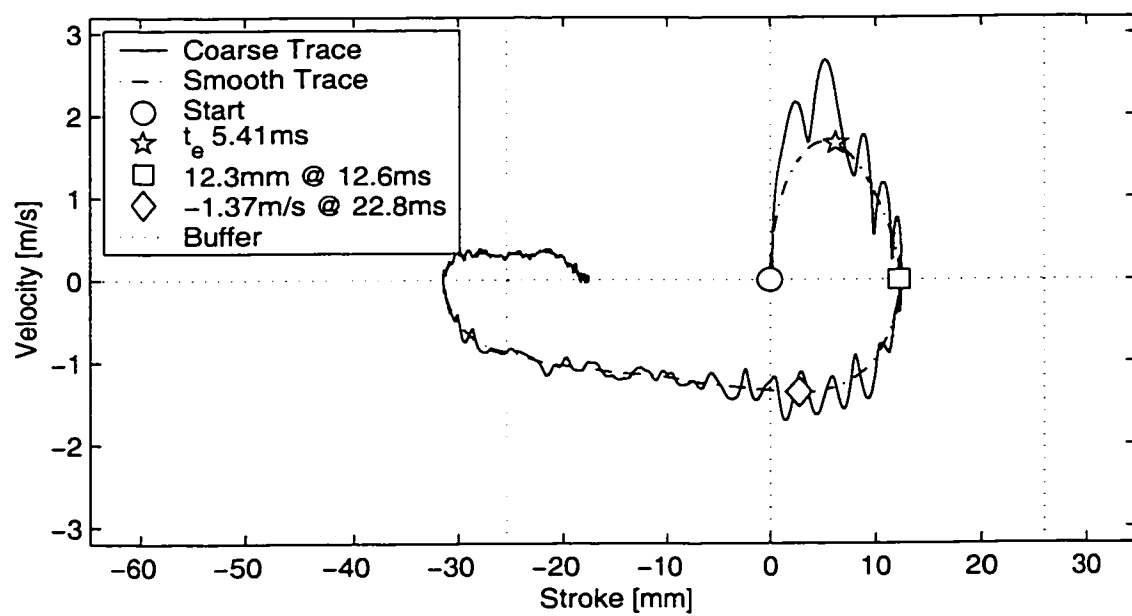
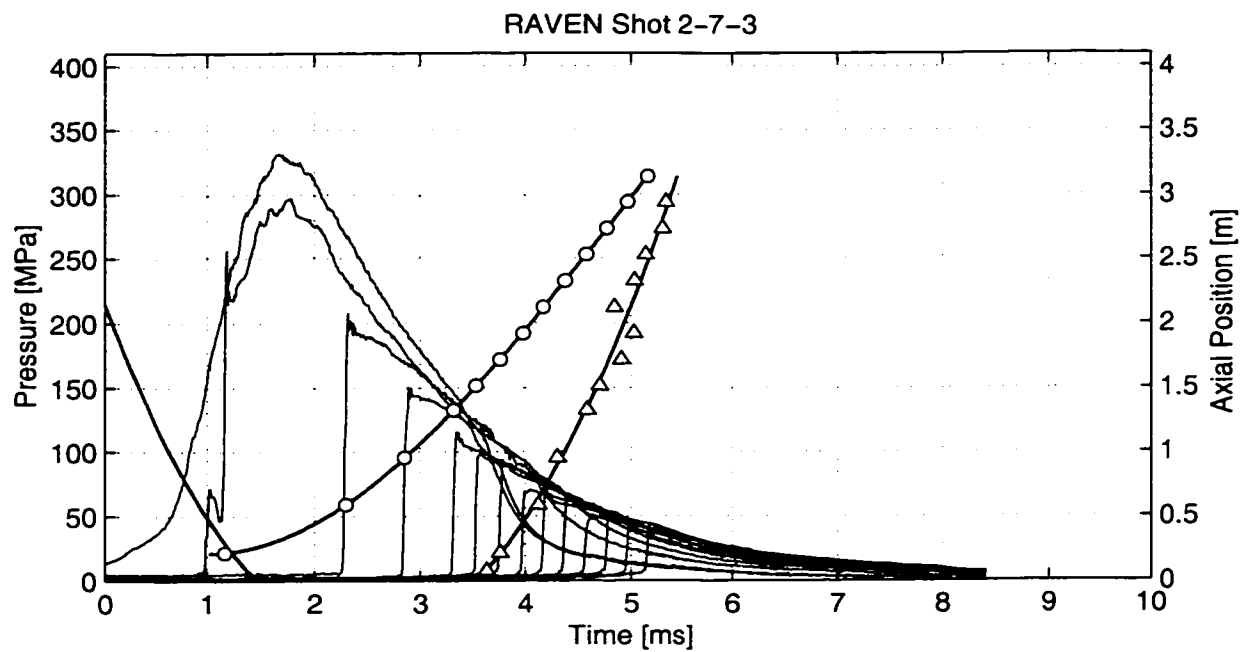


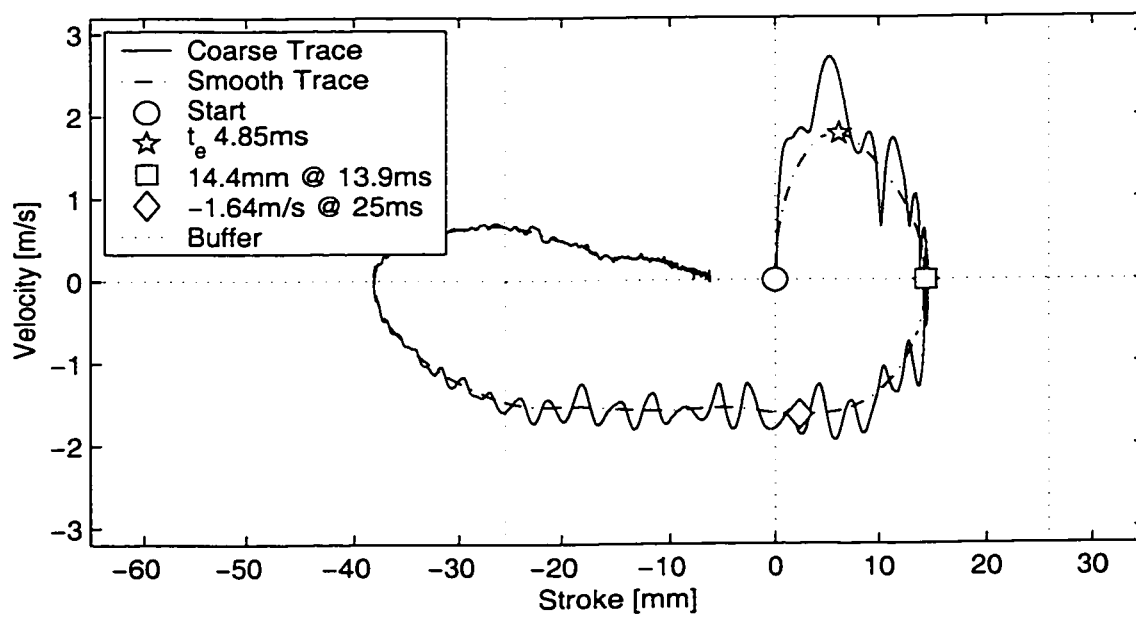
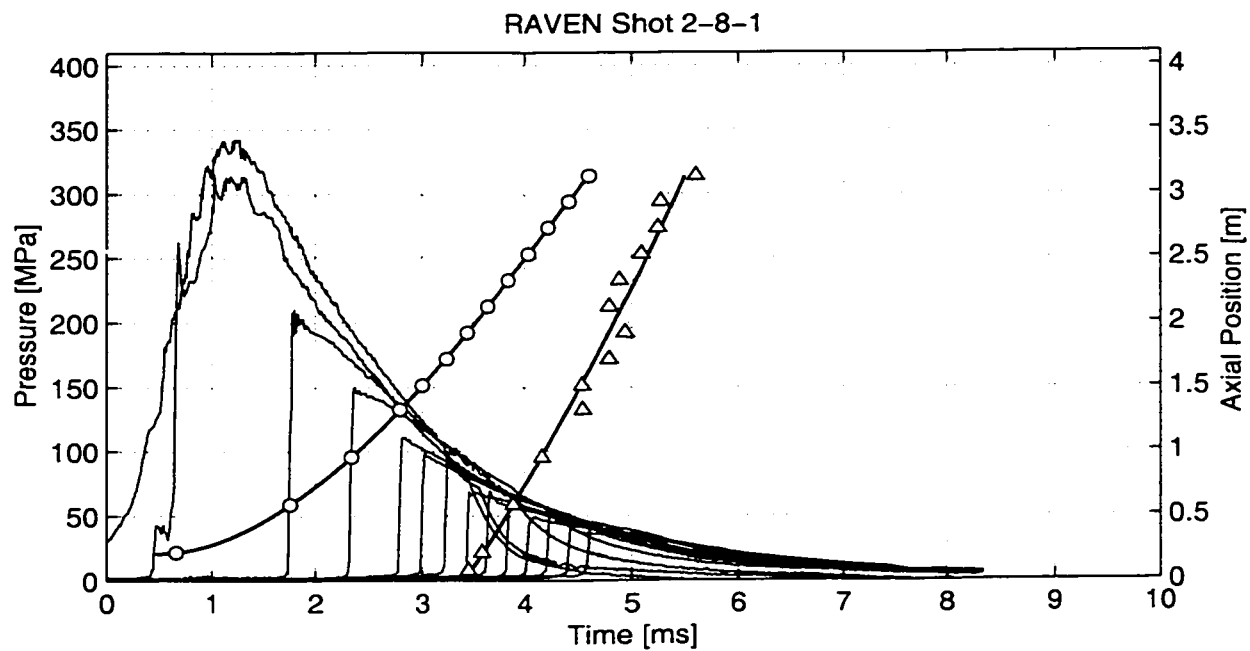


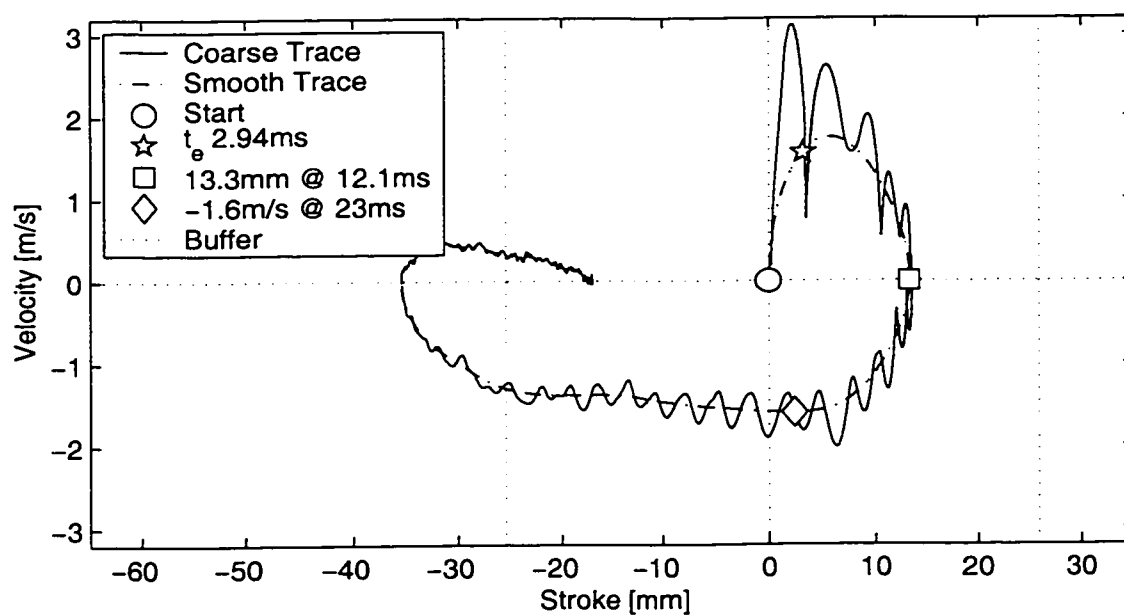
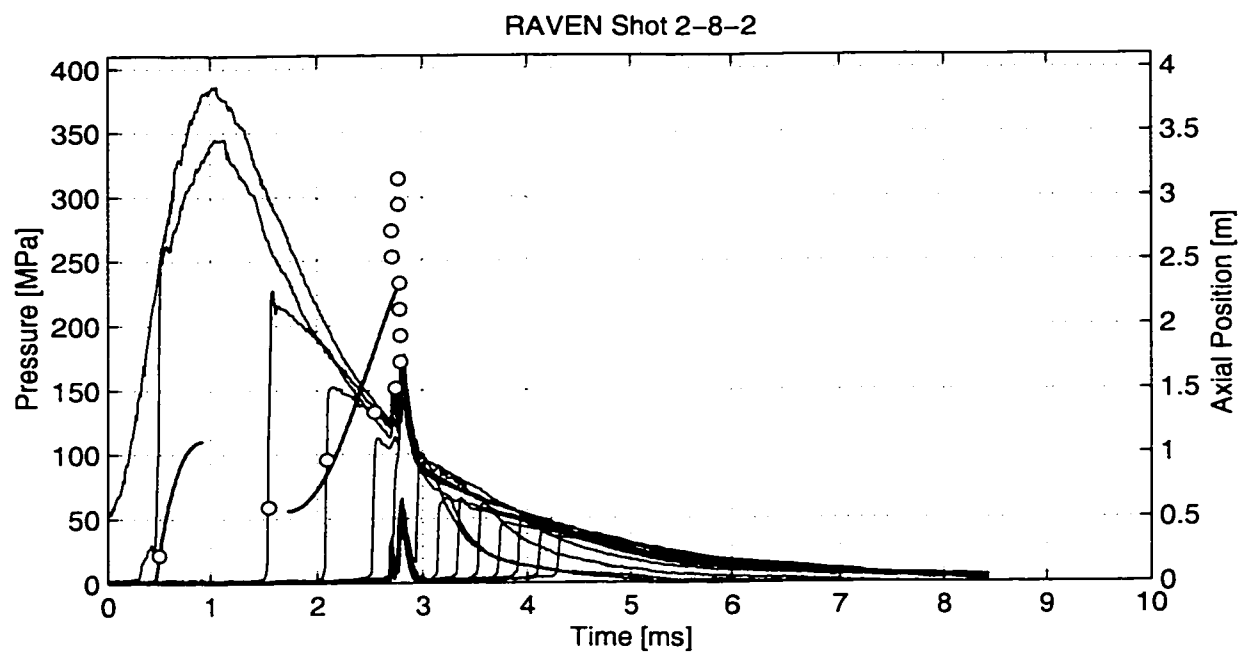


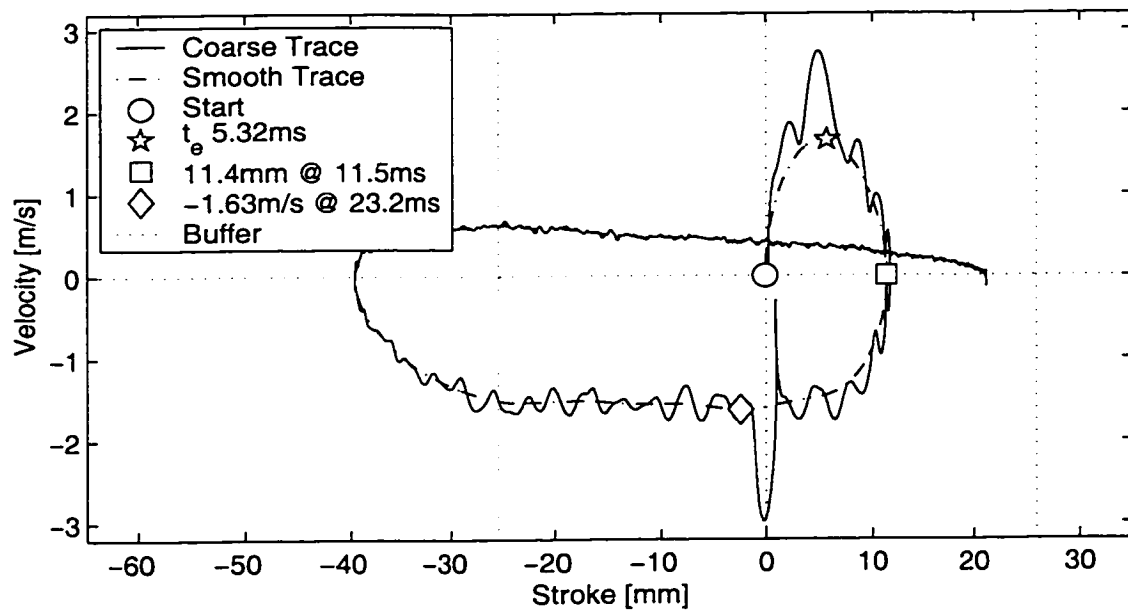
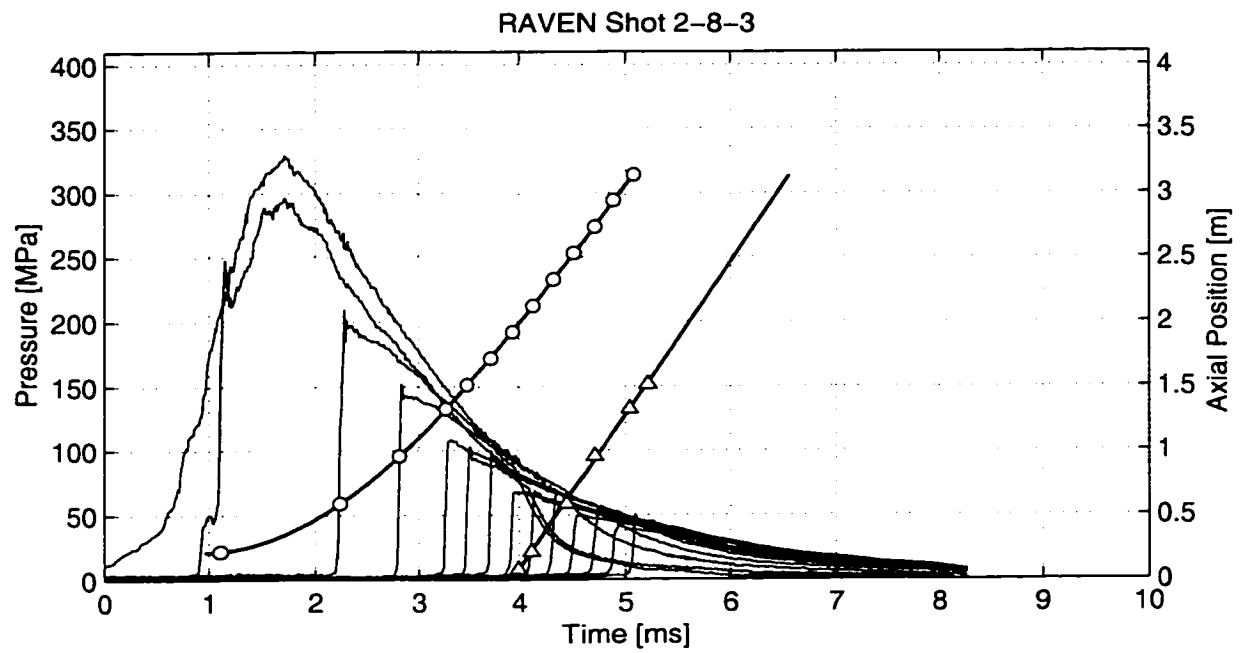


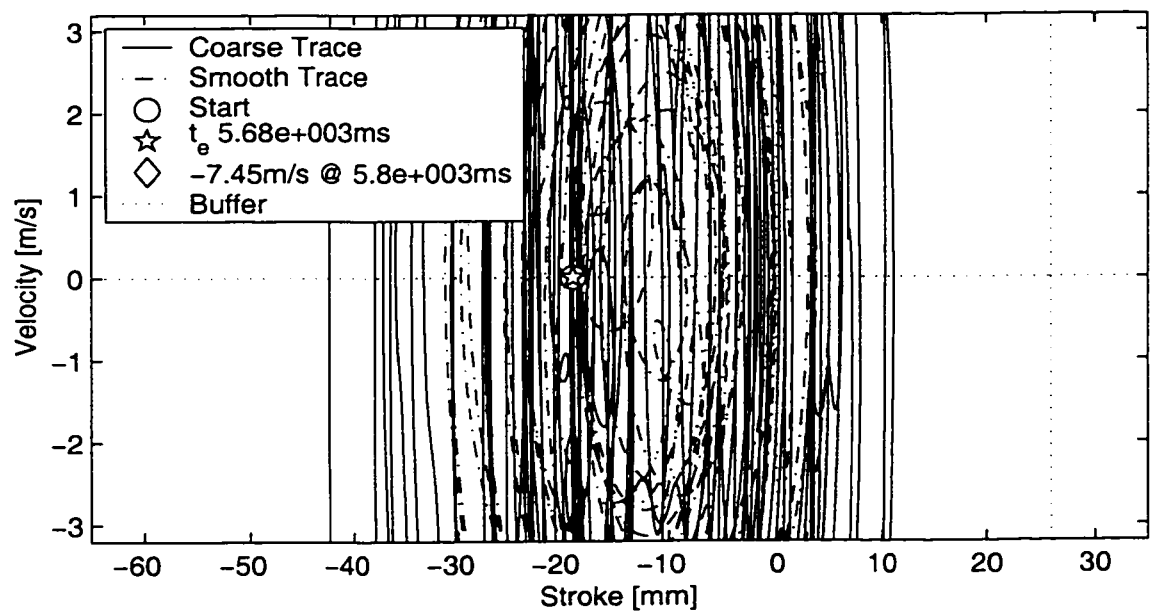
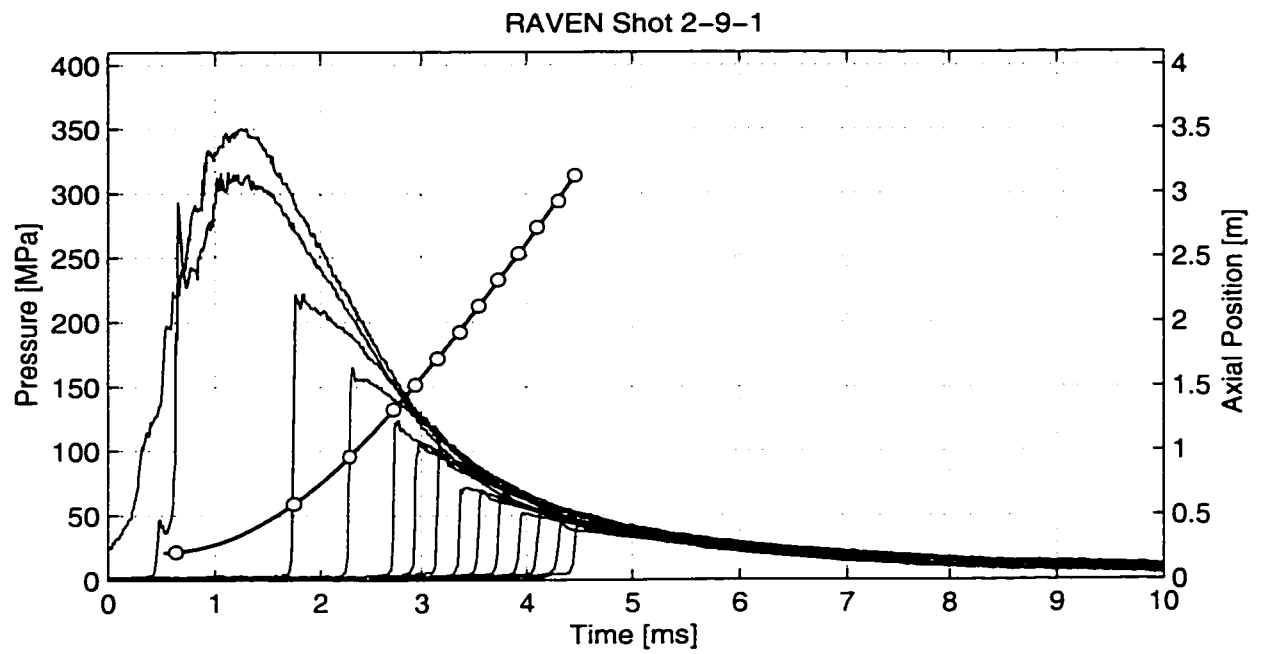




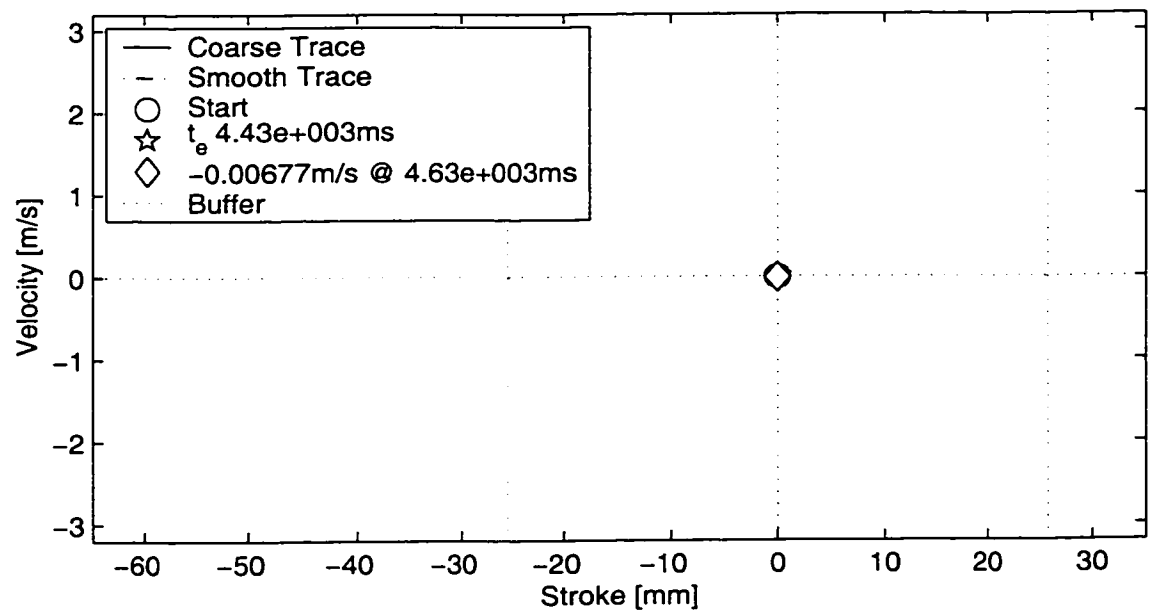
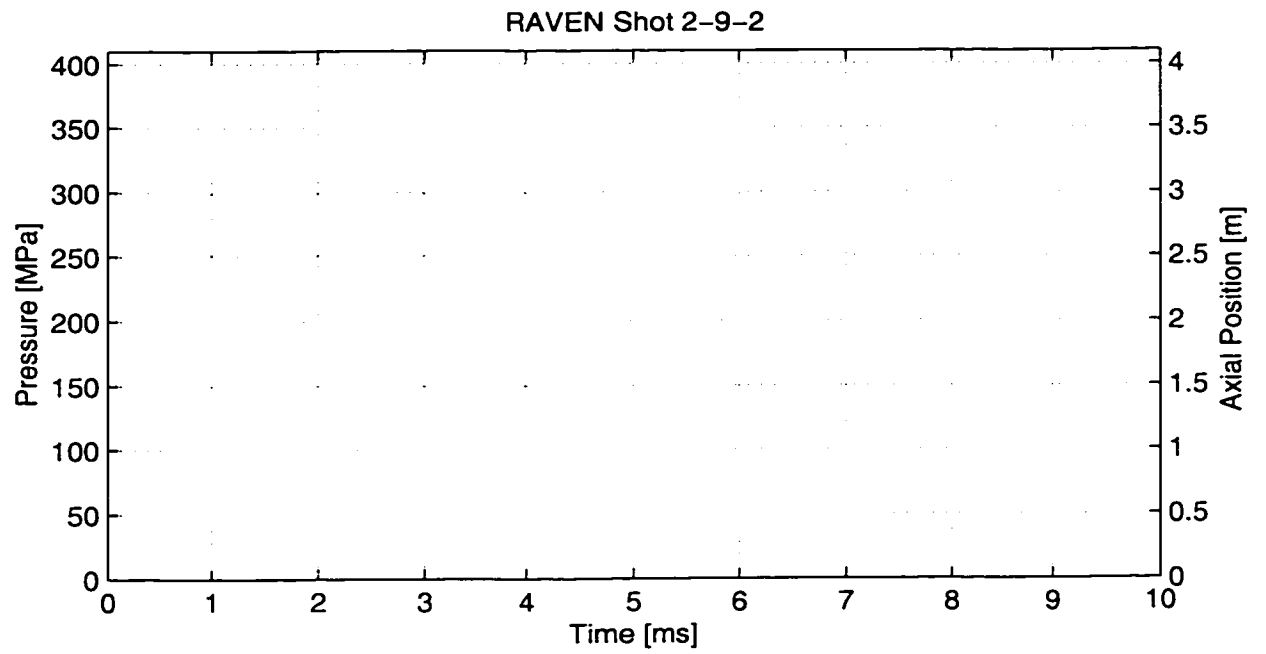


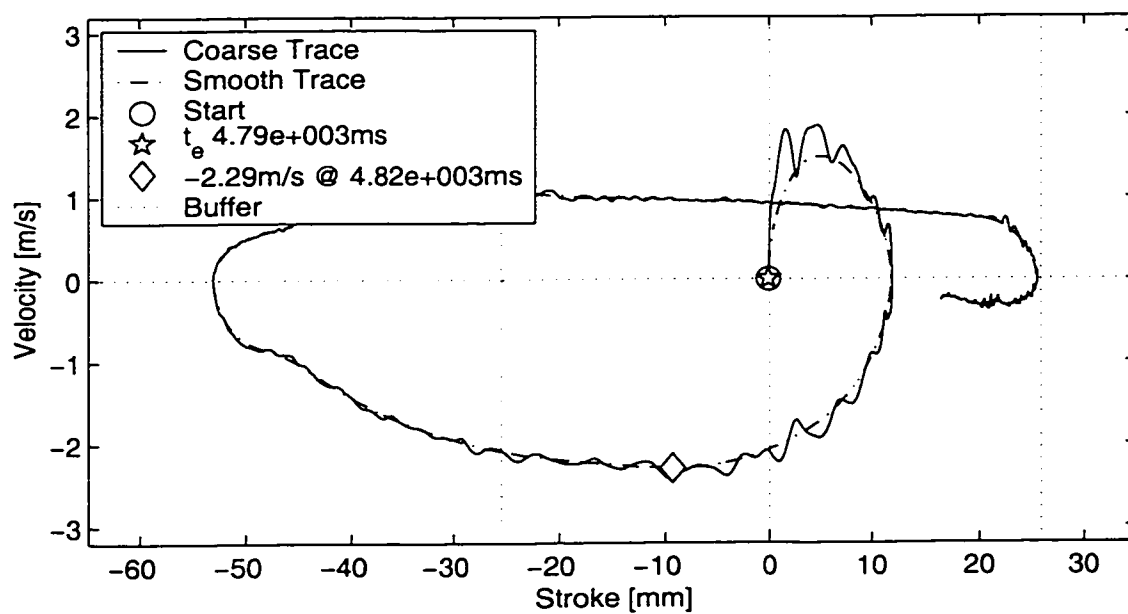
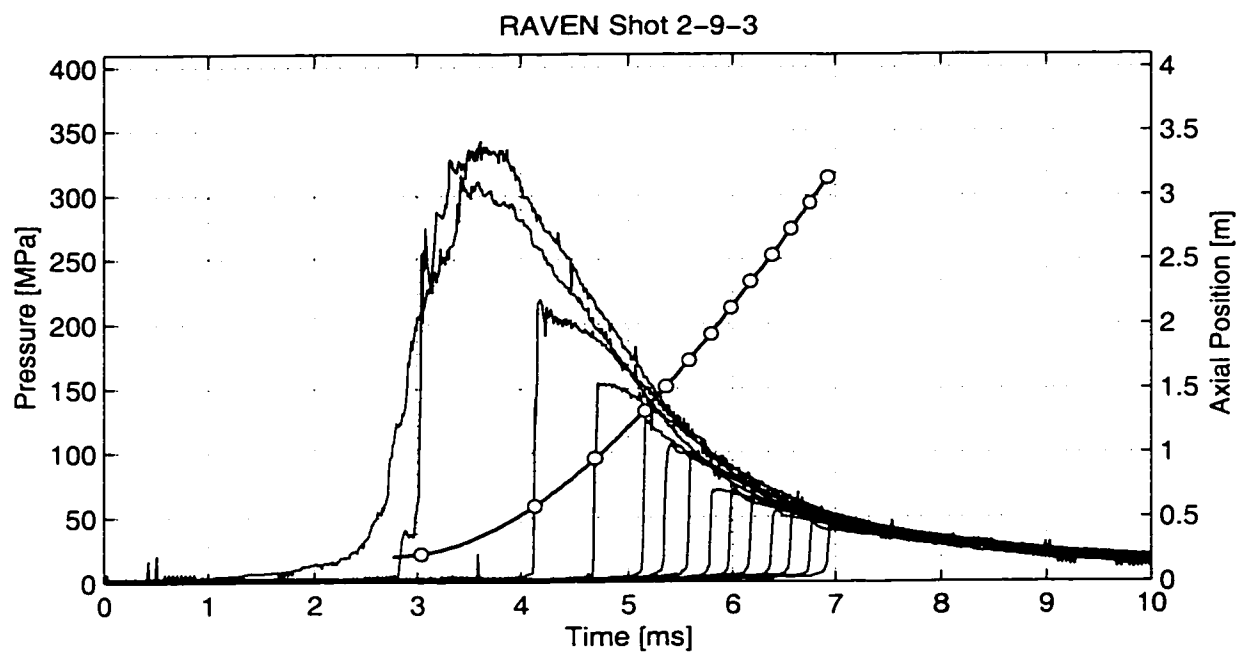


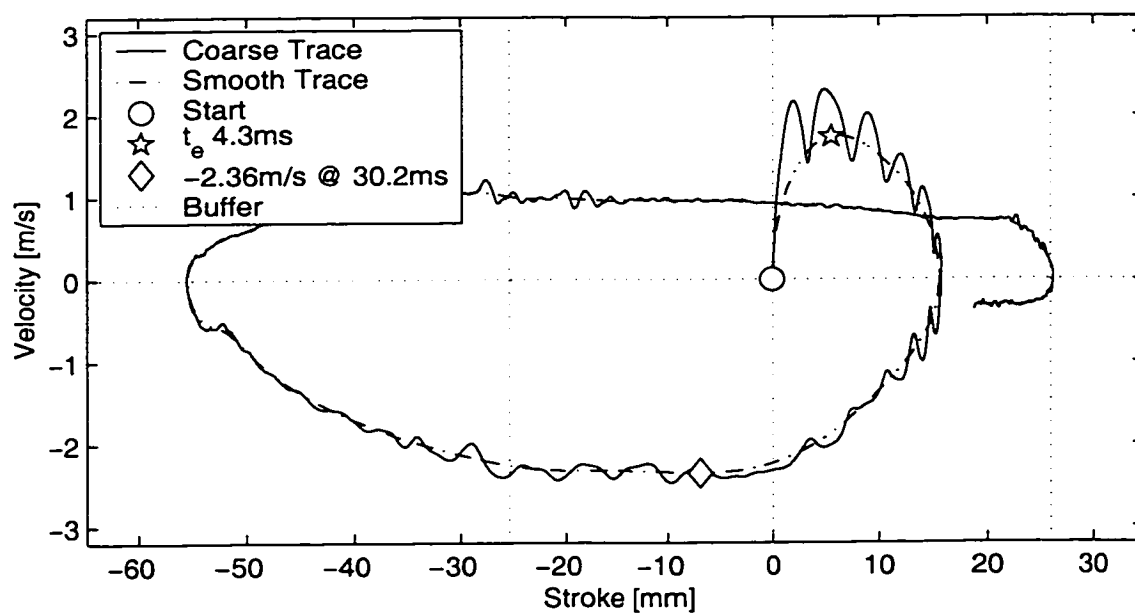
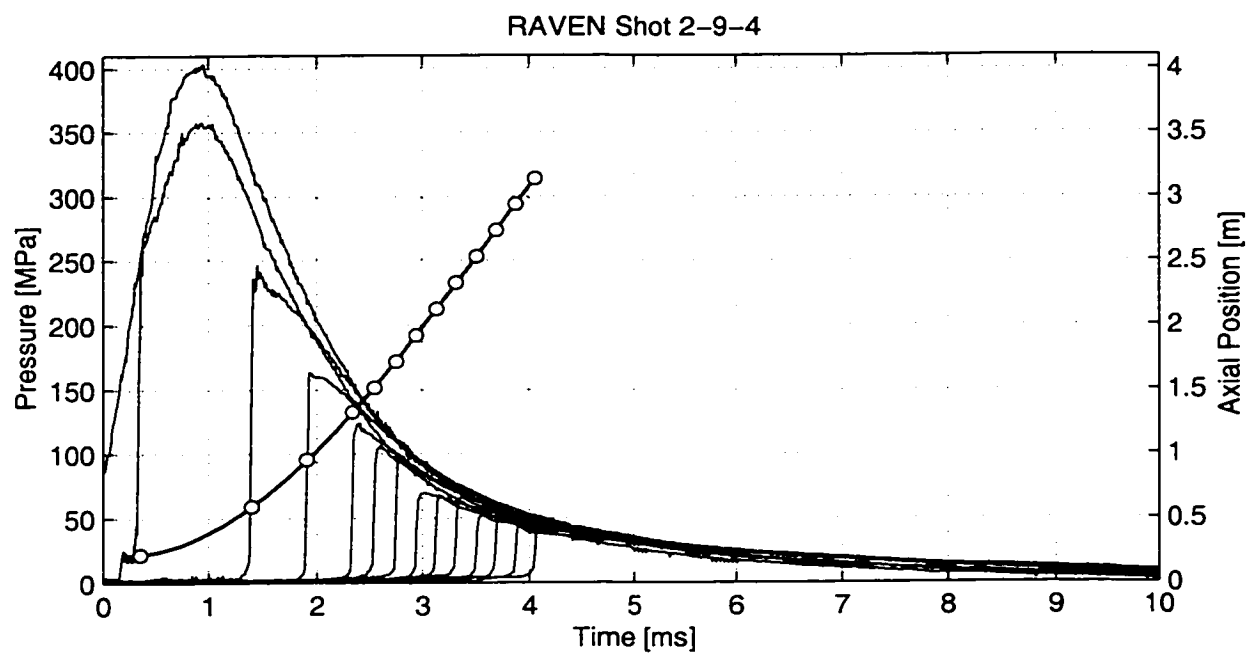












## APPENDIX B MATLAB® FILES

Four of the Matlab® files authored to model the interior ballistics are included for reproducibility. The code was run using version 6.1.0.450 (R12.1) on PCWIN.

The first file, **ff1dperf.m**, computes the form function of a deterred, single perforation grain as described in Section 7.1.4.2. The second file, **runR2dxvf.m**, is a script file that calls upon third file, **R2dxf.m**, to run the interior ballistics for each of the configurations tested and generate the model portions of the figures include in Section 8.3. The fourth file, **R2d1f.m**, is a script file to compute the interior ballistics of the closed breech gun. This file was used to generate Figures 7.2-1, 7.2-2, and 7.2-3 as well as the model energy results presented in Table 7.2-2.

### Matlab File: ff1dperf.m

```
1 function [v,s] = ff1dperf(L,D,P,x,deter);
2 % Form Function for 1 Perf dettered.
3 %
4 % communicated by
5 % Fred Robbins, "Interior Ballistics, Theorys, Models and
6 % Computer Codes," Fre-Lin Associates, Havre de Grace, MD,
7 % Taught @ Benet Labs, Watervliet Arsenal, NY, 24-26 Oct 00.
8 %
9 % Dettered model, e.kathe March 02.
10 %
11 % L: Length of Grain [m]
12 % D: Outer Diameter of Grain [m]
13 % P: Perforation Diameter [m]
14 % w: Web [m]
15 % x: Thickness burned off [m]
16 % v: Volume of grain [m^3]
17 % s: Surface Area of grain [m^2]
18 %
19 % Master Inputs: L,D,P,x,delta
20 %
21 % where det is the detterent as follows:
22 %
23 % deter(1), percent reduction in burn rate coefficient.
24 % deter(2), is the outer diameter depth
25 % It will be assumed that the detterent is half as thick on the perf
26 % In keeping with Steifel, pp 11, ARSCD-TR-80005, June 80.
27 %
28 w = (1/2)*(D - P); % Assuming coaxial Perf [m]
29 d = P; % [m]
30 %
31 rt3 = sqrt(3); % Square Root of 3 used often.
32 %
33 xw = w/2; % Burnout
34 %
35 % vo = (pi/4)*L*(D^2); % Initial Volume [m^3]
36 % so = 2*vo/L + pi*L*(D + d); % Initial Surface Area [m^2]
37 % 2 ends of grain (projected prism) plus length area.
38 %
39 %
40 yd = deter(2); % Inhibit depth of outer grain
41 a = 1/deter(1); % Burn rate change
```

```

42     pd = yd/2 ;% Half inhibit depth assumptino on perf and ends
43     xpd = a*pd; % Depth that an unsloved burn would make in same time.
44     xyd = a*yd;
45     %
46     p = x - (a-1)*pd;
47     indx = find(x < xpd);
48     p(indx) = (1/a)*x(indx);
49     %
50     y = x - (a-1)*yd;
51     indx = find(x < xyd);
52     y(indx) = (1/a)*x(indx);
53     %
54     % plot((p+P),x,'r',(D-y),x,'b')
55     %
56     v = 0*x;
57     s = 0*x;
58     %
59     % Look where burn out not occured
60     %
61     ind = find([p+y]<w);
62     %
63     v(ind) = (pi/4)*(L - 2*p(ind)).*[(D - 2*y(ind)).^2 - (P + 2*p(ind)).^2];
64     s(ind) = [2*v(ind)./(L - 2*p(ind))] + pi*(L - 2*p(ind)).*[(D - 2*y(ind)) + (P +
        2*p(ind))];
65     %
66

```

**Matlab File: runR2dxvf.m**

```
1      %
2      mgc = 297.6;
3      pflag = 1;
4      %
5      %
6      %
7      mr = 35.9;
8      %
9      ptitle = 'Heavy/Early R2-3';
10     testind = [9,11];
11     indiv = 1;
12     [mv_h,pmax_h,pmz,Z,Zt,dtvent] = R2dxf(mr,mgc,indv,testind);
13     if pflag
14         figure(2)
15         print -deps -tiff -r300 H:\PhD\disertation\Media\MlabPlots\R2d3_PXT.eps
16     end
17     %
18     ptitle = 'Heavy/Nominal R2-2';
19     testind = [4:8];
20     indiv = 2;
21     [mv,pmax,pmz,Z,Zt,dtvent] = R2dxf(mr,mgc,indv,testind);
22     if pflag
23         figure(2)
24         print -deps -tiff -r300 H:\PhD\disertation\Media\MlabPlots\R2d2_PXT.eps
25     end
26     %
27     ptitle = 'Heavy/Intermediate R2-4';
28     testind = [12:14];
29     indiv = 3;
30     [mv,pmax,pmz,Z,Zt,dtvent] = R2dxf(mr,mgc,indv,testind);
31     if pflag
32         figure(2)
33         print -deps -tiff -r300 H:\PhD\disertation\Media\MlabPlots\R2d4_PXT.eps
34     end
35     %
36     %
37     %
```

HEAVY

SERIES:=====

=====

LIGHT

SERIES:=====

=====

```

38     mr = 20.9;
39     %
40     ptitle = 'Light/Early R2-6';
41     testind = [18:20];
42     indiv = 1;
43     [mv_L, pmax_L, pmz, Z, Zt, dtvent] = R2dxf(mr, mgc, indiv, testind);
44     if pflag
45         figure(2)
46         print -deps -tiff -r300 H:\PhD\disertation\Media\MlabPlots\R2d6_PXT.eps
47     end
48     %
49     ptitle = 'Light/Nominal R2-5';
50     testind = [15:17];
51     indiv = 2;
52     [mv, pmax, pmz, Z, Zt, dtvent] = R2dxf(mr, mgc, indiv, testind);
53     if pflag
54         figure(2)
55         print -deps -tiff -r300 H:\PhD\disertation\Media\MlabPlots\R2d5_PXT.eps
56     end
57     %
58     ptitle = 'Light/Intermediate R2-7';
59     testind = [21:23];
60     indiv = 3;
61     [mv, pmax, pmz, Z, Zt, dtvent] = R2dxf(mr, mgc, indiv, testind);
62     if pflag
63         figure(2)
64         print -deps -tiff -r300 H:\PhD\disertation\Media\MlabPlots\R2d7_PXT.eps
65     end
66     %
67     ptitle = 'Light/Late R2-8';
68     testind = [24,26];
69     indiv = 4;
70     [mv, pmax, pmz, Z, Zt, dtvent] = R2dxf(mr, mgc, indiv, testind);
71     if pflag
72         figure(2)
73         print -deps -tiff -r300 H:\PhD\disertation\Media\MlabPlots\R2d8_PXT.eps
74     end
75     %
76     %
77     %
78     mgc = 405.9;

```

NonVenting SERIES:

=====

=====



```

79     mr = 31.8;
80     %
81     ptitle = 'Non-Vent R2-9';
82     testind = [27:30];
83     indiv = 4;
84     [mv_nv,pmax_nv,pmz,Z,Zt,dtvent] = R2dxf(mr,mgc,indv,testind);
85     if pflag
86         figure(2)
87         print -deps -tiff -r300 H:\PhD\dissertation\Media\MlabPlots\R2d9_PXT.eps
88     end
89     %
90     %
91     fid = fopen(['H:\PhD\dissertation\MFiles\Tables\IB35\CB\IB_mv_h.txt'],'wt+');
92     fprintf(fid,'%5.0f',round(mv_h));
93     st = fclose(fid);
94     fid =
           fopen(['H:\PhD\dissertation\MFiles\Tables\IB35\CB\IB_p
           max_h.txt'],'wt+');
95     fprintf(fid,'%4.0f',round(pmax_h/1e6));
96     st = fclose(fid);
97     %
98     fid = fopen(['H:\PhD\dissertation\MFiles\Tables\IB35\CB\IB_mv_L.txt'],'wt+');
99     fprintf(fid,'%5.0f',round(mv_L));
100    st = fclose(fid);
101    fid =
           fopen(['H:\PhD\dissertation\MFiles\Tables\IB35\CB\IB_p
           max_L.txt'],'wt+');
102    fprintf(fid,'%4.0f',round(pmax_L/1e6));
103    st = fclose(fid);
104    %
105    fid = fopen(['H:\PhD\dissertation\MFiles\Tables\IB35\CB\IB_mv_nv.txt'],'wt+');
106    fprintf(fid,'%5.0f',round(mv_nv));
107    st = fclose(fid);
108    fid =
           fopen(['H:\PhD\dissertation\MFiles\Tables\IB35\CB\IB_p
           max_nv.txt'],'wt+');
109    fprintf(fid,'%4.0f',round(pmax_nv/1e6));
110    st = fclose(fid);
111

```

## Matlab File: R2dx.m

```
1 function [mv,pmax,pmz,Z,Zt,dtvent] = R2dx(mr,mgc,indv,testind,Fib1)
2 %
3 % Barrel Data
4 %
5 DL = 35e-3; % Land (Bore) Diameter [m]
6 DG = 36.2e-3; % Groove Diameter [m]
7 GLR = 24*(1.991)/(pi*35 - 24*1.991); % Groove to Land Ratio
8 L = 2.963; % Projectile Travel [m]
9 Tw = 1/28; % Twist in turns per caliber.
10 % mr = 35.9; % Mass of recoiling inertial breech [Kg]
11 % mgc = 405.9; % Mass of blow forward cannon barrel
12 f = 0.5; % fraction of work done against bore friction that heats bore
13 To = 273; % Initial Wall Temperature [K]
14 ho = 11.35; % Heat transfer coefficient [W/(m^2 K)]
15 Dw = 82.9e-6; % Chamber Wall thickness (heat trans) [m]
16 Cpw = 460.28; % Heat Capacity of Wall [J/(Kg K)]
17 rhow = 7861.2; % Wall Density [Kg/m^3]
18 Rpm = [0 0; % Resistance to Recoil Motion Curve
19 0 0.20]; % Force [N] Time [s]
20 Pg = 0; % Pressure in front of bullet [Pa]
21
22 %
23 % Pressure Probe Locations:
24 %
25 xprobe = [0.0795,0.2163,0.5878,0.9561,1.3244,1.5149,1.7181, ...
26 1.9213,2.1245,2.3277,2.5309,2.7341,2.9373,3.1405];
27 %
28 % Vent Distances
29 %
30 % indv = 2;
31 xvent = [48.88e-3;56.37e-3;75.31e-3;94.25e-3];
32 % testind = [4:8]
33 %
34 % Cartridge and shear plug data
35 %
36 Lcc = 155e-3; % Cartridge Case Length [m]
37 vo = 367.25e-6; % Empty Chamber Volume [m^3]
38 Dc = 55e-3; % Chamber Diameter [m]
39 Pshear = 220e6; % Pressure to shear plug (Set high for closed breech)
40 if nargin < 5;
41 Ps2f = Pshear*0.64;
```

```

42     else
43         Ps2f = Pshear*Fib1
44     end
45     Ps3f = 0;
46     vrc = [Ps2f 0.000; % Breech Resistance Travel Curve
47         Ps3f 0.010]; % Pressure [Pa] Travel [m]
48     %
49     % Bullet Data
50     %
51     mp = 0.550; % Projectile Mass [Kg]
52     %
53     brm = [4.4763e6 0.000; % Bullet Resistance Travel Curve
54         35.0e6 0.001; % Pressure [Pa] Travel [m]
55         5.5e6 0.002;
56         5.5e6 2*L];
57     %
58     % Igniter Data
59     CI = 2.3e-3; % Initial Mass of Igniter [Kg]
60     ToI = 2188; % Igniter Flame Temp [K]
61     FI = 290e3; % Igniter Force [J/Kg]
62     gI = 1.2184; % Igniter Ratio of Specific Heats
63     bI = 785e-6; % Igniter Co-Volume [m^3/Kg]
64     %
65     % Propellants (Column Vectors for mutiple propellants)
66     C = [0.333]; % Intial Propellant Mass [Kg]
67     Toi = [2200]; % Propellant Flame Temperature [K]
68     F = [912e3]; % Propellant Force [J/Kg]
69     g = [1.259]; % Ratio of Specific Heats for Propellant
70     b = [1104e-6]; % Propellant Co-Volume [m^3/Kg]
71     rho = [1570]; % Propellant Density [Kg/m^3]
72     beta = [0.002175]; % Burn Rate coefficeint [(m/s)/(MPa^alpha)]
73     alpha = [0.78]; % burn rate exponent
74     %
75     % Grain Geometry
76     %
77     % [Shape,OD,GLEN,DPERF,SLW;... per below
78     %
79     % OD outer diameter
80     % GLEN length of the grain
81     % DPERF is the perforation diameter
82     % SLW slot width
83     %
84     % Shape names (8 characters)

```

```

85 % 1) Sphere -NA-      2) Cylinder -NA-
86 % 3) Stick -NA-      4) Strip -NA-
87 % 5) Single          6) Seven
88 % 7) nineteen -NA-   8) hex7 -NA-
89 % 9) hex19 -NA-      10) monolithic -NA-
90 %                   11) Single Perf Detered
91 geom = [11,1994e-6,2608e-6,250e-6,nan];
92 deter = [0.70;130e-6];
93 %
94 % Integration Control
95 %
96 dt = 0.000005; % time step [s]
97 %
98 plotflag = 0;
99 %
100 %
=====
=====

101 %
102 % Compute Bore Area
103 %
104 if DG > DL
105     Db = sqrt((GLR*DG^2)/(GLR+1)+(DL^2)/(GLR+1));% Eq. 1.3
106 else
107     Db = DL;
108 end
109 A = (pi/4)*Db^2; % Eq. 1.2
110 Ac = (pi/4)*Dc^2; % Chamber Area [m^2]
111 Lcn = (vo - Lcc*A)/(Ac-A);
112 %
113 Lc = vo/A; % Fictitious Chamber Length embedded in eq. 7.13
114 %
115 Ct = sum(C) + CI; % Total Mass of Propellants and Igniter
116 %
117 xp = Lcc; % Initial Postion of Projectile
118 vp = 0; % Initial Velocity of Projectile
119 ap = 0; % Initial Acceleration of Projectile
120 %
121 xr = 0; % Initial Recoil Position
122 vr = 0; % Initial Recoil Velocity
123 ar = 0; % Initial Recoil Acceleration
124 %
125 xgc = Lcn; % Initial Gun Chambrage Location

```

```

126   vgc = 0; % Initial Chambrage Velocity
127   agc = 0; % Initial Chambrage Acceleration
128   %
129   xrwf = sqrt(-1); % Intialize and flag RWFront
130   xpr = (xp - Lcc) - (xgc - Lcn); % Relative Travel of Bullet Down Bore
131   %
132   P = 0; % Start mean pressure [Pa]
133   %
134   t = 0; % Start time = 0 [s]
135
136   Ept = 0; % Energy [J] Lost to Projectile Translation
137   Epr = 0; % Energy [J] Lost to Projectile Rotation
138   Ep = 0; % Energy [J] Lost to Propellant Translation
139   Ebr = 0; % Energy [J] Lost to Bore Resistance
140   Er = 0; % Energy [J] Lost to Recoil
141   Ed = 0; % Enerty [J] Lost to Air Resistance
142   Eh = 0; % Energy [J] Lost to Wall Heating
143
144   Tc = To; % Start Temperature of Bore Wall [K]
145   n = size(C,1); % number of propellants
146   Z = zeros(n,1); % Start Mass Fraction of Propellants burned
147   r = zeros(n,1); % Start burn depth of each propellant [m]
148   gvo= zeros(n,1); % Intialize the orginal grain volume [m^3]
149   gv = zeros(n,1); % Intialize the burnt grain volume [m^3]
150   Cp = [F.*g]./[[g-1].*[Toi]]; % Constant Pressure Heat Capacity [J/(Kg K)]
151   CpI = FI*gI/((gI-1)*ToI); %
152   Cv = Cp./g; % Constant Volume Heat Capacity [J/(Kg K)]
153   CvI = CpI/gI;%
154   Egas = CvI*ToI*CI + sum([Cv.*Toi.*C]); % Total Chemical Energy
155   lambda = (13.2 + 4*log10(Db))^-2;% Nordheim Friction Factor 7.15
156   %
157   % Compute Original Grain Volume [m^3]
158   for i = 1:n
159       if geom(i,1)==6
160           [gvo(i),s] = ff7perf(geom(i,3),geom(i,2),geom(i,4),0);
161       elseif geom(i,1)==5
162           [gvo(i),s] = ff1perf(geom(i,3),geom(i,2),geom(i,4),0);
163       elseif geom(i,1)==11
164           [gvo(i),s] = ff1dperf(geom(i,3),geom(i,2),geom(i,4),0,deter);
165       end
166   end
167   %
168   tv = [];

```

```

169   pv = [];
170   pbv = [];
171   pov = [];
172   xv = [];
173   vv = [];
174   xrv = [];
175   vrv = [];
176   arv = [];
177   xgcv = [];
178   vgcx = [];
179   agcv = [];
180   xrwfv = [];
181   trwfv = [];
182   vrwfv = [];
183   Em = [];
184   Zm = [];
185   data = [];
186   counter = 0;
187   counter2 = 0;
188   pmat = 0*xprobe;
189   %
190   if plotflag
191       figure(1)
192       figset('p',6.0,3.5,11)
193       hgpl = plot([0 (Lcc)],[0 0]);
194       xlabel('x [m]')
195       ylabel('P [Pa]')
196       tplotv = [0];
197   end
198
199   %
200   while xpr < L % While bullet in barel
201       counter = counter + 1;
202       %
203       % Start Changing Variables
204       % =====
205       %
206       %
207       xvv = ((xgc-Lcn)-xr); % Recoil stroke for vent
208       xpr = (xp - Lcc) - (xgc - Lcn); % Relative Travel of Bullet Down Bore
209       %
210       % Volumes of Gas behind bullet and other locations
211       %

```

```

212 Wcb = Ac*(xgc-xr); % Volume between breech and chambrage
213 Wp = Wcb + A*(xp + (Lcc-Lcn) -xr); % Volume behind projectile
214 Wp = A*(xp-xr) + (Ac-A)*(xgc-xr); % Volume Behind Projectile [m^3] eq. 7.2
215 Wgc = Wcb;
216 Ngc = Wgc/Wp;
217 %
218 % Projectile Bore Resistance (required for pressures)
219 %
220 br = interp1(brm(:,2),brm(:,1),xpr); % 1D table lookup resistance [Pa]
221 %
222 % Pressure to release bullet and breech:
223 %
224 Pss = br(1,1) + Pg; % Pressure to achieve Shot Start
225 % Pshear = Pshear; % Pressure to achieve Breech Start
226 % -----
227 %
228 if vgc == vp % Bore resistance doesn't start until the projectile begins to move
229     br = 0; % The problem is neagive breech pressures from Lagrange if br isn't
                zero'd.

230 end
231 % Projectile Base, Breech Face, and Gun Chambrage Pressure
232 %
233 Pb = [P + Ct*(br + Pg)/(3*mp)]/[1+Ct/(3*mp)]; % Lagrange Eq. 1.4 [Pa]
234 Po = Pb + (Ct/(2*mp))*(Pb -br -Pg); % Lagrange Eq. 3.1 [Pa]
235 Pgc = Pb + Ct/(2*mp)*(1-Ngc.^2)*(Pb - br - Pg); % Corner (13)pp344
236 %
237 % Pressure at Bore Gauges
238 %
239 Wbg = A*(xprobe + (xgc-Lcc) -xr) + (Ac-A)*(xgc-xr); % Probes ride the barrel
                with xgc
240 ind = find(xprobe<Lcc);
241 Wbg(ind) = Ac*(xprobe(ind) + (xgc-Lcc) - xr); % Find chamber probe.
242 Nbg = Wbg/Wp;
243 Pbg = Pb + Ct/(2*mp)*(1-Nbg.^2)*(Pb - br - Pg); % Pressure at probes
244 %
245 ind = find( xp < (xprobe + (xgc-Lcc))); % Find probes bullet hasn't crossed.
246 Pbg(ind) = 0; % Set pressur to zero ahead of bullet.
247 %
248 %
249 % Recoil Resistances:
250 %
251 % Time Based Recoil Resistance Curve (Gun mount aproximation)
252 %

```

```

253     if t < RPm(size(RPm,1),2)
254         Fr = interp1(RPm(:,2),RPm(:,1),t); % 1D table lookup resistance [Pa]
255     else
256         Fr = RPm(size(RPm,1),1);
257     end
258     %
259     % Barrel/Breech Spatial Resistance Curve
260     %
261     if xvv < vrc(size(vrc,1),2)
262         if xvv <= 0 % Don't let breech resistance add to shear.
263             Ffb = 0;
264         else
265             Ffb = interp1(vrc(:,2),vrc(:,1),xvv);
266         end
267     else
268         Ffb = vrc(size(vrc,1),1);
269     end
270     if Ffb > Po;
271         Ffb = Po; % Don't let friction push breech forward, it can't exceed driving
                    % pressure.
272     end
273     %
274     if ( (Pb > Pss) & (Po > Pshear) ) % After shot and breech start
275         %
276         Pss = 0; % Once shot start is achieved, there is no more shot start
277         Pshear = 0; % Ibid
278         %
279         ap = A*(Pb - br - Pg)/mp; % Projectile Acceleration
280         ar = (Ac*(Ffb - Po))/mr; % Inertial Breech Motion (Should be
                    % negative)
281         agc = ((Ac-A)*Pgc + A*br + Fr - Ffb*Ac)/mgc; % Gun Chamber Motion
282         %
283     elseif ( (Pb > Pss) & (Po <= Pshear) ) % After shot-start, before breech shear
284         %
285         Pss = 0; % Once shot start is achieved, there is no more shot start
286         %
287         ap = A*(Pb - br - Pg)/mp; % Projectile Acceleration
288         ar = ((Ac-A)*Pgc + A*br + Fr - Ac*Po)/(mr + mgc); % Closed Breech Gun
                    % Acc (Should be negative)
289         agc = ar; % -----
290         %
291     elseif ( (Pb <= Pss) & (Po > Pshear) ) % After breech-shear but before shot-
                    % start

```



```

292      %
293      Pshear = 0; % Once breech start is achieved, there is no more shearing
294      %
295      ap = (A*(Pb - Pg) + (Ac-A)*Pgc + ...
296            Fr - Ffb*Ac)/(mp+mgc); % Projectile & Barrel Acceleration
297      ar = Ac*(Ffb - Po)/mr; % Inertial breech Acc (Should be negative)
298      agc = ap; % -----
299      %
300      else % Before breech or shot start, no mass motion, no
           recoil.

301      ap = 0;
302      ar = 0;
303      agc = 0;
304      end
305      %
306      % Integration of Acceleration and Velocity into Motion
307      %
308      % Projectile
309      vp = vp + ap*dt; % Integrate acceleration to velocity and [m/s]
310      xp = xp + vp*dt; % Integrate velocity to position [m]
311      % Breech
312      vr = vr + ar*dt; % Integrate acceleration to velocity and [m/s]
313      xr = xr + vr*dt; % Integrate velocity to position [m] %
314      % Barrel
315      vgc = vgc + agc*dt; % Integrate acceleration to velocity and [m/s]
316      xgc_old = xgc;
317      xgc = xgc + vgc*dt; % Integrate velocity to position [m]
318      %
319      % Equation of State:
320      %
321      % Wp = Volume Behind Projectile [m^3] eq. 7.2
322      Wg2 = sum([C.*[1-Z]./rho]); % Volume of unburnt propellant [m^3]
323      Wg3 = sum([C.*b.*Z])+CI*bI; % Covolume of burnt propellant gas [m^3]
324      Wg = Wp - Wg2 - Wg3; % Volume Behind Projectile available for gas [m^3]
325      T = (sum([F.*C.*Z]./[g-1])+FI*CI/(gI-1)-Ept-Epr-Ep-Ebr-Er-Ed-Eh)/ ...
326          (sum([F.*C.*Z]./[g-1].*Toi)+FI*CI/((gI-1)*Toi)); % Gas Temp 7.3 [K]
327      mg = sum([C.*Z]) + CI;
328      rhog = mg/(Wp-Wg2); % Gas Density, correcting for grains
329      Rg = (sum([F.*C.*Z]./Toi)+FI*CI/Toi)/mg; % Mass weighted gas R [J/Kg/K]
330      gg = (sum([g.*C.*Z]) + gI*CI)/mg; % Mass Weighted gamma
331      P = mg*Rg*T/Wg; % Mean Gas Pressure 7.1 [Pa]
332      %
333      if counter < 2

```

```

334     pig = P;
335     vig = Wg;
336     vubp = Wg2;
337 end
338
339
340 if ( xvv > xvent(indv) ) % Combined blowback breech and blowforward barrel
    stroke to vent
341     if ~isreal(xrwf)
342         xrwf = xr; % Detect initiation of wave and assign start point.
343         counterrwf = 0;
344     end
345     counterrwf = counterrwf + 1;
346     if xrwf < xgc
347         Wrwf = Ac*(xrwf-xr); % Volume Behind Rarefaction Wavefront
348     else
349         Wrwf = Wcb + A*(xrwf-xgc); %
350     end
351     %
352     % Dont' let Rarefactoin Wave overtake projectile or get out of muzzle
353     if (xrwf >= xp) | (xrwf >= (L + (xgc - Lcn)))
354         xrwf = nan;
355         Wrwf = nan;
356     end
357     Nrwf = Wrwf/Wp;
358     Prwf = Pb + Ct/(2*mp)*(1-Nrwf.^2)*(Pb - br - Pg); % Pressure at Rarefactoin
    Wavefront
360     Trwf = Prwf*(1/rhog)/Rg;
361     arwf = sqrt(gg*Rg*Trwf)/(1 - (Wg3/mg)*rhog); % Sonic Velocity at wave
    front
362     vgrwf = vr + Nrwf*(vp-vr); % Gas Velocity at Wave Front
363     vrwf = arwf + vgrwf; % Right Running Characteristic Speed
364     trwf = t;
365     if vrwf < 0
366         vrwf = nan
367     end
368     xrwf = xrwf + dt*vrwf;
369     if isfinite(xrwf)

```

```

370     xrwfv = [xrwfv;xrwf];
371     trwfv = [trwfv;trwf];
372     vrwfv = [vrwfv;vrwf];
373     end
374     %end
375 end
376
377
378 %
379 %
380 % Heat Transfer to Wall
381  $A_w = 2*A + \pi*Db*(x_p - x_r + ((A_c-A)/A)*(x_{gc}-x_r));$  % Exposed bore area 7.13
382     [m^2]
383  $T_c = (E_h + f*E_{br})/(C_{pw}*rho_w*A_w*D_w) + T_o;$  % Temperature of wall 7.20 [K]
384  $rho_m = (sum(C.*Z)+CI)/(W_g+W_{g3});$  % Mean gas Density 7.17 [Kg/m^3] As
385     implemented in code
386  $C_{pm} = (sum([F.*g.*C.*Z]/[g-1].*T_{oi})+(FI*gI*CI)/((gI-1)*T_{oi}))/$ 
387      $(sum([C.*Z])+CI);$  % 7.19 [J/(Kg K)]
388  $v_m = v_p/2;$  % Mean Gas Velocity 7.16 [m/s]
389  $h = lambda*C_{pm}*rho_m*v_m+h_o;$  % Heat Transfer Coefficient Nordheim et al
390     eq. 7.14 [W/(m^2 K)]
391  $Q_d = A_w*h*(T-T_c);$  % Heat Transfer Rate 7.12
392 %
393 %
394 %
395  $E_{pt} = (1/2)*m_p*v_p^2;$  % Energy [J] Lost to Projectile Translation 7.4
396  $E_{pr} = \pi^2*m_p*v_p^2*Tw^2/4;$  % Energy [J] Lost to Projectile Rotation 7.5
397  $E_p = (1/6)*C_t*v_p^2;$  % Energy [J] Lost to Propellant Translation 7.6
398  $E_{br} = E_{br} + A*br*v_p*dt;$  % Energy [J] Lost to Bore Resistance 7.8
399  $E_r = (1/2)*m_r*v_r^2 ...$ 
400      $+ (1/2)*m_{gc}*v_{gc}^2;$  % Energy [J] Lost to Recoil 7.9
401  $E_d = A*[E_d + v_p*P_g*dt];$  % Energy [J] Lost to Air Resistance 7.10
402  $E_h = E_h + Q_d*dt;$  % Energy [J] Lost to Barrel Heating 7.11
403 %
404 %
405  $rd = beta.*[(P/10^6).^alpha];$  % Burn Rate 5.2 [m/s]
406  $r = r + rd*dt;$  % Burn Depth [m] between 6.2 and 7.1
407 %
408 for i = 1:n

```

```

405     if geom(i,1)==6
406         [gv(i),s] = ff7perf(geom(i,3),geom(i,2),geom(i,4),r);
407     elseif geom(i,1)==5
408         [gv(i),s] = ff1perf(geom(i,3),geom(i,2),geom(i,4),r);
409     elseif geom(i,1)==11
410         [gv(i),s] = ff1dperf(geom(i,3),geom(i,2),geom(i,4),r,deter);
411     end
412 end
413 Z = 1 - gv./gvo; % mass fraction of propellant that has burned
414 %
415 if rem((counter-1),10)==0
416     counter2 = counter2+1;
417     data = [data;[t ap vp xp P Pb Po]];
418     % xp/(L + Lcc + xgc - Lcn)
419 end
420 tv = [tv;t];
421 pv = [pv;P];
422 pbv = [pbv;Pb];
423 pov = [pov;Po];
424 xv = [xv;xp];
425 vv = [vv;vp];
426 xrv = [xrv;xr];%
427 vrv = [vrv;vr];
428 arv = [arv;ar];
429 agcv = [agcv;agc];
430 xgcv = [xgcv;xgc];%
431 vgc = [vgcv;vgc];%
432 Em = [Em;[Ept Epr Ep Ebr Er Ed Eh]];
433 Zm = [Zm;Z];
434 pmat = [pmat; Pbg];
435 %
436
437 % Plot some results
438 if plotflag
439     npgc = 50;
440     if (counter/npgc) == round(counter/npgc)
441         xgv = linspace(xr,xp,80); % X gradient vector
442         Wgv = A*(xgv-xr) + (Ac-A)*(xgc-xr);
443         ind = find(xgv<xgc);
444         Wgv(ind) = Ac*(xgv(ind)-xr);
445         Ngv = Wgv/Wp;
446         P xv = Pb + Ct/(2*mp)*(1-Ngv.^2)*(Pb - br - Pg);
447         figure(1)

```

```

448         hgpls = line(xgv,Pxv/1e6);
449         hgpl = [hgpl;hgpls];
450         set(hgpl,'Color','b');
451         tplotv = [tplotv;t];
452     end
453 end
454 %
455     t = t+dt;
456 end
457 %
458 %
459 if plotflag
460     %
461     axis([-0.5 3.5 0 430]);
462     hl = line((xv),pbv/1e6); % Add base pressure to plot.
463     set(hl,'LineStyle','-','Marker','.', 'MarkerSize',5,'Color','r');
464     hl = line((xrv),pov/1e6); % Add base pressure to plot.
465     set(hl,'LineStyle','-','Marker','none','MarkerSize',5,'Color','k');
466     % print -deps -tiff -r300 H:\PhD\dissertation\Media\MlabPlots\R2d2_PPX.eps
467 end
468 %
469 pmat(1,:) = [];
470 mv = max(vv);
471 pmax = max(pov);
472 %
473 pmz = pbv(length(pbv));
474 %
475 if Z < 1;
476     Zt = -1;
477 else
478     ind = find (Zm(:,1)<1);
479     Zt = tv(max(ind))/max(tv);
480 end
481 %
482
483 Ec = sum([C.*F./(g-1)]) + CI*FI/(gI-1);
484 %
485 % Ept = (1/2)*mp*vp^2;    % Energy [J] Lost to Projectile Translation 7.4
486 %Epr = pi^2*mp*vp^2*Tw^2/4;% Energy [J] Lost to Projectile Rotation 7.5
487 %Ep = (1/6)*Ct*vp^2;    % Energy [J] Lost to Propellant Translation 7.6
488 %Ebr = Ebr + A*br*vp*dt; % Energy [J] Lost to Bore Resistance 7.8
489 %Er = (1/2)*mr*vr^2 ...
490 % + (1/2)*mgc*vgc^2;    % Energy [J] Lost to Recoil 7.9

```

```

491 %Ed = A*[Ed + vp*Pg*dt]; % Energy [J] Lost to Air Resistance 7.10
492 %Eh = Eh + Qd*dt; % Energy [J] Lost to Barrel Heating 7.11
493 %
494 %
495 figure(2)
496 figset('p',6.0,3.5,11)
497 %
498 hp = plot(tv*1e3,xv*100);
499 set(hp,'LineStyle','-','Marker','.', 'MarkerSize',5,'Color','r')
500 hold on;
501 %
502 hg = plot(tv*1e3,pbv/1e6);
503 set(hg,'LineStyle',':', 'Color','k')
504 hl = plot(tv*1e3,pmat(:,1:14)/1e6);
505 %
506 if ( (min(testind) > 3) & (max(testind) < 27) )
507     load xpoly2.mat;
508     load TestResults.mat;
509     load H:\PhD\dissertation\MFiles\Data\All\rwavepropnew; % Replace initial
                                RWF points
510     matrwft = rwfmat; % with new ones.
511     %
512     for i = testind
513
514         tx1 = tv - max(tv) + te(i);
515         xpt1 = polyval(polymatxp(i,:),tx1);
516         [y,ind] = min(xpt1);
517         xpt1(1:ind) = nan*xpt1(1:ind);
518         % hxp = line(tv*1e3,xpt1*100);
519         hxp2 = line([matxpt(i,:)+ max(tv) - te(i)]*1e3,xprobe(2:14)*100);
520         set(hxp2,'LineStyle','none','Marker','o','Color','b')
521         xrwfx = polyval(polymatrwf(i,:),tx1);
522         % hrwf = line(tv*1e3,xrwfx*100);
523         hrwf2 = line([matrwft(i,:)+ max(tv) - te(i)]*1e3,xprobe*100);
524         set(hrwf2,'LineStyle','none','Marker','^','Color','r')
525     end
526     %
527     %
528     tventtest = mean(matrwft(testind,1)-te(testind)+max(tv));
529     tventib = interp1(xrwfv,trwfv,xprobe(1));
530     dtvent = tventib-tventtest;
531     hr = plot(trwfv*1e3,xrwfv*100,'r-');
532     set(hr,'LineWidth',2)

```

```

533     else
534         dtvent = nan;
535     end
536     %
537     hold off;
538     %
539     ylabel('Pressure [MPa]');
540     xlabel('Time [ms]');
541     av1 = [0 5 0 425];
542     ax1 = gca;
543     axis(av1)
544     % hl = legend('{x_p}','{P_b}','{P_1}','{P_2}','{P_3}',...
545     %     '{P_4}','{P_5}','{P_6}','{P_7}','{P_8}','{P_9}',...
546     %     '{P_{10}}','{P_{11}}','{P_{12}}','{P_{13}}',2);
547
548     %
549     ax2 = axes('Position',get(ax1,'Position'),...
550         'XAxisLocation','bottom',...
551         'YAxisLocation','right',...
552         'Color','none',...
553         'XColor','k',...
554         'YColor','k');
555     hlxp = line(tv*1e3,xv);
556     set(hlxp,'LineStyle','-','Marker','.', 'MarkerSize',5,'Color','r','Visible','off')
557     av2 = [av1(1:2),av1(3:4)/100];
558     axis(av2)
559     ylabel('Projectile Travel [m]')
560
561

```

### Matlab File: R2d1f.m

```
1 % 35mm Inertial Breech
2 % Closed Breech Standard
3
4 %
5 % Barrel Data
6 %
7 DL = 35e-3; % Land (Bore) Diameter [m]
8 DG = 36.2e-3; % Groove Diameter [m]
9 GLR = 24*(1.991)/(pi*35 - 24*1.991); % Groove to Land Ratio
10 L = 2.963; % Projectile Travel [m]
11 Tw = 1/28; % Twist in turns per caliber.
12 mr = 36.4; % Mass of recoiling inertial breech [Kg]
13 mgc = 297.6; % Mass of blow forward cannon barrel
14 f = 0.5; % fraction of work done against bore friction that heats bore
15 To = 273; % Initial Wall Temperature [K]
16 ho = 11.35; % Heat transfer coefficient [W/(m^2 K)]
17 Dw = 82.9e-6; % Chamber Wall thickness (heat trans) [m]
18 CpW = 460.28; % Heat Capacity of Wall [J/(Kg K)]
19 rhow = 7861.2; % Wall Density [Kg/m^3]
20 RPM = [0 0; % Resistance to Recoil Motion Curve
21 0 0.20]; % Force [N] Time [s]
22 Pg = 0; % Pressure in front of bullet [Pa]
23
24 %
25 % Pressure Probe Locations:
26 %
27 xprobe = [0.0795,0.2163,0.5878,0.9561,1.3244,1.5149,1.7181, ...
28 1.9213,2.1245,2.3277,2.5309,2.7341,2.9373,3.1405];
29 %
30 % Vent Distances
31 %
32 indv = 2;
33 xvent = [48.88e-3;56.37e-3;75.31e-3;94.25e-3];
34 testind = 1:3;
35 %
36 % Cartridge and shear plug data
37 %
38 Lcc = 155e-3; % Cartridge Case Length [m]
39 vo = 367.25e-6; % Empty Chamber Volume [m^3]
40 Dc = 55e-3; % Chamber Diameter [m]
41 Pshear = 550e6; % Pressure to shear plug (Set high for closed breech)
```



```

42 Ps2f = Pshear*0.64;
43 Ps3f = 0;
44 vrc = [Ps2f 0.000; % Breech Resistance Travel Curve
45     Ps3f 0.010]; % Pressure [Pa] Travel [m]
46 %
47 % Bullet Data
48 %
49 mp = 0.550; % Projectile Mass [Kg]
50 %
51 brm = [4.4763e6 0.000; % Bullet Resistance Travel Curve
52     35.0e6 0.001; % Pressure [Pa] Travel [m]
53     5.5e6 0.002;
54     5.5e6 2*L];
55 %
56 % Igniter Data
57 CI = 2.3e-3; % Initial Mass of Igniter [Kg]
58 ToI = 2188; % Igniter Flame Temp [K]
59 FI = 290e3; % Igniter Force [J/Kg]
60 gI = 1.2184; % Igniter Ratio of Specific Heats
61 bI = 785e-6; % Igniter Co-Volume [m^3/Kg]
62 %
63 % Propellants (Column Vectors for mutiple propellants)
64 C = [0.333]; % Intial Propellant Mass [Kg]
65 Toi = [2200]; % Propellant Flame Temperature [K]
66 F = [912e3]; % Propellant Force [J/Kg]
67 g = [1.259]; % Ratio of Specific Heats for Propellant
68 b = [1104e-6]; % Propellant Co-Volume [m^3/Kg]
69 rho = [1570]; % Propellant Density [Kg/m^3]
70 beta = [0.002175]; % Burn Rate coefficeint [(m/s)/(MPa^alpha)]
71 alpha = [0.78]; % burn rate exponent
72 %
73 % Grain Geometry
74 %
75 % [Shape,OD,GLEN,DPERF,SLW;... per below
76 %
77 % OD outer diameter
78 % GLEN length of the grain
79 % DPERF is the perforation diameter
80 % SLW slot width
81 %
82 % Shape names (8 characters)
83 % 1) Sphere -NA- 2) Cylinder -NA-
84 % 3) Stick -NA- 4) Strip -NA-

```

```

85 % 5) Single          6) Seven
86 % 7) nineteen -NA-  8) hex7    -NA-
87 % 9) hex19   -NA-    10) monolithic -NA-
88 %              11) Single Perf Detered
89 geom = [11,1994e-6,2608e-6,250e-6,nan];
90 deter = [0.70;130e-6];
91 %
92 % Integration Control
93 %
94 dt = 0.000005; % time step [s]
95 %
96 %

```

=====

```

97 %
98 % Compute Bore Area
99 %
100 if DG > DL
101     Db = sqrt((GLR*DG^2)/(GLR+1)+(DL^2)/(GLR+1)); % Eq. 1.3
102 else
103     Db = DL;
104 end
105 A = (pi/4)*Db^2; % Eq. 1.2
106 Ac = (pi/4)*Dc^2; % Chamber Area [m^2]
107 Lcn = (vo - Lcc*A)/(Ac-A);
108 %
109 Lc = vo/A; % Fictitious Chamber Length embedded in eq. 7.13
110 %
111 Ct = sum(C) + CI; % Total Mass of Propellants and Igniter
112 %
113 xp = Lcc; % Initial Postion of Projectile
114 vp = 0; % Initial Velocity of Projectile
115 ap = 0; % Initial Acceleration of Projectile
116 %
117 xr = 0; % Initial Recoil Position
118 vr = 0; % Initial Recoil Velocity
119 ar = 0; % Initial Recoil Acceleration
120 %
121 xgc = Lcn; % Initial Gun Chambrage Location
122 vgc = 0; % Initial Chambrage Velocity
123 agc = 0; % Initial Chambrage Acceleration
124 %
125 xrwf = sqrt(-1); % Intialize and flag RWFront

```

```

126 xpr = (xp - Lcc) - (xgc - Lcn); % Relative Travel of Bullet Down Bore
127 %
128 P = 0; % Start mean pressure [Pa]
129 %
130 t = 0; % Start time = 0 [s]
131
132 Ept = 0; % Energy [J] Lost to Projectile Translation
133 Epr = 0; % Energy [J] Lost to Projectile Rotation
134 Ep = 0; % Energy [J] Lost to Propellant Translation
135 Ebr = 0; % Energy [J] Lost to Bore Resistance
136 Er = 0; % Energy [J] Lost to Recoil
137 Ed = 0; % Enerty [J] Lost to Air Resistance
138 Eh = 0; % Energy [J] Lost to Wall Heating
139
140 Tc = To; % Start Temperature of Bore Wall [K]
141 n = size(C,1); % number of propellants
142 Z = zeros(n,1); % Start Mass Fraction of Propellants burned
143 r = zeros(n,1); % Start burn depth of each propellant [m]
144 gvo= zeros(n,1); % Intialize the orginal grain volume [m^3]
145 gv = zeros(n,1); % Intialize the burnt grain volume [m^3]
146 Cp = [F.*g]./[[g-1].*[Toi]]; % Constant Pressure Heat Capacity [J/(Kg K)]
147 CpI = FI*gI/((gI-1)*ToI); %
148 Cv = Cp./g; % Constant Volume Heat Capacity [J/(Kg K)]
149 CvI = CpI/gI;%
150 Egas = CvI*ToI*CI + sum([Cv.*Toi.*C]); % Total Chemical Energy
151 lambda = (13.2 + 4*log10(Db))^( -2); % Nordheim Friction Factor 7.15
152 %
153 % Compute Original Grain Volume [m^3]
154 for i = 1:n
155     if geom(i,1)==6
156         [gvo(i),s] = ff7perf(geom(i,3),geom(i,2),geom(i,4),0);
157     elseif geom(i,1)==5
158         [gvo(i),s] = ff1perf(geom(i,3),geom(i,2),geom(i,4),0);
159     elseif geom(i,1)==11
160         [gvo(i),s] = ff1dperf(geom(i,3),geom(i,2),geom(i,4),0,deter);
161     end
162 end
163 %
164 tv = [];
165 pv = [];
166 pbv = [];
167 pov = [];
168 xv = [];

```

```

169 vv = [];
170 xrv = [];
171 vrv = [];
172 arv = [];
173 xgcv = [];
174 vgcx = [];
175 agcv = [];
176 xrwfv = [];
177 trwfv = [];
178 vrwfv = [];
179 rv = [];
180 Em = [];
181 Zm = [];
182 data = [];
183 counter = 0;
184 counter2 = 0;
185 pmat = 0*xprobe;
186 %
187 figure(1)
188 figset('p',6.0,3.5,11)
189 hgpl = plot([0 (Lcc)],[0 0]);
190 xlabel('Axial Position [m]')
191 ylabel('Pressure [MPa]')
192 tplotv = [0];
193
194 %
195 while xpr < L % While bullet in barrel
196     counter = counter + 1;
197     %
198     % Start Changing Variables
199     % =====
200     %
201     %
202     xv = ((xgc-Lcn)-xr); % Recoil stroke for vent
203     xpr = (xp - Lcc) - (xgc - Lcn); % Relative Travel of Bullet Down Bore
204     %
205     % Volumes of Gas behind bullet and other locations
206     %
207     Wcb = Ac*(xgc-xr); % Volume between breech and chambrage
208     Wp = Wcb + A*(xp + (Lcc-Lcn) -xr); % Volume behind projectile
209     Wp = A*(xp-xr) + (Ac-A)*(xgc-xr); % Volume Behind Projectile [m^3] eq. 7.2
210     Wgc = Wcb;
211     Ngc = Wgc/Wp;

```

```

212 %
213 % Projectile Bore Resistance (required for pressures)
214 %
215 br = interp1(brm(:,2),brm(:,1),xpr); % 1D table lookup resistance [Pa]
216 %
217 % Pressure to release bullet and breech:
218 %
219 Pss = br(1,1) + Pg; % Pressure to achieve Shot Start
220 % Pshear = Pshear; % Pressure to achieve Breech Start
221 % -----
222 %
223 if vgc == vp % Bore resistance doesn't start until the projectile begins to move
224     br = 0; % The problem is neagive breech pressures from Lagrange if br isn't
                zero'd.

225 end
226 % Projectile Base, Breech Face, and Gun Chambrage Pressure
227 %
228 Pb = [P + Ct*(br + Pg)/(3*mp)]/[1+Ct/(3*mp)]; % Lagrange Eq. 1.4 [Pa]
229 Po = Pb + (Ct/(2*mp))*(Pb -br -Pg); % Lagrange Eq. 3.1 [Pa]
230 Pgc = Pb + Ct/(2*mp)*(1-Ngc.^2)*(Pb - br - Pg); % Corner (13)pp344
231 %
232 % Pressure at Bore Gauges
233 %
234 Wbg = A*(xprobe + (xgc-Lcc) -xr) + (Ac-A)*(xgc-xr); % Probes ride the barrel
                with xgc

235 ind = find(xprobe<Lcc);
236 Wbg(ind) = Ac*(xprobe(ind) + (xgc-Lcc) - xr); % Find chamber probe.
237 Nbg = Wbg/Wp;
238 Pbg = Pb + Ct/(2*mp)*(1-Nbg.^2)*(Pb - br - Pg); % Pressure at probes
239 %
240 ind = find( xp < (xprobe + (xgc-Lcc))); % Find probes bullet hasn't crossed.
241 Pbg(ind) = 0; % Set pressur to zero ahead of bullet.
242 %
243 %
244 % Recoil Resistances:
245 %
246 % Time Based Recoil Resistance Curve (Gun mount aproximation)
247 %
248 if t < RPm(size(RPm,1),2)
249     Fr = interp1(RPm(:,2),RPm(:,1),t); % 1D table lookup resistance [Pa]
250 else
251     Fr = RPm(size(RPm,1),1);
252 end

```

```

253 %
254 % Barrel/Breech Spatial Resistance Curve
255 %
256 if xvv < vrc(size(vrc,1),2)
257     if xvv <= 0 % Don't let breech resistance add to shear.
258         Ffb = 0;
259     else
260         Ffb = interp1(vrc(:,2),vrc(:,1),xvv);
261     end
262 else
263     Ffb = vrc(size(vrc,1),1);
264 end
265 if Ffb > Po;
266     Ffb = Po; % Don't let friction push breech forward, it can't exceed driving
                pressure.
267 end
268 %
269 if ( (Pb > Pss) & (Po > Pshear) ) % After shot and breech start
270     %
271     Pss = 0; % Once shot start is achieved, there is no more shot start
272     Pshear = 0; % Ibid
273     %
274     ap = A*(Pb - br - Pg)/mp; % Projectile Acceleration
275     ar = (Ac*(Ffb - Po))/mr; % Inertial Breech Motion (Should be
                negative)
276     agc = ((Ac-A)*Pgc + A*br + Fr - Ffb*Ac)/mgc; % Gun Chambrage Motion
277     %
278 elseif ( (Pb > Pss) & (Po <= Pshear) ) % After shot-start, before breech shear
279     %
280     Pss = 0; % Once shot start is achieved, there is no more shot start
281     %
282     ap = A*(Pb - br - Pg)/mp; % Projectile Acceleration
283     ar = ((Ac-A)*Pgc + A*br + Fr - Ac*Po)/(mr + mgc); % Closed Breech Gun
                Acc (Should be negative)
284     agc = ar; % -----
285     %
286 elseif ( (Pb <= Pss) & (Po > Pshear) ) % After breech-shear but before shot-
                start
287     %
288     Pshear = 0; % Once breech start is achieved, there is no more shearing
289     %
290     ap = (A*(Pb - Pg) + (Ac-A)*Pgc + ...
291         Fr - Ffb*Ac)/(mp+mgc); % Projectile & Barrel Acceleration

```

```

292     ar = Ac*(Ffb - Po)/mr;           % Inertial breech Acc (Should be negative)
293     agc = ap;                        % -----
294     %
295     else                             % Before breech or shot start, no mass motion, no
                                     recoil.
296         ap = 0;
297         ar = 0;
298         agc = 0;
299     end
300     %
301     % Integration of Acceleration and Velocity into Motion
302     %
303     % Projectile
304     vp = vp + ap*dt; % Integrate acceleration to velocity and [m/s]
305     xp = xp + vp*dt; % Integrate velocity to postion [m]
306     % Breech
307     vr = vr + ar*dt; % Integrate acceleration to velocity and [m/s]
308     xr = xr + vr*dt; % Integrate velocity to postion [m] %
309     % Barrel
310     vgc = vgc + agc*dt; % Integrate acceleration to velocity and [m/s]
311     xgc_old = xgc;
312     xgc = xgc + vgc*dt; % Integrate velocity to postion [m]
313     %
314     % Equation of State:
315     %
316     % Wp = Volume Behind Projectile [m^3] eq. 7.2
317     Wg2 = sum([C.*[1-Z]./rho]); % Volume of unburnt propellant [m^3]
318     Wg3 = sum([C.*b.*Z])+CI*bI; % Covolume of burnt propellant gas [m^3]
319     Wg = Wp - Wg2 - Wg3; % Volume Behind Projectile availabe for gas [m^3]
320     T = (sum([F.*C.*Z]./[g-1])+FI*CI/(gI-1)-Ept-Epr-Ep-Ebr-Er-Ed-Eh)/ ...
321         (sum([F.*C.*Z]./[g-1].*Toi)+FI*CI/((gI-1)*Toi)); % Gas Temp 7.3 [K]
322     mg = sum([C.*Z]) + CI;
323     rhog = mg/(Wp-Wg2); % Gas Density, correcting for grains
324     Rg = (sum([F.*C.*Z]./Toi)+FI*CI/Toi)/mg; % Mass weighted gas R [J/Kg/K]
325     gg = (sum([g.*C.*Z]) + gI*CI)/mg; % Mass Weighted gamma
326     P = mg*Rg*T/Wg; % Mean Gas Pressure 7.1 [Pa]
327     %
328     if counter < 2
329         pig = P;
330         vig = Wg;
331         vubp = Wg2;
332     end
333

```

```

334                                     %%%%%%%%%%
                                     %%%%%%%%%%
                                     %%%%%%%%%%
                                     %%%%%%%%%%
335 if ( xvv > xvent(indv) ) % Combined blowback breech and blowforward barrel
                                     stroke to vent
336     if ~isreal(xrwf)
337         xrwf = xr; % Detect initiation of wave and assign start point.
338         counterrwf = 0;
339     end
340     counterrwf = counterrwf + 1;
341     if xrwf < xgc
342         Wrwf = Ac*(xrwf-xr); % Volume Behind Rarefaction Wavefront
343     else
344         Wrwf = Wcb + A*(xrwf-xgc); %
345     end
346     %
347     % Dont' let Rarefactoin Wave overtake projectile or get out of muzzle
348     if (xrwf >= xp) | (xrwf >= (L + (xgc - Lcn)))
349         xrwf = nan;
350         Wrwf = nan;
351     end
352     Nrwf = Wrwf/Wp;
353     Prwf = Pb + Ct/(2*mp)*(1-Nrwf.^2)*(Pb - br - Pg); % Pressure at Rarefactoin
354                                     Wavefront
355     Trwf = Prwf*(1/rhog)/Rg;
356     arwf = sqrt(gg*Rg*Trwf)/(1 - (Wg3/mg)*rhog); % Sonic Velocity at wave
                                     front
357     vgrwf = vr + Nrwf*(vp-vr); % Gas Velocity at Wave Front
358     vrwf = arwf + vgrwf; % Right Running Characteristic Speed
359     trwf = t;
360     if vrwf < 0
361         vrwf = nan
362     end
363     xrwf = xrwf + dt*vrwf;
364     if isfinite(xrwf)
365         xrwfv = [xrwfv;xrwf];
366         trwfv = [trwfv;trwf];
367         vrwfv = [vrwfv;vrwf];
368     end
369     %end

```



```

370     end
371
372                                     %%%%%%%%%%
                                     %%%%%%%%%%
                                     %%%%%%%%%%
                                     %%%%%%%%%%
373     %
374     %
375     % Heat Transfer to Wall
376     Aw = 2*A + pi*Db*(xp - xr + ((Ac-A)/A)*(xgc-xr)); % Exposed bore area 7.13
                                     [m^2]
377     Tc = (Eh + f*Ebr)/(Cpw*rhow*Aw*Dw) + To; % Temperature of wall 7.20 [K]
378     rhom = (sum(C.*Z)+CI)/(Wg+Wg3); % Mean gas Density 7.17 [Kg/m^3] As
                                     implemented in code
379     Cpm = (sum([F.*g.*C.*Z]/[(g-1).*Toi])+(FI*gI*CI)/((gI-1)*ToI))/
                                     (sum([C.*Z])+CI); % 7.19 [J/(Kg K)]
380     vm = vp/2; % Mean Gas Velocity 7.16 [m/s]
381     h = lambda*Cpm*rhom*vm+ho; % Heat Transfer Coefficient Nordheim et al
                                     eq. 7.14 [W/(m^2 K)]
382     Qd = Aw*h*(T-Tc); % Heat Transfer Rate 7.12
383     %
384     %
385     %
386     Ept = (1/2)*mp*vp^2; % Energy [J] Lost to Projectile Translation 7.4
387     Epr = pi^2*mp*vp^2*Tw^2/4; % Energy [J] Lost to Projectile Rotation 7.5
388     Ep = (1/6)*Ct*vp^2; % Energy [J] Lost to Propellant Translation 7.6
389     Ebr = Ebr + A*br*vp*dt; % Energy [J] Lost to Bore Resistance 7.8
390     Er = (1/2)*mr*vr^2 ...
391     + (1/2)*mgc*vgc^2; % Energy [J] Lost to Recoil 7.9
392     Ed = A*[Ed + vp*Pg*dt]; % Energy [J] Lost to Air Resistance 7.10
393     Eh = Eh + Qd*dt; % Energy [J] Lost to Barrel Heating 7.11
394     %
395     %
396     rd = beta.*[(P/10^6).^alpha]; % Burn Rate 5.2 [m/s]
397     r = r + rd*dt; % Burn Depth [m] between 6.2 and 7.1
398     %
399     for i = 1:n
400         if geom(i,1)==6
401             [gv(i),s] = ff7perf(geom(i,3),geom(i,2),geom(i,4),r);
402         elseif geom(i,1)==5
403             [gv(i),s] = ff1perf(geom(i,3),geom(i,2),geom(i,4),r);
404         elseif geom(i,1)==11

```

```

405         [gv(i),s] = ff1dperf(geom(i,3),geom(i,2),geom(i,4),r,deter);
406     end
407 end
408 Z = 1 - gv./gvo; % mass fraction of propellant that has burned
409 %
410 if rem((counter-1),10)==0
411     counter2 = counter2+1;
412     data = [data;[t ap vp xp P Pb Po]];
413     % xp/(L + Lcc + xgc - Lcn)
414 end
415 tv = [tv;t];
416 pv = [pv;P];
417 pbv = [pbv;Pb];
418 pov = [pov;Po];
419 xv = [xv;xp];
420 vv = [vv;vp];
421 xrv = [xrv;xr];%
422 vrv = [vrv;vr];
423 arv = [arv;ar];
424 agcv = [agcv;agc];
425 xgcv = [xgcv;xgc];%
426 vgc = [vgcv;vgc];%
427 rv = [rv;r]; %
428 Em = [Em;[Ept Epr Ep Ebr Er Ed Eh]];
429 Zm = [Zm;Z];
430 pmat = [pmat; Pbg];
431 %
432
433 % Plot some results
434 npgc = 50;
435 if (counter/npgc) == round(counter/npgc)
436     xgv = linspace(xr,xp,80); % X gradient vector
437     Wgv = A*(xgv-xr) + (Ac-A)*(xgc-xr);
438     ind = find(xgv<xgc);
439     Wgv(ind) = Ac*(xgv(ind)-xr);
440     Ngv = Wgv/Wp;
441     P xv = Pb + Ct/(2*mp)*(1-Ngv.^2)*(Pb - br - Pg);
442     figure(1)
443     hgpls = line(xgv,P xv/1e6);
444     hgpl = [hgpl;hgpls];
445     set(hgpl,'Color','b');
446     tplotv = [tplotv;t];
447 end

```

```

448
449     %
450     t = t+dt;
451 end
452
453
454
455
456
457
458
459
460
461
462
463
464
465
466
467
468
469
470
471
472
473
474
475
476
477 %
478 axis([-0.5 3.5 0 430]);
479 hl = line((xv),pbv/1e6); % Add base pressure to plot.
480 set(hl,'LineStyle','-','LineWidth',2,'Marker','none','MarkerSize',5,'Color','r');
481 hlr = line((xrv),pov/1e6); % Add base pressure to plot.
482 set(hlr,'LineStyle','-','Marker','none','MarkerSize',5,'Color','k');
483 legend([hgpls;hl],'Pressure Gradient's','Projectile Base Pressure')
484 print -deps -tiff -r300 H:\PhD\dissertation\Media\MlabPlots\R2d1_PPX.eps
485 %
486 pmat(1,:) = [];
487 mv = max(vv);
488 pmax = max(pov);
489 %
490 pmz = pbv(length(pbv));

```

```

491 %
492 % Burnout Compuation:
493 if Z < 1;
494     Zt = -1;
495 else
496     ind = find (Zm(:,1)<1);
497     Zt = tv(max(ind))/max(tv);
498 end
499 %
500 % % deter = [0.70;130e-6];
501 tdID = nan;
502 tdOD = nan;
503 if max(r) > (deter(2)/2)/deter(1);
504     [y,ind] = min(abs(rv-(deter(2)/2)/deter(1)));
505     tdID = tv(ind);
506     if max(r) > deter(2)/deter(1);
507         [y,ind] = min(abs(rv-deter(2)/deter(1)));
508         tdOD = tv(ind);
509     end
510 end
511
512 Ec = sum([C.*F./(g-1)]) + CI*FI/(gI-1);
513 %
514 % Ept = (1/2)*mp*vp^2;    % Energy [J] Lost to Projectile Translation 7.4
515 %Epr = pi^2*mp*vp^2*Tw^2/4;% Energy [J] Lost to Projectile Rotation 7.5
516 %Ep = (1/6)*Ct*vp^2;    % Energy [J] Lost to Propellant Translation 7.6
517 %Ebr = Ebr + A*br*vp*dt; % Energy [J] Lost to Bore Resistance 7.8
518 %Er = (1/2)*mr*vr^2 ...
519 % + (1/2)*mgc*vgc^2; % Energy [J] Lost to Recoil 7.9
520 %Ed = A*[Ed + vp*Pg*dt]; % Energy [J] Lost to Air Resistance 7.10
521 %Eh = Eh + Qd*dt;      % Energy [J] Lost to Barrel Heating 7.11
522 %
523 %
524 fid = fopen(['H:\PhD\dissertation\MFiles\Tables\IB35\CB\Ptrans.txt'],'wt+');
525 fprintf(fid,'%5.2f',round([Ept/Ec]*10000)/100);
526 st = fclose(fid);
527 fid = fopen(['H:\PhD\dissertation\MFiles\Tables\IB35\CB\Prot.txt'],'wt+');
528 fprintf(fid,'%5.2f',round([Epr/Ec]*10000)/100);
529 st = fclose(fid);
530 fid = fopen(['H:\PhD\dissertation\MFiles\Tables\IB35\CB\Friction.txt'],'wt+');
531 fprintf(fid,'%5.2f',round([Ebr/Ec]*10000)/100);
532 st = fclose(fid);
533 fid = fopen(['H:\PhD\dissertation\MFiles\Tables\IB35\CB\Recoil.txt'],'wt+');

```

```

534 fprintf(fid,'%5.2f',round([Er/Ec]*10000)/100);
535 st = fclose(fid);
536 fid = fopen(['H:\PhD\dissertation\MFiles\Tables\IB35\CB\Propellant.txt'],'wt+');
537 fprintf(fid,'%5.2f',round([Ep/Ec]*10000)/100);
538 st = fclose(fid);
539 fid =
        fopen(['H:\PhD\dissertation\MFiles\Tables\IB35\CB\Heatv
        sProjo.txt'],'wt+');
540 fprintf(fid,'%5.2f',round([Eh/Ept]*10000)/100);
541 st = fclose(fid);
542 fid =
        fopen(['H:\PhD\dissertation\MFiles\Tables\IB35\CB\Heatv
        sProjo.txt'],'wt+');
543 fprintf(fid,'%5.2f',round([Eh/Ept]*10000)/100);
544 st = fclose(fid);
545 fid =
        fopen(['H:\PhD\dissertation\MFiles\Tables\IB35\CB\Muzzl
        eVelocity.txt'],'wt+');
546 fprintf(fid,'%5.0f',round(max(vv)));
547 st = fclose(fid);
548 fid =
        fopen(['H:\PhD\dissertation\MFiles\Tables\IB35\CB\MaxP
        ressure.txt'],'wt+');
549 fprintf(fid,'%4.0f',round(max(pov)/1e6));
550 st = fclose(fid);
551 fid = fopen(['H:\PhD\dissertation\MFiles\Tables\IB35\CB\TBurnout.txt'],'wt+');
552 fprintf(fid,'%4.2f',(round(Zt*max(tv)*1e5)/1e2));
553 st = fclose(fid);
554 % deter = [0.70;130e-6];
555 fid =
        fopen(['H:\PhD\dissertation\MFiles\Tables\IB35\CB\Detter
        entID.txt'],'wt+');
556 fprintf(fid,'%4.2f',(round(tdID*1e5)/1e2));
557 st = fclose(fid);
558 fid =
        fopen(['H:\PhD\dissertation\MFiles\Tables\IB35\CB\Detter
        entOD.txt'],'wt+');
559 fprintf(fid,'%4.2f',(round(tdOD*1e5)/1e2));
560 st = fclose(fid);
561 %
562 figure(2)
563 figset('p',6.0,3.5,11)
564 %

```

```

565 hp = plot(tv*1e3,xv*100);
566 set(hp,'LineStyle','-.','LineWidth',2,'Marker','none','MarkerSize',5,'Color','r')
567 hold on;
568 if 0
569     load xpoly2.mat;
570     load TestResults.mat;
571     for i = testind
572
573         tx1 = tv - max(tv) + te(i);
574         xpt1 = polyval(polymatxp(i,:),tx1);
575         [y,ind] = min(xpt1);
576         xpt1(1:ind) = nan*xpt1(1:ind);
577         % hxp = line(tv*1e3,xpt1*100);
578         hxp2 = line([matxpt(i,:)+ max(tv) - te(i)]*1e3,xprobe(2:14)*100);
579         set(hxp2,'LineStyle','none','Marker','o','Color','b')
580         xrwfx = polyval(polymatrwf(i,:),tx1);
581         % hrwf = line(tv*1e3,xrwfx*100);
582         hrwf2 = line([matrwft(i,:)+ max(tv) - te(i)]*1e3,xprobe*100);
583         set(hrwf2,'LineStyle','none','Marker','^','Color','r')
584     end
585 end
586 %
587 %
588 hg = plot(tv*1e3,pbv/1e6);
589 set(hg,'LineStyle',':', 'Color','k')
590 hl = plot(tv*1e3,pmat(:,1:14)/1e6);
591 %
592 if 0 %(ar ~= agc)
593     tventtest = mean(matrwft(testind,1));
594     tventib = interp1(xrwfv, trwfv, xprobe(1));
595     dtvent = tventib-tventtest;
596     hr = plot(trwfv*1e3,xrwfv*100,'r-');
597     set(hr,'LineWidth',2)
598 end
599 hold off;
600 %
601 ylabel('Pressure [MPa]');
602 xlabel('Time [ms]');
603 av1 = [0 5 0 425];
604 ax1 = gca;
605 axis(av1)
606 % hl = legend('{x_p}','{P_b}','{P_1}','{P_2}','{P_3}',...
607 %     '{P_4}','{P_5}','{P_6}','{P_7}','{P_8}','{P_9}',...

```

```

608 % '{P_{10}}','{P_{11}}','{P_{12}}','{P_{13}}',2);
609 %
610 hL = legend([hl(1);hg;hp],'Pressure Probes','Base Pressure','Projectile Travel')
611 %
612 ax2 = axes('Position',get(ax1,'Position'),...
613     'XAxisLocation','bottom',...
614     'YAxisLocation','right',...
615     'Color','none',...
616     'XColor','k',...
617     'YColor','k');
618 hlxp = line(tv*1e3,xv);
619 set(hlxp,'LineStyle','-','Marker','.', 'MarkerSize',5,'Color','r','Visible','off')
620 av2 = [av1(1:2),av1(3:4)/100];
621 axis(av2)
622 ylabel('Projectile Travel [m]')
623 % title(ptitle)
624
625 print -deps -tiff -r300 H:\PhD\dissertation\Media\MlabPlots\R2d1_PXT.eps
626
627
628
629 % Rarefaction Wave Back From Muzzle
630 %
631 xrwf = max(xv);
632 xrwfv = 0*xv;
633 vrwfv = 0*vv;
634 vgrwfv = 0*vv;
635 arwfv = 0*vv;
636 xrwfv = nan*xv;
637 vrwfv = nan*vv;
638 vgrwfv = nan*vv;
639 arwfv = nan*vv;
640 %
641 i = size(tv,1);
642 while xrwf>xr
643     t = tv(i);
644     xp = xv(i);
645     vp = vv(i);
646     xr = xrv(i);
647     vr = vrv(i);
648     xgc = xgcv(i);
649     Pb = pbv(i);
650     vc1 = A*(xp-xr) + (Ac-A)*(xgc-xr); % Total Volume behind projo

```

```

651 vc2 = sum([C.*[1-Z]./rho]);% Volume of unburnt propellant [m^3]
652 vc3 = sum([C.*b.*Z])+CI*bI;% Covolume of burnt propellant gas [m^3]
653 vc = vc1 - vc2 -vc3; % Volume Behind Projectile available for gas [m^3]
654 mg = sum([C.*Z]) + CI; % Mass of gases evolved.
655 Rg = (sum([F.*C.*Z]./Toi)+FI*CI/ToI)/mg; % Mass weighted gas R [J/Kg/K]
656 gg = (sum([g.*C.*Z]) + gI*CI)/mg; % Mass Weighted gamma
657 br = interp1(brm(:,2),brm(:,1),(xp-xr)); % 1D table lookup resistance [Pa]
658 %
659 Qc = Ac*(xgc - xr); % Volume behind chambrage
660 xcc = Qc/Ac; % Constant Bore Length behind Chambrage
661 %
662 if xrwf > xcc
663 % Before the chambrage, the bore is a constant bore gun
664 Q = A*(xrwf-xr) + (Ac-A)*(xgc-xr); % Volume Behind Rarefaction Wave
665
666 else
667 % In the chamber we need to map the gas properties
668 % from the long Langrange chamber to the real one.
669 %
670 Q = Ac*(xrwf-xr); % Total Volume Behind Rarefaction Wave Front
671 end
672 Prwf = Pb + Ct/(2*mp)*(1-(Q/vc1).^2)*(Pb - br - Pg);
673 Trwf = Prwf*(vc/mg)/Rg;
674 arwf = sqrt(gg*Rg*Trwf)/(1 - vc3/vc); % Sonic Velocity at wave front
675 vgrwf = vr + Q/vc1*(vp-vr); % Gas Velocity at Wave Front
676 vrwf = arwf + vgrwf; % Right Running Characteristic Speed
677 xrwf = xrwf - dt*vrwf;
678 %
679 xrwfv(i) = xrwf;
680 vrwfv(i) = vrwf;
681 vgrwfv(i) = vgrwf;
682 arwfv(i) = arwf;
683 i = i-1;
684 end
685
686
687 figure(3)
688 figset('p',6.0,7,11)
689 subplot(211);
690 hp = plot(tv*1e3,xv,'b-',tv*1e3,xrwfv,'r-',t*1e3,xv(i),'b^', ...
691 t*1e3,0,'ro',max(tv)*1e3,max(xv),'rs',...
692 [t t]*1e3,[0 xv(i)],'k:');
693 axis([0 5 0 3.25])

```



```

694 ylabel('Axial Position [m]')
695 legend('Projectile Travel','Rarefaction Wave-Front', ...
696        ['Projectile ' num2str(round((xv(i)-min(xv))/(max(xv)-min(xv))*1000)/10) '% of
        Travel'], ...
697        ['Release at ' num2str(round(t*1e5)/1e2) ' ms'], ...
698        ['Shot-Exit at ' num2str(round(max(tv)*1e5)/1e2) ' ms'],2)
699 subplot(212);
700 plot(tv*1e3,vv,'b-',tv*1e3,vrwf,'r-.',tv*1e3,arwf,'m:',tv*1e3,vgrwf,'g--')
701 axis([0 5 0 2010])
702 ylabel('Velocity [m/s]')
703 xlabel('Time [ms]')
704 legend('Projectile Velocity','Rarefaction Wave-Front', ...
705        ['Sonic Velocity Contribution'], ...
706        ['Gas Velocity Contribution'],2)
707
708 print -deps -tiff -r300 H:\PhD\dissertation\Media\MlabPlots\R2d1_RWFXT.eps

```